Alma Mater Studiorum – Università di Bologna
in cotutela con Università di RWTH Aachen

DOTTORATO DI RICERCA IN

CHIMICA

Ciclo XXX°

Settore Concorsuale: 03/C2

Settore Scientifico Disciplinare: CHIM/04

OPEN-CELL METALLIC FOAMS COATED BY ELECTRODEPOSITION AS STRUCTURED CATALYSTS FOR ENERGY AND ENVIRONMENTAL APPLICATIONS

Presentata da: **Phuoc Hoang Ho**

Coordinatore Dottorato

Prof. Aldo Roda

Supervisore

Prof. Giuseppe Fornasari

Co-supervisore

Asst. Prof. Patricia Benito

Supervisore

Prof. Regina Palkovits

Esame finale anno 2018

University of Bologna

Department of Industrial Chemistry

RWTH Aachen University

ITMC

Open-cell metallic foams coated by electrodeposition as structured catalysts for energy and environmental applications

DOCTORAL THESIS

SINCHEM - Sustainable Industrial Chemistry

Erasmus Mundus - Joint Doctoral Research Program

Cycle XXX of doctoral program in

Chemistry

Coordinator: Prof. Aldo RODA

Supervisor (HOME): Prof. Giuseppe FORNASARI

Asst. Prof. Patricia BENITO

Supervisor (HOST): Prof. Dr. Regina PALKOVITS

PHUOC HOANG HO

May 2018

"Open-cell metallic foams coated by electrodeposition as structured catalysts for energy and environmental applications"

Der Fakultät für Mathematik, Informatik und Naturwissenschaften der RWTH Aachen University vorgelegte Dissertation zur Erlangung des akademischen Grades eines Doktors der Naturwissenschaften

von

M.Sc. HỒ HOÀNG PHƯỚC

aus *BẾN TRE, VIỆT NAM*

ACKNOWLEDGEMENTS

Inayat for his valuble time in translation the abstract of my thesis into German. I would like to appreciate Prof. Domenica Tonelli, Prof. Erika Scavetta, Dr. Marco Monti, Ylea Vlamidis and other members in "analitica Laboratorio" for the help provided during the preparation of the catalysts. I would also thank Matteo Ambrosetti, Pio Giuseffi for giving a great time during my mobility at Politecnico di Milano.

Without the help from Professor Regina Palkovits's group, I could not complete my research mobility at RWTH Aachen University. Special thanks to Chalachew Mebratu for giving nice discussion and "beer" time in Aachen, and my sincere colleague Christian Landini for all things that he supported me from Bologna to Aachen. Thanks to Dr. Magdalena Jablonska for her help in both doing the setup of my experiment and guiding me a new topic of N_2O decomposition, and other members of the group for wonderful time with a lot of cakes and of course German beer in the Lab. I am in Johannes Niemeier's debt for correcting my German abstract more than perfect. I would also like to thank Dr. Stefanie Mersmann and Dr. Stefan Palkovits for their support in the official procedure.

In addition, I would like to acknowledge my family and friends who supported me during my time in Europe. Thank my grandmother, Mom, Dad, my young sister as well as my cousin Ms. Ho Ngoc Hao and her family in Germany for their constant love and help. Thanks to Ha V. Le my brother and bestie for his instant support in both work and life. It is not a forgettable memory about a twelve-day journey through five fantastic places in summer 2015, and other trips with Dang Khoa and Kim Hoang. I owe a debt of gratitude to all my close friends: my brother Phuoc, Long, Duy, Duc – Trang, Phuc, Thom, Khoa, Trinh, Thang, Canh, Do, Bach for their constant concern. Sincerely thank to Long for processing the format of my thesis; Phuc and Thom for their help in the design of nice images using SOLIDSWORK. Thanks to other friends in Italy: Binh – Nga, Le Hong Lam, Tinh, Nhan, Man, Meggi Quynh and other Vietnamese families in Bologna for an enjoyable time of my life in Italy.

Finally, I would like to thank SINCHEM program for giving me a great opportunity of study in Europe. How nice is the program! Thanks to Professor Stefania Albonetti – fantastic coordinator of the program. She always takes care me and other students like a mom for all things from the life and academic issues that new students, especially foreigner, usually face at the beginning of Ph.D. study. Thanks to all SINCHEM guys for great time we stay together. I am in debt from all the secretaries and administrative staffs involving in the SINCHEM program at the University of Bologna, RWTH Aachen, and Politecnico di Milano: Marina Grandini, Rosanna Antonino, Angela Maritato, Cristina Caretti, Professor Alessandra Beretta, and Dr. Stefanie Mersmann.

Bologna, 18th December 2017.

Phuoc Hoang Ho.

ABSTRACT

Structured catalysts based on open-cell metallic foams offer a great potential for process intensification of fast, highly exo-/endothermic and diffusion-controlled catalytic processes. For the development of such structured catalysts, the choice of coating technique used to deposit the active phase on the foam surface is very crucial, as the coating technique strongly influences the properties of the coated layer and in turn the activity/selectivity of the obtained structured catalysts. In this regard, the *electro-base generation method* has been proposed as a promising option that allows for coating of (even small pore) foams with avoidance of pore clogging which is a common drawback of conventional wash-coating technique. The thesis aims to improve the electrodeposition method and widen its applicability in the preparation of structured catalysts.

In this respect, the first part of this thesis focuses on the investigation of the electrochemical processes, taking place during the electrodeposition of Mg-Al hydrotalcite, thereby studying the role of nitrate (of respective cations) concentration and reduction. Understanding the reactions involved in the electrodeposition helps to identify the main steps that determine the properties of the coating, and provides possible solutions to improve the method. In fact, by using a new electrochemical set-up, the control on the electrodeposition is achieved in terms of homogeneity and composition of the coated layer.

In the second part of this thesis, a modified method for the electrodeposition of active phase on metallic foams is proposed and its applicability is demonstrated in the preparation of following catalyst systems for the use in energy and environmental catalytic processes: i) Rh/Mg/Al on both FeCrAl and NiCrAl foams for the catalytic partial oxidation of CH_4, ii) Pd-CeO_2 on FeCrAl foam (different pore sizes) for oxidation of CO, and iii) Rh/Mg/Al, Rh-CeO_2, and Co_3O_4 on FeCrAl foam for catalytic decomposition of N_2O. The aforementioned catalyst systems exhibit satisfactory performances in the respective test reactions, thus confirming the potential of using electrodeposition in preparing the structured catalysts.

SOMMARIO

I catalizzatori strutturati basati su schiume metalliche a celle aperte offrono una grande opportunità per l'intensificazione di processi catalitici veloci, fortemente eso/endotermici e controllati dalla diffusione. Per lo sviluppo di tali catalizzatori strutturati, la scelta di una tecnica di ricoprimento, utilizzabile per depositare la fase attiva sulla superficie della schiuma, è cruciale, poiché questa tecnica influisce fortemente sulle proprietà dello strato di ricoprimento e in genere sull'attività/selettività dei catalizzatori strutturati ottenuti. In considerazione di questo, il *metodo di elettro-generazione di basi* è stato proposto come una promettente opzione, che permette il ricoprimento di schiume (anche a pori piccoli) evitando il blocco dei pori, che è lo svantaggio usuale della tecnica convenzionale di washcoating.

Questa tesi ha lo scopo di perfezionare il metodo di elettrodeposizione e ampliarne l'applicabilità nella preparazione dei catalizzatori strutturati.

A tal fine, la prima parte di questo lavoro si concentra sull'analisi dei processi elettrochimici, che avvengono durante l'elettrodeposizione di Mg-Al idrotalcite, attraverso lo studio del ruolo della concentrazione e della riduzione dei nitrati (dei rispettivi cationi). La comprensione delle reazioni coinvolte nell'elettrodeposizione aiuta ad identificare le principali fasi, che determinano le proprietà del ricoprimento, e a fornire le possibili soluzioni per il miglioramento del metodo. Infatti, mediante l'uso di una nuova apparecchiatura elettrochimica, è stato raggiunto il controllo dell'elettrodeposizione in termini di omogeneità e composizione dello strato di ricoprimento.

Nella seconda parte di questo lavoro, un metodo modificato per l'elettrodeposizione della fase attiva su schiume metalliche è stato proposto e la sua applicabilità dimostrata nella preparazione dei seguenti sistemi catalitici per l'uso in processi energetici e ambientali: i) Rh/Mg/Al sia su schiuma FeCrAl che NiCrAl per l'ossidazione parziale catalitica di CH_4; ii) Rh/Mg/Al, $Rh-CeO_2$ e Co_3O_4 su schiuma FeCrAl per la decomposizione catalitica di N_2O; iii)

Pd-CeO$_2$ su schiuma FeCrAl (con differenti dimensioni dei pori) per l'ossidazione di CO. Tali sistemi catalitici, preparati per elettrodeposizione, presentano attività soddisfacenti nelle rispettive prove di reazione, così confermando la potenzialità della tecnica di elettrodeposizione nella preparazione dei catalizzatori strutturati.

KURZBESCHREIBUNG

Strukturierte Katalysatoren, die auf offenzelligen metallischen Schäumen basieren, besitzen großes Potential für die Prozessintensivierung von schnellen, stark sowohl exo- als auch endothermen und diffusionskontrollierten katalytischen Prozessen. Für die Entwicklung solcher strukturierter Katalysatoren ist die Wahl der Beschichtungsmethode für das Aufbringen der aktiven Phase auf der Schaumoberfläche enorm wichtig, da die Beschichtungstechnik einen starken Einfluss auf die Eigenschaften der Beschichtung und damit die Aktivitä und Selektivität des erhaltenen strukturierten Katalysators hat. In diesem Zusammenhang wurde die "*electro-base generation method*" (*elektrolytische Abscheidung*) als eine vielversprechende Möglichkeit zum Beschichten von (selbst kleinporigen) Schäumen vorgeschlagen, die das bei konventionellen wash-coating Techniken üblicherweise auftretende Problem der Porenverstopfung vermeidet.

Das Ziel der vorliegenden Arbeit ist es, die elektrolytische Abscheidungsmethode zu verbessern und ihre Anwendbarkeit auf die Herstellung strukturierter Katalysatoren auszuweiten.

Im ersten Teil der Arbeit liegt der Fokus auf der Untersuchung der elektrochemischen Prozesse, die während der elektrolytischen Abscheidung von Mg-Al-Hydrotalciten ablaufen. Dabei wird analysiert, welchen Einfluss die Konzentration und Reduktion des Nitrates in den entsprechenden Ausgangssalzen auf den Abscheidungsprozess haben. Dabei müssen die Reaktionen der elektrochemischen Beschichtung verstanden werden, um Hauptprozesse zu ermitteln, die die Eigenschaften der Beschichtung bestimmen, um Möglichkeiten zur Methodenverbesserung zu finden. Tatsächlich konnte durch die Verwendung eines neuartigen elektrochemischen Setups ein Fortschritt in Bezug auf Homogenität und Zusammensetzung der Beschichtung erreicht werden.

Im zweiten Teil der Arbeit wird eine modifizierte Methode für die elektrochemische

Abscheidung der aktiven Phase auf metallischen Schäumen vorgeschlagen und die Anwendbarkeit dieser Methode wird für die Herstellung der folgenden Katalysatorsysteme, die für energetische und umweltrelevante Prozesse verwendet werden, demonstriert: i) Rh/Mg/Al sowohl auf FeCrAl als auch NiCrAl Schäumen für die katalytische partielle Oxidation von Methan; ii) Pd-CeO$_2$ auf FeCrAl Schaum (verschiedene Porengrößen) für die Oxidation von CO; und iii) Rh/Mg/Al, Rh-CeO$_2$ und Co$_3$O$_4$ auf FeCrAl Schaum für die katalytische Zersetzung von N$_2$O. Die zuvor genannten Katalysatorsysteme, die durch elektrochemische Abscheidung hergestellt wurden, zeigen zufriedenstellende Ergebnisse in den entsprechenden Testreaktionen. Damit bestätigen sie das Potential der elektrochemischen Abscheidungsmethode für die Herstellung strukturierter Katalysatoren.

Table of content

List of Tables

List of Figures and Schemes

Chapter 1. Introduction

Extension of this chapter has been submitted to Elsevier for Chapter 15 in the book Horizons in Sustainable Industrial Chemistry and Catalysis.

P.H. Ho, M. Ambrosetti, G. Groppi, E. Tronconi, R. Palkovits, G. Fornasari, A. Vaccari, P. Benito, Structured catalysts based on open-cell foams for energy and environmental applications.

1.1 Metallic foams and sustainable industrial chemistry

Improving the sustainability while maintaining the competitiveness of the chemical industry is one of the critical goals highlighted in the roadmap of science and technology on catalysis for Europe to "move ahead for sustainable future" [1]. Forced by the economic competition, environmental problems and the depletion of the fossil fuels, it is necessary to move to new refinery and petrochemistry in which the use of CH_4, light olefins, and biomass are preferable. To do that a broad approach has been proposed emphasizing on an innovation in catalysis taking the shape through push and pull factors. The former relates to the growing insight into the molecular basis of catalysis, while the latter concerns not only the demand to increase the energy efficiency and reduce waste chemicals, but also the growing demand in industry to build up novel production routes for chemicals and fuels to improve competitiveness [2]. To reach the pull factors, several aspects have been proposed, which could be classified into finding new approaches/processes or improvement of existing processes. Although new developments are more prioritized (e.g. substitution of fossil fuel derived products, the use of biomass, production of renewable H_2, CO_2 utilization, integration of solar energy to chemical and fuels production), implementing the improvements is important in several existing processes, e.g. hydrogen and syngas technology (steam reforming, catalytic partial oxidation, water gas shift reaction), chemicals production (selective oxidation, methanol synthesis, CO_2 methanation, and Fischer-Tropsch synthesis). One example of scenario about development and improvement in petrochemistry is presented in Fig. 1.1.
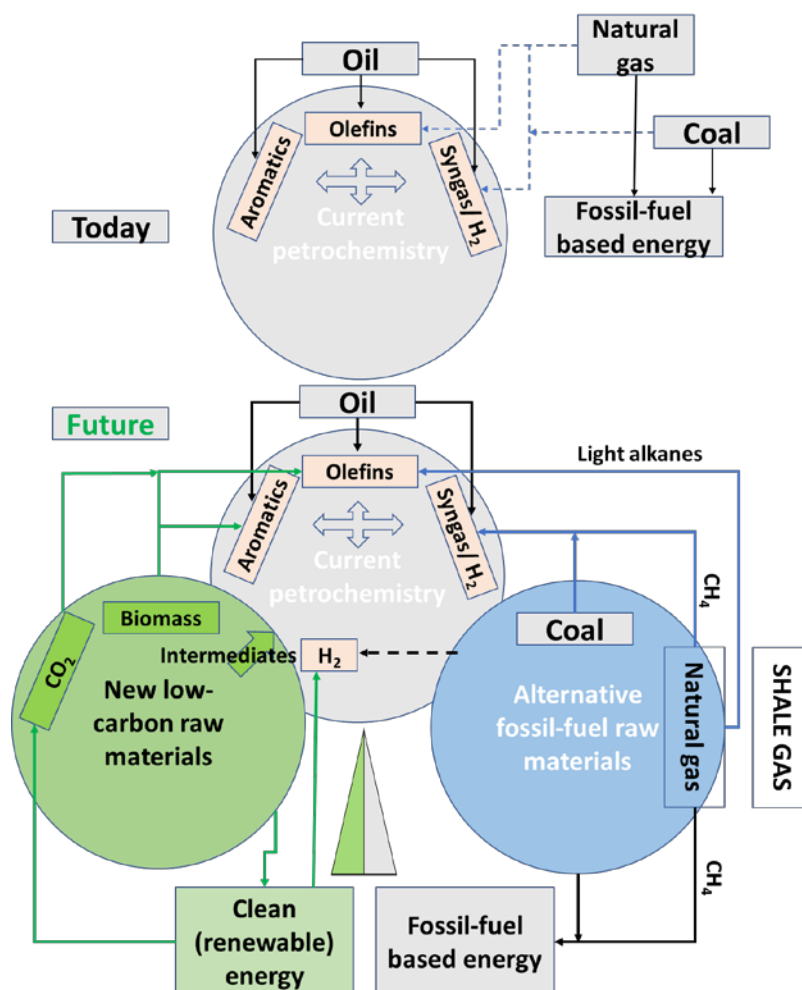
Figure 1.1. Evolution in the scenario of raw materials from current petrochemistry to the future scenario for a sustainable and low carbon chemical production (Adapted from [3] with permission of The Royal Society of Chemistry).

In this context, process intensification has a key role to achieve an improvement toward a more economic and sustainable chemistry for the future since it can be applied to all the scales in chemical processes, i.e. from molecular level to meso- and macro scale [4]. Process intensification (PI) is a broad term and many definitions have been proposed since it was introduced in 1970's [5]. In a simplistic view, PI is known as qualitative statements like "cheaper, smaller, cleaner" or related to two common words "innovative" and "substantial", which show the characterization and target of the PI [4]. For chemists and chemical engineers, PI concepts based on the major manufactures of PI equipment mainly focus on how to enhance transport rate and give every molecule the same processing experience. PI tends to suggest

either a drastic improvement by re-designing conventional unit operations ("hardware" technologies) or a development of new process-control methods ("software" technologies) (Fig. 1.2) and hence this could help to: i) improve the control of reactor kinetics giving higher selectivity/reduced waste products, ii) higher energy efficiency, iii) reduce capital costs, and iv) reduce inventory/improve intrinsic safety/fast response times.
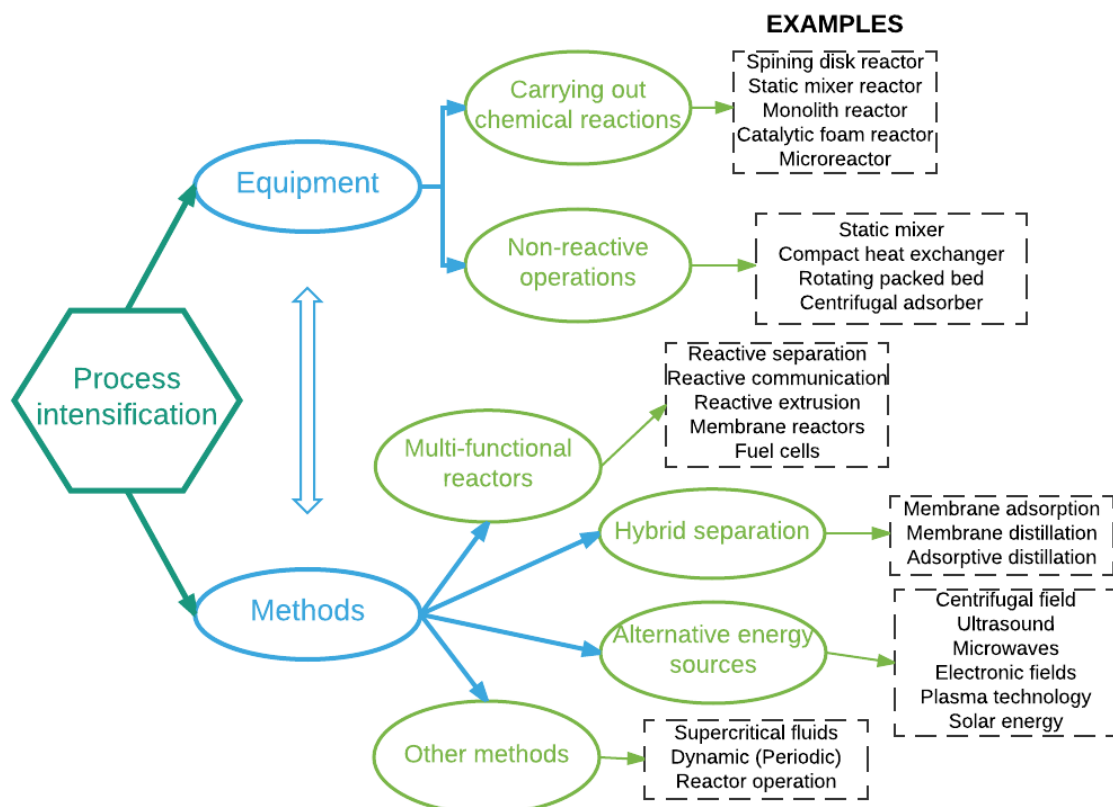
Figure 1.2. Process intensification and its component (Adapted from [4]).

In heterogeneous catalytic processes, structured catalysts and reactors have been proposed as a great opportunity for implementation of some process solutions into industrial practice, such as to enhance the heat and mass transfer rate as well as to reduce the pressure drop [6, 7]. Structured catalysts and reactors are wide research topics involving both chemistry and chemical engineering fields. They are like "a big game" dealing with 3D structured supports with different shapes coated with several types of catalytic materials. Currently both academia and industry are involved in production of 3D supports, development of coating techniques, applications in catalytic processes, and construction of structured reactors. Although ceramic

honeycomb monoliths, a standard representative of structured catalysts, have been extremely successful in commercial application for environmental treatments of exhaust emissions from automobiles and power stations since 1980's, their extensive usage in other catalytic processes is still limited due to two main issues: i) relatively lower load of catalytic active phase compared to that in a bed of bulk pellets with the same volume ii) limitations in the temperature control in several endo-/exothermic processes [8]. These issues could be overcome by metallic open-cell foams. Other possible application of metallic foams is as 3D electrodes, a novel electrode concept in electrocatalysis. This opens a wide range of applications of metallic foams in H_2 production by H_2O electrolysis, conversion of biomass based materials, fuel cells, electro-organic synthesis as proposed in the roadmap in science and catalysis of European near future [6]. Although metallic foams have been recognized as potential supports in structured catalysts, bringing them in real catalysis applications needs simultaneous developments in the coating technique and reactor design [9].

1.2 State of art

1.2.1 Structured catalysts

Structured catalysts are composed of a support, pre-shaped in a given 3D structure, and a layer of catalytic material [10], Fig. 1.3. The selection of the support (shape and material) depends on the process applications, e.g. operation temperature, suitability of corrosion tolerance, chemically inert, turning of transport properties while the coating properties (adhesion, composition, loading, dispersion of active phase) determine the reactivity of the structured catalyst in a given reaction. Almost all important catalytic materials or supports, i.e. zeolite, ceria, alumina, and mixed oxides, which can incorporate a large variety of active phases from transition to noble metals, can be coated, and hence structured catalysts with a wide range of applications prepared (Fig. 1.3).

Structured supports are made by ceramic (Al_2O_3, cordierite, and SiC), metallic (single elements, i.e. Al, Ni, Cu, Co, or alloy, i.e. stainless steel, Inconel, FeCrAl, NiCrAl, FeNiCrAl), and carbonaceous materials (activated carbon, reticulated vitreous carbon), adopting several 3D configurations, i.e. honeycomb, corrugated sheet, gauze, foam, fiber, knitted wire packing, or periodic open celluar structures (POCS) [11] (Table 1.1). These materials fulfills a wide range of competitive requirements in the design of reactors (light weight, mechanical strength) or process applications (corrosion resistance, enhancement of heat transfer). On the other hand, the geometry of the support determines the dynamic parameters of the fluids, which are important for the mass and heat transfer [12-14].
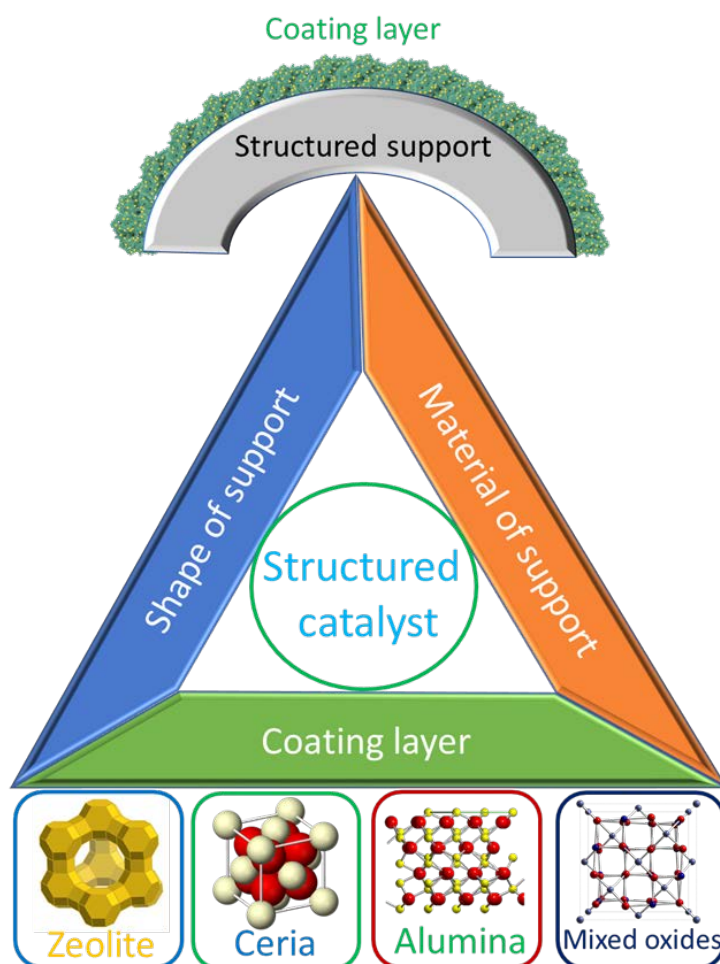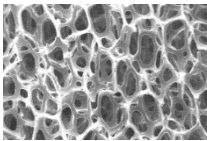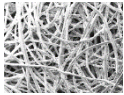
Figure 1.3. Overview of structured catalysts.

Table 1.1. Commercial structured supports made of ceramic, metallic and carbonaceous materials

Shape	Material	Reference
Honeycomb monolith	Cordierite, mullite, Al_2O_3, SiC, SiO_2 Cu, Al, Fe FeCrAl, FeNiCrAl, SS 304, Aluminum alloy Activated carbon	[15-21]
Open-cell foam	Al_2O_3, SiC, Si_3N_4, $B_{12}C_3$, BN, ZrO_2 Cu, Co, Fe, Ni, Al, Zn, Ag*, Sn*, Au* NiFeCrAl, Inconel, NiCrAl, FeCrAl, Stainless steel AISI 316, Zamak 410 (Zn/Al/Cu/Mg), Monel, Aluminum alloy Reticulated vitreous carbon	[22-25] * Not yet commercialized
Gauze	90 % Pt/Rh Al	[26]
Wire-mesh	Al_2O_3 Fe, Pd/Ni, Pt/Ir Monel alloy 400, SS AISI 304 316, 904; Inconel, Monel, Hastelloy, FeCrAl	[23, 27, 28]
Corrugated sheet	Al_2O_3 Cu, Al NiCrAl, FeCrAl, NiFeCrAl Inconel, Steel, Stainless Steel, Brass	[29, 30]
Fiber	Al_2O_3, Al_2O_3/SiO_2, $Al_2O_3/SiO_2/B_2O_3$, SiC, FeCrAl	[23]

Honeycombs with square, triangle, or circular parallel channels generate a laminar flow path without radial-mixing of the gas, leading to some limitations in mass and heat transfer and therefore, in the control of temperature in endo-/exothermic chemical processes [8]. The

extrusion is well consolidated technology to obtain ceramic honeycombs, but is quite challenging to produce metallic ones. Therefore, the rolling of corrugated sheets has been introduced (Table 1.1). Nevertheless, these corrugated sheets lack of cross-sectional continuity of the solid matrix, even if the sheets/layers are welded together [31]. Hence, corrugated or wire-mesh monoliths perform radial thermal conductivities much worse than those obtained by the extrusion. It is also noted that the wire-mesh could provide relatively a large geometrical surface area and less pressure drop than other types of monoliths. Knitted gauze is a special case made of 10 % Rh/Pt used for NH_3 oxidation reaction in nitric acid plant. Considering mass and heat transfer issues, open-cell foams are the most relevant structured supports to overcome them.

Open-cell foams are 3D cellular materials made of interconnected solid struts, which enclose cavities (the cells), communicating by windows (the pores) (Fig. 1.4). They provide a disruptive and tortuous flow path and hence an exceptional mixing as well as supply or release of the heat to/from the surface especially in case of metallic foams. In other words, metallic foams can overcome some issues of the honeycomb monoliths, still maintaining and even improving their advantages. This type of materials has been commercialized in the past two decades by more than 30 companies all over the world [32], and several types of materials at acceptable quality and cost levels are available [33-35]. The choice of the open-cell foam metallic materials is governed by the following considerations [10]: i) tolerance of operation conditions such as high temperature or oxidative and corrosive substances requires a stable alloy, i.e. FeCrAl, NiCrAl [36, 37]; ii) when the heat transfer is a crucial factor, a highly thermal conductive material like Cu could be used, whenever temperatures are below 720 ºC [38, 39]. The combination of different foam materials and coatings has led to structured catalysts for H_2 and syngas production, CH_3OH and Fischer-Tropsch synthesis, methanation, selective oxidation, total oxidation, and H_2O splitting as summarized in Table 1.2.
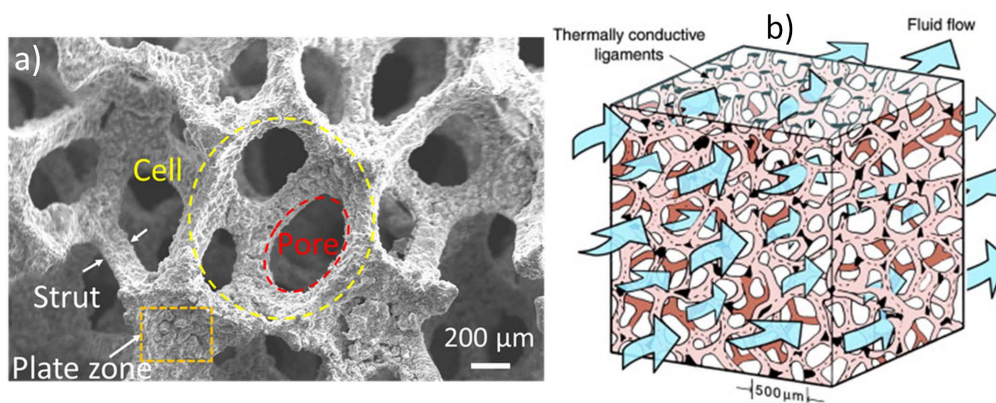
Figure 1.4. a) SEM image of FeCrAl open cell foam (1200 µm cell size) supplied by Alantum and b) tortuous flow path of the fluid passing through its structure. Figure b was reprinted from [40] with permission of Elsevier.

Table 1.2. Coated metal foams and their applications reported recently in the literature

Type of foam	Supplier	Coating layer	Coating technique	Reaction	Ref.
Ni	Alantum	CoNi-HTs	Electrodeposition	Oxygen evolution reaction (OER)	[41]
Ni, 110 ppi	Shenzhen Hanbo	Ru-ZrO$_2$/carbon nano tube	CH$_4$ decomposition + incipient wetness impregnation	Selective CO methanation	[42]
Ni, 110 ppi	Shenzhen Hanbo	Ru-Ni/Al$_2$O$_3$	Evaporation-induced-self-assembly + impregnation	CO selective methanation in H$_2$-rich gas	[43]
Ni	-	CoS nanosheet	Electrodeposition + hydrothermal ion-exchange	OER	[44]
Ni	Ailantian	FeCoNi mixed hydroxide	Electrodeposition	OER	[45]
Ni (320 g/m^2)	Changle	Ni-P	Chemical plating	H$_2$ production from Microbial electrolysis cell	[46]
Ni, 100 ppi	Changsha Lyrun	MgO	Hydrothermal reaction	Catalytic oxy-CH$_4$ reforming	[47]
Ni	-	Pd-Fe	Impregnation-calcination-reduction	Dimetridazole degradation	[48]
Ni	-	CoB	Electroless plating	Hydrolysis of NaBH$_4$	[49]
Ni, 100 ppi	Changsha Lyrun	Ag-CuO$_x$	Sequential galvanic-deposition method	Hydrogenation of DMO	[50]

Ni	-	CeO$_2$-NiO-Al$_2$O$_3$	Wet chemical etching technique	Dehydrogenation of C$_2$H$_6$	[51]
Ni	Jilin Zhuoer Technology	Pd or PdSn	Wet impregnation	Hydrogenation of α-methylstyrene	[52]
Ni	Shanghai Zhongwei	Carbon nanotubes (CNT) -Al$_2$O$_3$	Washcoat Al$_2$O$_3$ and chemical vapor deposition of CNT	Aerobic oxidation of cumene	[53]
Ni	MTI Korea	Ni$_3$Se$_2$	Hydrothermal washcoat	OER	[54]
Ni, 100 ppi	Changsha Lyrun	PdNi (alloy)	Galvanic exchange reaction	Combustion of coalbed CH$_4$	[55]
Ni	Kunshan Electronic	NiCoO$_2$	Urea hydrothermal treatment	Hybrid energy storage	[56]
Ni, 100 ppi	Changsha Lyrun	NiO-MO$_x$-Al$_2$O$_3$ (M = Ce or Mg)	Hydrothermal treatment + incipient impregnation	Catalytic partial oxidation of CH$_4$	[57]
Ni, 110 ppi	-	Fe/Ni phosphides	Hydrothermal treatment	Electrochemical water splitting	[58]
Ni	-	Ni- γ-Al$_2$O$_3$	Washcoating	SR (CO$_2$) of CH$_4$	[59]
Ni	Ailantian	MnO$_2$@NiCo$_2$O$_4$	Hydrothermal treatment	NH$_3$-SCR of NO (de-NO$_x$)	[60]
Cu	Ailantian	Fe$_2$O$_3$@CuO$_x$	Hydrothermal treatment	NH$_3$-SCR of NO (de-NO$_x$)	[61]
Cu	As-prepared	Ni/Mg$_3$AlO$_x$ (γ-Al$_2$O$_3$)	Washcoating	Solar thermal reforming of CH$_4$ with CO$_2$	[38]
Cu	Kunshan Jiayisheng	CuO nanowire	Heat treatment 500 ºC, 5 h	Plasma oxidation of Toluene	[62]
Cu, 45 ppi	Porvair	Cu-ZnO-Al$_2$O$_3$	Washcoating	CH$_3$OH synthesis	[39]
Ni or Cu 100 ppi or NiCu alloy	-	Ni/Al$_2$O$_3$	Wet chemical etching technique	Methanation of syngas	[63]
Al, 120 ppi	Suzhou Taili	CuO-ZnO	Hydrothermal deposition	CO$_2$ hydrogenation to CH$_3$OH	[64]
Al, 10, 20, 40 ppi	ERG	NiPd/CeO$_2$-Al$_2$O$_3$	Washcoating	Selective hydrogenation of 1,3-butadiene	[65]
Al, SiC, Al$_2$O$_3$ 30-40 ppi	-	Ni-Ru/Ceria-Zirconia	Dipped coating + impregnation	Methanation	[66]

Al, 10, 20, and 40 ppi	ERG	Pt/CeO$_2$- γ-Al$_2$O$_3$	Washcoating and impregnation	Water gas shift	[67]
NiFe	Suzhou Taili	-	Bare or acid etching	OER	[68]
Nichrome, Steel	-	Pd; Pd+ LaCoO$_3$	Thermal or chemical deposition	Benzene or phenol oxidation	[69]
FeCrAl, 50 ppi	Porvair, Metpore	Pt 2.9 and 4.3 mg/cm^3	Electrodeposition	Combustion of CH$_3$OH	[70]
FeCrAl, 50 ppi	Porvair, Metpore	Rh, Rh/AlPO$_4$	Electrodeposition Washcoating	CPO of CH$_4$	[71]
AISI 316	Goodfellow cambridge	Ru/Al$_2$O$_3$ Ni/Al$_2$O$_3$ Ru	Washcoating + Impregnation	Dry reforming of CH$_4$	[72]
FeCrAl, 20, 30 ppi	Selee	Cu-SSZ-13 Cu-ZSM-5	Hydrothermal synthesis + ion exchange	SCR of NO$_x$ with NH$_3$	[73]
FeCrAl (0.4-0.5 mm cell)	-	Pd–Rh/CeZrO$_2$–Al$_2$O$_3$	Washcoating	Steam reforming (SR) of model biogas	[37]
Fe-Al-Ni-Cr	-	Pt-Rh /CeO$_2$-ZrO$_2$-Al$_2$O$_3$	Washcoating	SR of CH$_4$	[74]
FeCrAl, 40 ppi	Porvair	Pd	Spontaneous deposition	Total oxidation of CO or CH$_4$	[75]
NiCrAl (0.4-0.5 mm cell)	-	Pd–Rh/CeZrO$_2$–Al$_2$O$_3$	Washcoating	Steam biogas reforming	[76]
NiCrAl 0.8 mm cell	-	Rh/Ce-Zr-Al	Thermal treatment + evaporation + impregnation	ATR of dodecane	[77]
FeCrAl, 60 ppi	Porvair	Ni-Al, Rh-Mg-Al HT derived	Electrodeposition	CPO or SR of CH$_4$	[36, 78-84]

1.2.2 Preparation of structured catalysts

The selection of the coating technique is of paramount importance for the development of structured catalysts able to replace conventional pelletized ones. The performances of the structured catalysts are determined by not only the properties of the coated materials (composition, size and dispersion of active species, loading, textural characteristics), but also

by the stability of the catalytic layer, thus the coating method must provide a sufficient load of active materials with enhanced adhesion to the support surface.

Several methods have been used to coat the structured substrates with approximately 140 patents on catalytic coatings from the years 1990 – 2010 registered mostly from US, Europe, Korea, Japan, and China [85]. In addition, some reviews summarize in detail the coating techniques [31, 86, 87]. There are two main approaches adopted: i) direct synthesis of the catalyst on the surface of the support or ii) coating of a ready-made catalyst, or support followed by impregnation of the active phase.

In case of metallic supports, the significant dissimilarity between thermal expansion coefficients of coating (usually a ceramic material) and support and the low interaction between metals and ceramic layers lead to the formation of creeps and peel-off of the coating. To improve the adhesion, metal supports are usually pretreated by thermal oxidation (oxide scale of Al_2O_3) [88-90] for FeCrAl or manganese and chromium oxides [91]), anodic oxidation [92-94], chemical treatment (both strong acids or bases, such as HCl, HNO_3 or NaOH, although much attention should be paid to avoid severe dissolution of the substrate [95-98]), or primer deposition [88]. In addition, chemical treatment may be also useful to remove surface oxide layer before doing the electrodeposition [99, 100].

Many techniques have been introduced for deposition of catalytic layers, including washcoating (dipcoating), spin-coating plasma spraying, electrostatic spraying, thermal spraying, sol-gel, chemical vapor deposition. The washcoating is the most widely used. It usually requires several consecutive steps including: i) preparation of powder materials, control their properties and disperse them into a solvent, ii) adjust the viscosity of the slurry, iii) coat and remove excess slurry, iv) drying and/or calcination; v) repeat the process until a desired loading is obtained [31, 101]. Additives are mandatory to control rheological properties of the slurry and coating features [86, 89]. The properties of the catalytic materials may be modified

during the washcoating procedure [39, 102-105]. For instance, the use of binders could block the micropores of zeolites [105] or the addition of colloidal ZnO during the washcoating of PdZnO may change in ZnO particle size and Pd dispersion [104], or even the drying and calcination steps can also affect to the coating [106]. Although dip-coating is well established, it is quite challenging to coat a small pore structured support without pore blockage, indeed from literature the technique is usually applied for medium or large pore foams [39, 65, 66].

Direct deposition routes, such as hydrothermal treatment [47, 56-58, 64] and galvanic displacement [55, 75], (Table 1.2), allow the catalyst or its precursor growing directly onto the surface of the structured support. Despite they show some advantages such as absence of any binder as well as stronger coating adhesion, these techniques face to some drawbacks such as loss of materials due to the precipitation taking place not only on the support surface, but also in liquid phase or limitation in solid loading by single coating step [107-111].

Electrochemical strategies and electrodeposition offer important advantages and unique possibilities in development of structured catalysts [36, 41, 44, 45, 70, 78, 79, 81, 82, 84, 112].

1.3 Electrodeposited structured catalysts for H_2 and syngas production

H_2 and syngas are essential in chemical, refinery, and energy processes. CH_4 mainly derived from natural gas accounted for approximate 80% of the world total H_2 production [113]. Recently, shale gas [114-117] and biogas (a mixture of CH_4 and CO_2) [118, 119] have been recognized as significant sources of CH_4, increasing the indispensable role of these sources in the future roadmap of H_2 technology despite the renewable energy is pushing to go beyond fossil fuel [6]. In Europe, there are more than 17,000 biogas plants built until 2015 with most contribution from Germany and Italy [120]. Nowadays, the well-established steam reforming (SR) is preferred in industrial technology, accounting for a significant portion of current H_2 production [121, 122]. However, the high endothermicity makes it intensively energy demanding.

$$CH_4 + H_2O \rightleftharpoons 3H_2 + CO \qquad (\Delta H^o_{298K} = +206 \text{ kJ mol}^{-1}) \qquad (1.1)$$
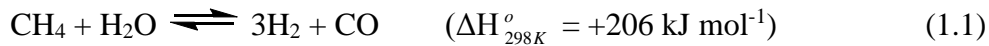
The catalytic partial oxidation (CPO) becomes an attractive route [123]. The reaction is simply described as:

$$CH_4 + \tfrac{1}{2} O_2 \rightarrow 2 H_2 + CO \qquad (\Delta H^o_{298K} = -36 \text{ kJ mol}^{-1}) \qquad (1.2)$$
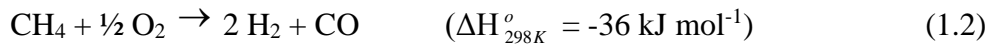
The process is exothermic and once preheated could be run autothermally producing a syngas with ratio $H_2/CO = 2/1$, suitable as feedstock for methanol synthesis or Fischer-Tropsch reaction. The CPO has been investigated to scale up for syngas and H_2 production by Eni [124], Shell [125] and ConocoPhillips (called the COPox[TM] technology) [126]. However, several challenging issues need to be considered when dealing with this process. Firstly, the CPO is operated at millisecond contact times with Gas Hourly Space Velocity (GHSV) around 500,000 h^{-1}, which is relatively higher than other syngas production processes. In one hand, this is more benificial in terms of reactor volume due to lower reactor and catalyst costs. But such high GHSV causes a high pressure-drop along the catalytic bed and consequently the catalyst must be sufficient in mechanical strength. Secondly, conversion of a large feedstock generates a huge amount of heat that must be dissipated to avoid the formation of hot spots as well as safety issues during the operation. The mechanism of hot spot formation is assumed to be related with the Lewis number, a ratio between thermal and mass diffusivity. In other words, the catalyst system for the CPO process should cope with heat and mass transfer limitations at high temperature.

Developing a structured reactor based on metallic open-cell foams, merging the architecture of metallic foams and highly active coating materials, will improve both heat and mass transfer as well as decrease pressure drop. Only few works deal with metallic foams as a structured support for CPO of CH_4 [36, 47, 57, 71, 78, 79]. Therefore, it remains a gap to be fulfilled in the use of metallic foams. Adopting this approach provides safety operation conditions, small and compact reactor size working under transient conditions, and reduction of energy demand.

All of them lead to a sustainable process, though to be reached many individual goals are required including the development of a well-defined coating technique, a general model for heat transfer prediction, an engineering correlation for the prediction of mass transfer coefficients, and the technical design of the reactor. In this section, we focus on the first point with an attempt to develop a coating procedure that can be an alternative to conventional washcoating method for the preparation of structured catalysts including small pore foams, namely the electrodeposition by the electro-base generation route.

The electro-base generation method is a facile electrochemical route allowing to coat in one-step at ambient temperature complex shaped metal structured supports with hydroxides or oxides [45, 78]. This method was originally employed for the preparation of nickel hydroxide electrodes [127], then extended for the synthesis of hydrotalcite-type (HT) compounds, layered mixed hydroxides, with general formula $[M^{2+}_{1-x}M^{3+}_x(OH)_2](A^{n-})_{x/n} mH_2O$ [128]. Since then it has been investigated and improved for the coating of HT materials on substrates with different shapes (plate, fiber, foam) and compositions (Pt, glassy carbon, Ni), extending to a wide range of application in electrochemistry as sensors [129-131], redox supercapacitors [132-134], and electrocatalysts [135-138]. Recently, the method has been improved by some of us to prepare metallic-foam structured catalysts adapting the strict requirements of catalysts for steam reforming (SR) or catalytic partical oxidation (CPO) of CH_4 [81] since HT compounds are widely used as catalysts or catalyst precursors for processes demanding tailored basic/acidic sites, relatively high specific surface area and/or metal dispersion [139, 140].

The deposition of HT compounds on the surface of a metallic structured support could be performed by generating a basic media at the interface of electrode-electrolyte by application of a cathodic potential or current pulse [78]. The set-up is quite simple including a three-electrode electrochemical cell connected to a potentiostat. The structured support is immersed in an aqueous solution containing nitrates of the cations being deposited. During the cathodic

pulse, the pH only increases near the foam surface and the selective precipitation of hydroxides occurs on it. In other words, the production of OH⁻ by electrochemical reactions (Eqs 1.3 – 1.6) and the consumption of OH⁻ by chemical precipitation (Eq 1.7) occur simultaneously at the vicinity of the structured support. It is necessary to reach selected pH values to obtain a HT material with well-controlled composition [139].

$$O_2 \text{ (g)} + 2H_2O + 4e^- \rightarrow 4\,OH^- \qquad\qquad E^0 = 0.400 \text{ V} \qquad (1.3)$$

$$NO_3^- + H_2O + 2e^- \rightarrow NO_2^- + 2\,OH^- \qquad\qquad E^0 = 0.010 \text{ V} \qquad (1.4)$$

$$NO_3^- + 7H_2O + 8e^- \rightarrow NH_4^+ + 10\,OH^- \qquad\qquad E^0 = -0.120 \text{ V} \qquad (1.5)$$

$$2H_2O + 2e^- \rightarrow H_2 + 2\,OH^- \qquad\qquad E^0 = -0.828 \text{ V} \qquad (1.6)$$

$$M^{n+} + ne^- \rightarrow M(OH)_n \downarrow \qquad\qquad (1.7)$$
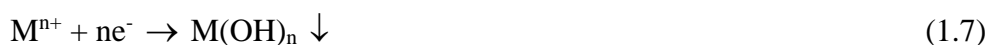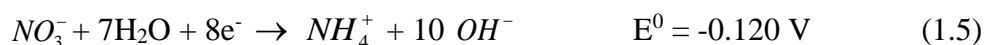
In one previous study from our group [141], it was demonstrated that the pH values near the foam surface generated by the electrosynthesis were sufficient for the precipitation of either Ni/Al or Mg/Al nitrate electrolytic solutions. However, the role of nitrate reduction in comparison with water or dissolved oxygen reduction for total OH⁻ generation as well as degree of nitrate reduction (Eq 1.4 or 1.5), and effect of metal nitrate concentration on the electrodeposition of HT compounds are still unknown.

Coating the complex structure of metallic foams with HT compounds as catalyst precursors faces many challenges to balance the load of the coating and its properties such as thickness, composition, and adhesion; unlike other known-applications (e.g. electrode, sensor, protection) wherein a thin coating layer is satisfactory. Coating features are determined by several factors, e.g. nature of the support (electrical conductivity and roughness [141]), geometrical parameters (size and shape), electrochemical set-up (electrical contact between the working electrode and the potentiostat [79], type of cell, and size of counter electrode), electrochemical parameters (precursors and concentration of electrolyte [78], potential applied, and synthesis time [84, 112]). They may be classified into two main groups: passive and active. The former are usually related to the nature or geometry of the support fixed by suppliers or given purposes, while the

latter are the ones modified to control the coating properties. During the electrodeposition of HT compounds, the deposition of a thicker layer on the tips of the strut than on the flat zones and the preferential coating of the material on the outside of the foam cylinder than the one inside are examples of impacts of passive factors. Composition of the electrolyte bath, synthesis time, and potential applied are common examples of active factors.

HT materials containing Ni and/or Rh are well-known catalyst precursors for syngas production from CH_4 via SR, CPO, or dry reforming [142]. Ni/Al HT precursors electrodeposited on FeCrAl foam (80 ppi) were prepared and after calcination and reduction proposed as structured catalysts for SR of CH_4 [143, 144]. A quite good control of composition with Ni/Al around 2.8/1 compared to 3/1 of the nominal value was obtained. Despite thin coating, they exhibited comparable catalytic performances with Ni commercial catalyst under industrial-type conditions (S/C = 1.7, P = 20 bar, contact time 4 s and T_{oven} = 900 ^{o}C) as shown in Fig. 1.5 [144].

Although the best electrosynthesized Ni catalyst worked well for SR, it was not active for the CPO due to the oxidation of Ni^0 active phase [80]. Therefore, Rh based catalysts were a better option for the CPO. However, noble metals were easily reducible and the deposition of Rh metallic particles, rather the inclusion of Rh^{3+} in the HT structure, might take place during the electrosynthesis decreasing the catalytic performances [79, 112]. The initial pH of the electrolyte could be increased to suppress the reduction of Rh^{3+} (by modification of reduction potential according to Pourbaix's diagram), but the the precipitation of bulk $Al(OH)_3$ should be suppressed, to achieve so, a pH value of 3.8 was used [84, 112]. In this way, the absence of Rh metallic particles during the electrodeposition process at -1.2 V vs SCE for 2000 s was achieved [36, 78, 79].
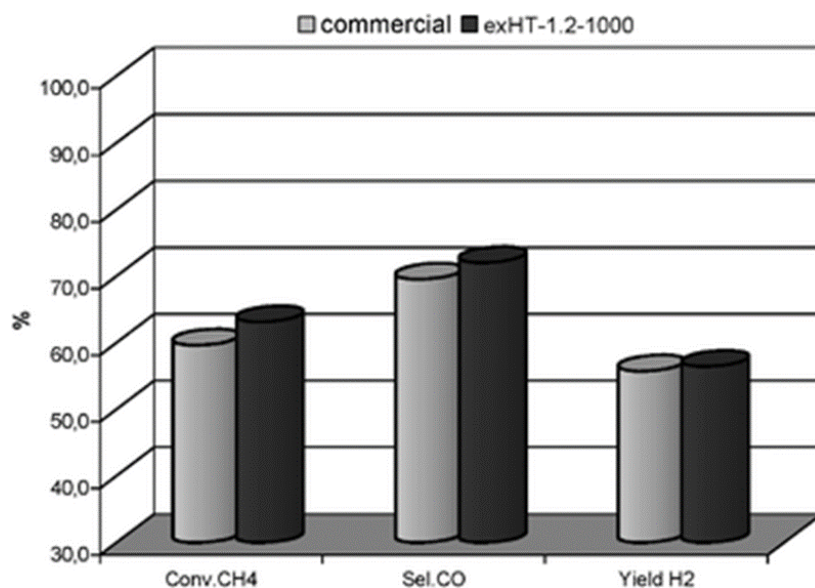
Figure 1.5. Catalytic activity of Ni-based commercial and electrosynthesized (0.03 M nitrate electrolyte, Ni/Al = 3/1, -1.2 V *vs SCE*, 1000 s) catalysts. Reprinted from [144] with permission of the Royal Society of Chemistry.

A change of Rh amount in electrolytic solution (Rh/Mg/Al = 11/70/19, 5/70/25, and 2/70/28 a.r.) did not alter the typical features of both the electrodeposited precursors and the catalyst, but did determine the size of Rh particles [78]. Differences in current distribution, due to inhomogeneous composition of the foams and different geometry of strut, node, and flat zone, accessibility of eletrolyte inside the foam (pore size effect), mass transfer limitation of electroactive species, decrease of pH with formation of thick layer, led to the following coating features: i) preferential electrodeposition on the tips of the strut resulting in a 5-15 µm thick, while a thinner layer (2-6 µm) was deposited in the flat zone; ii) a sequential precipitation of hydroxides of different composition, i.e. growing of an outer layer rich in Rh and Al precipitates on the top of the existing deposits consiting of first $Mg(OH)_2$ and second HT layer.

The thickness and chemical composition of the electrodeposited precursors strongly determined the properties of the catalytic layer obtained after calcination at 900 °C for 12 h. The outer layers in thick coating zones developed a high number of cracks and the solid easily detaches, whereas Mg-rich coatings or those with well-defined compositon were more stable after calcination step. During calcination, both the decomposition of the HT precursor and the

18

oxidation of the foam took place simultaneously. In this process, the chemical reaction between Al coming from the foam and Mg in the coating led to the formation of spinel phases, inhibiting the formation of MgO phase in the coating and the protective Al_2O_3 scale on the foam. Thus, this interfacial spinel phase increased the coating adhesion to the support, but it also modified the Rh distribution in the catalyst (mainly presence in spinel phase, some Rh^0 and Rh_2O_3) and therefore its reducibility [36].

The catalytic activities of Rh/Mg/Al structured catalysts in CPO tests depended on both amount of active sites and Rh particle size. Feeding a diluted feedstock ($CH_4/O_2/He = 2/1/20$ v/v, 63,300 h^{-1}) after the reduction pretreatment, the catalyst with large number of Rh (e.g. $Rh_{11}Mg_{70}Al_{29}$) reached quickly stable conversion values, while the catalysts containing lower amount of Rh ($Rh_5Mg_{70}Al_{25}$ and $Rh_2Mg_{70}Al_{28}$) activated with time-on-stream (TOS) due to the presence of the hardly reducible Rh^{3+} species stabilized inside the spinel phase (Figure 1.6) [78]. Remarkably, at 15,250 h^{-1} the best catalyst tested could reach 90% of CH_4 conversion with high selectivity to syngas (>90%). Multiple processes are involved in CH_4 conversion including the exothermic total or partial oxidation reactions, followed by the endothermic steam reforming (SR). As the oxidations are fast and controlled by O_2 mass transfer, the contribution of the catalyst for the consecutive SR mainly respond for the differences in CH_4 conversion and syngas selectivity. A small number of available Rh^0, formation of big particles or existence of unreduced Rh^{3+} species could slow down the CH_4 conversion by SR and hence decease overall catalytic performance of the catalysts. When feeding concentrated gas mixtures, the heat generated by exothermic reactions promoted the catalytic activity but also favor the sintering of Rh metallic particles leading to the slight deactivation of the catalyst, and it was more visible in the case of high Rh loading sample (e.g. $Rh_{11}Mg_{70}Al_{19}$) (Fig. 1.6). In fact, characterization of spent catalysts by FEG-SEM evidenced that the higher the amount of Rh loading, the larger the Rh particles were.
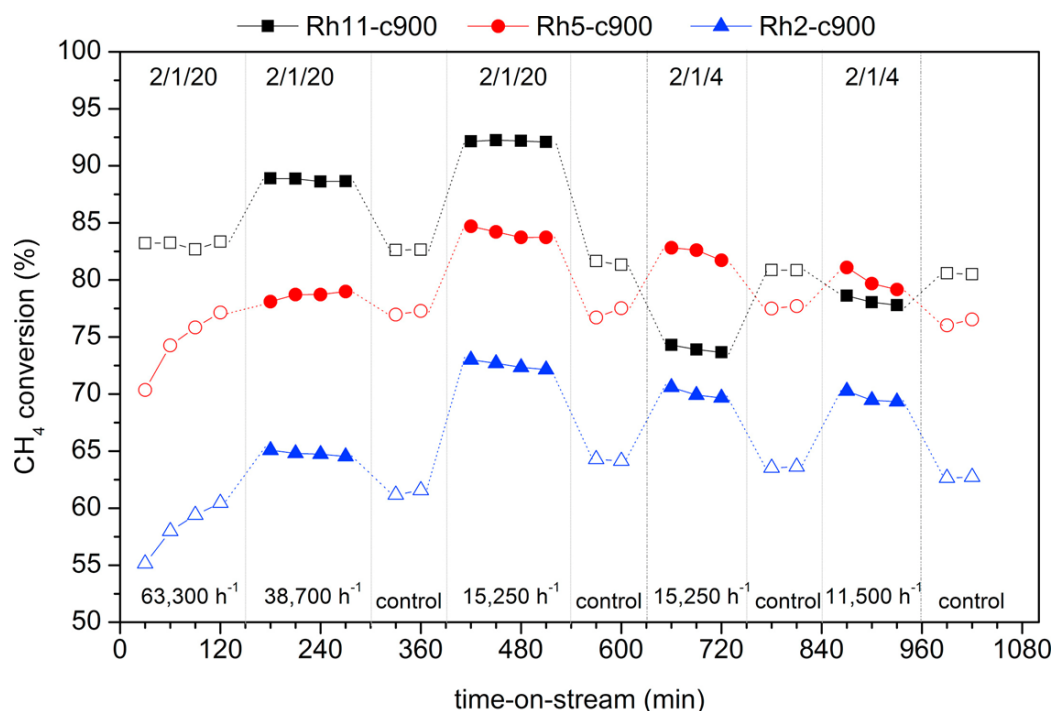
Figure 1.6. Evolution of CH_4 conversion with time-on-stream obtained with catalyst synthesized using different electrolytic solutions (Rh/Mg/Al = 11/70/19, 5/70/25, and 2/70/28 a.r., 0.03 M) at -1.2 V vs SCE for 2000 s, calcination at 900 °C for 12 h. Test conditions: T_{oven} = 750 °C, $CH_4/O_2/He$ = 2/1/20 and 2/1/4 v/v, GHSV = 63,300, 38,700, 15,250, and 11,500 h^{-1}). Reprinted from [78] with permission of Elsevier.

The effect of Rh/Mg/Al electrolyte concentration on the electrodeposition of HT compounds on the foam was investigated. The use of a 0.06 M nitrate solution (instead of 0.03 and 0.10 M solutions) with $Rh_5Mg_{70}Al_{25}$ produced a more compact layer with thickness up to 15–20 µm on struts and around 5 µm on flat zones (nodes). The composition was close to the expected one (Rh/Mg/Al = 4/68/28 a.r.) in some parts of the foam, but the sequential precipitation phenomena still took place where thicker layers are coated. The best coverage of the HT precursor in terms of thickness and homogeneity obtained with 0.06 M, instead of 0.03 or 0.10 M solutions, improved the coating properties of the calcined catalyst, i.e. less cracks and detachments, 5-15 wt.% Rh, and hence it exhibited better performances. Compared to the catalyst prepared by 0.03 M, the one from 0.06 M performed outstanding CH_4 conversion in all reaction conditions, about 10% and 4% higher in diluted and concentrated feedstock, respectively.

To evaluate the feasibility of the electrodeposition coating technique, a rough comparison between previous results and those obtained with these electrodeposited catalysts is made in Table 1.3. Although it is quite challenging since the CPO tests were performed under different conditions, some appropriate points could be summarized: i) Rh/Mg/Al structured catalyst could reach satisfactory catalytic performances, ii) Rh is stabilized in HT derived materials, decreasing sintering of Rh particles under the CPO test.

Table 1.3. Comparison of Rh-based catalyst on FeCrAl foams in the CPO of CH_4

Catalyst/Support	Coating properties	Condition of CPO tests	CH_4 conversion and syngas selectivity	Ref.
Rh/Mg/Al = (5/70/25 a.r.), FeCrAl 60 ppi, electrodeposition	5-15 wt.% Rh by EDS, 10-80 nm Rh particles (used catalyst)	$V_{foam} = 1.87$ cm^3 15,520-63,300 h^{-1} $CH_4/O_2/He = 2/1/4$, 2/1/20	$X_{CH4} = 80\%$, Y_{syngas} around 90% (diluted feed) $X_{CH4} = 85\%$, Y_{syngas} between 85-90% (concentrated feed)	[78]
Rh, FeCrAl 50 ppi, electrodeposition	4.7-9.0% Rh a.r., < 150 nm particle (after electrodeposition), 270 nm (used catalyst)	$V_{foam} = 2.44$ cm^3 55,300 h^{-1} $CH_4/O_2 = 2/1$	$X_{CH4} = 64.5\%$ $Y_{CO} = 54.3\%$ $Y_{H2} = 54.0\%$	[71]
Rh/AlPO$_4$, FeCrAl 50 ppi, washcoat	0.86 wt.% Rh/AlPO$_4$, FeCrAl, 50 ppi	55,300 h^{-1} $V_{foam} = 2.44$ cm^3 $CH_4/O_2 = 2/1$	$X_{CH4} = 63.3\%$ $Y_{CO} = 56.7\%$ $Y_{H2} = 50.0\%$	[71]

In summary, the electro-base generation method is a promising technique allowing to coat metallic foams of small pores (60 – 80 ppi) with HT materials as precursors. The catalysts obtained through calcination at high temperature possess a strong interfacial interaction between the coating and the foam due to a solid state chemical reaction forming a $MgAl_2O_4$ layer, despite of some cracks and detachments. The catalysts reach a satisfactory CH_4 conversion and syngas selectivity in both diluted and concentrated feedstocks. However, the

electrodeposition of HT compounds, e.g. Rh, Mg, Al, still face the following issues: i) control of coating composition; ii) replenishment of the electrolyte at the electrode-electrolyte interface, mainly in the inner part of the foam; iii) decrease the crack formation during drying and calcination; iv) effect of the foam size when scaling up. The first point is related to control of the pH generation near the support surface, which is associated to the role of nitrate reduction as well as the influence of metal concentration during the electrodeposition. The second point generates an idea about the necessity of a movable flow instead of static state during the deposition. When the first and second point are solved, they can help to improve the quality of the coating; although other solution, that could be considered, is the use of some additives to avoid the cracks. The last issue requires further studies on the effect of foam size during the electrodeposition.

1.4 Metallic foams as structured catalysts for environmental applications

Despite ceramic monolith reactors are well-established for exhaust gas treatment in environmental applications, the use of metallic foams as support is an attractive approach [145]. Metallic foams not only inherit the advantages of ceramic foams, based on unique foam configuration like large geometrical surface area, radial mixing of the fluid, low pressure drop, but also possess more distinctive features based on properties of metallic materials such as high mechanical strength and thermal conductivity [8]. However, moving to metallic foams still requires more studies on both heat and mass transfer properties, which are tightly associated with properties of the coated layers defined by the coating techniques.

Heat transfer coefficients, related to conductive, convective, and radiative heat transfer, depend on both foam properties (materials, porosity, and pore size) and operating conditions (gas composition and flow rate) [146-148]. The effective radial and axial conductivity as well as the wall heat transfer coefficients under reaction relevant conditions for chemical process

are very important for both reactor design and process operation to predict the thermal behavior of the foam structured reactors. Therefore, many studies on heat transfer properties of metallic foams have been performed on a wide range of foam pore size (from large to small pores, 10 to 100 ppi) with different materials (from poor to highly thermal conductivity, FeCrAl, Cu/Al) [12, 40, 146-149]. The effective radial conductivity for Al foam (40 ppi, ~89% porosity) is around 7.7 W m^{-1} K^{-1}, which is comparable or higher than typical effective radial thermal conductivity in technical packed bed reactors [146]. For either large or small pore foams (high cell densities), the conductive contribution dominates the radial effective thermal conductivity, whereas the wall heat transfer coefficient is mainly related to the heat transport resistance in the gas between inner surface of the reactor wall and outer surface of the foam. The heat transport resistance, is proportional to the thermal conductivity of the flushing gas and inversely proportional to cell diameter (effect of gap size), so the wall heat transfer coefficient is independent on the flow rate unlike ones requested in packed bed reactors. Therefore, to achieve high heat transfer rates, it is not necessary to reach very high flow velocites (generating more pressure drop and high energy costs), but it is sufficient to reduce the gap size effect or to use shorter tubes in the tubular reactor (resulting in more compact configuration of process intensification) [147, 148]. In fact, decreasing of the gap size by a package foam system has been proposed [9, 150]. However, the above studies only considered the bare foam without coating. The presence of the coated layers may change the heat transfer properties due to the differences in thermal conductivity. Increasing of the coating thickness causes both a rise of pressure drop and a decrease of the gas-solid interfacial heat transfer as predicted from computational fluid dynamics (CFD) method [149]. Futher studies on practical data are still lacking.

FeCrAl foams (10, 20, and 40 ppi) washcoated with Pd/γ-Al_2O_3 exhibited outstanding advantages over packed beds in the CO oxidation in a trade-off consideration between pressure

drop and mass transfer performances [151], but they performed slightly worse than honeycomb monoliths. However, in fast diffusion-limited processes such as CO oxidation, in which pressure drop is a minor concern, metallic foams could obtain comparable conversions to honeycombs with a remarkable decrease of the reactor size by a factor of 2.5–3, in the case of 20 ppi foam instead of a 600 cpsi monolith as shown in Fig. 1.7.
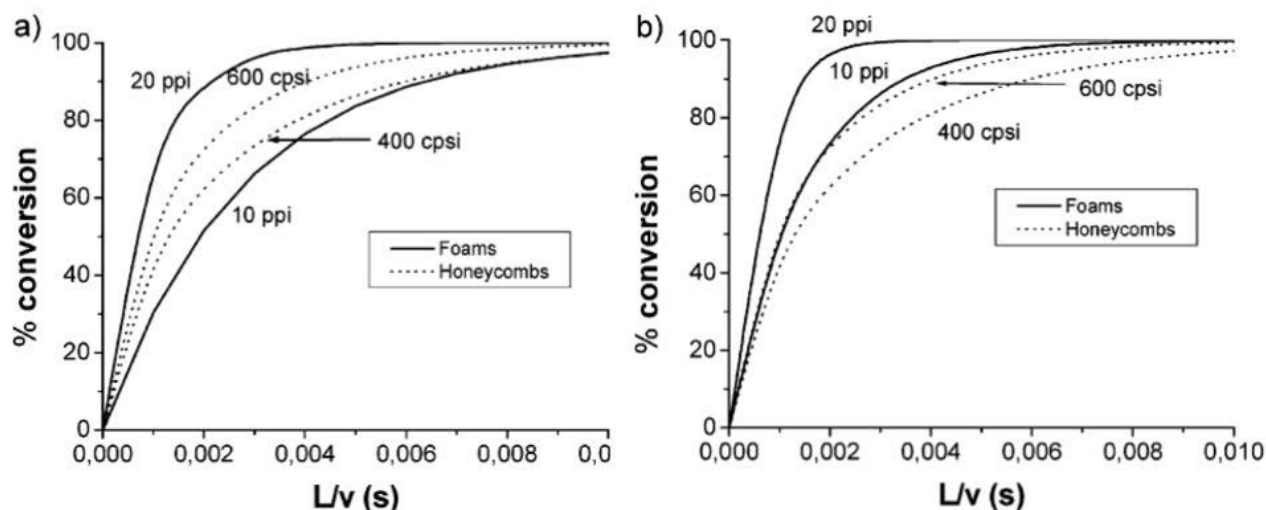
Figure 1.7. Calculated conversions in foams (open volume fraction $\varepsilon = 0.95$) and honeycombs ($\varepsilon = 0.7$) versus reactor length (L) for two different feed flow velocities (v): (a) 5 m/s and (b) 20 m/s. Reprinted with permission from [151]. Copyright (2005) American Chemical Society.

The mass transfer coefficients and the activity of the catalysts in diffusion-controlled regime are strongly dependent on the coating procedure. The differences in Pd loading and total washcoat loading and homogeneity obtained by a sol-gel (sequential deposit of γ-Al_2O_3 and wet impregnation of $Pd(NO_3)_2$) and a slurry route (powder Pd/γ-Al_2O_3 was dispersed into slurry) significantly influence on the activity in diffusion controlled regime in which the former catalyst performed a mass transfer coefficient 15-20% higher than that of the latter one.

When using small pore foams, the pore blockage could be avoided by direct deposition of metallic particles using galvanic displacement method. The galvanic deposition of Pd onto Ni foam (100 ppi, 95% porosity) [55] and FeCrAl foam (medium pore 40 ppi) [75] takes place spontaneously as soon as the support is immersed into an aqueous solution containing any Pd

salt due to a large disparity of reduction potentials between Pd^{2+}/Pd^0 (or Pd^{4+}/Pd^0) and Ni^{2+}/Ni^0 or Fe^{2+}/Fe^0 (Fe^{3+}/Fe^0) pairs, respectively. The concentration of the precursor [152] and the pH strongly influenced the properties of the Pd coating in terms of loading and particle size (Fig. 1.8) [75]. Following this method, Pd loadings around 1.0 wt.% and 1.7 wt.% were obtained, on Ni and FeCrAl foams, respectively, suitable for catalyzing the abatement of O_2 existing in coalbed by O_2-lean catalytic combustion of CH_4 and CO oxidation.
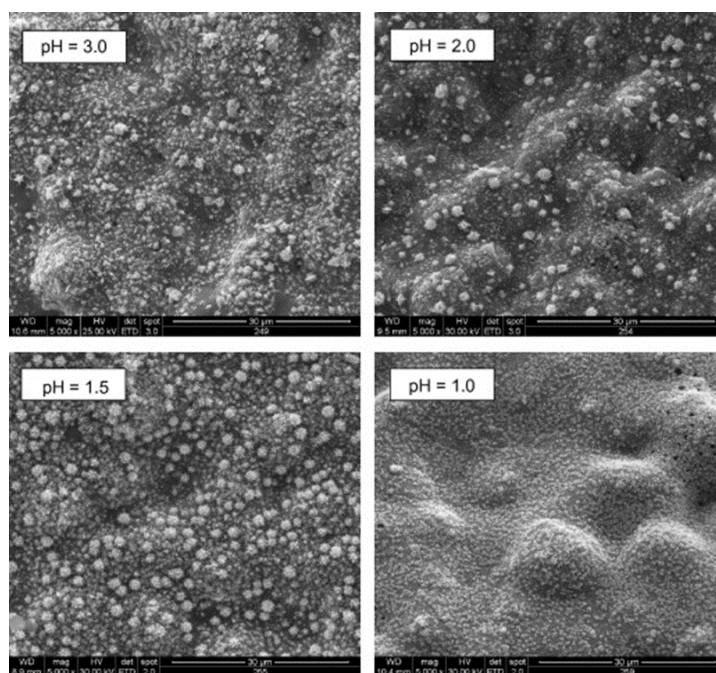
Figure 1.8. SEM images of Pd-modified FeCrAl foams obtained by spontaneous deposition from 0.005 M $PdCl_2$ solution of different pH for 30 min. Reprinted from [75] with permission of Elsevier.

The Pd nanoparticles (< 5 nm) deposited on Ni foams suffer from activation-promotion processes during *in situ* reaction activation ($CH_4/O_2/N_2$ = 40/3/57 v/v, 480 ^{o}C, 1 h) due to the simultaneous auto-reduction of both NiO and PdO and formation of PdNi alloy, by diffusion of Ni into Pd nanoparticles. The surface reconfiguration results in a 4-fold increase in the available Pd atomic surface. In a simulated gas reaction mixture after activation, $CH_4/O_2/N_2$ = 40/3/57 v/v at 350 ^{o}C and GHSV = 12,000 mL $gcat^{-1}$ h^{-1} a complete conversion of O_2 (~ 3.75% CH_4 conversion) was reached with TOF 292 h^{-1} and the catalyst was stable under 500 h of time-on-stream without reaction oscillation and performance deterioration. More important, as the

catalytic combustion of coalbed CH_4 is fast and strongly exothermic, the excellent permeability and heat conductivity of the foams are of paramount importance. The foam structured bed generated much lower pressure drop than particulate Pd/SiO_2 (0.2 mm particle size) (Fig. 1.9A). Although the formation of hot spots was not avoided within the foam, the temperature rising calculated by computational fluid dynamics (CFD) was intensively lowered (70 vs 290 °C for the foam and pellet, respectively) (Fig. 1.9 B).
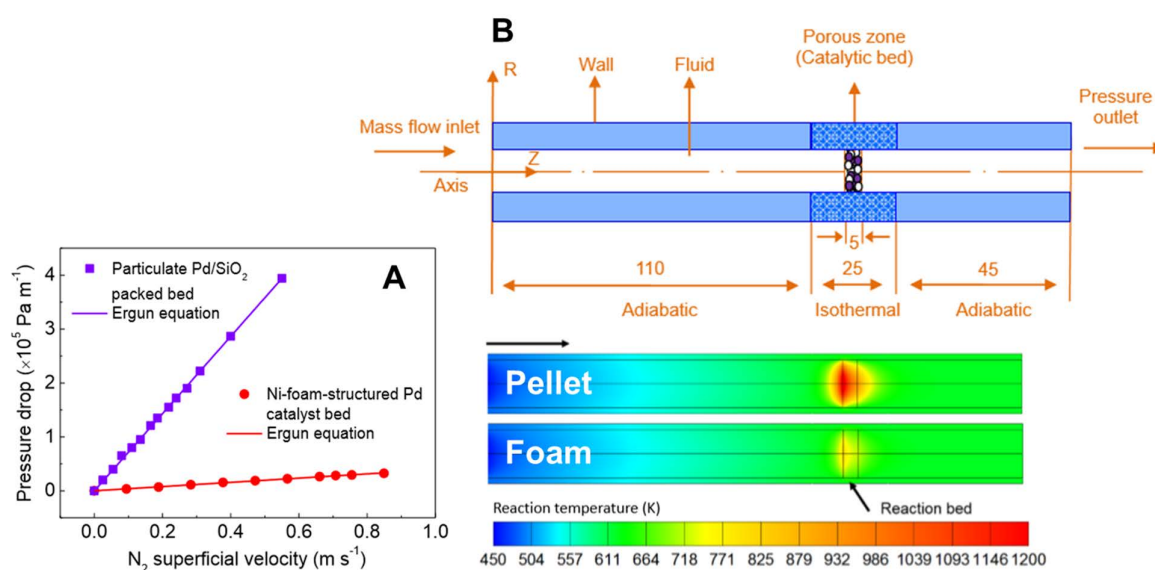
Figure 1.9. A) Profiles of pressure drop per meter as a function of N_2 superficial velocity over monolithic PdNi(alloy)/Ni-foam catalyst bed and particulate Pd/SiO_2 (0.2 mm) packed bed and B) Schematic diagram of the physical system and temperature distributions at steady-state inside monolithic PdNi(alloy)/Ni-foam bed and particulate Pd/SiO_2 packed bed. Reprinted from [55] with permission of Elsevier.

The galvanic displacement method is however limited to the direct deposit of noble metals (e.g. Pd, Ag) onto the surface of metallic supports in which the galvanic potentials of reductant/oxidant between two pairs are largely different. Such direct coating of active species onto the substrate may lead to a low surface area and metallic particles prone to the sintering, especially for high temperature applications.

As an alternative, the *in situ* hydrothermal synthesis (one or two steps) was proposed. This route is typically used for the in situ synthesis of zeolites or urea assisted co-precipitation of

mixed hydroxides onto the foam surface. Either ZSM-5 or SSZ-13 zeolite were hydrothermally synthesized and coated on FeCrAl foam, the incorporation of Cu took place in a following step by Cu-ion-exchange[153]. The resulting structured catalysts were evaluated in the SCR of NO_x in the presence of NH_3; however, this survey study just confirmed the potentiality of the coating method and provided brief conclusions about enhanced performances as well as better hydrothermal stability of Cu-SSZ 13 than that of Cu-ZSM 5. Further studies on optimization of the synthesis conditions and stability tests are lacking.

In the two-step hydrothermal treatment, coatings made by layers of different composition could be prepared. Ni-Co mixed hydroxides are synthesized by the urea-assisted co-precipitation in a first step and then the $KMnO_4$ hydrothermal pyrolysis creates a MnO_2 phase. As a result, $MnO_2@NiCo_2O_4@Ni$ foam structured catalysts for NH_3-SCR of NO were obtained [60]. These catalysts exhibited a superior catalytic performance for the NH_3-SCR of NO at low temperature and high H_2O resistance (Fig. 1.10).
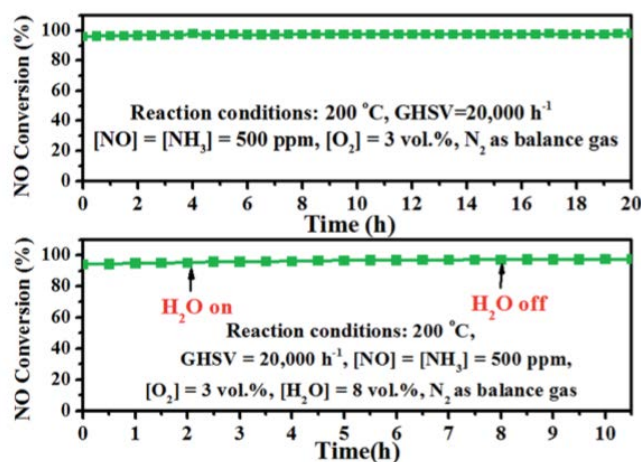
Figure 1.10. Stability and H_2O resistance test at 200 ºC of the $MnO_2@NiCo_2O_4@Ni$ foam catalyst. Adapted from [60] with permission of The Royal Society of Chemistry.

The advantages of the hydrothermal procedure are related to the applicability to the deposition of a different oxides (or their precursors) onto several metallic foams, modifying the source of basic media. For instance, Fe_2O_3 precursors are coated using NaOH as basic source on a pre-oxidized Cu foam containing a CuO_x layer [61]. The obtained $Fe_2O_3@CuO_x/Cu$

foam catalyst showed a high activity in NH_3-SCR of NO both in a wide operating temperature range and in a stability test in the presence of inhibitors, such as SO_2 and H_2O. A co-existence of both H_2O (8 vol.%) and SO_2 (250 ppm) caused a decrease of only ca. 4% in NO conversion but the activity was recovered when stopping the supply of the inhibitors (Fig. 1.11).
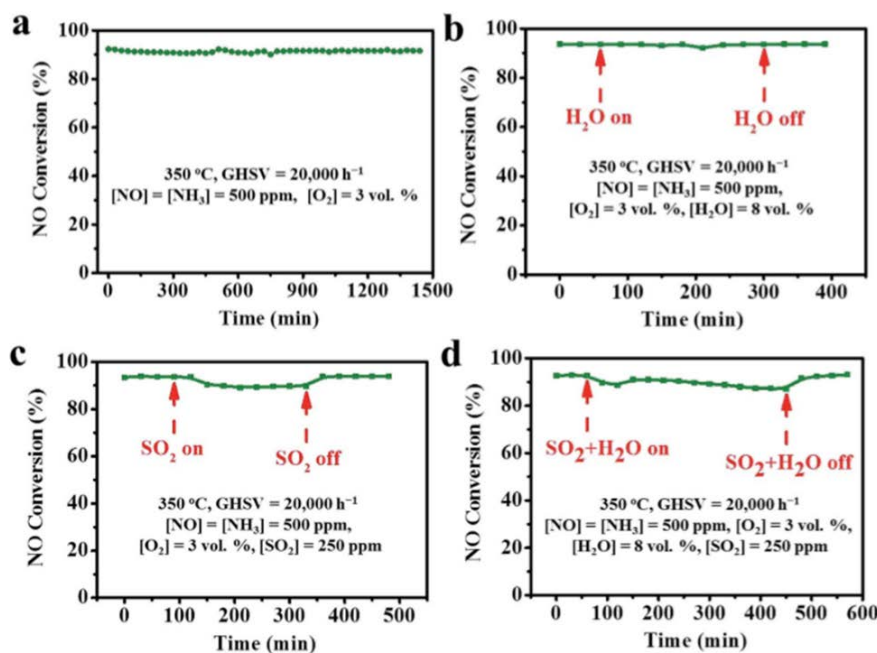
Figure 1.11. NH_3-SCR of NO performance of the Fe_2O_3@CuO_x foam. Adapted from [61] with permission of The Royal Society of Chemistry.

However, the main drawback of the hydrothermal method is that the solid is selectively deposited not only on the support surface but also in bulk solution. Therefore, it has limitations for the preparation of noble metal-based catalysts which are common in environmental catalysis process.

In short summary, the structured catalysts based on metallic foams exhibit satisfactory performances for environmental applications. Future research may focus on: i) improving or finding more powerful coating techniques, allowing to obtain good coatings on different types of metallic foams (pore size, materials), ii) applications of metallic foam structured catalysts for other environmental related processes, and iii) investigation on models for heat/mass transfer of real coated foams.

1.5 Aims and outline of the thesis

Based on the opportunies of the electrodeposition method for coating of the metallic foams with small pores as well as wide-range applications of the open-cell foam structured catalysts in energy and environmental processes, this thesis aims to fulfill the gaps with following research:

o Investigation about the role of nitrate reduction on the electrochemical and chemical processes involved in the electrodeposition of hydrotalcite-like compounds (HTs) (Chapter 2).

o Influence of metal nitrate concentration on the electrodeposition of HTs (Chapter 3).

o Improvement of the electrodeposition of Rh/Mg/Al HTs on FeCrAl foams by modification of electrochemical set-up, and its effect on activity of the catalysts on the catalytic partial oxidation of CH_4 (Chapter 4).

o Application of the electrosynthesis for coating Rh/Mg/Al HTs on NiCrAl foams and use in the catalytic partial oxidation of CH_4 (Chapter 5).

o Challenges of the electrosynthesis in the preparation of Pd-CeO_2 structured catalysts, with presence of a highly reduced element Pd in the electrolyte and study of catalytic activity on CO oxidation reaction (Chapter 6).

o Feasibility of electrosynthesis in preparation of structured catalysts with different composition, e.g. Rh/Mg/Al HT-derrived materials, Rh-CeO_2, Co_3O_4 for catalytic decomposition of N_2O (Chapter 7).

1.6 References

1. P. Lanzafame, S. Perathoner, G. Centi, S. Gross, E.J.M. Hensen, Catal. Sci. Technol. 7 (2017) 5182-5194.

2. S. Perathoner, S. Gross, E.J.M. Hensen, H. Wessel, H. Chraye, G. Centi, ChemCatChem 9 (2017) 904-909.

3. P. Lanzafame, G. Centi, S. Perathoner, Chem. Soc. Rev. 43 (2014) 7562-7580.

4. V. Piemonte, M. De Falco, A. Basile, Sustainable Development in Chemical Engineering Innovative Technologies, John Wiley & Sons, West Sussex, UK, 2013.

5. F.M. Dautzenberg, M. Mukherjee, Chem. Eng. Sci. 56 (2001) 251-267.

6. S. Perathoner, G. Centi, Science and Technology Roadmap on Catalysis for Europe - 2017. http://www.catalysiscluster.eu/ (accessed 25/11/2017).

7. D. Reay, C. Ramshaw, A. Harvey, Process Intensification Engineering for Efficiency, Sustainability and Flexibility, 2nd ed., Elsevier, Oxford, UK, 2013.

8. E. Tronconi, G. Groppi, C.G. Visconti, Curr. Opin. Chem. Eng. 5 (2014) 55-67.

9. C.G. Visconti, G. Groppi, E. Tronconi, Catal. Today 273 (2016) 178-186.

10. P. Avila, M. Montes, E.E. Miró, Chem. Eng. J. 109 (2005) 11-36.

11. K. Pangarkar, T.J. Schildhauer, J.R. van Ommen, J. Nijenhuis, F. Kapteijn, J.A. Moulijn, Ind. Eng. Chem. Res. 47 (2008) 3720-3751.

12. L. Giani, G. Groppi, E. Tronconi, Ind. Eng. Chem. Res. 44 (2005) 9078-9085.

13. W. Liu, S. Roy, Chem. Eng. Sci. 59 (2004) 4927-4939.

14. S. Raimondeau, D.G. Vlachos, Chem. Eng. J. 90 (2002) 3-23.

15. H. Takashi, O. Tsuneaki, Patent US 5064609 A, 1991.

16. H. Takashi, M. Hiroshige, A. Fumio, O. Tsuneaki, Patent US 5292485 A, 1994, Ngk Insulators Ltd.

17. C. Willard, H. Lin, O. Anthony, S. Charles, Patent US 20030100448 A1, 2003.

18. https://www.environmental-expert.com/products/applied-catalysts-model-acmc-activated-carbon-monolith-catalysts-552730 (accessed 25/11/2017).

19. https://www.plascore.com/honeycomb/honeycomb-cores/stainless-steel/ (accessed 25/11/2017).

20. https://www.thomasnet.com/products/ceramic-honeycomb-96001060-1.html (accessed 25/11/2017).

21. E. Tronconi, G. Groppi, T. Boger, A. Heibel, Chem. Eng. Sci. 59 (2004) 4941-4949.

22. http://www.alantum.com/en/view.php?mn=111 (accessed 23/10/2017).

23. http://www.goodfellow.com/E/Foam.html (accessed 23/10/2017).

24. http://www.ergaerospace.com/Material-Applications-guide.html (accessed 23/10/2017).

25. http://www.reade.com/products/open-cell-metal-foam (accessed 23/10/2017).

26. B.T. Horner, Platinum Metals Rev. 35 (1991) 58-64.

27. H. Sun, Y. Zhang, X. Quan, S. Chen, Z. Qu, Y. Zhou, Catal. Today, 139 (2008) 130-134.

28. https://www.porvairfiltration.com/263-sinterflo-m-metal-mesh.html (accessed 23/10/2017).

29. http://www.corrugated-metals.com/materials.html (accessed 23/10/2017).

30. https://www.industrialmetalsupply.com/Products/Metals (accessed 23/10/2017).

31. A. Montebelli, C.G. Visconti, G. Groppi, E. Tronconi, C. Cristiani, C. Ferreira, S. Kohler, Catal. Sci. Technol. 4 (2014) 2846-2870.

32. F. Garcia-Moreno, Materials 9 (2016) 85. DOI: http://dx.doi.org/10.3390/ma9020085.

33. J. Banhart, H.-W. Seeliger, Adv. Eng. Mater. 14 (2012) 1082-1087.

34. L.P. Lefebvre, J. Banhart, D.C. Dunand, Adv. Eng. Mater. 10 (2008) 775-787.

35. http://www.metalfoam.net/companies.html (accessed 24/09/2017).

36. P. Benito, W. de Nolf, G. Nuyts, M. Monti, G. Fornasari, F. Basile, K. Janssens, F. Ospitali, E. Scavetta, D. Tonelli, A. Vaccari, ACS Catal. 4 (2014) 3779-3790.

37. P.S. Roy, A.S.K. Raju, K. Kim, Fuel 139 (2015) 314-320.

38. J. Qi, Y. Sun, Z. Xie, M. Collins, H. Du, T. Xiong, J. Energy Chem. 24 (2015) 786-793.

39. A. Montebelli, C.G. Visconti, G. Groppi, E. Tronconi, S. Kohler, H.J. Venvik, R. Myrstad, Appl. Catal. A Gen. 481 (2014) 96-103.

40. C.Y. Zhao, Int. J. Heat Mass Transfer 55 (2012) 3618-3632.

41. S. Yoon, J.-Y. Yun, J.-H. Lim, B. Yoo, J. Alloys Compd. 693 (2017) 964-969.

42. J. Xiong, X. Dong, Y. Song, Y. Dong, J. Power Sources 242 (2013) 132-136.

43. C. Wang, D. Ping, X. Dong, Y. Dong, Y. Zang, Fuel Process. Technol. 148 (2016) 367-371.

44. P. Guo, Y.-X. Wu, W.-M. Lau, H. Liu, L.-M. Liu, J. Alloys Compd. 723 (2017) 772-778.

45. Y. Li, S. Yang, H. Li, G. Li, M. Li, L. Shen, Z. Yang, A. Zhou, Colloids Surf. A Physicochem. Eng. Asp. 506 (2016) 694-702.

46. F. Li, W. Liu, Y. Sun, W. Ding, S. Cheng, Int. J. Hydrog. Energy 42 (2017) 3641-3646.

47. R. Chai, Y. Li, Q. Zhang, G. Zhao, Y. Liu, Y. Lu, Mater. Lett. 171 (2016) 248-251.

48. Y. Liu, Z. Yu, Y. Hou, Z. Peng, L. Wang, Z. Gong, J. Zhu, D. Su, Catal. Commun. 86 (2016) 63-66.

49. S. Guo, Q. Wu, J. Sun, T. Chen, M. Feng, Q. Wang, Z. Wang, B. Zhao, W. Ding, Int. J. Hydrog. Energy 42 (2017) 21063-21072.

50. Y. Chen, L. Han, J. Zhu, P. Chen, S. Fan, G. Zhao, Y. Liu, Y. Lu, Catal. Commun. 96 (2017) 58-62.

51. Z. Zhang, L. Han, R. Chai, Q. Zhang, Y. Li, G. Zhao, Y. Liu, Y. Lu, Catal. Commun. 88 (2017) 90-93.

52. Y.-Z. Liu, Y. Luo, G.-W. Chu, J.-F. Chen, Catal. Today 273 (2016) 34-40.

53. C. Mu, K. Huang, T. Cheng, H. Wang, H. Yu, F. Peng, Chem. Eng. J. 306 (2016) 806-815.

54. A. Sivanantham, S. Shanmugam, Appl. Catal. B Environ. 203 (2017) 485-493.

55. Q. Zhang, Y. Li, R. Chai, G. Zhao, Y. Liu, Y. Lu, Appl. Catal. B Environ. 187 (2016) 238-248.

56.   X. Xu, H. Zhao, J. Zhou, R. Xue, J. Gao, J. Power Sources 329 (2016) 238-246.

57.   R. Chai, Z. Zhang, P. Chen, G. Zhao, Y. Liu, Y. Lu, Micropor. Mesopor. Mat. 253 (2017) 123-128.

58.   C. Xiao, B. Zhang, D. Li, Electrochim. Acta 242 (2017) 260-267.

59.   D. Park, D.J. Moon, T. Kim, Fuel Process. Technol. 124 (2014) 97-103.

60.   Y. Liu, J. Xu, H. Li, S. Cai, H. Hu, C. Fang, L. Shi, D. Zhang, J. Mater. Chem. A 3 (2015) 11543-11553.

61.   C. Fang, L. Shi, H. Hu, J. Zhang, D. Zhang, RSC Adv. 5 (2015) 11013-11022.

62.   M. Zheng, D. Yu, L. Duan, W. Yu, L. Huang, Catal. Commun. 100 (2017) 187-190.

63.   Y. Li, Q. Zhang, R. Chai, G. Zhao, F. Cao, Y. Liu, Y. Lu, Appl. Catal. A Gen. 510 (2016) 216-226.

64.   Z. Liang, P. Gao, Z. Tang, M. Lv, Y. Sun, J. CO$_2$ Utiliz. 21 (2017) 191-199.

65.   F.J. Méndez, O. Sanz, M. Montes, J. Guerra, C. Olivera-Fuentes, S. Curbelo, J.L. Brito, Catal. Today 289 (2017) 151-161.

66.   M. Frey, T. Romero, A.-C. Roger, D. Edouard, Catal. Today 273 (2016) 83-90.

67.   V. Palma, D. Pisano, M. Martino, Int. J. Hydrog. Energy 42 (2017) 23517-23525.

68.   Y. Liang, Q. Liu, A.M. Asiri, X. Sun, Y. He, Int. J. Hydrog. Energy 40 (2015) 13258-13263.

69.   A.N. Pestryakov, V.V. Lunin, V.P. Petranovskii, Catal. Commun. 8 (2007) 2253-2256.

70.   S. Cimino, A. Gambirasi, L. Lisi, G. Mancino, M. Musiani, L. Vázquez-Gómez, E. Verlato, Chem. Eng. J. 285 (2016) 276-285.

71.   E. Verlato, S. Barison, S. Cimino, F. Dergal, L. Lisi, G. Mancino, M. Musiani, L. Vázquez-Gómez, Int. J. Hydrog. Energy 39 (2014) 11473-11485.

72.   L. Sang, B. Sun, H. Tan, C. Du, Y. Wu, C. Ma, Int. J. Hydrog. Energy 37 (2012) 13037-13043.

73.   J. Kryca, P.J. Jodłowski, M. Iwaniszyn, B. Gil, M. Sitarz, A. Kołodziej, T. Łojewska, J. Łojewska, Catal. Today 268 (2016) 142-149.

74.   P.S. Roy, N.-K. Park, K. Kim, Int. J. Hydrog. Energy 39 (2014) 4299-4310.

75.   S. Cimino, R. Gerbasi, L. Lisi, G. Mancino, M. Musiani, L. Vázquez-Gómez, E. Verlato, Chem. Eng. J. 230 (2013) 422-431.

76.   P.S. Roy, C.S. Park, A.S.K. Raju, K. Kim, J. CO$_2$ Utiliz. 12 (2015) 12-20.

77.   W.Y. Choi, J.W. Lee, M.J. Kim, C.J. Park, Y.H. Jeong, H.-Y. Choi, N.-K. Park, T.J. Lee, Int. J. Precis. Eng. Manufact.-Green Technol. 4 (2017) 183-189.

78.   P. Benito, G. Nuyts, M. Monti, W. De Nolf, G. Fornasari, K. Janssens, E. Scavetta, A. Vaccari, Appl. Catal. B Environ. 179 (2015) 321-332.

79.   P. Benito, M. Monti, W. De Nolf, G. Nuyts, G. Janssen, G. Fornasari, E. Scavetta, F. Basile, K. Janssens, F. Ospitali, D. Tonelli, A. Vaccari, Catal. Today 246 (2015) 154-164.

80.   F. Basile, P. Benito, G. Fornasari, M. Monti, E. Scavetta, D. Tonelli, A. Vaccari, A novel electrochemical route for the catalytic coating of metallic supports, in: E.M. Gaigneaux, M.

Devillers, S. Hermans, P.A. Jacobs, J.A. Martens, P. Ruiz (Eds.) Studies in Surface Science and Catalysis, Elsevier, Amsterdam, NL, vol. 175, 2010, pp. 51-58.

81. P. Benito, F. Basile, G. Fornasari, M. Monti, E. Scavetta, D. Tonelli, A. Vaccari, Electrosynthesized Structured Catalysts for H_2 Production, New Strategies in Chemical Synthesis and Catalysis, Wiley-VCH, Weinheim, Germany, 2012, pp. 201-217.

82. F. Basile, P. Benito, G. Fornasari, V. Rosetti, E. Scavetta, D. Tonelli, A. Vaccari, Appl. Catal. B Environ. 91 (2009) 563-572.

83. F. Basile, P. Benito, S. Bugani, W. De Nolf, G. Fornasari, K. Janssens, L. Morselli, E. Scavetta, D. Tonelli, A. Vaccari, Adv. Funct. Mater. 20 (2010) 4117-4126.

84. P. Benito, M. Monti, I. Bersani, F. Basile, G. Fornasari, E. Scavetta, D. Tonelli, A. Vaccari, Catal. Today 197 (2012) 162-169.

85. L.N. Protasova, M.H.J.M.d. Croon, V. Hessel, Rec. Patents Chem. Eng. 5 (2012) 28-44.

86. V. Meille, Appl. Catal. A Gen. 315 (2006) 1-17.

87. T.A. Nijhuis, A.E.W. Beers, T. Vergunst, I. Hoek, F. Kapteijn, J.A. Moulijn, Catal. Rev. 43 (2001) 345-380.

88. X. Wu, D. Weng, S. Zhao, W. Chen, Surf. Coat. Technol. 190 (2005) 434-439.

89. L. Giani, C. Cristiani, G. Groppi, E. Tronconi, Appl. Catal. B Environ. 62 (2006) 121-131.

90. A.R. Tadd, B.D. Gould, J.W. Schwank, Catal. Today 110 (2005) 68-75.

91. L.M. Martínez T, O. Sanz, M.I. Domínguez, M.A. Centeno, J.A. Odriozola, Chem. Eng. J. 148 (2009) 191-200.

92. N. Burgos, M. Paulis, M. Montes, J. Mater. Chem. 13 (2003) 1458-1467.

93. C. Fukuhara, K. Kawamorita, Appl. Catal. A Gen. 370 (2009) 42-49.

94. O. Sanz, L.C. Almeida, J.M. Zamaro, M.A. Ulla, E.E. Miró, M. Montes, Appl. Catal. B Environ. 78 (2008) 166-175.

95. L. Brewer Gerald, Patent US3867313 A, 1975, Universal Oil Production.

96. J.P. Reymond, Catal. Today 69 (2001) 343-349.

97. A. Suknev, A.C. van Veen, A. Toktarev, E. Sadovskaya, B. Bal'zhinimaev, C. Mirodatos, Catal. Commun. 5 (2004) 691-695.

98. L. del Río, G. Marbán, Appl. Catal. B Environ. 126 (2012) 39-46.

99. H. Yan, D. Zhang, J. Xu, Y. Lu, Y. Liu, K. Qiu, Y. Zhang, Y. Luo, Nanoscale Res. Lett. 9 (2014) 424-424.

100. L. Wang, Y. Xie, C. Wei, X. Lu, X. Li, Y. Song, Electrochim. Acta 174 (2015) 846-852.

101. P. Caze, D. Letourneur, P. Marques, C. Remy, P. Woehl, Patent WO2003074174 A1, 2003, Corning Incorporated.

102. J. Lefevere, S. Mullens, V. Meynen, J. Noyen, Chem. Papers 68 (2014).

103. I. Reyero, I. Velasco, O. Sanz, M. Montes, G. Arzamendi, L.M. Gandía, Catal. Today 216 (2013) 211-219.

104. F.J. Echave, O. Sanz, M. Montes, Appl. Catal. A Gen. 474 (2014) 159-167.

105. F.-C. Buciuman, B. Kraushaar-Czarnetzki, Catal. Today 69 (2001) 337-342.

106. V.G. Milt, S. Ivanova, O. Sanz, M.I. Domínguez, A. Corrales, J.A. Odriozola, M.A. Centeno, Appl. Surf. Sci. 270 (2013) 169-177.

107. M.J.M. Mies, J.L.P. van den Bosch, E.V. Rebrov, J.C. Jansen, M.H.J.M. de Croon, J.C. Schouten, Catal. Today 110 (2005) 38-46.

108. E. Włoch, A. Łukaszczyk, Z. Żurek, B. Sulikowski, Catal. Today 114 (2006) 231-236.

109. A. Eleta, P. Navarro, L. Costa, M. Montes, Micropor. Mesopor. Mat. 123 (2009) 113-122.

110. S. Catillon, C. Louis, R. Rouget, Topics Catal. 30 (2004) 463-467.

111. J.M. Zamaro, M.A. Ulla, E.E. Miró, Micropor. Mesopor. Mat. 115 (2008) 113-122.

112. F. Basile, P. Benito, G. Fornasari, M. Monti, E. Scavetta, D. Tonelli, A. Vaccari, Catal. Today 157 (2010) 183-190.

113. A. Simpson, A. Lutz, Int. J. Hydrog. Energy 32 (2007) 4811-4820.

114. A. Al-Douri, D. Sengupta, M.M. El-Halwagi, J. Nat. Gas Sci. Eng. 45 (2017) 436-455.

115. J. Martinez-Gomez, F. Nápoles-Rivera, J.M. Ponce-Ortega, M.M. El-Halwagi, Appl. Therm. Eng. 110 (2017) 678-685.

116. Z.I. S G Adiya, V. Dupont, T. Mahmud, Fuel Process. Technol. 159 (2017) 128-144.

117. S.H. Tan, P.I. Barton, Energy 141 (2017) 398-422.

118. A. Abuşoğlu, S. Demir, E. Özahi, Int. J. Hydrog. Energy 41 (2016) 13426-13435.

119. G. Nahar, D. Mote, V. Dupont, Renew. Sustain. Energy Rev. 76 (2017) 1032-1052.

120. Statistical report of European Biomass Association 2016. http://www.aebiom.org/statistical-report-2016/ (access 25/11/2017)

121. S.M. Mousavi Ehteshami, S.H. Chan, Energy Technol. Policy 1 (2014) 15-22.

122. T.L. LeValley, A.R. Richard, M. Fan, Int. J. Hydrog. Energy 39 (2014) 16983-17000.

123. J.N. Armor, Catal. Lett. 101 (2005) 131-135.

124. L.E. Basini, A. Guarinoni, Ind. Eng. Chem. Res. 52 (2013) 17023-17037.

125. L.L.G. Jacobs, P.W. Lednor, P.J.M. Van Loon, M. Oosterveld, K.A. Vonkeman, Patent US5639401 A, 1997, Shell Oil.

126. H.A. Wright, J.D. Allison, D.S. Jack, G.H. Lewis, S.R. Landis, Prepa. Pap. Am. Chem. Soc., Div. Fuel Chem. 48 (2003) 2.

127. P.K. Ng, E.W. Schneider, J. Electrochem. Soc. 133 (1986) 17-21.

128. L. Indira, P.V. Kamath, J. Mater. Chem. 4 (1994) 1487-1490.

129. D. Tonelli, E. Scavetta, M. Giorgetti, Anal. Bioanal. Chem. 405 (2013) 603-614.

130. I. Gualandi, M. Monti, E. Scavetta, D. Tonelli, V. Prevot, C. Mousty, Electrochim. Acta 152 (2015) 75-83.

131. I. Gualandi, E. Scavetta, Y. Vlamidis, A. Casagrande, D. Tonelli, Electrochim. Acta 173 (2015) 67-75.

132. M. Shao, R. Zhang, Z. Li, M. Wei, D.G. Evans, X. Duan, Chem. Commun. 51 (2015) 15880-15893.

133. Y. Vlamidis, E. Scavetta, M. Giorgetti, N. Sangiorgi, D. Tonelli, Appl. Clay Sci. 143 (2017) 151-158.

134. J. Wang, L. Wang, X. Chen, Y. Lu, W. Yang, J. Solid State Electrochem. 19 (2015) 1933-1948.

135. X. Yu, M. Zhang, W. Yuan, G. Shi, J. Mater. Chem. A 3 (2015) 6921-6928.

136. X. Long, Z. Ma, H. Yu, X. Gao, X. Pan, X. Chen, S. Yang, Z. Yi, J. Mater. Chem. A 4 (2016) 14939-14943.

137. Y. Vlamidis, E. Scavetta, M. Gazzano, D. Tonelli, Electrochim. Acta 188 (2016) 653-660.

138. L. Qian, W. Chen, M. Liu, Q. Jia, D. Xiao, ChemElectroChem 3 (2016) 950-958.

139. F. Cavani, F. Trifirò, A. Vaccari, Catal. Today 11 (1991) 173-301.

140. P. Benito, F.M. Labajos, J. Rocha, V. Rives, Micropor. Mesopor. Mat. 94 (2006) 148-158.

141. M. Monti, P. Benito, F. Basile, G. Fornasari, M. Gazzano, E. Scavetta, D. Tonelli, A. Vaccari, Electrochim. Acta 108 (2013) 596-604.

142. F. Basile, P. Benito, G. Fornasari, A. Vaccari, Appl. Clay Sci. 48 (2010) 250-259.

143. F. Basile, P. Benito, G. Fornasari, V. Rosetti, E. Scavetta, D. Tonelli, A. Vaccari, Appl. Catal. B Environ. 91 (2009) 563-572.

144. F. Basile, P. Benito, P. Del Gallo, G. Fornasari, D. Gary, V. Rosetti, E. Scavetta, D. Tonelli, A. Vaccari, Chem. Commun. (2008) 2917-2919.

145. J.W. Kim, B.K. Choi, M.J. Jang, Patent US 20170210090 A1, 2017, Alantum.

146. E. Bianchi, T. Heidig, C.G. Visconti, G. Groppi, H. Freund, E. Tronconi, Chem. Eng. J. 198-199 (2012) 512-528.

147. P. Aghaei, C.G. Visconti, G. Groppi, E. Tronconi, Chem. Eng. J. 321 (2017) 432-446.

148. E. Bianchi, T. Heidig, C.G. Visconti, G. Groppi, H. Freund, E. Tronconi, Catal. Today 216 (2013) 121-134.

149. W. Peng, M. Xu, X. Li, X. Huai, Z. Liu, H. Wang, Chem. Eng. Sci. 161 (2017) 92-108.

150. G. Groppi, E. Tronconi, C.G. Visconti, A. Tasso, R. Zennaro, Patent WO/2015/033266, 2015, Eni S.P.A.

151. L. Giani, G. Groppi, E. Tronconi, Ind. Eng. Chem. Res. 44 (2005) 4993-5002.

152. E. Verlato, S. Cattarin, N. Comisso, A. Gambirasi, M. Musiani, L. Vázquez-Gómez, Electrocatal., 3 (2012) 48-58.

153. J. Kryca, P.J. Jodłowski, M. Iwaniszyn, B. Gil, M. Sitarz, A. Kołodziej, T. Łojewska, J. Łojewska, Catal. Today, 268 (2016) 142-149.

Chapter 2. Reactions involved in the electrodeposition of Mg-Al hydrotalcite-type compounds on FeCrAl foams and plates

P. H. Ho, M. Monti, E. Scavetta, D. Tonelli, E. Bernardi, L. Nobili, G. Fornasari, A. Vaccari, P. Benito, Electrochimica Acta 222 (**2016**) 1335 – 1344.

Chapter 2

2.1 Introduction

The electrodeposition of HT compounds is based on the generation of a basic media at the electrode–electrolyte interface by application of a cathodic potential or current pulse [1]. The electrolytic bath usually contains nitrates of the cations to be deposited, while KNO_3 as supporting electrolyte should be avoided whenever K interferes in the final application of the material [2]. The nitrate reduction, H_2 evolution and O_2 reduction were proposed to occur during electrodeposition of HT compounds at a Pt electrode [3], but a detailed study of the electrochemical reactions is lacking.

The electrodeposition is considered as a simple, low cost and fast method to control the thickness of hydroxide and/or oxide deposited films [4]. However, a good HT coating, in terms of thickness and composition, can be obtained only if a suitable and constant pH for the precipitation of a HT phase is achieved during the cathodic pulse all over the support surface. The rates of OH^- production and OH^- consumption by cation precipitation have, therefore, to be balanced. These issues may be easily achieved for small Pt electrodes and when simple and thin Ni/Al HT coatings are prepared [5]. Conversely, it is more challenging to tailor the thickness and to ensure a homogeneous deposition of HT compounds with three or more cations in the layers over large and complex supports, such as Rh/Mg/Al and Rh/Ni/Mg/Al on FeCrAl foams. Thus, it is reported that the composition of the solid deposited differs from that in the electrolytic solution [6,7].

The support features (*i.e.*, morphology, composition and electrical conductivity) determine the activity in the reduction reactions, potential and current distribution as well as mass transfer processes. It is well–known that the electrochemical reduction of nitrate is a complex process; its products, rate and mechanism depend not only on the support, but also on the pH of the electrolytic solution, concentration of nitrates, current density, mass transport regime, temperature, and presence of species in the solution that inhibit or promote some reduction

steps [8]. Moreover, during the electrodeposition of HT compounds, two further issues should be considered: i) the growing of the film, which alters the conductivity and the area available for nitrate adsorption; ii) the continuous modification of the pH, and, therefore, of the nitrate reduction potential and electrochemical products. The nitrate reduction to nitrite has been assumed to take place during the electrodeposition of HT compounds on Pt and gold substrates [9-11]; however, both NO_2^- and NH_4^+ species could be produced during an electro–base generation method [12,13].

Hence, the first step for the improvement of the properties of HT compounds electrodeposited on FeCrAl foams is to understand the electrochemical processes taking place at the electrolyte-foam interface and if they are modified by the support shape or during the electrodeposition pulse. So far, no detailed study has been reported either on the electrochemical reactions occurring during the HT compounds synthesis or on the effect of the support shape on these reactions. In the past, it was studied the mechanism of deposition of Mg/Al HT compounds and the pH generated at the electrode-electrolyte interface using Pt supports [14]; only a rough correlation between Pt and FeCrAl foam was proposed.

The aim of this chapter was, therefore, to investigate the electrochemical processes occurring during the electrodeposition of Mg/Al HT compounds on FeCrAl materials and to evidence if they are influenced by the shape of the support, making a comparison between foams and plates. The nitrate, water and oxygen reduction reactions were investigated through linear sweep voltammetry (LSV) and potentiostatic cathodic reduction by modifying the composition of the electrolytic bath. The nitrate activity was investigated with: i) solutions free of precipitating cations, *i.e.,* containing only KNO_3; ii) solutions containing $Mg(NO_3)_2$ and $Al(NO_3)_3$ with Mg/Al atomic ratio (a.r.) equal to 3/1. The analysis of the nitrate reduction products was performed by ex-situ ion chromatography. On the other hand, the water and oxygen reductions were studied with chloride salts, largely used in the study of hydrogen

evolution reactions and in the electrodeposition of ZnO in the presence of dissolved O_2 [15].

The electrochemical results were correlated to both the pH developed near the supports and the

features of the synthesized solids.

2.2 Experimental

2.2.1 Electrochemical set-up

Electrochemical measurements were carried out in a single compartment three-electrode

cell using a potentiostat (Autolab, PGSTAT128N, Eco Chemie, Netherlands) with GPES

software. The working electrodes were plates (0.6 x 1.5 x 0.01 cm) and open-pore foam

cylinders (0.4 x 1.19 cm, ca. 0.2 g) made of FeCrAl. Before performing the tests, the plates

were mechanically abraded by a 210 grit SiC emery paper, then rinsed with distilled water –

soap – distilled water and dried at 60 ºC. The roughness of the plates increases of $\sim 30\%$ after

abrasion. The electrical contact for the plates was made with a copper wire, and it was well

insulated by two layers of Teflon tape and parafilm to ensure that only a fixed area of both

sides of the plate (about 1.20 cm^2) acted as a working electrode. The foams were rinsed with

acetone and water, and then dried at 60 ºC. The electrical contact of the foams was made with

Pt wire as described elsewhere [6].

The counter electrode was a Pt cylindrical grid (approximate 18 cm^2) placed at ~ 1.0 cm

around the working electrode. A saturated calomel electrode (SCE) was used as a reference

electrode and all potentials were quoted *vs* SCE. The reference electrode was positioned in the

middle of the plate and the counter electrode or on the top of the foam; in both configurations

it was at a distance shorter than 1.0 mm from the working electrode.

2.2.2 Linear sweep voltammetries and potentiostatic cathodic reductions

LSVs were recorded from 0 to -1.4 V at 1, 10, and 50 mV s^{-1} scan rate. Potentiostatic

cathodic reductions were performed at -1.2 V *vs* SCE for 500 to 2000 s, under natural convective conditions.

Electrolytic solutions were prepared using ultra-pure deionised water (UPW) provided by a Millipore filtration instrument (electrical resistivity 18.2 MΩ cm). Solutions containing 0.135 M KNO_3 or KCl were prepared; the pH of the solutions was adjusted to 3.8 [16] by adding 0.1 M HNO_3 or HCl, respectively. In some tests, 1 M KCl or KOH was added. The study of the electrodeposition of Mg/Al HT compounds was conducted in aqueous solutions containing a mixture of $Mg(NO_3)_2$ and $Al(NO_3)_3$ or $MgCl_2$ and $AlCl_3$ with Mg/Al = 3/1 a.r. and total metal concentration of 0.06 M. This concentration provided a pH around 3.7 at 20 ${}^oC$, thus the pH was not modified before the tests. Solutions containing the single nitrates, $Mg(NO_3)_2$ (0.0675 M) and $Al(NO_3)_3$ (0.045 M) were also prepared.

The dissolved O_2 was removed in selected electrolytic solutions by bubbling N_2. During the electrochemical measurements, the electrochemical cell was protected by a N_2 flow in the headspace to avoid O_2 contamination.

The uncompensated resistance (R_u) in the electrochemical cell was measured with a CH Instruments Mod. 660A, according to the method proposed by He and Faulkner [17]. All the measurements were repeated three times and the obtained average values were summarized in Table 2.1. The low R_u values led to small Ohmic drops (smaller than 50 mV) in most of the experiments. However, when a high current was recorded the potential scans were corrected by ohmic drop, assuming a constant R_u during the scans.

The high foam surface required a large surface Pt counter electrode to assure the passage of the current. However, a large Pt counter electrode probably enhanced the anodic reaction producing H^+ [18]. To study this effect, the sizes of both the plate and the counter electrode were decreased. The results (not shown) were not largely modified suggesting that the H^+ formation, although taking place, did not modify the shape of both LSV and chronoamperometry (CA) reported in this chapter.

Table 2.1. Compositions of the prepared electrolytic solutions and average values of the uncompensated resistance (R_u) of the electrochemical cell using the plate or the foam as working electrode

Solution	Concentration / M	R_u / Ω	
		Plate	**Foam**
KNO_3	0.135	6.5	3.0
KCl	0.135	6.5	3.0
Mg/Al-NO_3	0.06	4.5	1.5
Mg/Al-Cl	0.06	4.5	1.5

2.2.3 Electrochemical impedance spectroscopy

Electrochemical impedance spectroscopy (EIS) measurements were carried out with a CH Instruments Mod. 660A, controlled by a personal computer via CH Instruments software. The temperature was kept constant using a thermostat HAAKE D8. The tests were performed in 0.01 M buffer solutions containing 2.0 mM $Fe(CN)_6^{3-/4-}$ as a redox probe, at a potential of 0.17 V vs SCE. The investigated frequency range was 100 mHz – 10 kHz.

2.2.4 pH measurements

pH measurements near the foam surface were performed using the pX1000 module (Metrohm) of Autolab equipped with a micro-pH electrode (METTLER TOLEDO, U402–M3–S7/200). The system was calibrated with buffer solutions at pH 2.00 and 9.21 (Hamilton) before each measurement. The sensitive bulb of the pH electrode was inserted in the foam via a small hole dug out in the centre of the cylinder.

For comparison purposes, titration of 100 mL of 0.06 M nitrate solutions containing a single cation (Al^{3+} or Mg^{2+}) or mixed cations (Mg^{2+}/Al^{3+} = 3/1) was carried out with 1 M NaOH solution. During the titration, NaOH solution was added every 0.25 mL, and pH was measured by a precise pH meter (HI-9126 Waterproof pH/ORP Meter with CalCheck, HANNA Instrument). Before using for the titration, the pH meter was calibrated with buffer solutions at pH 4.01 and 10.01. The precipitation pH values obtained were used to design the plot in Scheme 2.1.

Reaction	Potential E° (V)
1. $NO_3^- + 2H^+ + 2e^- \rightarrow NO_2^- + 2H_2O$	0.934
2. $NO_3^- + 2H_2O + 2e^- \rightarrow NO_2^- + 2OH^-$	0.010
3. $NO_3^- + 10H^+ + 8e^- \rightarrow NH_4^+ + 3H_2O$	0.360
4. $NO_3^- + 7H_2O + 8e^- \rightarrow NH_4^+ + 10OH^-$	-0.120
5. $2H_3O^+ + 2e^- \rightarrow H_2 + 2H_2O$	0.000
6. $2H_2O + 2e^- \rightarrow H_2 + 2OH^-$	-0.828
7. $O_2 + 2H^+ + 2e^- \rightarrow H_2O_2$	0.700
8. $H_2O_2 + 2H^+ + 2e^- \rightarrow 2H_2O$	1.760
9. $O_2 + H_2O + 2e^- \rightarrow HO_2^- + OH^-$	-0.065
10. $HO_2^- + H_2O + 2e^- \rightarrow 3OH^-$	0.867

Scheme 2.1. Electrochemical reactions of reduction of nitrate, H_2O and O_2; and pH domains for the precipitation of single hydroxides and Mg/Al HT compounds.

2.2.5 Characterization of the coatings

Scanning electronic microscopy coupled with energy dispersive spectroscopy (SEM/EDS) analyses were performed by using an EVO 50 Series Instrument (LEO ZEISS) equipped with an INCAEnergy 350 EDS micro analysis system and INCASmartMap to image the spatial variation of elements in a sample (Oxford Instruments Analytical). An accelerating voltage of 20 kV was applied with a spectra collection time of 60 s, and point measurements were performed in 10–15 regions of interest. Secondary electron images were collected.

X-ray diffraction (XRD) analysis of the film grown on FeCrAl plates was carried out using a PANalytical X'Pert diffractometer equipped with a copper anode ($\lambda_{mean} = 0.15418$ nm) and a fast X'Celerator detector. The measurement was performed with a step of 0.05° (2θ scale).

2.2.6 Analysis of the electrochemical reduction products

The solution near the foam surface (0.5 mL) was withdrawn at different potentials or at different times during potential sweeps or chronoamperometric experiments, respectively. A syringe equipped with a handy small plastic tube was inserted into a hole in the foam. The hole was placed in the center of the foam and its depth was half of the foam length to ensure that only the solution at the vicinity of the foam was collected. The sample was then diluted to a concentration suitable for the analytical detection. NO_2^- and NH_4^+ were determined by Ion

Exchange Chromatography (Metrohm 761 Compact IC), with and without chemical suppression, respectively. NO_2^- was separated by a Metrosep A Supp 4/5 Guard/4.0 column (5 x 4 mm) followed by a SHODEX SI–90 4E column (250 × 4 mm), with isocratic elution (1.7 mM $NaHCO_3$ and 1.8 mM Na_2CO_3) and a flow rate of 1.2 mL min^{-1}. NH_4^+ was separated on a Metrosep C4/150 column (150 × 4 mm) with isocratic elution (4 mM tartaric acid and 1 mM dipicolinic acid) and a flow rate of 1.2 mL min^{-1}. All solutions were prepared using ACS grade reagents (purity ≥ 99.5%) and UPW; stock standard solutions (1000 mg L^{-1}) of each ion were supplied by Ultra Scientific. The measurements were performed twice (by carrying out independent experiments) and the same trend was observed in both cases.

2.3 Results and discussion

The cathodic nitrate reduction was investigated using electrolytic solutions containing KNO_3, or $Mg(NO_3)_2$ and $Al(NO_3)_3$ (Mg/Al = 3/1 a.r.) as shown in Table 2.1. The concentration of nitrate electroactive species was kept constant in both solutions (0.135 M), but not the ionic strength. The contribution of the water reduction reaction to the overall process was analysed using nitrate–free solutions; to this aim measurements in solutions containing chlorides (KCl or $MgCl_2$ and $AlCl_3$) at the same total concentrations as nitrate solutions were carried out. Lastly, the role of O_2 reduction was evaluated using de-aerated solutions. In Scheme 2.1, the possible electrochemical reactions were summarized.

The effective surface area values of the electrodes were determined under LSV (50 mV s^{-1}) for the one-electron reduction of $K_3[Fe(CN)_6]$ [2.0 mM in water with 0.1 M KNO_3] by means of the Randles-Sevcik equation (1). Each measurement was repeated three times.

$$i_p = 2.69 \times 10^5 \, n^{3/2} A \, D^{1/2} \, C \, v^{1/2} \tag{2.1}$$

where i_p is the peak current (A), n (=1) is the number of electrons transferred, A is the effective area of the electrode (cm^2), D is the diffusion coefficient of $[Fe(CN)_6]^{3-}$ (taken to be $7.60 \times 10^-$

^{6} cm^{2} s^{-1}), C is the concentration (mol cm^{-3}), ν is the scan rate (V s^{-1}). These measurements

allowed to estimate an electrochemical active area of 4.13 $\pm$ 0.17 cm^{2} for the foam and 0.31

$\pm$ 0.01 cm^{2} for the plate. The current densities reported in this chapter were calculated using

these electrochemically active areas.

2.3.1 Linear sweep voltammetry

LSVs were performed at several scan rates, *i.e.*, 1, 10 and 50 mV s^{-1}. The role of supporting

electrolyte [19] and pH [8] on the reduction processes was also studied.

2.3.1.1 KNO$_3$ and KCl solutions

LSV curves carried out at 1 mV s^{-1}, in the 0.0 – -1.4 V range, at plates and foams soaked in

KCl or KNO$_3$ 0.135 M solutions were displayed in Fig. 2.1. At the plates, the onset potential

of the reduction wave depended on the electrolyte, being -1.1 V in KCl and -0.9 V in KNO$_3$;

the cathodic current was related to water reduction (H$_2$ evolution) in the first case and to the

overlapped nitrate and water reduction in the second case.
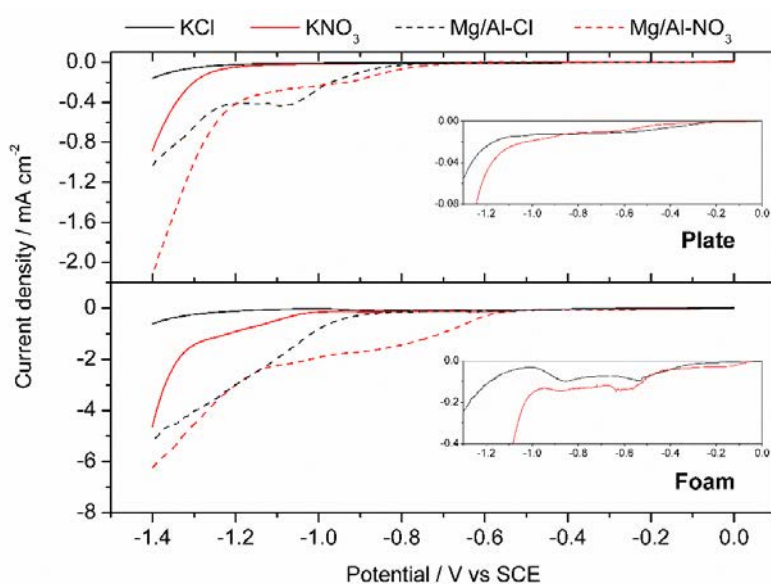
Figure 2.1. LSV curves recorded at plates and foams in 0.135 M KCl, 0.135 M KNO$_3$, 0.06 M Mg/Al–Cl and 0.06 M Mg/Al–NO$_3$ solutions. Inset: magnification of the LSV curves in 0.135 M KCl, 0.135 M KNO$_3$ at plates and foams. Scan rate: 1 mV s^{-1}; Potential range: 0 – -1.4 V.

The onset potentials of H_2 evolution and nitrate reduction processes occurred at quite similar values at the foams. However, the wave was more intense for the foam than the plate in the -0.9 to -1.3 V range. Moreover, two additional small waves were observed at -0.5 V and -0.9 V, when the foams were dipped in both KCl and KNO_3 solutions, which could be attributed to the two–step O_2 reduction [20]; although, the reduction of some oxides in the FeCrAl foam and the H_2 evolution cannot be discarded. The current density increased in that potential range with increasing the scan rate (Fig. 2.2) and the two small waves moved towards more cathodic potentials. In KCl solution at a scan rate of 50 mV s^{-1}, the two peaks merged; furthermore, a plateau was observed at a potential more cathodic than -1.05 V. In KNO_3 solution, several reduction processes occurred, particularly at 10 mV s^{-1}, which made the peak assignment more difficult.
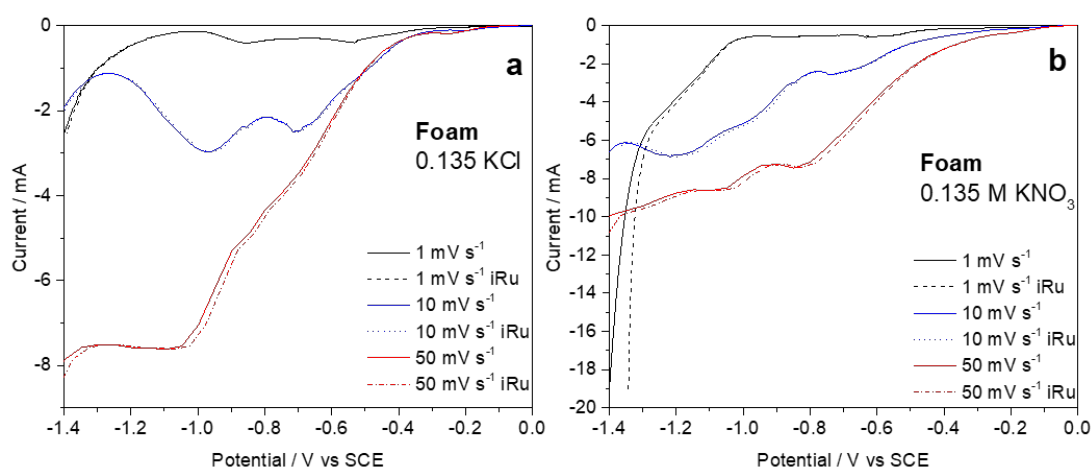
Figure 2.2. LSV curves at different scan rates (1, 10 and 50 mV s^{-1}) with Ohmic drop corrections at foams (a) 0.135 M KCl and (b) 0.135 M KNO_3.

The addition of 1 M KCl did not modify the onset potential in the 1 mV s^{-1} sweep potential experiments (Fig. 2.3). The current increased more steeply than in absence of chlorides despite they were reported to inhibit the nitrate reduction [8]. On the other hand, the LSV response was sensitive to the pH (Fig. 2.3), an increase in the pH lead to a shift in the reduction potential towards more negative values [8].
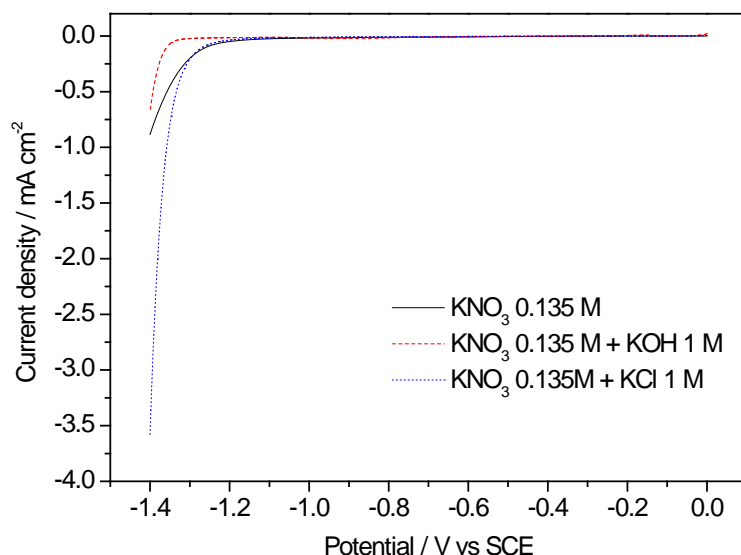
Figure 2.3. LSV curves (1 mV s^{-1}, 0 – -1.4 V) recorded at plates in 0.135 M KNO$_3$ solution with different supporting electrolytes.

2.3.1.2   *Mg/Al–NO$_3$ and Mg/Al–Cl solutions*

The voltammetric response in presence of precipitating cations (Fig. 2.1), *i.e.*, potential domains and current densities reached in the polarization profiles, depended on the support shape and composition of the deposition bath. However, a general trend was observed: the addition of the precipitating cations to the electrolytic solutions led to a steeper wave shifted to less cathodic potentials than in cation-free solutions.

At the plates, the potential sweep at 1 mV s^{-1} showed a sigmoidal wave, the plateau being more remarkable for chlorides than for nitrates solution. The reduction started at $\sim$ -0.65 V and -0.75 V in nitrates and chlorides solutions, respectively, and the plateau was reached at $\sim$ -0.92 V and -1.05 V. These results suggested a mass transfer limited process. In chlorides solution, it could be related to the contribution of O$_2$ reduction, which is mass transfer controlled [21-23]; however, in these experiments the formation of H$_2$ bubbles was already observed at -0.9 V. The second cathodic wave above -1.2 V corresponded to the reduction of water with H$_2$ bubble formation in chlorides solution, while in nitrates solution the nitrate reduction may also take place.

On the other hand, a continuous current increase was recorded at the foam when the potential was scanned towards more negative values, and a large current density was recorded (Fig. 2.1). Regarding the composition of the deposition bath, for chlorides solution, the onset potential was in the range -0.8 V – -0.9 V, while for nitrates solution the reduction started earlier (-0.5 V – -0.6 V). It is noteworthy that unlike for the plates H_2 bubbles were not observed. Indeed, on planar surfaces the bubbles accumulate [24], while they are dispersed on the foam [25].

The reduction waves in potential sweep scans in de-aerated solutions shifted towards more negative potentials at both plates and foams (in Fig. 2.4 only the results obtained at plates are shown). Therefore, the oxygen reduction occurred in the potential range -0.5 V – -0.9 V contributing to the pH increase in both chlorides and nitrates solutions.
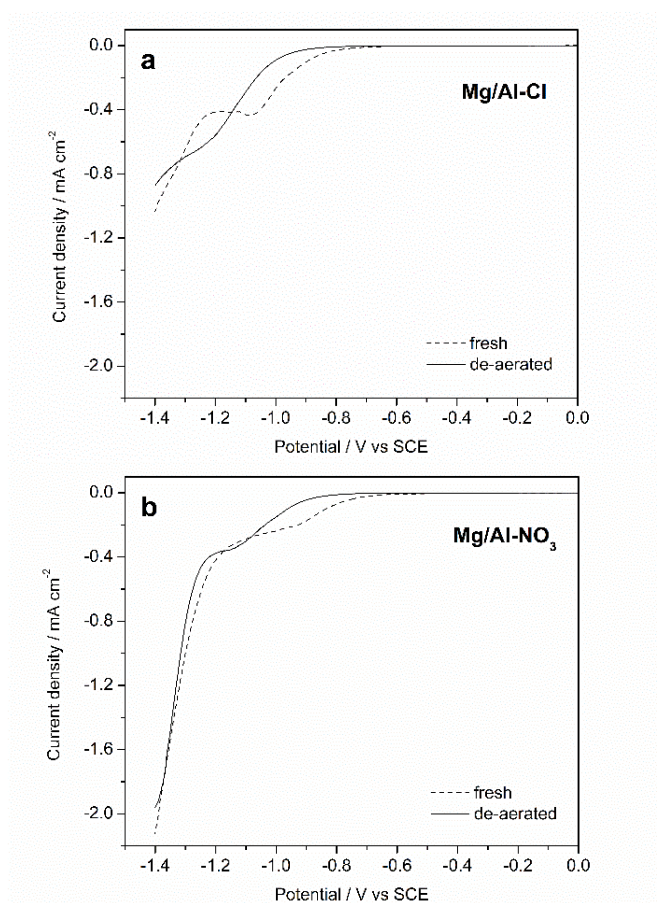
Figure 2.4. LSV curves recorded at plates in fresh and de-aerated 0.06 M Mg/Al–Cl (a) and 0.06 M Mg/Al–NO$_3$ (b) solutions. Scan rate: 1 mV s^{-1}; Potential range: 0 – -1.4 V.

Lastly, the presence of 0.1 M KNO₃ as the supporting electrolyte increased the current registered (Fig. 2.5), although the shape of the curve was not modified.
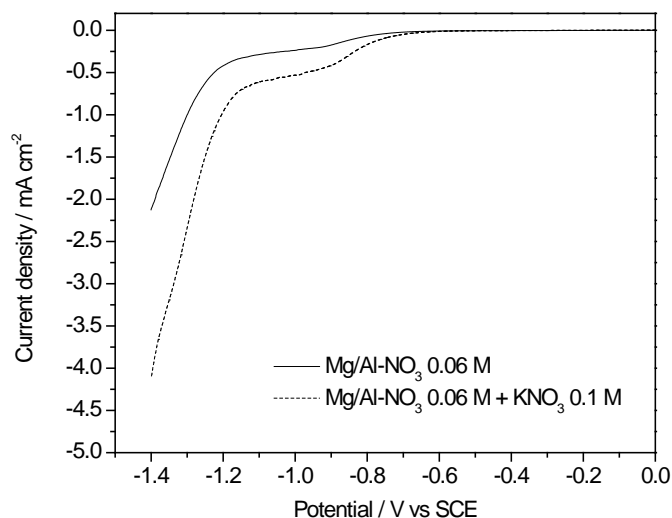
Figure 2.5. LSV curves (1 mV s⁻¹, 0 – -1.4 V) recorded at plates in 0.06 M Mg/Al-NO₃ solution with and without 0.1 M KNO₃ supporting electrolyte.

By increasing the scan rate to 10 and 50 mV s⁻¹, at the plate (Fig. 2.6a), the current increases and the reduction peak plateau shifts slightly towards more negative values, even after Ohmic drop correction. The shift is due to the increase of the internal diffusion resistance within the pseudocapacitive material. The results are related to irreversible systems [26,27], which are also mass transfer limited.
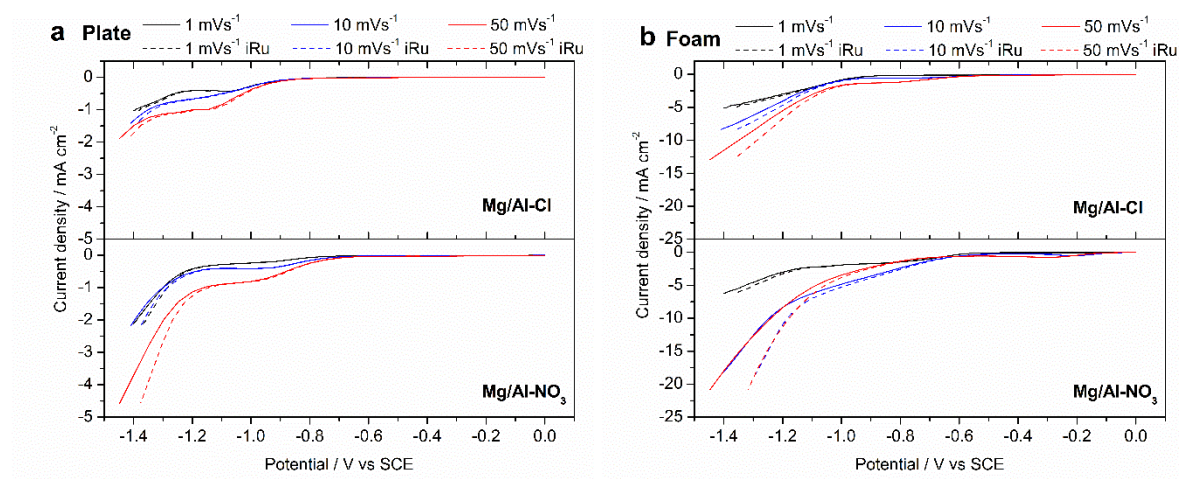
Figure 2.6. LSV curves recorded at different scan rates at plates (a) and foams (b) in 0.06 M Mg/Al–Cl and 0.06 M Mg/Al–NO₃ solutions. Scan rate: 1, 10 and 50 mV s⁻¹; Potential range: 0 – -1.4 V.

By changing the scan rate at the foams immersed in chlorides solution (Fig. 2.6b), despite the absence of a well–defined limited diffusion step, the same trend as that at the plates was observed, *i.e.*, the current density increases with increasing the scan rate and the reduction slightly shifted towards more negative potentials. On the other hand, for nitrate solution, the absence of a well-defined trend in the traces recorded at 10 and 50 mV s^{-1} could be due both to some parts of the surface that are not accessible at high charging-discharging rates and to the saturation of the electroactive sites. The higher current could also produce a large Ohmic drop causing distortion of the curves [28]; although in the present case the Ohmic drop was not high. Finally, at the foams the not planar surface of the struts may also modify the mass transport phenomena.

2.3.1.3 *Effect of the type of precipitating cation*

The catalytic effect of cations observed during the nitrate reduction has been previously reported either in absence or presence of electrodeposition processes. A double layer effect was reported during the nitrate reduction in solutions containing cations of different radii and charge [29]. The cations were located at the outer Helmholtz plane (OHP) and acted as an attracting center for nitrates, forming an instantly neutral ion pair, which was not repelled by the negatively charged electrode.

During the electrodeposition, either reduction or adsorption of cations could take place. The reduction of Zn^{2+} [23] or Ni^{2+} [30] to metals increased the electrode surface area and promoted the nitrate reduction. On the other hand, the adsorption of cations such as Zr^{4+}, La^{3+} [31] and Zn^{2+} [32,33] on the working electrode surface favored the nitrate reduction and, therefore, the precipitation of the hydroxides or oxides. The enhancement was related not only to the cation-nitrate interaction, but also to the logarithm of the stability constant of the monohydroxide complex of the cations [34]. The higher the stability constant was, the more positive potential

was needed for the nitrate reduction. Metals with high stability constants of the hydroxide complexes would favor the reduction of nitrate since OH^- are consumed and the equilibrium is shifted according to the Le Chatelier's principle.

Herein, LSV curves recorded in solutions containing only $Mg(NO_3)_2$ or $Al(NO_3)_3$ confirmed that the shift was related to the type of cation (Fig. 2.7). The concentration of the solutions was selected to keep constant the nitrate concentration as in $Mg/Al–NO_3$ solutions, *i.e.* 0.0675 M $Mg(NO_3)_2$ and 0.045 M $Al(NO_3)_3$. The reduction wave onset depended on the solution type, being at the same potential for $Al(NO_3)_3$ and $Mg/Al–NO_3$ solutions, while requiring an overpotential of -1.2 V with $Mg(NO_3)_2$ solution. The increase in the $Mg(NO_3)_2$ concentration (from 0.0675 M to 0.135 M) increased the double layer effect and the amount of Mg^{2+} available for OH^- consumption, thus the peak shifted to less cathodic potentials; however, the reduction potential was still more cathodic than the one for the solutions having the HT ratio. These results suggested that the presence of cations precipitating at low pH, namely with high stability constant of the hydroxides, such as Al^{3+}, fostered the reduction processes.
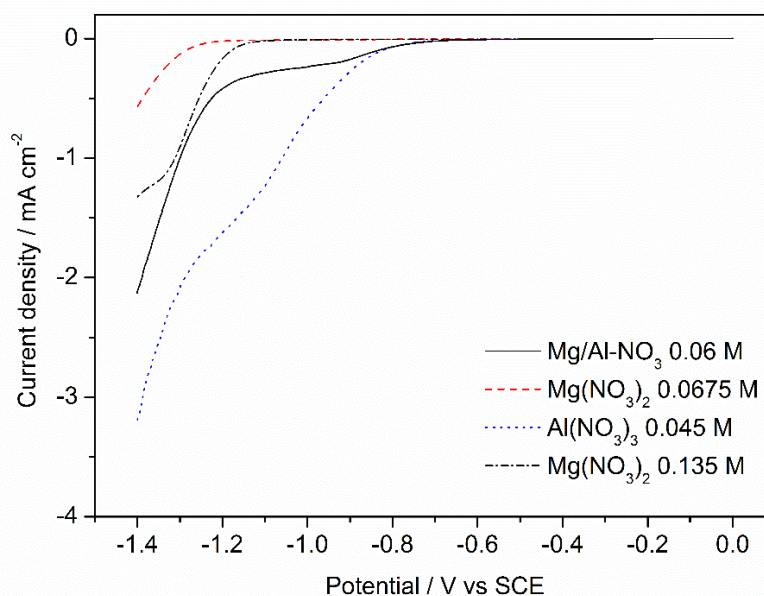
Figure 2.7. LSV curves recorded at the plate in 0.06 M $Mg/Al–NO_3$, 0.045 M $Al(NO_3)_3$, and 0.0675 M and 0.135 M $Mg(NO_3)_2$ solutions. Scan rate: 1 mV s^{-1}; Potential range: 0 – -1.4 V.

In the present study, we observed that the cations did not only promote the nitrate reduction, but a similar effect also occurred in the chlorides solutions. Mg^{2+} and Al^{3+} cannot be reduced at these potentials, thus it would appear that the cations have a catalytic effect on the reduction of the solvent, as previously reported for $SmCl_3$ aqueous solution [35].

2.3.2 Potentiostatic experiments

Current transient curves were recorded at -1.2 V for times ranging from 500 to 2000 s, *i.e.*, under electrodeposition conditions suitable to prepare HT compounds that can be used as catalyst precursors [7]. According to the information obtained in previous sections, the potential corresponds to the reduction of nitrate, dissolved oxygen and H_2 evolution. Moreover, as previously observed in the LSV curves, a larger current density was recorded at foams than at plates.

The dependence of the current density on time during the application of -1.2 V for 500 s in KNO_3 and KCl solutions was displayed in Fig. 2.8. The sharp decrease in the current density during the first 10 s is due to the consumption of the electroactive species near the support and thickening of the diffusion layer. However, at long times the convection may hinder the expansion of the diffusion layer [36]. The limiting current was only slightly higher for KNO_3 than KCl solutions; this could be related to a different number of exchanged electrons in the electrochemical reactions or to the occurrence of non–Faradaic processes; however, in both cases the current was low.
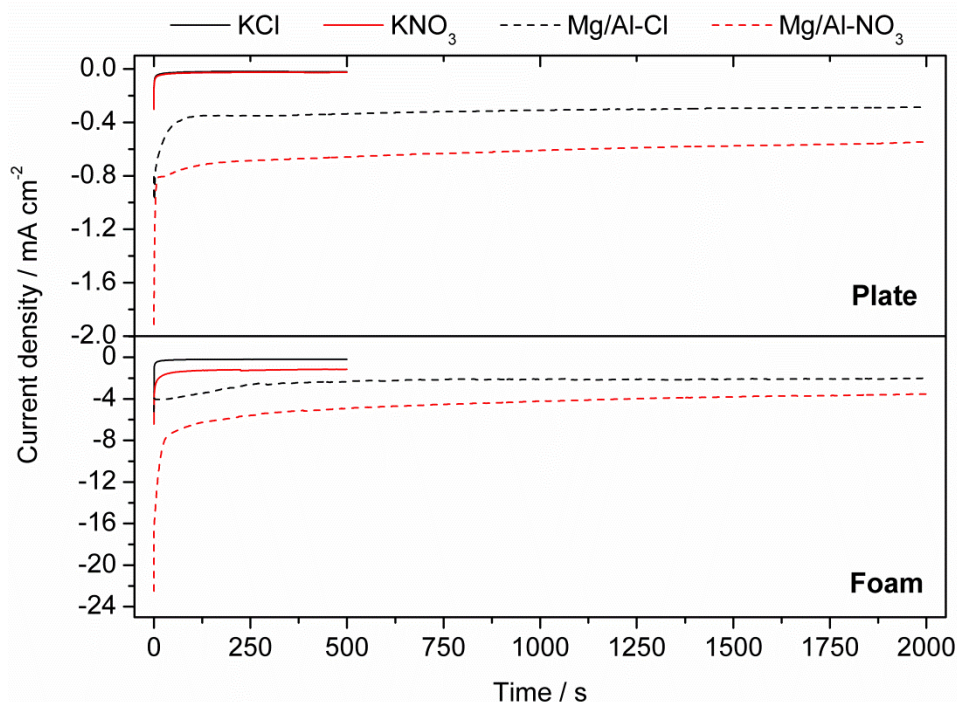
Figure 2.8. Current transient curves recorded at plates and foams at -1.2 V in 0.135 M KCl, 0.135 M KNO$_3$, 0.06 M Mg/Al–Cl and 0.06 M Mg/Al–NO$_3$ solutions.

The nitrate reduction at very cathodic potentials observed during potential sweep experiments, and the low current density exchanged in potentiostatic measurements indicated a low activity of the FeCrAl alloy for nitrate reduction. The resistance of the support and the increase of the pH during the experiments may contribute to this behaviour.

The limiting current density increased in presence of cations both at plates and foams. The current density was always larger at foams, and the plateau was reached at longer electrodeposition time, about 200 s for the plate and 500 s for the foam (Fig. 2.8). The differences in the current density may be related to the enhancement of the reduction reactions as observed in the potential sweeps. However, in the case of nitrates, the modification of the reduction mechanism affected the exchanged electrons (see below). Unlike KNO$_3$ and KCl solutions, the current smoothly decreased with the pulse length. This behaviour could be related to the formation of an insulating hydroxide layer [37]; nevertheless, the higher consumption of electroactive species in presence of cations may modify the mass transfer processes.

2.3.3 Nitrite and ammonium ions concentration

The trend in the concentration of nitrite and ammonium ions close to the foam surface during potential sweeps (1 mV s^{-1}) and current transient curves (-1.2 V, 2000 s) were investigated in KNO$_3$ and Mg/Al–NO$_3$ solutions. It should be remarked that it was not possible to analyze only the composition of the electrode/electrolyte interface, thus NO$_2^-$/NH$_4^+$ concentration ratios are given in Tables 2.2 and 2.3. The solutions were withdrawn in a sequential way, namely using the same foam and taking them out at different potentials or electrodeposition times, during either a potential sweep or current transient curve. To study if the removal of the solution affected the results obtained in the following analyses, selected analyses were performed in solutions coming from a single withdrawal. The results showed a similar trend in both cases.

During the potential sweep in KNO$_3$, the solutions were analyzed at -0.5, -0.9 and -1.2 V, while in Mg/Al–NO$_3$ at -0.4, -0.65, -0.9 and -1.2 V. In KNO$_3$, at -0.5 V, only NH$_4^+$ was detected and it may be ascribed to an early nitrate reduction. By increasing the applied potential both NO$_2^-$ and NH$_4^+$ were produced. The concentration of NO$_2^-$ steadily increased, being higher than NH$_4^+$ concentration at -1.2 V. The presence of cations modified the NO$_2^-$/NH$_4^+$ ratio. NO$_2^-$ concentration increased with the potential but NH$_4^+$ concentration was always higher.

Table 2.2. NO$_2^-$/NH$_4^+$ molar concentrations ratio during LSV (1 mV s^{-1}) at the foam in 0.135 M KNO$_3$ and 0.06 M Mg/Al-NO$_3$ solutions

KNO$_3$		Mg/Al-NO$_3$	
Potential / V vs SCE	NO$_2^-$/NH$_4^+$	Potential / V vs SCE	NO$_2^-$/NH$_4^+$
-0.5	0.00	-0.4	0.03
-	-	-0.65	0.08
-0.9	0.30	-0.9	0.38
-1.2	3.20	-1.2	0.41

Table 2.3. NO_2^-/NH_4^+ molar concentrations ratio during current transient curves (-1.2 V *vs* SCE) at the foam in 0.135 M KNO_3, 0.06 M Mg/Al-NO_3 and 0.0675 M $Mg(NO_3)_2$ solutions

Time / s	KNO_3	Mg/Al-NO_3	$Mg(NO_3)_2$
250	2.63	1.42	-
1000	3.63	1.24	-
2000	2.43	0.25	1.54

The trend of NO_2^- and NH_4^+ concentrations during current-potential curves at 250, 1000 and 2000 s in KNO_3 and Mg/Al–NO_3 solutions was summarized in Table 2.3. In KNO_3 solution, NO_2^- was the main reaction product along the 2000 s pulse. On the other hand, NO_2^- steadily decreased in presence of Mg^{2+} and Al^{3+}, while the concentration of NH_4^+ remained almost constant. The effect of the cations in the decrease of NO_2^- production seemed to be mainly due to the presence of Al^{3+}, since when only $Mg(NO_3)_2$ is present in the solution, NO_2^- overcome NH_4^+ production.

The different behaviours may be related to the pH values reached at the cathode surface. All the nitrate reductions involve protonation [8], thus the reduction products depend on the pH, which changed during electrodeposition. Moreover, from a thermodynamic point of view, at low pH the reduction to ammonia is more favoured, while at high pH the reduction to NO_2^- has a lower reduction potential. To correlate the pH with the reduction products, the pH of the solutions analyzed by ion chromatography was measured with litmus paper, obtaining two different trends in absence or presence of precipitating cations.

In KNO_3 solution, high pH values were achieved during sweep potential and choronoamperometric transient curves. The pH increased to 8 at -0.5 V and reached a value of about 12–13 at -1.2 V. The results were corroborated by performing the pH measurement with a glass micro-electrode immersed in the middle of the foam. The pH achieved during the potential pulse at -1.2 V was kept almost constant at 12 – 13 from 250 to 2000 s, in agreement with the pH values reached during the potential sweep at the same potential. A similar pH

increase was reported by Nobial et al. using a gold working electrode immersed in a 0.1 M

KNO_3 solution [20]. The pH increase at low potentials was related to O_2 reduction; although

here it would appear that also some nitrates were reduced.

In presence of cations, the pH of the solution was around 4 in both potential sweep and

pulse measurements, favouring the formation of NH_4^+ rather than NO_2^-. The buffering of the

pH was related to the OH^- consumption by the cations. During the LSV, mainly Al^{3+} ions

precipitated (corroborated by SEM/EDS), hence it would appear that the Al^{3+} precipitation kept

the pH low and might inhibit the precipitation of Mg^{2+}, likewise in titration curves [5,14,38].

However, although a similar pH was recorded in the current transient curves, both Mg^{2+} and

Al^{3+} ions precipitate (see below). The pH measurement might not be reliable in such a case due

to the not efficient replenishment of the solution inside the foam. This hypothesis was

supported by the observation that, with only the 0.0675 M $Mg(NO_3)_2$ solution, the pH at 250 s

was basic while after 2000 s it was acid.

2.3.4 SEM/EDS and XRD characterization of electrodeposited films

The films deposited on plates and foams from chlorides and nitrates solutions at -1.2 V for

2000 s were characterized by SEM/EDS and XRD. Regardless of the bath composition,

nanoparticles were electrodeposited forming a thicker film on the foam than on the plate surface

(Fig. 2.9). Furthermore, a larger amount of solid precipitated from the nitrates solution. For

instance, a 1 – 2 µm layer was coated on the plate with chlorides solution, while the thickness

was 4 – 10 µm with nitrates precursors. On the foam, a 2 – 4 µm layer was obtained with the

chlorides bath while a 5 – 15 µm coating was achieved with the nitrates electrolyte. The

composition of the solids was like that previously reported by some of us for Rh/Mg/Al HT

compounds [7].
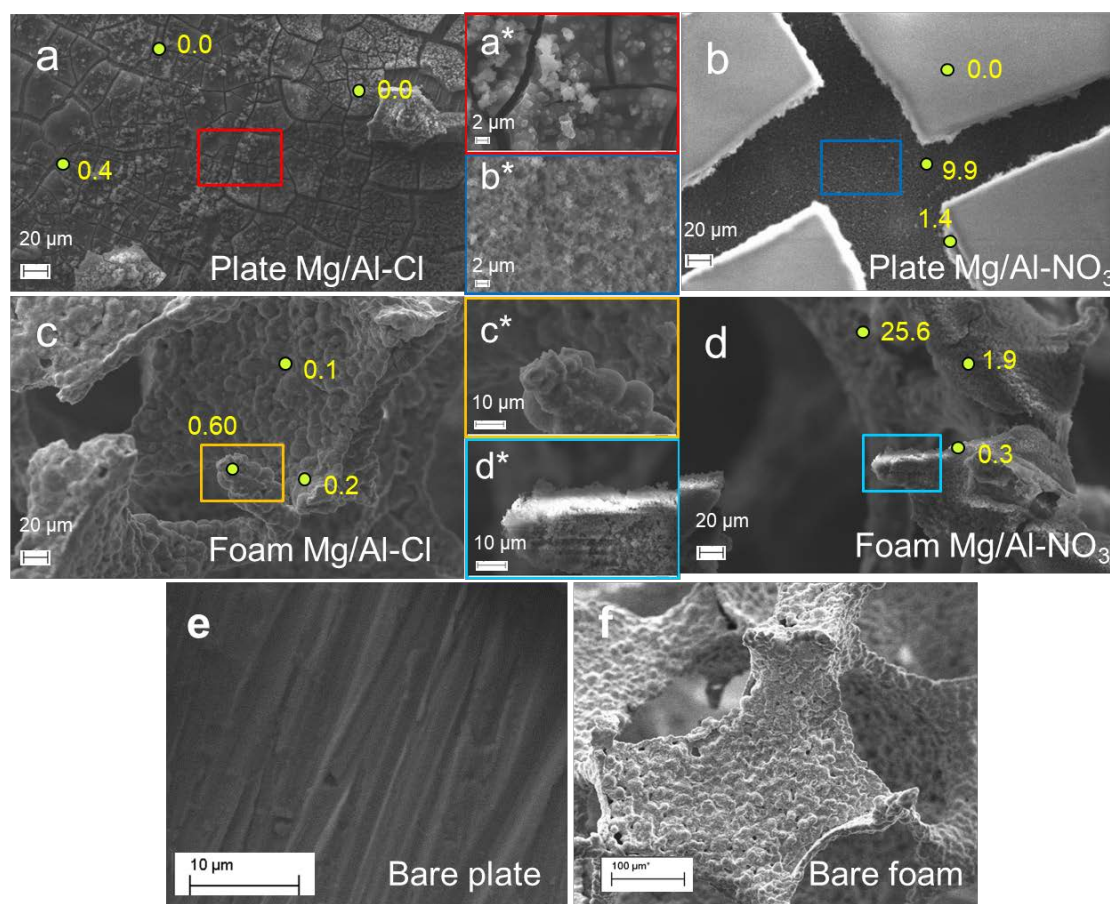
Figure 2.9. SEM images of the plates (a, a*, b, b*) and foams (c, c*, d, d*) coated in 0.06 M Mg/Al–Cl and 0.06 M Mg/Al–NO₃ solutions at -1.2 V for 2000 s. The numbers are the Mg/Al ratio values of some regions of interest. SEM image of a bare plate (e) and foam (f).

Mg/Al ratio values in Fig. 2.9 were estimated from EDS spectra displayed in Fig. 2.10 and Fig. 2.11. These values evidenced that a sequential precipitation of Mg–rich, Mg/Al, and Al–rich layers of hydroxides occurred with nitrates solutions, and at the foam, differences were found between tips of the struts and plate zones. Thicker and Al–enriched coatings were deposited on the tips of the struts than in plate zones. It should be remarked that the data reported for the foams were taken in the outer cylinder surfaces, thinner layers were obtained in the centre of the foam.
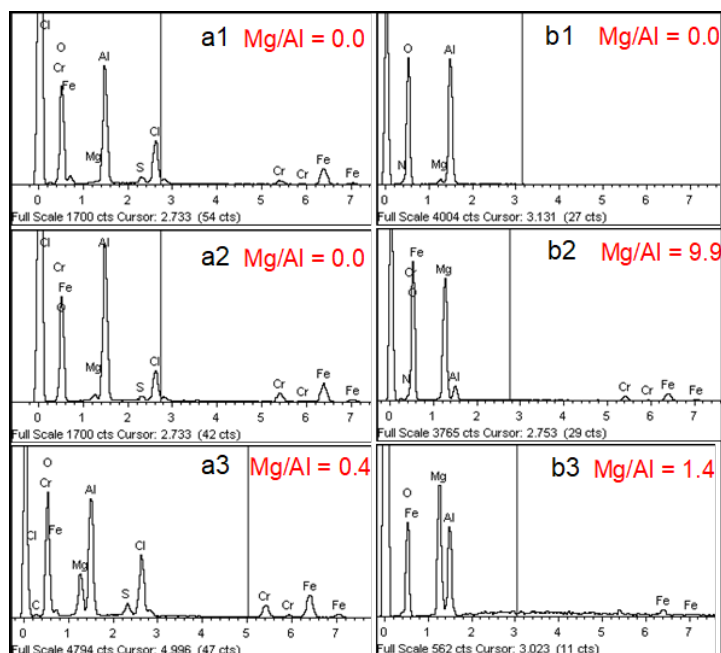
Figure 2.10. EDS spectra taken in regions of interest of a plate coated in 0.06 M Mg/Al–Cl (a1, a2, a3) and 0.06 M Mg/Al–NO$_3$ solutions (b1, b2, b3) at -1.2 V for 2000 s.
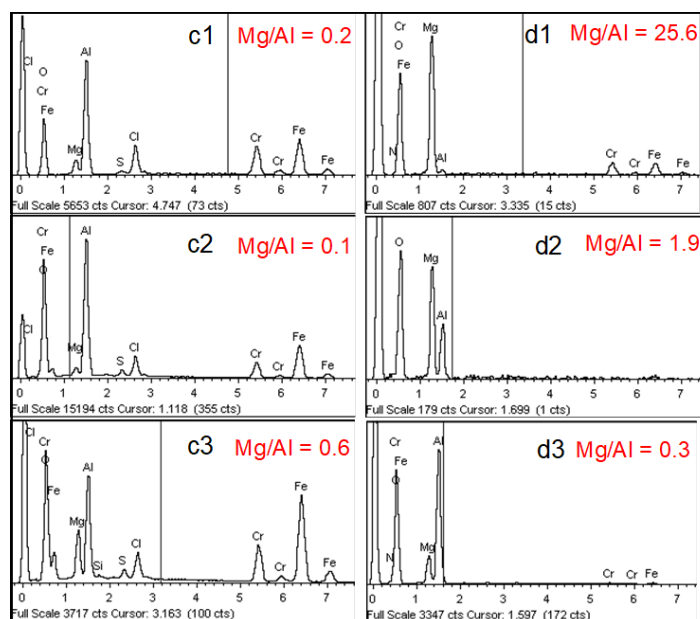
Figure 2.11. EDS spectra taken in regions of interest of a foam coated in 0.06 M Mg/Al–Cl (c1, c2, c3) and 0.06 M Mg/Al–NO$_3$ solutions (d1, d2, d3) at -1.2 V for 2000 s.

The formation of brucite and hydrotalcite-type compounds intercalated with nitrates [39] in the plate coated with the 0.06 M Mg/Al–NO$_3$ solution was confirmed by XRD (Fig. 2.12). On the other hand, an aluminum-rich solid precipitated using Mg/Al–Cl solutions.
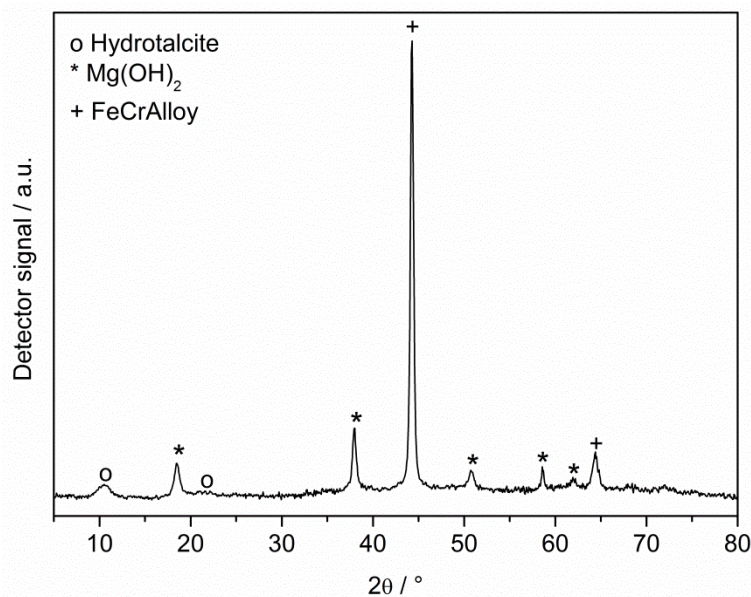
Figure 2.12. XRD pattern of a plate coated in a 0.06 M Mg/Al–NO$_3$ solutions at -1.2 V for 2000 s.

The pH values near the foam surface may explain the differences between chlorides and nitrates solutions. Thus, the pH was measured during the current transient curves at -1.2 V for 2000 s with Mg/Al–Cl and Mg/Al–NO$_3$ solutions using a pH microelectrode (Fig. 2.13). The shape of both pH-time curves was rather similar, nevertheless lower pH values were reached in chlorides solution. During the first electrodeposition seconds, values around 6 – 6.5 were reached. After 250 s, the pH rapidly increased to 8.5 and 10.5 for chlorides and nitrates solutions, respectively. An 8.5 pH value may explain the precipitation of only few amounts of Mg^{2+} as hydroxide during the deposition, Scheme 2.1. However, despite the pH 10.5 was suitable for the precipitation of pure Mg/Al HT compounds [40], the composition of the deposited solid was not the expected one.

The regions in pH–time curves correspond to the two steps observed in current-transition time plots, i.e. the initial abruptly decrease in the current and the plateau. Making a comparison between both plots, it would appear that a constant current does not mean a constant pH. Therefore, both the OH⁻ generation and consumption should be considered; the former was due to the reduction reactions, while the latter was related to the transfer of the cations to the electrode surface.
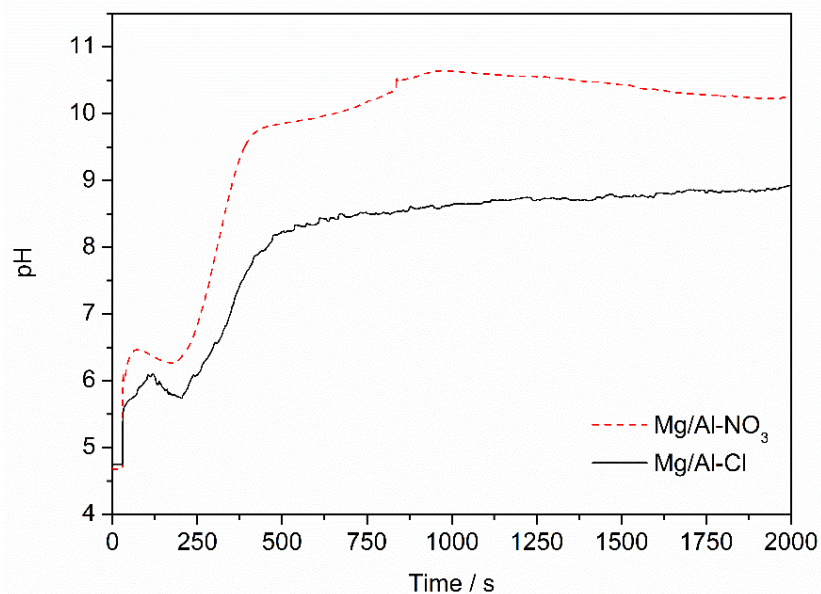
Figure 2.13. Evolution of the pH near the foam surface immersed in 0.06 M Mg/Al–Cl and 0.06 M Mg/Al–NO₃ solutions during the current transient curve (-1.2 V for 2000 s).

2.3.5 Plates versus foams

Considering all the previous comments, the differences in the electrochemical behaviour and properties of the coating between plates and foams may be related to: i) the electrical conductivity of the support; ii) the H_2 bubble formation; and iii) the mass transfer of the electroactive species and cations towards the electrode surface.

EIS experiments were carried out to further investigate the electrochemical features of the foam and the plate electrode materials, and to assess their different characteristics in terms of charge transfer resistance (R_{ct}).

Fig. 2.14 showed the impedance spectra plotted in the form of complex plane diagrams (Nyquist plots), normalized with respect to the electrochemically active area (calculated as previously described). The experimental data were simulated by using the software developed by Boukamp using a Randle's equivalent circuit (shown as an inset in Fig. 2.14). Independently from the electrode type the R_s value was very close to zero, reflecting in both cases a good cell geometry (the reference electrode is placed very close to the working electrode surface); R_{ct}

values were slightly different, resulting 4740 and 4515 $\Omega.cm^2$ for the foam and the plate, respectively. This result indicated that the geometry does not significantly affect the R_{ct} and, consequently the conductivities of the foam and plate can be considered almost similar.

On the other hand, the visual inspection of the samples during the tests suggested that the H_2 bubble formation differed on foams and plates. Bubbles tended to accumulate on planar substrates [24] and to favour the solid detachment, while they rapidly dissipated in the solution with no bubble accumulation on the electrode surface for foams [25].
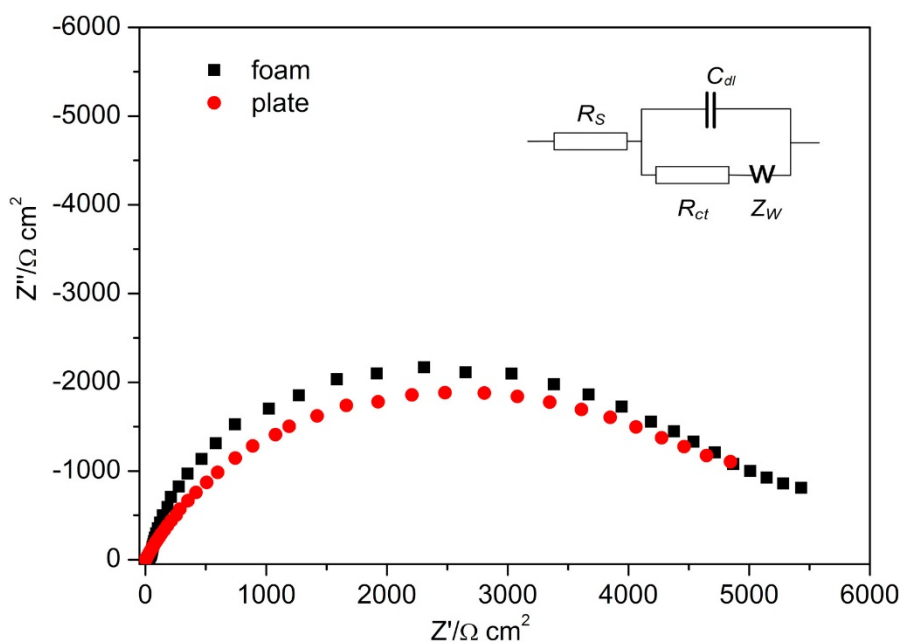
Figure 2.14. Nyquist plots obtained at 0.17 V in the frequency range 100 mHz – 10 kHz in a 2.0 mM $Fe(CN)_6^{3-}$ solution containing 0.1 M KNO_3. Inset: Randle's equivalent circuit.

Considering the mass transfer of the electroactive species and cations to the electrode surface, the rough foam surface may favour the mass transport phenomena and microelectrode effects may take place on foam supports due to the small size of the struts. A microelectrode effect has been also reported in filaments [41], laminated threads [36], microstructure arrays [42,43]. However, the typical behaviour of the microelectrodes was not observed in the LSV curves, but it could be related to the overlapping of several reduction processes.

Lastly, the differences observed in the composition and thickness of the film on the foam surface may be related to: i) current gradients within the foam; ii) local inhomogeneities in

mass transport [36]; iii) the modification of the working electrode surface [43,44]; or iv) to the not efficient replenishment of the solution inside the porous support [45,46].

2.4 Conclusions

Nitrate and oxygen reduction as well as H_2 evolution took place simultaneously during the cathodic electrodeposition of Mg/Al HT compounds at FeCrAl plates and foams through the electro-base generation method using Mg^{2+} and Al^{3+} nitrate salts as precursors. All the electrochemical reactions contributed to the pH increase near the support, but the nitrate reduction was mandatory to reach a pH able to precipitate both Mg^{2+} and Al^{3+} cations.

Regardless of the working electrode shape, the alloy dipped in KNO_3 showed a low activity in nitrate reduction. The precipitating cations, and in particular Al^{3+}, catalyzed the reduction processes leading to the shift of the onset potentials to less cathodic values and increasing the current density. Nitrates were reduced to both nitrite and ammonia, being their amount dependent on the potential applied, synthesis time and presence of cations.

The use of a foam rather than a plate as working electrode did not largely alter either the electrical conductivity or the reduction potentials, while it decreased the H_2 bubble accumulation and increased the current density. The 3D rough structure of interconnected micro struts may promote the transport of the liquid through the electrode/electrolyte interface. Consequently, a thicker coating was deposited on the foam surface. However, the pH near the electrode surface was not the only factor to control the composition of the deposited film.

Chapter 2

2.5 References

1.   G.H.A. Therese and P.V. Kamath, Chem. Mater. 12 (2000) 1195–1204.

2.   P. Benito, M. Monti, I. Bersani, F. Basile, G. Fornasari, E. Scavetta, D. Tonelli, A. Vaccari, Catal. Today 197 (2012) 162–169.

3.   B.E. Prasad, P. Vishnu Kamath, K. Vijayamohanan, Langmuir 27 (2011) 13539–13543.

4.   L.-K. Tsui, G. Zangari, Electrochemical Synthesis of Metal Oxides for Energy Applications, in: S. Djokíc (Editor), Electrodeposition and Surface Finishing – Fundamentals and Applications, Chapter 4, Springer, New York, (2014) 217-239.

5.   I. Gualandi, M. Monti, E. Scavetta, D. Tonelli, V. Prevot, C. Mousty, Electrochem. Acta 152 (2015) 75–83.

6.   P. Benito, M. Monti, W. De Nolf, G. Nuyts, G. Janssen, G. Fornasari, E. Scavetta, F. Basile, K. Janssens, F. Ospitali, D. Tonelli, A. Vaccari, Catal. Today 246 (2015) 154–164.

7.   P. Benito, G. Nuyts, M. Monti, W. De Nolf, G. Fornasari, K Janssens, E. Scavetta, A. Vaccari, Appl. Catal. B Environ. 179 (2015) 321–332.

8.   C. Milhano, D. Pletcher, The electrochemistry and electrochemical technology of nitrate, in: Modern Aspects of Electrochemistry No. 45 (Eds. R. E. White) Springer, New York, 2009, pp 1–61.

9.   I. Gualandi, E. Scavetta, Y. Vlamidis, A. Casagrande, D. Tonelli, Electrochim. Acta 173 (2015) 67–75.

10.   M.S. Yarger, E.M.P. Steinmiller, K.-S. Choi, Inorg. Chem. 47 (2008) 5859–5865.

11.   V. Prevot, C. Forano, A. Khenifi, B. Ballarin, E. Scavetta, C. Mousty, Chem. Commun. 47 (2011) 1761–1763.

12.   T. Yoshida, M. Tochimoto, D. Schlettwein, D. Wöhrle, T. Sugiura, H. Minoura, Chem. Mater. 11 (1999) 2657–2667.

13.   L. Arurault, P. Monsang, J. Salley, R.S. Bes, Thin Solid Films 466 (2004) 75– 80.

14.   M. Monti, P. Benito, F. Basile, G. Fornasari, M. Gazzano, E. Scavetta, D. Tonelli, A. Vaccari, Electrochim. Acta 108 (2013) 596–604.

15.   T. Pauporte, D. Lincot, Electrochim. Acta 45 (2000) 3345–3353.

16.   F. Basile, P. Benito, G. Fornasari, M. Monti, E. Scavetta, D. Tonelli, A. Vaccari, Catal. Today 157 (2010) 183–190.

17.   P. He, L.R. Faulkner, Anal. Chem. 58 (1986) 517–523.

18.   V.-M. Guérin, J. Rathousky, Th. Pauporté, Sol. Energy Mater. Sol. Cells 102 (2012) 8–14.

19.   S.R. Belding, R.G. Compton, J. Electroanal. Chem. 683 (2012) 1–13.

20.   M. Nobial, O. Devos, O.R. Mattos, B. Tribollet, J. Electroanal. Chem. 600 (2007) 87–94.

21.   A. Duchatelet, G. Savidand, N. Loones, E. Chassaing, D. Lincot, J. Electrochem. Soc. 161 (2014) D3120–D3129.

22.   S. Peulon, D. Lincot, J. Electrochem. Soc. 145 (1998) 864–874.

23.   A.G. Marrani, F. Caprioli, A. Boccia, R. Zanoni, F. Decker, J. Solid State Electrochem. 18 (2014) 505–513.

24.   H. Matsushima, T. Nishida, Y. Konishi, Y. Fukunaka, Y. Ito, K. Kuribayashi, Electrochim. Acta 48 (2003) 4119–4125.

25.   X. Lu, C. Zhao, Nat. Commun. 6 (2015) 6616.

26.   L.R.F. Allen, J. Bard, Electrochemical Methods: Fundamentals and Applications, 2nd Edition, John Wiley & Sons, New York, 2000.

27.   J.F. Su, I. Ruzybayev, I. Shah, C.P. Huang, Appl. Catal. B Environ. 180 (2016) 199–209.

28.   H. Zhao, J. Chang, A. Boika, A.J. Bard, Anal. Chem. 85 (2013) 7696−7703.

29.   I. Katsounaros, G. Kyriacou, Electrochim. Acta 52 (2007) 6412–6420.

30.   M. Merrill, M. Worsley, A. Wittstock, J. Biener, M. Stadermann, J. Electroanal. Chem. 717–718 (2014) 177–188.

31.   J.A. Cox, A. Brajter, Electrochim. Acta 24 (1979) 517–520.

32.   T. Yoshida, D. Komatsu, N. Shimokawa, H. Minoura, Thin Solid Films 451–452 (2004) 166–169.

33.   M. Wadowska, T. Frade, D. Siopa, K. Lobato, A. Gomes, ECS Electrochem. Lett. 2 (2013) D40–D42.

34.   N. Ogawa, S. Ikeda, Anal. Sci. Suppl. 7 (1991) 1681–1684.

35.   E.J. Ruiz, R. Ortega-Borges, L.A. Godínez, T.W. Chapman, Y. Meas-Vong, Electrochim. Acta 52 (2006) 914–920.

36.   T. Loewenstein, A. Hastall, M. Mingebach, Y. Zimmermann, A. Neudeck, D. Schlettwein, Phys. Chem. Chem. Phys. 10 (2008) 1844–1847.

37.   M. Kahl, T. D. Golden, Electroanalysis 26 (2014) 1664–1670.

38.   J.W. Boclair, P.S. Braterman, Chem. Mater. 11 (1999) 298–302.

39.   Z.P. Xu, H.C. Zeng, J. Phys. Chem. B, 105 (2001) 1743-1749.

40.   F. Basile, P. Benito, G. Fornasari, A. Vaccari, Appl. Clay Sci. 48 (2010) 250–259.

41.   M. Rudolph, T. Loewenstein, E. Arndt, Y. Zimmermann, A. Neudeck, D. Schlettwein, Phys. Chem. Chem. Phys. 11 (2009) 3313–3319.

42.   M. Stumpp, C. Lupo, D. Schlettwein, J. Electrochem. Soc. 159 (2012) D717–D723.

43.   C. Lupo, M. Stumpp, D. Schlettwein, J. Appl. Electrochem. 45 (2015) 105–113.

44.   I. Gualandi, A. G. Solito, E. Scavetta, D. Tonelli, Electroanalysis 24 (2012) 857–864.

45.   R. Abdallah, F. Geneste, T. Labasque, H. Djelal, F. Fourcade, A. Amrane, S.Taha, D. Floner, J. Electroanal. Chem. 727 (2014) 148–153.

46.   S. Cimino, A. Gambirasi, L. Lisi, G. Mancino, M. Musiani, L. Vázquez-Gómez, E. Verlato, Chem. Eng. J. 285 (2016) 276–285.

Chapter 3. Effect of metal nitrate concentration on the electrodeposition of hydrotalcite-like compounds on open-cell foams

Chapter 3

3.1 Introduction

In chapter 2, we studied the reactions involved during the electrodeposition of Mg/Al HT compounds on FeCrAl foams, making a comparison with results obtained at FeCrAl plates. Nitrate reduction, but also oxygen reduction and hydrogen evolution, occur at the FeCrAl foam interface generating the basic media. Among them, nitrate reduction was major contribution in pH increase near the support surface. Moreover, it was reported a catalytic effect of cations in reduction processes.

The concentration of the electrolyte is a key parameter since it modifies not only the amount of nitrate available to increase the pH, and consequently the nitrate reduction rate [1-4], but also the transport of cations to the working electrode, and, therefore, the number of cations consuming OH^- by precipitation of the hydroxides. The nitrate salt concentration plays an important role in the deposition rate and properties of the solids such as particle size and morphology in the deposition of single hydroxides or oxides, i.e. $Ni(OH)_2$ [5-7], CeO_2 [8], ZnO [9-12], $Mg(OH)_2$ [13], and SiO_2 [14]. In the deposition of multiple hydroxides, the nitrate concentrations may also influence on the composition of the solids, for example, the electrodeposited hydrotalcite-like (HT) compounds [15-16].

In the electrodeposition of Rh/Mg/Al HT compounds on FeCrAl foams, we found that the differences between the compositions of the electrolyte and the electrodeposited material as well as the homogeneity of the coating improve by increasing the concentration of the electrolyte from 0.03 M to 0.06 M; though using a 0.10 M solution does not provide any further improvement [16]. In fact, an increase of the concentration caused a negative impact for $Ni(OH)_2$ electrodeposition [6]; a less amount of deposited solid was taken into account by the formation of species that migrate away from the working electrode, a behaviour depending on the pH value generated.

This chapter aims to elaborate the knowledge about the deposition of Mg/Al HT compounds

on metal foams by investigating the influence of nitrate concentration on both electrochemical processes and solid morphology and composition, as well as how the latter are modified with the deposition time. Therefore, potential scans or cathodic pulses were applied to foams dipped into electrolytes containing different nitrate concentrations in both the presence and absence of Mg^{2+} and Al^{3+} cations like as in chapter 2. Measurement of the pH near the vicinity of the supports was link to correlate with properties of the solids formed at several deposition times. The synthesis conditions were those reported for the preparation of structured catalysts: -1.2 V *vs* SCE for 2000 s and total metal concentrations of 0.03, 0.06 and 0.10 M, with a Mg/Al atomic ratio (a.r.) equal to 3/1. KNO_3 concentrations were chosen to add the same nitrate concentrations (0.0675, 0.135, 0.225 M) as those deriving from the metal salts. For comparison purposes, some experiments were also performed using FeCrAl plates.

3.2 Experimental

3.2.1 Electrochemical measurements

The supports (FeCrAl foam and plate) and electrochemical set-up were the same as mentioned in chapter 2, there was only a difference in the electrolyte solutions.

Electrolytic solutions were prepared using ultra-pure deionised water (UPW) provided by a Millipore filtration instrument (electrical resistivity 18.2 MΩ cm). Aqueous solutions of KNO_3 with concentrations from 0.0675 to 0.225 M were prepared and the initial pH of solutions was adjusted to 3.8 by adding 0.10 M HNO_3. The study of the electrodeposition of Mg/Al HT compounds was conducted in aqueous solutions containing a mixture of $Mg(NO_3)_2$ and $Al(NO_3)_3$ with Mg/Al = 3/1 a.r. and total metal concentration of 0.03, 0.06, or 0.10 M. These concentrations provided a pH around 3.5 – 3.7 at 20 $^\circ$C. It was noted that the concentrations of KNO_3 solution were set to keep the same total nitrate concentration as in corresponding Mg/Al-NO_3 solutions for comparison purposes, for example, KNO_3 0.0675 M

and Mg/Al-NO$_3$ (Mg/Al = 3/1) 0.03 M contain the same total nitrate concentration of 0.0675 M.

The uncompensated resistance (R_u) in the electrochemical cell was measured by a CH Instruments Mod. 660A, according to the method proposed by He and Faulkner et al. [17]. All the experiments were repeated thrice. The R_u values decreased by increasing the total metal concentration, 2.5 Ω for 0.03 M and 1.5 Ω for 0.06 M and 0.10 M solutions. The low R_u values led to small Ohmic drops (smaller than 50 mV) in most of the experiments. However, when a high current was recorded, potential scans were corrected by Ohmic drops, assuming a constant R_u during the scans.

Linear Sweep Voltammetries (LSVs) were recorded at 1 mV s^{-1} scan rate, to reach the steady-state, in a potential range from 0 to -1.4 V. Potentiostatic cathodic reductions were carried out at -1.2 V for 100 to 2000 s, under natural convective conditions. Current densities were plotted using the electroactive area of the foam, 4.13 ± 0.17 cm^2, calculated in chapter 2, under LSV (50 mV s^{-1}) for the one-electron reduction of K$_3$[Fe(CN)$_6$] by means of the Randles-Sevcik equation.

3.2.2 Characterization of the coatings

Except SEM/EDS and XRD characterization, which were the same as mentioned in chapter 2, this work employed more characterization techniques including Attenuated Total Reflection (ATR), micro Raman, and High-resolution transmission electron microscopy (HRTEM).

Attenuated Total Reflection (ATR) measurements were recorded by using a Bruker Alpha instrument equipped with a diamond crystal. The analyses were performed on the coated FeCrAl plates. Each spectrum in the 4000 – 400 cm^{-1} range was accumulated from 32 individual measurements recorded by a nominal resolution of 2 cm^{-1} to minimize the noise signal.

Micro-Raman measurements were performed in a Renishaw Raman Invia configured with a Leica DMLM microscope (obj. 5×, 20×, 50×). The available sources are an Ar^+ laser (514.5 nm, P_{max} =30 mW) and a diode-laser (780.0 nm, P_{max} =300 mW). The system is equipped with edge filters to cut Rayleigh scattering, monochromators (1800 lines/mm for Ar^+ laser, and 1200 lines/mm for diode laser) and a Charge-Coupled Device (CCD) thermoelectrically cooled (203 K) detector. Measurements were performed with the Ar^+ Laser (514.5 nm) at power level P_{out}= 3 mW. Each spectrum was recorded by four accumulations and time for each accumulation was 30s.

High-resolution transmission electron microscopy (HRTEM) characterization was carried out by a TEM/STEM FEI TECNAI F20 microscope, equipped with an EDS analyser. Powder materials were collected by scratching the foam surface and then suspended in ethanol under ultrasonic for 20 minutes. The suspension was subsequently deposited on an Au grid with lacey multi-foil carbon film and dried at 100 °C before doing the measurement.

3.2.3 pH measurements

pH measurements near the foam surface were performed using the pX1000 module (Metrohm) of Autolab equipped with a micro-pH electrode (METTLER TOLEDO, U402-M3-S7/200). Before each measurement, the system was calibrated with standard buffer solutions at pH 2.00, 4.01, 7.00, and 9.21 (Hamilton) (Fig. 3.1). The sensitive bulb of the pH electrode was inserted into a foam (0.6 x 1.19 cm) via a small hole dug out in the centre of the cylinder. This set-up was previously introduced in chapter 2. The pH measurements can be considered like those proposed by Deligianni and Romankiw, who used a flat electrode to measure the pH of the volume contained in the holes of a Pt grid [18] and that was later used by other authors [19-23] and with stainless steel [24] and gold mesh [25-27]. Nobial et al. [28] studied the nitrate reduction using a gold mesh.
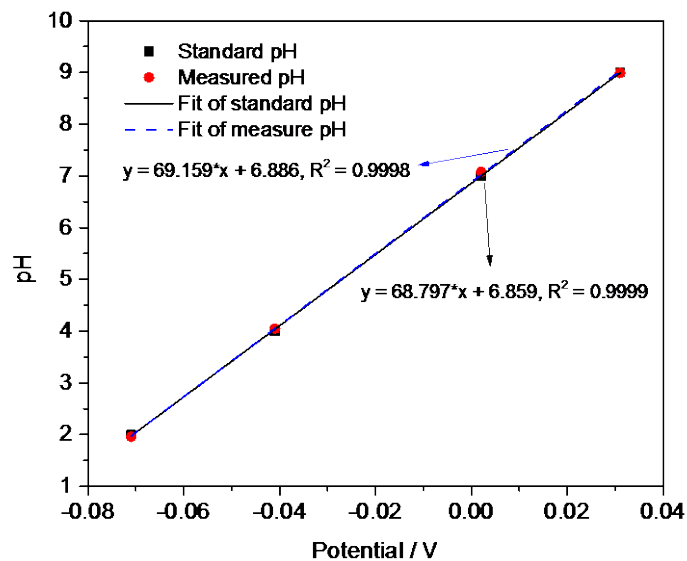
Figure 3.1. Calibration of micro pH-meter with four standard buffer solutions (pH 2.00, 4.01, 7.00, and 9.21) before performing the pH measurements.

Current and pH values were recorded simultaneously during the cathodic pulses at foams immersed in KNO_3 and $Mg/Al-NO_3$ solutions. The measurements were performed under the same conditions used for electrodepositions; however, an initial step at 0.0 V for 30 s was set to stabilize the signal of the micro-electrode. The hole in the middle of the foam may favour the replenishment of the solution in the inner part of the foam. Although it should be remarked that the pH measured may differ from the one reached in the interface electrode-electrolyte, the pH measurements here performed in combination with the characterization of the deposits obtained at different times gave valuable information about the effect of the concentration and time on the precipitation of HT-like compounds.

For comparison purposes, titrations of 100 mL of $Mg^{2+}/Al^{3+} = 3/1$ solutions with concentrations 0.03, 0.06 and 0.10 M were carried out with NaOH solution, Fig. 3.2. During the titration, 0.25 mL NaOH solution (0.25 M) were added each time, and pH was measured by a precise pH meter (HI-9126 Waterproof pH/ORP Meter with CalCheck, HANNA Instrument).
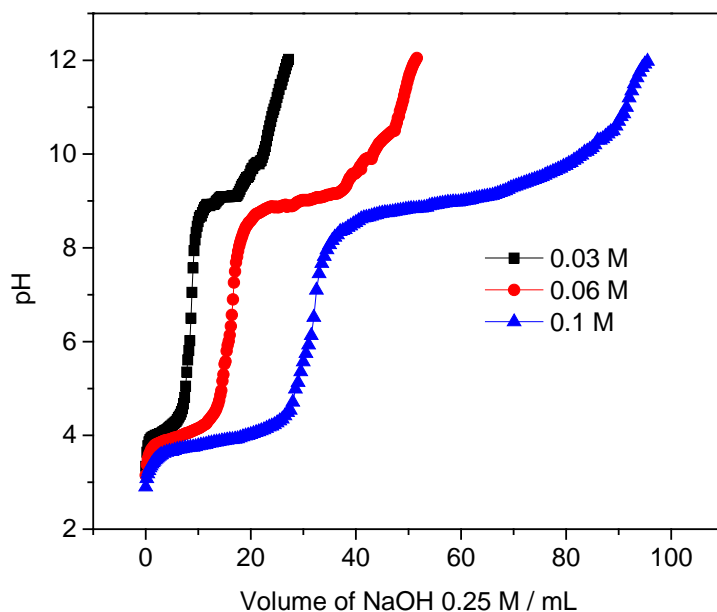
Figure 3.2. Titration curves of Mg^{2+} and Al^{3+} nitrate solutions (Mg/Al a.r. = 3/1) (0.03, 0.06 and 0.10M) with NaOH 0.25M.

3.3 Results and discussion

3.3.1 Electrochemical characterization and pH measurements in KNO_3 and Mg/Al nitrate solutions

Potential sweeps and current transients recorded at foam working electrodes dipped into KNO_3 electrolytes are shown in Fig. 3.3a, b. Cathodic waves due to the reduction of nitrate and H_2 evolution were recorded in LSV experiments (Fig. 3.3a). During the pulse at -1.2 V for 1000 s (Fig. 3.3b) the current density quickly decreased in 50 – 100 s, reaching then a limiting value. An increase in KNO_3 concentration from 0.0675 to 0.225 M provoked the shift of the onset potentials in LSV curves toward less negative potentials [29] and the recorded current density increased in both cathodic waves and potentiostatic pulses. There was a perfect linear relationship between KNO_3 concentration and current density in current transients at 100 s, and almost linear at 500 s (inset Fig. 3.3b).
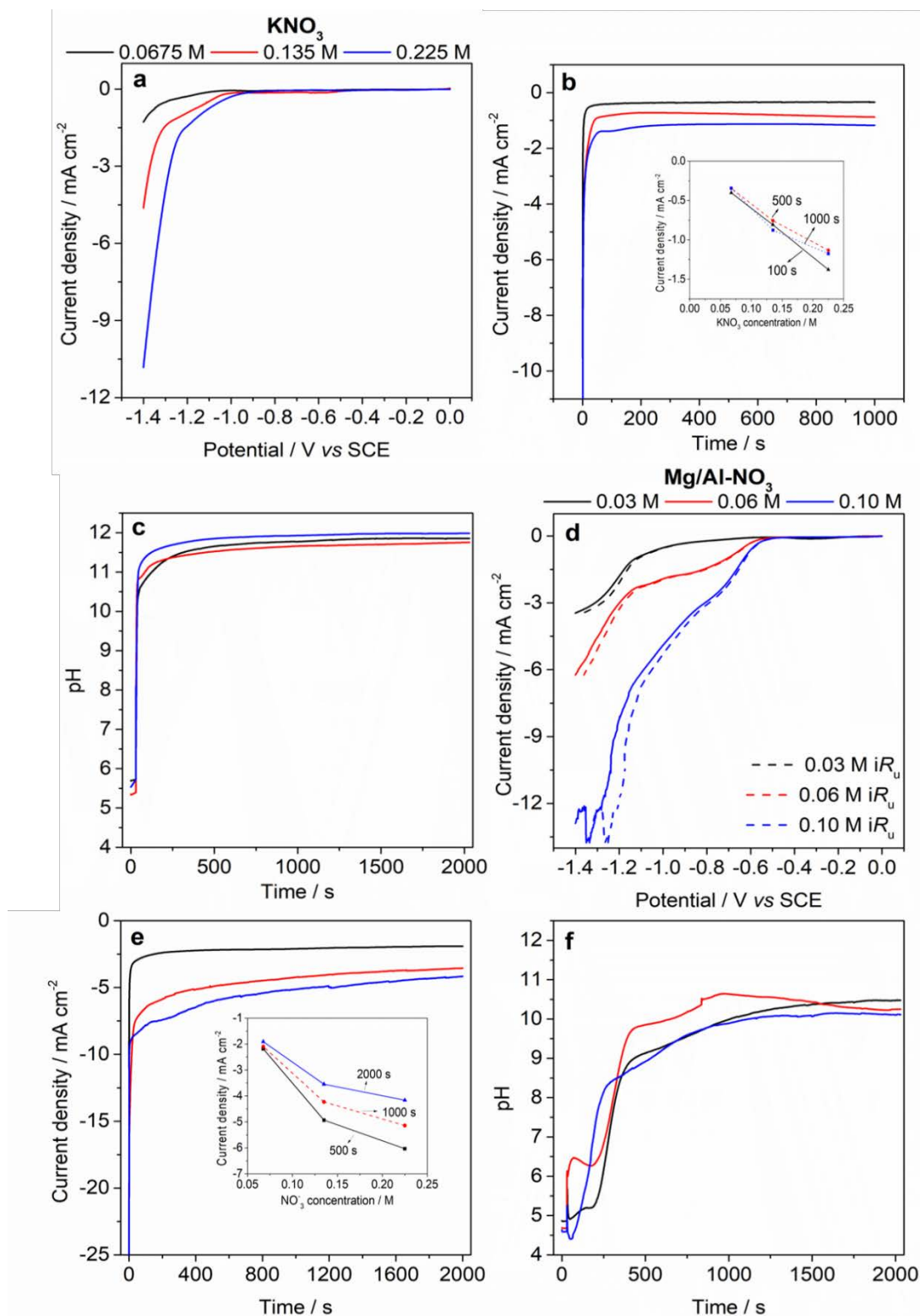
Figure 3.3. Electrochemical and pH measurements at the foams at different concentrations of KNO_3 and Mg/Al electrolytes: LSV (a and d), current transients (b and e), and pH (c and f). Insets b and e: dependence of current densities on total nitrate concentrations at different times; 0.0675, 0.135 and 0.225 M nitrate concentration in inset e corresponds to the nitrate concentration in 3/1 Mg/Al 0.03, 0.06 and 0.10 M solutions. LSV: scan rate 1 mV s^{-1} and potential range 0 – -1.4 V. Chronoamperometry: -1.2 V for 2000 s.

It is well-known that the concentration of the electrolytic bath modifies both the ionic strength and the number of electroactive species available for reduction processes, decreases the convection and increases the diffusion due to the formation of a thinner diffusion layer [30]. Moreover, the higher the nitrate concentration is, the lower the H_2 evolution occurs [4]. In this work, reduction processes at -1.2 V at the foam may follow a first order kinetics in the 0.0675 – 0.225 M concentration range, namely a typical surface reaction behaviour [1, 4]. The slight deviation from the linearity at long times may be related to the ineffective replenishment of the solution at the electrode-electrolyte interface, but the effect of the anodic reaction cannot be discarded since a single compartment-cell was employed. Conversely, experiments performed in a 0.50 M KNO_3 solution (not shown) deviated negatively from the linearity, suggesting the saturation of the active sites.

For all the three Mg^{2+} and Al^{3+} nitrate solutions (Fig. 3.3d, e), the presence of precipitating cations led to a catalytic effect in the reduction processes as reported in chapter 2. Namely, reduction overpotentials during scans shifted toward more positive cathodic values, Fig. 3.3d, and the current recorded during the potentiostatic deposition significantly increased (e.g. about 4 times at 0.03 M, Fig. 3.3e) in comparison to the experiments without precipitating cations. In the LSV curves, the current density and onset potentials depended on the total metal concentration. During the deposition step at -1.2 V for 2000 s (Fig. 3.3e), the limiting current density plateau was attained using the 0.03 M solution, whereas the current density smoothly decreased throughout the pulse with both 0.06 and 0.10 M solutions. Unlike in KNO_3, even at short deposition times (500 s), the current no longer increased proportionally with the metal nitrate concentration. This behaviour also differed from what occurred in the LSV curves, where the current density increased linearly if the total metal concentration was increased. To explain this trend, two consequential issues should be considered. A thicker and more insulating hydroxide layer was deposited with 0.06 and 0.10 M solutions than that obtained

with the 0.03 M solution (*vide infra*), which may alter the electrochemical behaviour. Moreover, the reduction of nitrates was fostered; therefore, the fast replenishment of the solution at the interface electrode-electrolyte could not occur during the potentiostatic pulse at -1.2 V, but it did in LSV curves recorded at low scan rate (1 mV s^{-1}).

At plates, the effects of the electrolyte concentration on potential scans and cathodic pulses were similar to those obtained at foams, above commented. In Fig. 3.4 the results obtained with the Mg^{2+} and Al^{3+} nitrate solutions were displayed, the only remarkable differences being the lower current densities recorded at plates with respect to the foams, as previously reported in chapter 2.
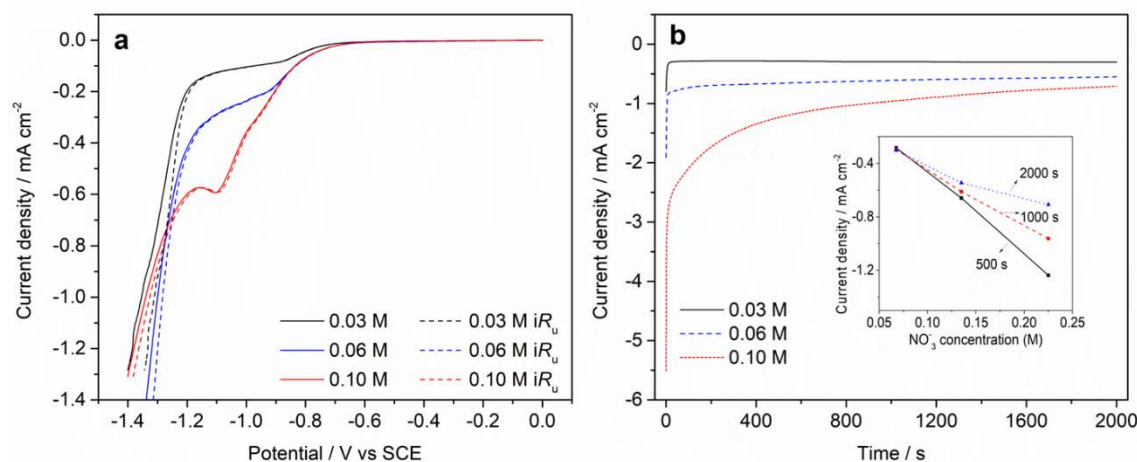
Figure 3.4. LSV curves (a) and current transient curves (b) recorded at the plates in 0.03, 0.06, and 0.10 M Mg^{2+} and Al^{3+} nitrate solutions (Mg/Al a.r. = 3/1). Inset b: dependence of current densities on total nitrate concentrations at different times. LSV: scan rate, 1 mV s^{-1}, potential range, 0 – -1.4 V. Chronoamperometry: -1.2 V for 2000 s.

To investigate the effect of the concentration of electrolytic solutions on the pH at the electrode-electrolyte interface, a pH microelectrode was inserted in the middle of the foam during the 2000 s cathodic pulses both in absence and presence of precipitating cations. The pH-time plots are shown in Fig. 3.3c, f. In KNO_3 solutions, a step pH increase occurred as the potential pulse started, reaching a plateau at around 11.0 – 12.0. The increase in the current due to the nitrate reduction at different concentrations did not have a clear effect on the pH values:

below 200 s, the pH and current followed the same trend, while in the plateau region some deviations occurred. The repetition of the measurement in the 0.135 M solution showed similar results (Fig. 3.5). Thus, the differences could be related to the diffusion of OH$^-$ away from the electrode; although it should be considered that pHs were close to the detection limit of the glass electrode. It is worthy to note that the values here obtained are like those previously obtained by us with a more concentrated KNO$_3$ solution (0.30 M) using a Pt mesh working electrode [31], and reported for nitrate reduction during LSV in 0.1 or 1 M KNO$_3$ solution at a gold mesh without stirring [28].
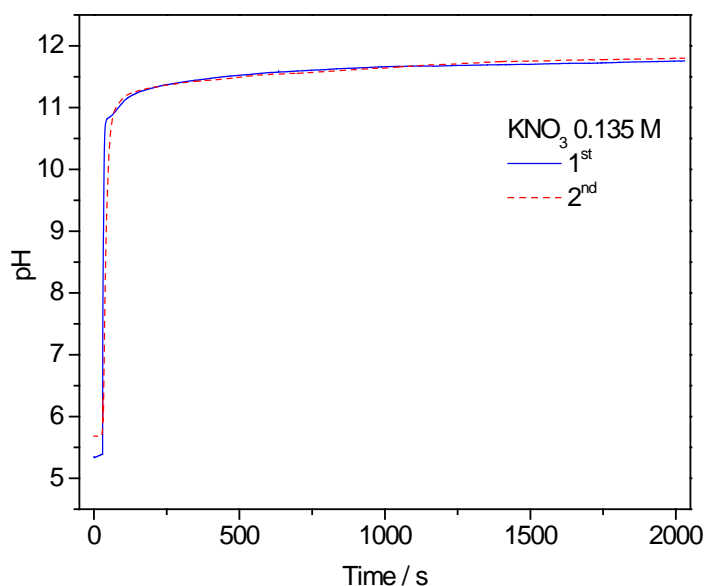
Figure 3.5. pH-time plots recorded in KNO$_3$ 0.135 M during the cathodic pulse at -1.2 V for 2000 s.

In presence of Mg^{2+} and Al^{3+} cations the pH decreased due to solid precipitation, Fig. 3.3f. The shapes of pH-time and current-time plots, however, differed. While the latter were mainly related to electrochemical processes (also including mass transport), pH-time plots were the combination of both electrochemical and chemical processes. The precipitation during electrodeposition could be considered similar to the homogeneous precipitation with urea [32, 33] or the titration of Mg^{2+} and Al^{3+} nitrate solutions with NaOH [34], since the base is in-situ generated close to the foam surface provoking the solid precipitation. In titration curves with NaOH of the electrolytic solutions, the two characteristic plateaus were identified at ca. 4.0 and

8.5, related to the precipitation of Al(OH)$_3$ or aluminium oxohydroxydes and the incorporation of Mg^{2+} species as the pH increased forming the HT-like structure [34]. An increase in the concentration of Mg/Al-NO$_3$ precursor in the range from 0.03 to 0.10 M did not alter the values at the plateau but did require a higher volume of NaOH for each precipitation step as shown in Fig. 3.2. The same trend was observed in the homogeneous precipitation with urea, although Al-rich solids containing Mg (Mg/Al ratio below 1) were found at pH values below 8.5.

In this work during the electrodeposition, the rate of OH$^-$ generation and consumption determined the precipitation process; moreover, in the motionless system here used both may depend on the replenishment of the solution near the foam surface (mass transfer). The pH-time plots for 0.03 M and 0.06 M solutions resembled NaOH titration curves and pH evolution in the homogeneous urea precipitation. The higher initial pH recorded for the 0.06 M solution may be related to a more efficient nitrate reduction. Indeed, in our previous work, we observed that higher pH values were recorded with nitrate than with chloride solutions keeping the same cation concentration as used in chapter 2. On the other hand, in the case of 0.10 M solution, a continuous pH increase was observed. After 1000 s, the pH near the foam surface was around 10, regardless of the solution concentration and the decrease of the current density recorded in 0.06 M and 0.10 M samples. These results suggested that a steady state was reached at the electrode-electrolyte interface, a balance between OH$^-$ produced by reduction reactions and those consumed by the solid precipitation was achieved, in agreement with results reported for rare-earth cuprate and nickelate materials [35]. Conversely, in the initial stages both the nitrate reduction and the cations precipitating determined the pH near the foam.

3.3.2 Characterization of the deposits

The morphology and composition of the solids deposited on foams at -1.2 V for 100 and 1000 s using 0.06 and 0.10 M solutions and for 2000 s with the three Mg^{2+} and Al^{3+} nitrate

solutions were analysed by SEM coupled with EDS. To estimate the Mg/Al ratios, EDS analyses were performed on the surface of struts and nodes connecting the struts; in these regions, when cracks are present the zones inside and outside the cracks were analysed; they represented thin and thick layers of deposits, respectively, a fact confirmed by the Fe signal from the support. The Mg/Al ratios shown in this work corresponded to general trends in the composition. Despite the accurate composition could not be given, replications of the depositions indicated that the trend in the data obtained modifying the electrolyte concentration was quite reproducible.

Point	Mg/Al (a.r)
1	0
2	1.34
3	4.85
4	3.47
1	5.02
2	0.97
3	5.19
4	1.40
1	6.64
2	0.26
3	10.24
4	2.65
5	0.58
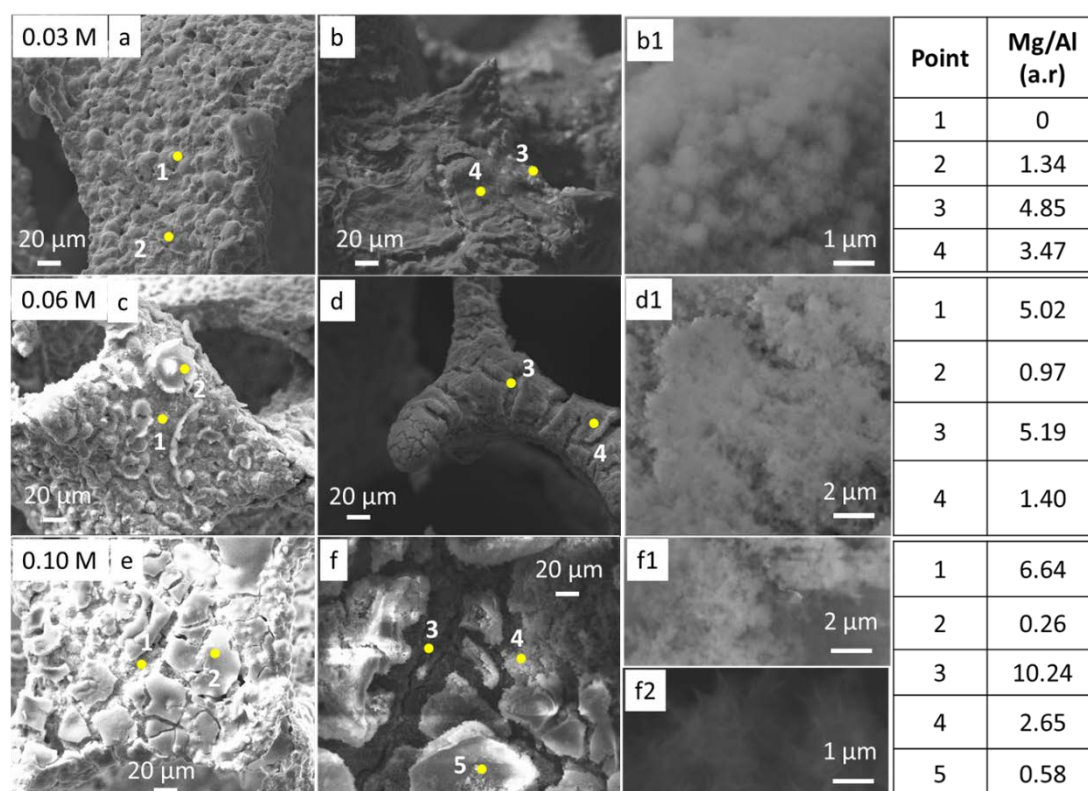
Figure 3.6. SEM images of the foams coated by Mg/Al-HT at different synthesis time: 0.03 M (a: 100 s; b and b1: 1000 s), 0.06 M (c: 100 s, d and d1: 1000 s) and 0.10 M (e: 100 s, f, f1 and f2: 1000 s).

At 100 s, Fig. 3.6a,c,e, a small amount of solid deposited over the foam surface. With the 0.03 M solution, the solid only deposited in some spots, by increasing the concentration to 0.06 M and 0.10 M a thin layer ($< 1\mu m$) was unevenly distributed on the surface of the foams. Mg/Al ratios estimated at representative regions of interest are shown in the table inserted in Fig. 3.6.

Al-rich deposits (Mg/Al < 1) were identified lying over the foam surface for 0.03 M or on the top of Mg-rich solids (Mg/Al > 5) for 0.06 and 0.10 M solutions. It seemed that the amount of Mg in Mg-rich deposits was related to the concentration of the electrolytic solution. The formation of an Al-rich layer agreed with the low pH values recorded below 100 s. On the other hand, the formation of a Mg-rich layer in both 0.06 and 0.10 M solutions, could be related to the local fast generation of a basic media, not be recorded during pH measurements in Fig. 3.3f. This behaviour could be enhanced in more concentrated solutions due to both a higher nitrate and Mg^{2+} concentrations.

Point	Mg/Al (a.r)
1	1.97
2	1.69
3	0.10
1	25.26
2	2.40
3	0.93
4	0.11
1	9.54
2	3.20
3	2.40
4	0.91
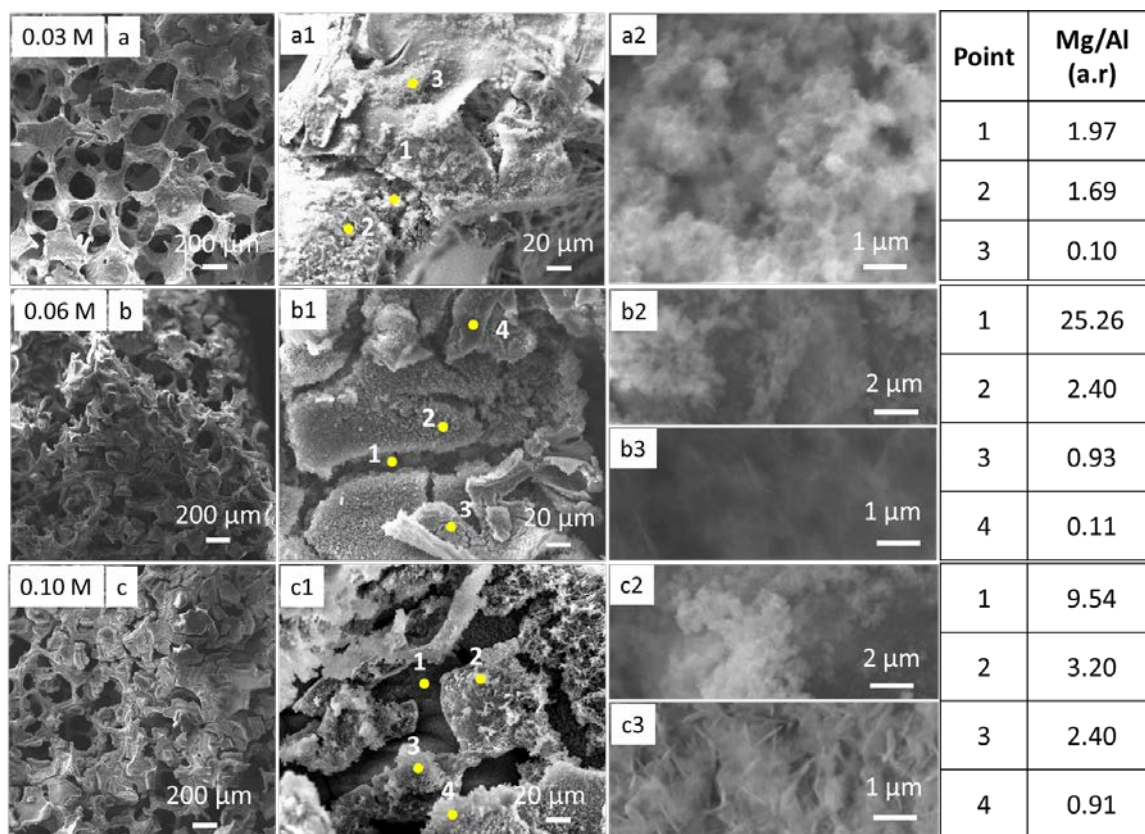
Figure 3.7. SEM images of the foams coated at -1.2 V *vs* SCE for 2000 s with Mg/Al nitrate solutions at different concentrations: 0.03 M (a, a1, a2), 0.06 M (b, b1, b2, b3), and 0.10 M (c, c1, c2, c3). The table summarizes Mg/Al ratios obtained from EDS spectra in the indicated regions of interest.

A 1000 s pulse was enough to evenly deposit the solid on the foam surface for 0.06 and 0.10 M solutions, while some uncoated zones were still observed using the 0.03 M solution, Fig. 3.6b, d, f. Solids with Mg/Al ratio around or above the 3/1 ratio precipitated in the 0.03 M

solution (points 3 and 4 in Fig. 3.6b). Alike at 100 s, the Mg-rich layer was observed using 0.06 and 0.10 M solutions; the Mg content was higher in 0.10 M samples (points 3 in Fig. 3.6d, f, and the right table), where a platelet-like morphology was observed (Fig. 3.6f2). They could be related to $Mg(OH)_2$ [36] or Mg-enriched HT-like phases [37]. On the top of this layer, agglomerates of particles with Mg/Al ratio around 1.40 – 2.65 deposited, in agreement with the pH values suitable for the precipitation of HT-like compounds. Finally, the Al-rich layer started to grow mainly in the sample prepared from the most concentrated solution, despite the similar pH values recorded.

At 2000 s (Fig. 3.7), SEM/EDS results were similar to those previously reported by us for Rh/Mg/Al HT samples, precursors of catalysts [16]. The amount of solid electrodeposited was proportional to the total metal concentration in the electrolytic bath; the loadings were 3.3, 6.6, and 8.9 wt.% for the samples prepared from the solutions 0.03, 0.06, and 0.10 M; respectively. Nevertheless, the best coating distribution and layer thickness, was achieved with the 0.06 M solution; layers of approximately 15 μm and 5 μm thickness were deposited on tips of struts and plate zones connecting them (Fig. 3.7b, b1). With 0.10 M solution, the precipitation of a large amount of solid led to the uncontrolled deposition of several layers of material, not well-adhered to the support, and to the pore blockage (Fig. 3.7c, c1).

Coatings were constituted by the layers of different morphology and composition, previously observed at 1000 s, namely platelets and spherical agglomerates of particles with different Mg/Al ratios as indicated by different points in Fig. 3.7a1, b1, c1. Larger Mg-rich platelets were deposited in more concentrated solutions, 300 – 400 nm, and 500 – 600 nm for samples prepared in 0.06, and 0.10 M, respectively (Fig. 3.7b3, c3). The differences in the Mg content above reported could not be found out here. This could be related to the difficulty in analysing the inner layer in the samples and the modifications in its thickness. Complementary information about this point will be obtained through combination with other characterization

techniques (*vide infra*). In the spherical agglomerates, the Al content increased moving from inner to outer layers regardless of the electrolyte bath, i.e. Mg/Al ratio were 2.40 and 0.93 in points 2 and 3, respectively, in Fig. 3.7b1. No remarkable differences were observed in the size of the agglomerates at the resolution of the SEM. To study effect of Mg/Al ratio on the formation of the Al-rich layer, one sample was prepared in an electrolytic bath containing a 0.06 M solution with Mg/Al = 4 (instead of Mg/Al = 3) at -1.2 V for 2000 s. The SEM/EDS results revealed that the Al-rich layer still grew despite such high Mg^{2+} content in the electrolyte (Fig. 3.8).

Point	Mg/Al (a.r.)
1	0.44
2	3.82
3	14.00
4	2.76
5	0.50
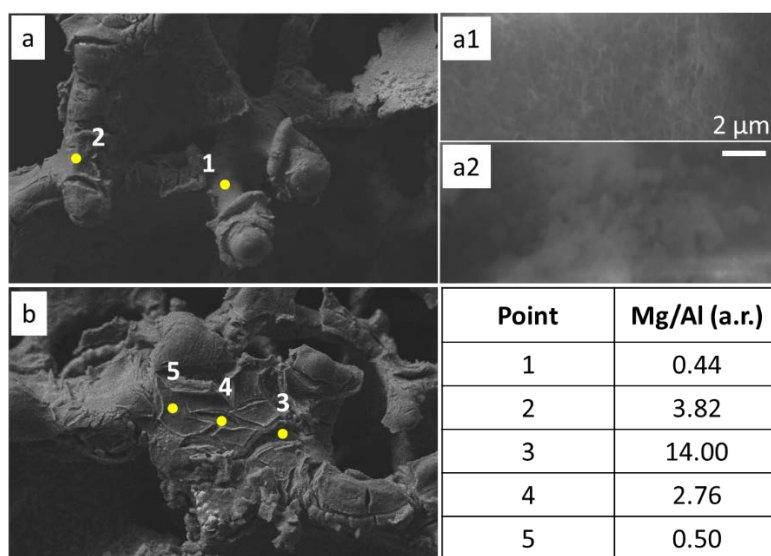
Figure 3.8. SEM images of the foams coated by Mg/Al-HT (Mg/Al = 4/1, 0.06 M, -1.2V vs SCE, 2000 s) at different locations: a) strut and b) plate zone. In which a1 and a2 are pictures zoomed in point 1 and 2. Table presents composition of locations indicated by yellow spots.

To deeply investigate the effect of the concentration on the morphology of particles within the agglomerates, the coating was detached and analysed by HRTEM. In Fig. 3.9, representative images of the coating prepared with the 0.03 M solution are shown. Collected HRTEM images evidenced the presence of thin nanosheets (5 – 20 nm). The low dispersion of the particles, due to a high particle-particle interaction, is characteristic of HT particles with poor crystallinity [38]. Both the interaction among the particles and the size seemed not to be significantly modified with the metal nitrate concentration. Only in the coating prepared from the 0.10 M solution, it would appear that the particles have a poorer defined morphology;

however, due to the particle agglomeration it was difficult to properly establish the differences. STEM analyses confirmed the presence of particles with Mg/Al ratio around 2.0, suitable for the precipitation of HT compounds, together with Al-rich and Mg-rich particles. High magnification images of Mg/Al particles exhibited areas of regular lattice fringes arranged in small domains. SAED patterns showed smooth diffraction rings with d values characteristics of (012), (018) and (113) planes of polycrystalline HT-like compounds.
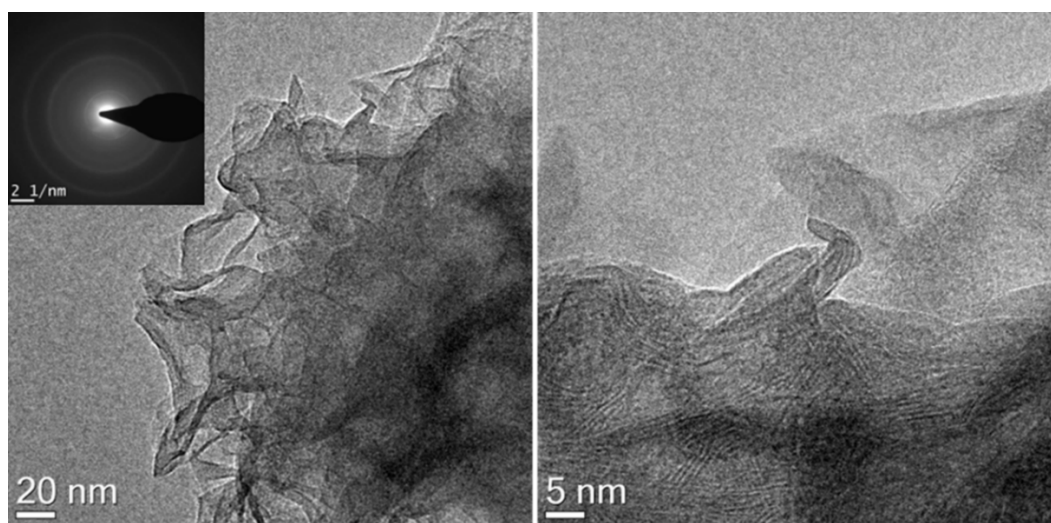
Figure 3.9. HRTEM images and SAED of the coating deposited on the foam at -1.2 V *vs* SCE for 2000 s with the 0.03 M Mg^{2+} and Al^{3+} nitrate solution.

From these results, it could be stated that the concentration of the solution not only governed the amount and distribution of electrodeposits on foam surfaces, but it may determine the initial steps of the precipitation process. Mg-rich amorphous particles deposited at short times, then the growth of well-defined platelet crystals took place, being this phenomenon metal nitrate dependent. The nitrate concentration may also determine the Mg/Al ratio, however, at long electrodeposition times the differences in composition were levelled, although layer thicknesses were different. Despite the pH recorded was suitable for the precipitation of HT-like compounds, an Al-rich layer was obtained, suggesting that either the pH measured deviated from the value reached close to the surface or other factors such as the ineffective replenishment of the solution, not only from nitrate but also cations, may be involved on this phenomenon.

Point	1	2	3	1	2	3	1	2	3	4
Mg/Al (a.r.)	21.34	1.69	0.06	6.70	1.83	0.07	5.73	2.93	1.66	0.09
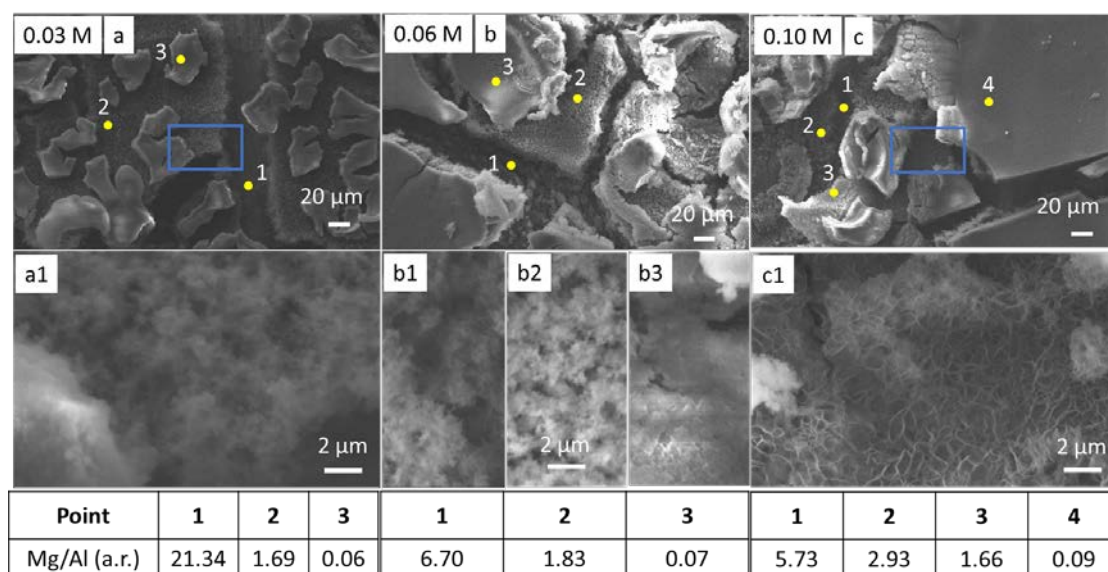
Figure 3.10. SEM images of the plates coated at -1.2 V *vs* SCE for 2000 s with Mg/Al nitrate solutions at different concentrations: 0.03 M (a, a1), 0.06 M (b, b1, b2, b3), and 0.10 M (c, c1). The table summarizes Mg/Al ratios obtained from EDS spectra in the indicated regions of interest.

The complexity of the foam shape made it difficult to structurally characterize the solids deposited, only the hydrotalcite-like phase was identified by SAED. Hence, electrodepositions were performed on FeCrAl plates at -1.2 V for 2000 s. Deposits were thinner than in foams, but the stratified layers were clearly identified, Fig. 3.10. The concentration of the nitrate metal solution modified the homogeneity and thickness of these layers and the size of the platelet-like particles, likewise in foams. In the 0.03 M sample, the Al-rich solid deposited as some flakes on the surface of thin layers. By increasing the concentration to 0.06 and 0.10 M, the flakes grew to form a continuous layer, and the platelet particles were identified. Since the coating thickness varies from 2 – 5 to 10 – 15 µm in the 0.03 to 0.10 M sample, it would appear that the formation of the Al-rich outer layer did not only depend on the solid thickness.

The crystalline phases and intercalated anions on the coatings were characterized by XRD, ATR and micro-Raman. Three series of plates were coated, and similar effects of nitrate concentration were observed, representative data is shown here. XRD patterns are displayed in Fig. 3.11, HT and $Mg(OH)_2$ reflections were clearly identified.
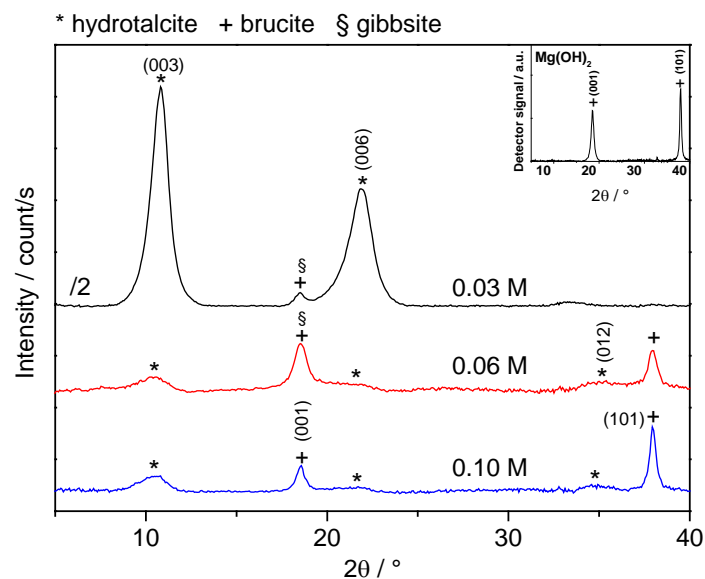
Figure 3.11. XRD patterns of FeCrAl plates coated at -1.2 V *vs* SCE for 2000 s with Mg/Al nitrate solutions at different concentrations. The patterns have been shifted vertically. Inset: XRD pattern of a plate coated using a Mg^{2+} nitrate solution.

Well-defined and intense basal (003) and (006) reflections of the HT phase were observed in patterns of coatings deposited from 0.03 M solutions [37], while the non-basal planes were not observed, indicating a preferential orientation/growth in the c direction. On the other hand, broad and low intense basal and non-basal HT reflections were recorded in both 0.06 and 0.10 M samples, characteristic of poor crystalline HT compounds. The d_{003} value, corresponding to a brucite-like layer and the interlayer region, was 8.03 Å for 0.03 M and ca. 8.40 Å for coatings obtained from more concentrated solutions, characteristic of nitrate intercalated HT compounds with anions parallel and tilted or stick-laying to the HT layers, respectively [39-42]. However, it was worthy to note that the Mg/Al ratio and the crystallinity of the samples, both being modified in the investigated samples, also determines the d_{003} value. The (101) reflection of the $Mg(OH)_2$ phase became more intense and sharper as the metal salt concentration increased, suggesting an enhanced crystallinity, which could be related to the larger platelet-like particles identified by SEM. The relative intensities of (101) and (001) reflections were modified with the metal concentration, in comparison with the pattern obtained for a plate coated with Mg nitrate (see inset Fig. 3.11). This behaviour could be related to the formation of the gibbsite

Al(OH)$_3$ phase, corresponding to the Al-rich layer identified by SEM, with a reflection overlapping the (001) of Mg(OH)$_2$; although the Mg(OH)$_2$ diffraction pattern also depends on the orientation of the particles [36].

The nature of interlayer anions in HT phases was investigated by ATR and Raman. Selected ATR spectra are displayed in Fig. 3.12; all the spectra recorded are shown in Fig. 3.13.
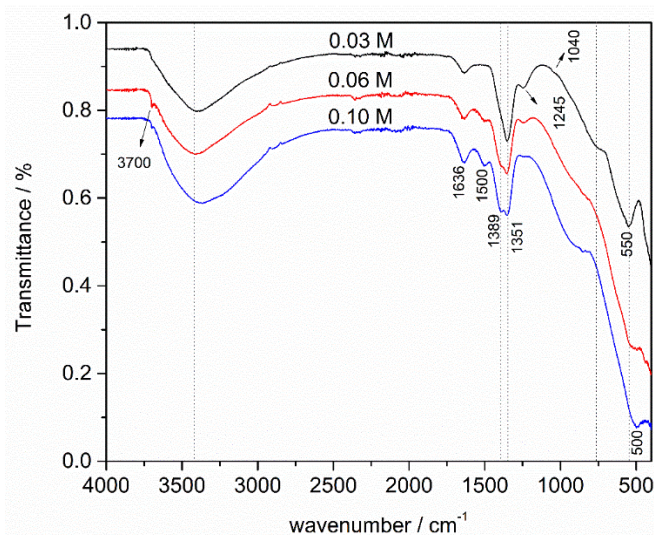
Figure 3.12. ATR spectra of FeCrAl plates coated at -1.2 V for 2000 s with Mg/Al nitrate solutions with different concentrations. The spectra have been shifted vertically.

The broad band attributed to the ν_{OH} of water (physisorbed and interlayer) and hydroxyl in the layers was centred at ca. 3450 cm^{-1}. Moreover, in some regions of samples prepared from 0.06 and 0.10 M solutions a sharp peak at ca. 3700 cm^{-1} due to ν_{OH} in Mg(OH)$_2$ was identified, in agreement with XRD. The bending vibration of water was recorded at ca. 1636 cm^{-1}. The shape of the bands in the 1570 and 1100 cm^{-1} range was modified with the metal salt concentration. A peak centred at 1351 cm^{-1} with a low intense band at 1245 cm^{-1} was recorded in the 0.03 M sample. This band became less intense as the concentration increased and an overlapped peak (1351 – 1389 cm^{-1}) with a new band at higher wavenumbers (1500 cm^{-1}) developed. XRD data suggested the inclusion of NO$_3^-$ in the interlayer region; however, the intense and narrow ν_3 antisymmetric NO$_3^-$ mode previously recorded for electrodeposited samples was not observed [43-44]. These spectra features suggested: i) a decrease in symmetry

of nitrate from D_{3h} to C_{2v} or C_s due to different orientation, which depended on nitrate concentration and interlayer order, however the ν_1 band was only recorded as a small shoulder at 1040 cm^{-1} in the 0.03 M sample; ii) the coexistence of CO_3^{2-} species in the interlayer region, due to the high affinity of HT-like compounds for CO_2, also with a distorted symmetry structure [45-48]; iii) the presence of carbonate or nitrate species in the $Mg(OH)_2$ phase, indeed, the spectra of electrodeposited $Mg(OH)_2$ showed a band at 1415 cm^{-1} with shoulders at 1328 and 1500 cm^{-1} (Fig. 3.13d). More information about the interlayer anions could be obtained from the low wavenumber region; however, lattice bands, which depended both on the crystallinity of the solids and composition, may obscure the differences [49].
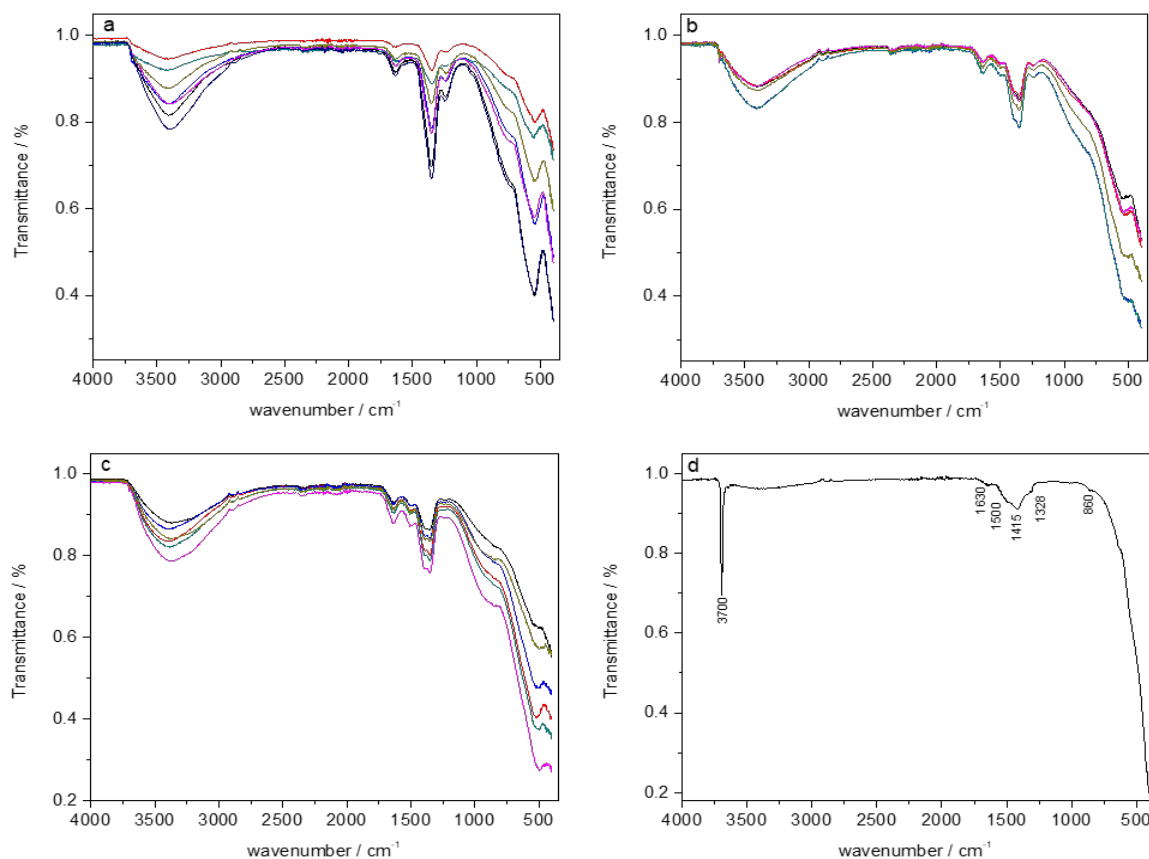
Figure 3.13. ATR spectra of the plates coated with solids from Mg/Al nitrate solutions at different concentrations: a) 0.03 M, b) 0.06 M, c) 0.10 M, and d) Mg $(NO_3)_2$ 0.0675 M.

Representative Raman spectra are shown in Fig. 3.14; all the spectra recorded can be found in Fig. 3.15. The samples prepared with 0.06 and 0.10 M solutions showed the typical bands of HT-like compounds intercalated with NO_3^- species [49]: the intense ν_1 symmetric stretching mode at

ca. 1050 cm^{-1}; the low intense and broad ν_3 antisymmetric mode in the 1300 – 1400 cm^{-1} range; and the ν_4 mode of nitrate at ca. 715 cm^{-1}. The presence of some CO_3^{2-} species in both samples, suggested by ATR, was confirmed by the shoulder at 1098 cm^{-1}. On the other hand, the spectra of the sample prepared from the 0.03 M solution showed the following features: the ν_1 mode was recorded as a band at 1043 cm^{-1} with a shoulder at 1053 cm^{-1}; the ν_3 at 1328 cm^{-1} was a broad and rather intense band; and a new band was recorded at ca. 805 cm^{-1}, which could be attributed to the ν_2 Raman inactive mode; while the ν_4 mode was recorded at 712 cm^{-1}. These features could be related to a lowering of the D_{3h} symmetry of nitrate, in agreement with ATR. The presence of CO_3^{2-} could also modify the shape of ν_1 and ν_3 bands. The sharp ν_{OH} band at 3650 cm^{-1} and the low intensity band at ca. 445 cm^{-1} of crystalline $Mg(OH)_2$ (Fig. 3.15d) were identified in some regions of all the samples. This confirmed the formation of brucite regardless of the electrolyte concentration, although it was more intense and abundant in spectra of the 0.10 M coatings, in agreement with XRD data. The broad band of the ν_{OH} in HT compounds separated into two components for the 0.03 M coatings. A similar behaviour was reported by [47] in FTIR spectra of HT intercalated with nitrate suggesting the presence of hydroxyl groups with two different environments; however, in this work we did not observe the two components in the ATR spectra.
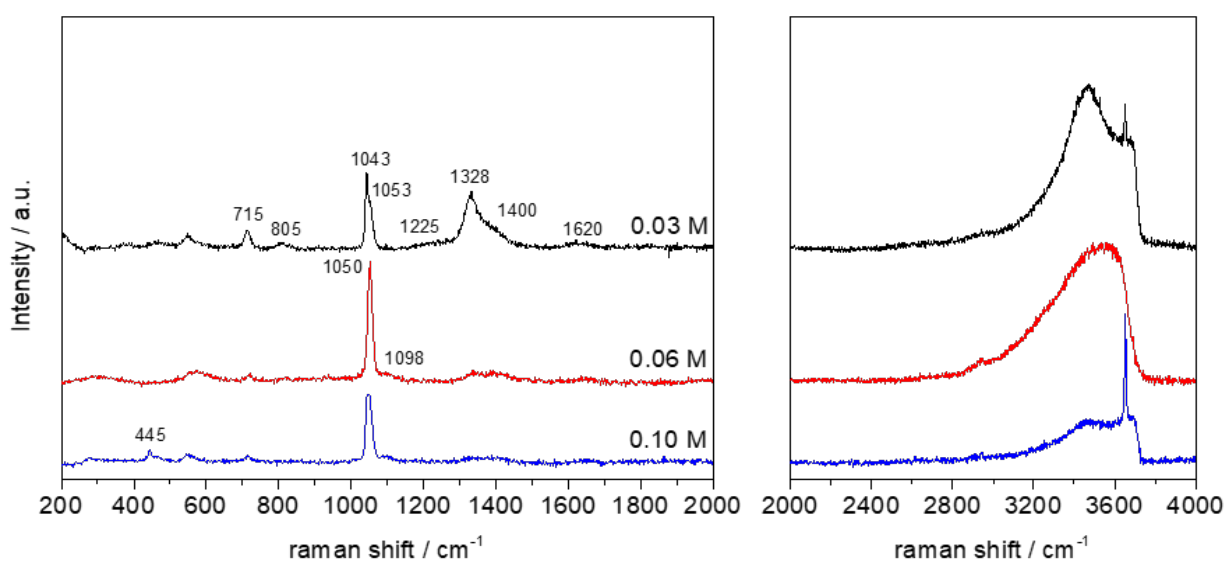
Figure 3.14. Raman spectra of FeCrAl plates coated at -1.2 V for 2000 s with Mg/Al nitrate solutions with different concentrations. The spectra have been shifted vertically.
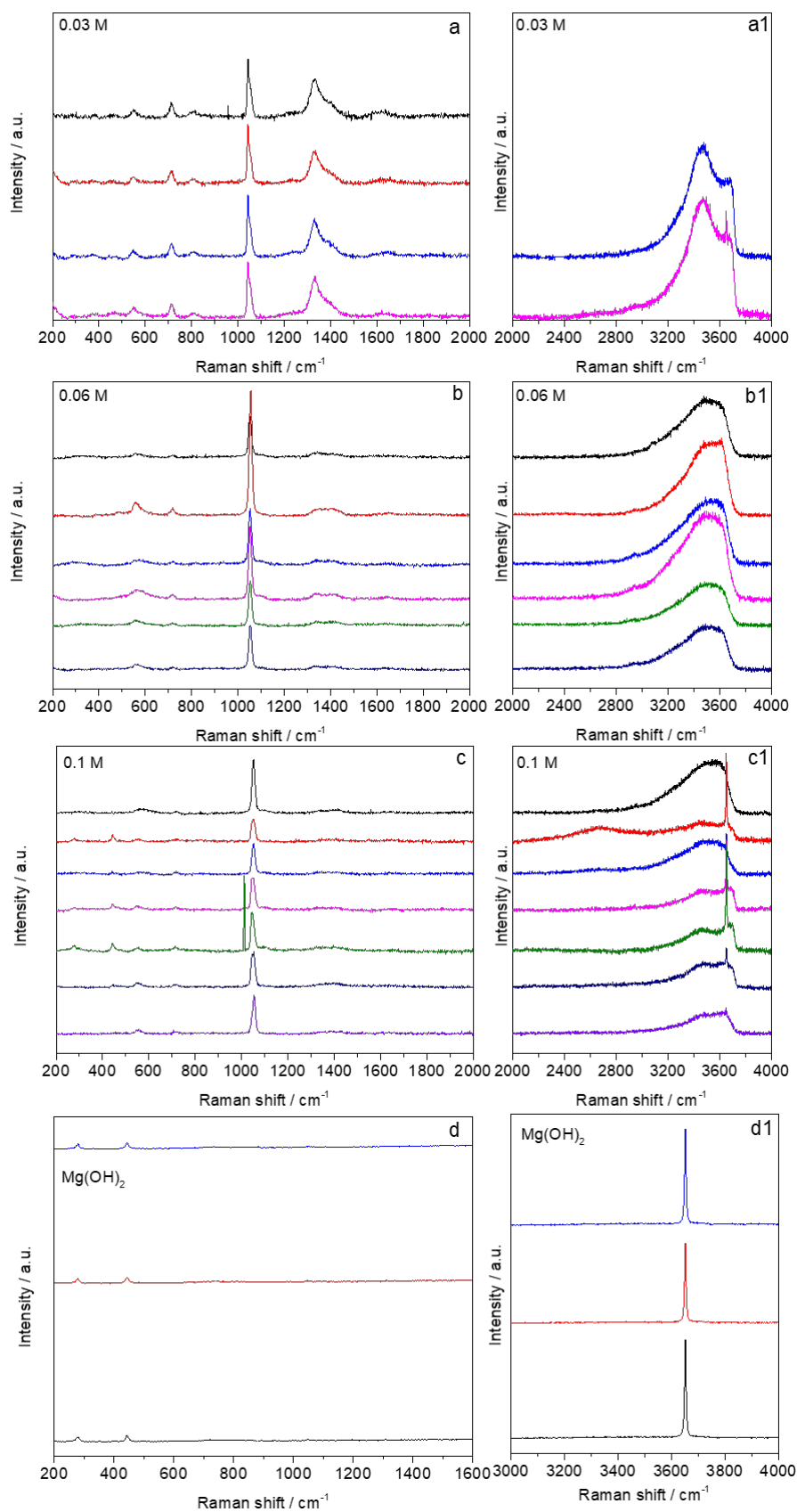
Figure 3.15. Raman spectra of the plates coated with solids from: Mg/Al nitrate solutions at different concentrations: 0.03 M (a and a1), 0.06 M (b and b1), 0.10 M (c and c1) and $Mg(NO_3)_2$ 0.0675 M (d and d1).

3.4 Conclusions

The metal nitrate concentration influenced both electrochemical OH^- production by nitrate reduction and chemical OH^- consumption by precipitation of cations during the electrodeposition of HT-like compounds.

The reduction processes, taking place during the application of a -1.2 V *vs* SCE pulse at FeCrAl open-cell foams immersed in nitrate solutions in absence of precipitating cations, followed a typical surface reaction behaviour at short times (below 500 s) in the nitrate concentration range from 0.0675 to 0.225 M. In the presence of Mg^{2+} and Al^{3+} precipitating cations with 0.03, 0.06 and 0.10 M total metal concentrations, however, the formation of an insulating hydroxide layer and/or the inadequate replenishment of the solution at the electrode-electrolyte interface may lead to the deviation from a first-kinetic order behaviour.

The concentration of the solution not only governed the amount and distribution of electrodeposited materials on foam surfaces (a low concentration provided thin coatings, while a high concentration the pore blockage), but also the initial steps of the precipitation process and structural and morphological characteristics of the coatings, which are of paramount importance for the preparation of structured catalysts.

Stratified layers of different composition and morphology deposited at long times regardless of the electrolytic bath; however, the crystallinity of the hydrotalcite-like and brucite phases (probably also gibbsite), the arrangement of nitrate anions inside the hydrotalcite-like phase, the size of $Mg(OH)_2$ or Mg-rich platelet particles, and the growth of the Al-rich layer were modified by the concentration of the electrolytic bath. The increase in the concentration from 0.03 to 0.10 M favoured the formation of larger and more crystalline $Mg(OH)_2$ particles, poor crystalline nitrate intercalated HT-like phases with a higher interlayer region, and fostered the formation of the Al-rich outer layer.

3.5 References

1. M. Wasberg, G. Horáknyi, Electrochim. Acta 40 (1995) 615-623.

2. D. De, J. D. Englehardt, E. E. Kalu, J. Electrochem. Soc. 147 (2000) 4224–4228.

3. M.T. de Groot, M.T.M. Koper, J. Electroanal. Chem. 562 (2004) 81–94.

4. I. Katsounaros, G. Kyriacou, Electrochim. Acta 53 (2008) 5477–5484.

5. K.-W. Nam, K.-B. Kim, J. Electrochem. Soc. 149 (2002) A346–A354.

6. C. C. Streinz, A. P. Hartman, S. Motupally, J. W. Weidner, J. Electrochem. Soc. 142 (1995) 1084– 1089.

7. M. Wohlfahrt-Mehrens, R. Oesten, P. Wilde, R.A. Huggins, Solid State Ionics 86–88 (1996) 841– 847.

8. Y. Hamlaoui, L. Tifouti, C. Remazeilles, F. Pedraza, Mater. Chem. Phys. 120 (2010) 172–180.

9. M. Izaki, T. Omi, J. Electrochem. Soc. 143 (1996) L53–L55.

10. M. Nobial, O. Devos, B. Tribollet, J. Cryst. Growth 327 (2011) 173–181.

11. S. Sun, S. Jiao, K. Zhang, D. Wang, S. Gao, H. Li, J. Wang, Q. Yu, F. Guo, L. Zhao, J. Cryst. Growth 359 (2012) 15–19.

12. G. Yao, M. Zhang, J. Lv, K. Xu, S. Shi, Z. Gong, J. Tao, X. Jiang, L. Yang, Y. Cheng, G. He, J. Electrochem. Soc. 162 (2015) D300–D304.

13. M. Dinamani, P. Vishnu Kamath, J. Appl. Electrochem. 34 (2004) 899–902.

14. G. Giordano, C. Durante, A. Gennaro, M. Guglielmi, J. Sol-Gel Sci. Technol. 76 (2015) 233–240.

15. E. Scavetta, A. Mignani, D. Prandstaller, D. Tonelli, Chem. Mater. 19 (2007) 4523–4529.

16. P. Benito, G. Nuyts, M. Monti, W. De Nolf, G. Fornasari, K Janssens, E. Scavetta, A. Vaccari, Appl. Catal. B Environ. 179 (2015) 321–332.

17. P. He, L.R. Faulkner, Anal. Chem. 58 (1986) 517–523.

18. H. Deligianni, L. T. Romankiw, IBM J. Res. Dev. 37 (1993) 85.

19. C. Deslouis, I. Frateur, G. Maurin, and B. Tribollet, J. Appl. Electrochem. 27 (1997) 482.

20. S. L. Díaz, O. R. Mattos1, O.E. Barcia, F.J. Fabri Miranda, Electrochim. Acta 47 (2002) 4091-4100.

21. A. I. C. Santana, S. L. Díaz, O. E. Barcia, O. R. Mattos, J. Electrochem. Soc. 156 (2009) D326-D330.

22. R. C. M. Salles, G. C.G. de Oliveira, S. L. Díaz, O. E. Barcia, O. R. Mattos, Electrochim. Acta 56 (2011) 7931–7939.

23. A. Fakhry, H. Cachet, C. Debiemme-Chouvy, Electrochim. Acta 179 (2015) 297–303.

24. J. Yang, S. Xu, W. Chen, J. Zang, J. Zhang, J. Electroanal. Chem. 670 (2012) 62–66.

25. C. Deslouis, I. Frateur, G. Maurin, B. Tribollet, J. Appl. Electrochem. 27 (1997) 482-492.

26. M. Uhlemann, A. Krause, A. Gebert, J. Electroanal. Chem. 577 (2005) 19–24.

27. J. J. Kelly, S. H. Goods, A. A. Talin, J. T. Hachman, J. Electrochem. Soc. 153(2006) C318-C324.

28. M. Nobial, O. Devos, O. R. Mattos, B. Tribollet, J. Electroanal. Chem. 600 (2007) 87–94.

29. F. Bouamrane, A. Tadjeddine, J.E. Butler, R. Tenne, C. Lévy-Clément, J. Electroanal. Chem. 405 (1996) 95–99.

30. T. Hreid, J. Li, Y. Zhang, H. J. Spratt, H. Wang, G. Will, RSC Adv. 5 (2015) 65114–65122.

31. M. Monti, P. Benito, F. Basile, G. Fornasari, M. Gazzano, E. Scavetta, D. Tonelli, A. Vaccari, Electrochim. Acta 108 (2013) 596–604.

32. P. Benito, F. M. Labajos, V. Rives, Cryst. Growth Des. 6 (2006) 1961-1966.

33. P. Benito, M. Herrero, C. Barriga, F. M. Labajos, V. Rives, Inorg. Chem. 47 (2008) 5453-5463.

34. J. W. Boclair, P. S. Braterman, Chem. Mater. 11 (1999) 298–302.

35. P. M. S. Monk, R. Janes, R. D. Partridge, J. Chem. Soc. Faraday Trans. 93 (1997) 3991–3997.

36. Y. Lv, Z. Zhang, Y. Lai, J. Li, Y. Liu, Cryst. Eng. Comm. 13 (2011) 3848–3851.

37. F. Cavani, F. Trifirò, A. Vaccari, Catal. Today 11 (1991) 173–301.

38. S. K. Yun, T. J. Pinnavaia, Chem. Mater. 7 (1995) 348–354.

39. J. Olanrewaju, B.L. Newalkar, C. Mancino, S. Komarneni, Mater. Lett. 45 (2000) 307–310.

40. M. del Arco, S. Gutierrez, C. Martin, V. Rives, J. Rocha, J. Solid State Chem. 151 (2000) 272–280.

41. Z. P. Xu and H. C. Zeng, J. Phys. Chem. B 105 (2001) 1743–1749.

42. R. P. Bontchev, S. Liu, J. L. Krumhansl, J. Voigt, T. M. Nenoff, Chem. Mater. 15 (2003) 3669–3675.

43. F. Basile, P. Benito, G. Fornasari, V. Rosetti, E. Scavetta, D. Tonelli, A. Vaccari, Appl. Catal. B Environ. 91 (2009) 563–572.

44. M. S. Yarger, E. M. P. Steinmiller, K. S. Choi, Inorg. Chem. 47 (2008) 5859–5865.

45. M. J. Hernandez-Moreno, M. A. Ulibarri, J.L. Rendon, C. J. Serna, Phys. Chem. Miner. 12 (1985) 34–38.

46. F. Rey, V. Fornes, J. M. Rojo, J. Chem. Soc. Faraday Trans. 88 (1992) 2233–2238.

47. Z. P. Xu and H. C. Zeng, Chem. Mater. 13 (2001) 4564–4572.

48. A. Alejandre, F. Medina, X. Rodriguez, P. Salagre, J. E. Sueiras, J. Catal. 188 (1999) 311–324.

49. J. T. Kloprogge, D. Wharton, L. Hickey, R. L. Frost, Am. Mineral. 87 (2002) 623–629.

Chapter 4. Electrosynthesized Rh/Mg/Al structured catalyst based on FeCrAl foam and reactivity for the catalytic partial oxidation of CH$_4$

Chapter 4

4.1 Introduction

Hydrotalcite-type (HT) compounds are well-known as catalysts or catalyst precursors for processes demanding tailored basic/acidic sites, relatively high specific surface area and/or metal dispersion [1-3]. Calcination at 450-600 °C produces basic mixed oxides that by reduction can form well-dispersed metallic species. Above ca. 800 °C a mixture of spinel and MgO-type phases, which supports metallic particles for high temperature catalytic processes, is formed. Therefore, coating them onto surface of open-cell metallic foams could create promising structured catlysts, exploiting the advantage of both HTs and open-cell metallic foam [4]. These HT-derived structured catalysts have been reported to enhance mass and heat transfer and/or reduce pressure drop in gas-phase processes such as the syngas production by steam reforming [5], oxy-reforming [6], partial oxidation [7], and ethanol reforming [8], in the total oxidation of volatile organic compounds [9], and in liquid-phase processes for the synthesis of biodiesel [10] and aldol condensation of acetone [11].

The electrodeposition, specifically the electro-base generation method, is "ideally" the best way to coat metallic supports *in situ* with HT-type materials as mentioned in chapter 2 and 3. Our group proposed this technique to synthesize HT compounds *in situ* on FeCrAl open-cell foams, in order to prepare structured catalysts for the Catalytic Partial Oxidation (CPO) of CH_4 to syngas [5,7]. However, during the preparation of thick Rh/Mg/Al HT coatings (10 – 15 µm), we observe the sequential precipitation of layers with different compositions as the synthesis time proceeds, which modifies composition, crystalline phases, Rh reducibility and metal particle size and, consequently, film stability and catalytic performances [12,13]. The challenging preparation of these Rh/Mg/Al HT films can be related to the formation of thick and insulating layers, and the inefficient replenishment of the electrolytic solution on the surface of the electrode at long times as mentioned in chapter 2 and 3. Although the differences in the precipitation pH, diffusion coefficients of the cations and the shape of the support could

also play a role in this phenomenon. Indeed, deviations in the expected composition of Ni/Co-[14,15] and Fe-containing compounds [16-18] deposited on Ni foams are reported notwithstanding thin films are prepared at short times. So far, only one article reports the coating by Fe-Co hydroxides of Ni foams with controlled composition by continuous electrodeposition at a constant current density of 10 mA cm^{-2} for 1800 s [19].

In porous supports, such as open-cell foams, limited mass transfer inside the pores, and generation of polarization potentials or changes in the local current density do not guarantee a uniform composition and thickness of deposits over the complete geometry [20,21]. Electrodepositions performed under forced convection, by pumping or agitation, and through pulse depositions, with stirring between the pulses, can improve the properties of the coating. The mechanical stirring replenishes the electrolytic solution and decreases the thickness of the diffusion layer during the electrodeposition [22,23]; however, in the coating of complex shaped supports an inhomogeneous flow rate and hence strongly scattering current density can be generated, creating inhomogeneity in the coating [24]. The use of short electrochemical pulses, allowing sufficient time (aided by stirring) between depositions, replenishes the local ion concentration creating a more homogeneous Fe distribution in Ni-Fe/Oxihydroxide on a Ni foam as well as modifying the texture of the film [25]. Finally, the use of flow cells improves the mass transfer in the preparation of ZnO over Cr and Au electrodes [26] and Cu on 3D graphite felts [27] by replenishing the solution inside the felt.

In this chapter, Rh/Mg/Al HT compounds electrodeposited on FeCrAl foams were prepared in a homemade flow-cell double-compartment electrochemical set-up. To study the feasibility of the procedure in preparing HT-derived structured catalysts, two samples with different Rh loading (2 and 5% as atomic ratio) were prepared, tested in the CPO of CH$_4$, and characterized at the different stages of their life-time by XRD, electron (FE-SEM, HRTEM) and synchrotron microscopic techniques (nano combined XRF/XRD tomography). In the past, it was

demonstrated the power of combined μ-XRF/XRD tomography to study the distribution of the elements and crystalline phases in the coating and the foam support [28,29]; here we further improved the quality of the data by using a nano-beam obtaining distributions with a higher spatial resolution. Sintering of Rh active phase under the harsh reaction conditions is one crucial issue during the operation of CPO [30]. The performance of structured catalysts depends on the Rh loading and thickness of the coating as well as on its stability; moreover, Rh metallic particle size, dispersion and stability against sintering are of paramount importance [31]. The tailoring of the latter can be easily achieved with coprecipitated HT-derived catalysts [2], thus, the final aim of chapter is to achieve a better control in the properties of electrodeposits to further improve the activity and stability of structured catalysts.

4.2 Experimental

4.2.1 Catalyst preparation

All chemicals were purchased from Sigma Aldrich: $Mg(NO_3)_2·6H_2O$ (> 99%), $Al(NO_3)_3·9H_2O$ (> 98%), $Rh(NO_3)_3$ solution (10 wt.% Rh in HNO_3). FeCrAl open-cell foam cylinders (80 ppi and 10 mm x 11.9 mm), cut from a panel, were used as structured supports.

Electrodepositions were performed in a homemade double-compartment flow electrochemical cell by FAVS Gnudi, using a potentiostat (Autolab, PGSTAT128N, Eco Chemie) with GPES software. A Pt coil (0.4 mm diameter and 40 cm in length) and a saturated calomel electrode (SCE) were used as counter and reference electrode (C.E. and R.E.), respectively. The working electrode was the FeCrAl foam in the cylindrical shape and it was assembled by a three-pronged Pt electrical contact as described elsewhere [12]. The working and counter electrode compartments were separated by a glass frit tube to avoid the mixture of the electrochemical reaction products. The reference electrode was in electrolytic contact with the main compartment *via* a Luggin capillary placed close 1 mm to the surface of the foam

cylinder. All potentials were reported with respect to SCE. Prior to coating, the foam was subsequently washed in acetone, water and then dried at 60 °C for 24 h.

The electrodepositions were performed by circulating the electrolyte during the coating process in the working electrode chamber with a flow rate of 2 mL min^{-1} by a peristaltic pump. Preliminary studies indicated that a lower (or no) or higher flow gave poorer results in terms of coating properties and catalytic activity. The synthesis conditions (potential applied, time and composition of the electrolytic solution) were like those used in depositions performed in the conventional single-compartment cell, i.e. a -1.2 V *vs* SCE pulse was applied for 2000 s to the foam immersed in an aqueous metal nitrate solution (0.06 M) containing Rh/Mg/Al atomic ratio (a.r.) 5/70/25 or 2/70/28, named Rh5 or Rh2, respectively [13]. It should be noted that in these electrolytes, the set-up reached a low uncompensated resistance (R_u) ca. 1-2 Ω in all of experiments. After electrodeposition, the coated foams were thoroughly washed with distilled water and dried at 40 °C for 24 h. The samples were then calcined at 900 °C for 12 h with a 10 °C min^{-1} heating rate.

4.2.2 Characterization of the coatings

The catalysts were characterized at different stages including after electrodeposition, calcination, and catalytic test by several techniques: XRD, SEM/EDS, HRTEM, micro-Raman, FESEM, and special nano XRD combined nano XRF. The first four techniques were already mentioned in chapter 2 and 3.

Field emission scanning electron microscopy (FESEM) analyses were conducted on a Zeiss LEO Gemini 1530 equipped with an Everhart-Thornley (E-T) secondary electron detector and a Scintillator BSE detector – KE Developments CENTAURUS. The accelerating voltages were 5 or 10 kV.

Combined nano X-ray Fluorescence (n-XRF) and nano X-ray Powder Diffraction (n-XRD)

measurements in tomographic mode were performed at the ID16b beamline of the European Synchrotron Radiation Facility (ESRF, Grenoble, France). The polychromatic beam from the undulator source was monochromatized to 29.6 keV using a Si (111) double crystal monochromator and subsequently focused on the sample by means of a Kirkpatrick-Baez mirror system, achieving a spot size of 80×70 nm (h x v). Two 2 x 3-element silicon drift detectors (KETEK GmbH D) collected the fluorescent radiation produced by the irradiated specimen under 90° from the incoming X-rays. A Frelon 2K (51×51 μm^2) detector positioned behind the sample was used to register the Debye rings produced by interference of the X-ray photons elastically scattered by the sample. For the tomographic experiments, samples were prepared by isolating individual struts (about 50 μm) from the foams and gluing them to the tip of glass capillaries, allowing an easy rotation in the beam. The sample moved horizontally with a 0.2 μm step size and was rotated over 180° with a 1.6 - 2.4° interval, depending on the sample. The data treatment was performed as reported elsewhere using the Spectrocrunch software for the analysis of the XRF signals [32] and the XRDUA software for the analysis of the XRD data [29,33].

The high primary beam energy of 29.6 keV, necessary to measure diffraction in transmission, combined with the measurement performed in air, caused the detection limits for low Z elements like Mg and Al to be poor due to the low absorption cross-section and air absorption respectively. Artefacts in the tomographic reconstruction (visible as rings or arcs) were primarily caused by the decision to use continuous rotation scanning and step-wise translation (as opposed to continuous translation and step-wise rotation as used in previous work). Although this scanning mode improved the particle statistics in diffraction (all crystal orientations around the rotation axes are measured when rotation is continuous as opposed to several discrete orientations when rotation is step-wise), an imperfect rotation and normalization for the changing X-ray flux caused artefacts. Nevertheless, the tomographic

reconstructions gave a good indication on the chemical composition of metal support and coating with 200 nm nominal resolution.

4.2.3 Catalytic test

CPO tests were conducted at atmospheric pressure using a quartz reactor (i.d. 10.0 mm) with one foam cylinder. The foam fitted well with the wall of the reactor to minimize any by-pass flow. Before carrying out the tests, the catalyst was reduced in-situ with 7.0 L h^{-1} H_2/N_2 (1/1) gas mixture at 750 ^{o}C for 2 h.

The activity of the catalysts was evaluated by modifying the reaction conditions (Table 4.1), i.e. setting up the oven at two temperature values (T_{oven} = 750 and 500 ^{o}C), modifying the Gas Hourly Space Velocity (GHSV) from 126,000 to 23,000 h^{-1} and feeding different concentrations of reagents ($CH_4/O_2/N_2$ = 2/1/20 and 2/1/4 v/v). Reaction conditions either feeding diluted gas mixtures ($CH_4/O_2/N_2$ = 2/1/20 v/v) or at a low oven temperature reduced the amount of heat developed by the exothermic reactions, making it possible to highlight the differences among catalysts. On the other hand, tests with a concentrated gas mixture ($CH_4/O_2/N_2$ = 2/1/4 v/v) and high oven temperature (750 °C) were used to study the stability of the catalysts against deactivation by sintering, coking and oxidation. Control tests were carried out after each reaction condition by feeding the initial one ($CH_4/O_2/N_2$ = 2/1/20 v/v, 126,000 h^{-1}) to check deactivation/activation processes.

The stability of the best catalysts was investigated through three reaction cycles including shut-down to room temperature and start-up to the reaction temperature, between them maintaining an inert flow of N_2. Each cycle consisted of two reaction conditions: i) T_{oven}= 500 °C, $CH_4/O_2/N_2$ = 2/1/20 v/v, GHSV = 30,500 h^{-1}; ii) T_{oven}= 750 °C, $CH_4/O_2/N_2$ = 2/1/4 v/v, GHSV = 30,500 h^{-1}.

The effluent products were analysed *on-line* after water condensation by a PerkinElmer Autosystem XL gas chromatograph, equipped with two TCDs and two Carbosphere columns using

Chapter 4

He as a carrier gas for CH4, O2, CO, and CO2 measurements, and N2 for H2 analysis. Oxygen conversion was completed in all tests. CH4 conversion and the selectivity in H2 and CO were calculated as reported elsewhere [34].

4.3 Results and discussion

4.3.1 Characterization of the HT precursors

Fig. 4.1a-d depict SEM images of the surface and cross-sections of foams coated with Rh5 electrolytic solution; similar results were obtained for Rh2 samples (Fig. 4.2). A 4.6 wt.% catalyst precursor deposited on the surface of the foams (both outer surface and strut cavities) regardless of the nominal Rh content. The layer thickness, estimated from the analysis of cross-section images, ranged between 5 to 20 µm on the outer surface of the struts and nodes connecting the struts; the thinner coatings were found inside the foam cylinder structure. Very thin layers (less than 1.5 µm) coated the cavities within the struts.

Point	Composition (atomic ratio)		
	Rh	Mg	Al
1	3	72	25
2	3	77	20
3	3	76	21
4	5	70	25
5	3	68	29
Average Rh2	1.9 ± 1.0	69.9 ± 6.8	28.2 ± 6.5
Average Rh5	4.2 ± 2.7	73.0 ± 6.1	22.8 ± 5.4
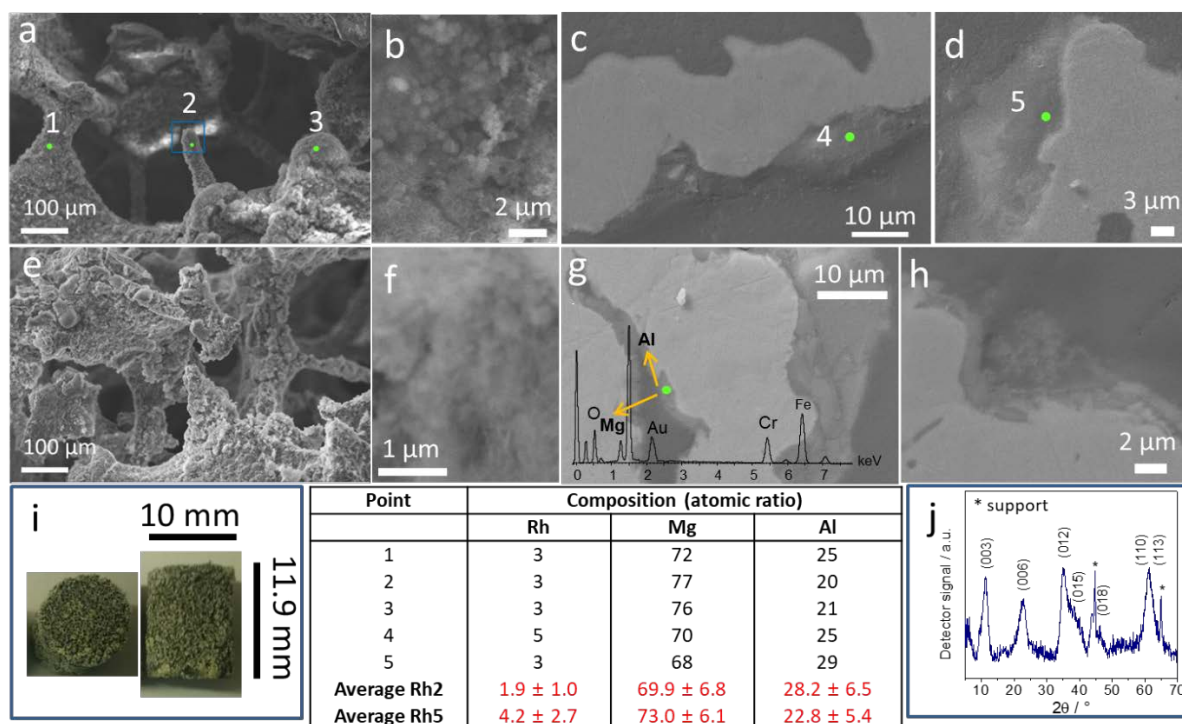
Figure 4.1. SEM images and composition of Rh5 catalysts: fresh (a, b, c, d) and after calcination (e, f, g, h). Here c, d, g, h showed cross-section of an embedded foam, i is an overview of one coated foam and j XRD pattern of the fresh coating.

The morphology and size of the particles was not modified with the flow, unlike as reported for the deposition of ZnO in an impinging cell, probably due to the low flow rate [32]. Platelet-like and spherical agglomerates of nanoparticles (100 – 400 nm) connected in a gel-like manner (Fig. 4.1a, b), characteristic of electrodeposited materials [13], were observed. Average deposit compositions (Rh/Mg/Al a.r.) were obtained from EDS analyses of the surface of at least 5 foams, the results are summarized in table in Fig. 4.1. Unlike in our previous studies, where an outer layer rich in Al and Rh deposited on all the thick layers [13]; Rh, Mg and Al evenly distributed in the coating, a feature also confirmed by EDS analysis performed in cross-sections (Fig. 4.1c, d), and the estimated composition was close to the nominal one. However, in some few points, Mg-rich and Al-rich layers were identified, the former in films with platelet-like particles and the latter in layers thicker than 20 µm.
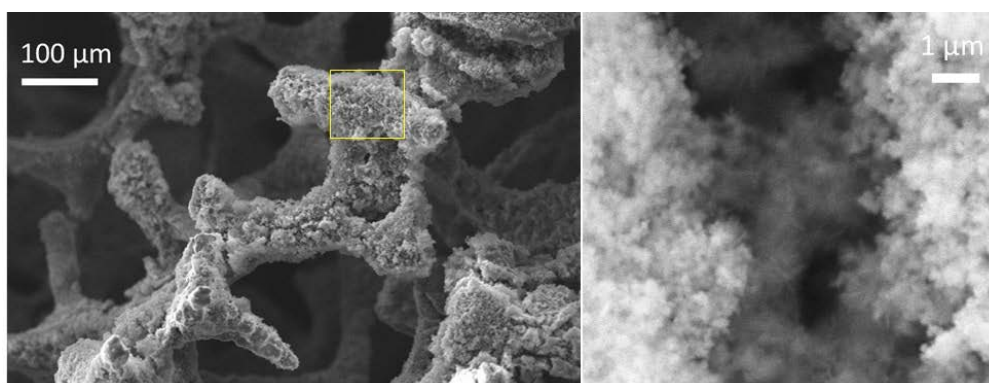
Figure 4.2. SEM images of Rh2 catalyst after electrodeposition.

XRD analysis of the as prepared coated foams was performed to identify the crystalline phases obtained through electrodeposition (Fig. 4.1j). The characteristic reflections of HT compounds intercalated with CO_3^{2-} were identified in the patterns, in contrast to the results in chapter 2 where NO_3^- and CO_3^{2-} species were found in the HT interlayer region together with a $Mg(OH)_2$ side phase.

The above results suggest that it was possible to coat cylinders of FeCrAl open-cell foams (80 ppi) by the electro-base method with HT compounds of rather controlled composition and crystalline phases whenever the layer thickness is below 20 µm. This behavior was likely

related to the separation of the anodic and cathodic compartments and the forced flow through the foam cylinder. The latter favors the replenishment of the electrolyte near the foam, although surfaces placed on the inner part of the cylinders were still less coated than those in the outer ones, probably because a part of the electrolyte bypassed the foam in the cell, the flow was slower in the inner part of the cylinder. The imperfect control of the flow may explain the deviations in the composition in some few points of the surface, although the effect of the formation of an insulating layer and some potential gradients could not be discarded. It was noted that the current profiles generated during the electrodeposition were identical for both Rh5 and Rh2 electrolytic solutions as shown in Fig. 4.3. The shape of the profiles was very similar to the one performed with nitrate bath containing only Mg^{2+} and Al^{3+} (total metal cations 0.06 M, Mg/Al = 3/1 as a.r.) in the single compartment electrochemical cell [21]. This provided an assumption that the electrochemical processes may proceed in the same way regardless of Rh content in the electrolyte and as a result the *in situ* precipitation occurred under similar conditions. This could explain why the quality of the coating was similar in both catalysts.
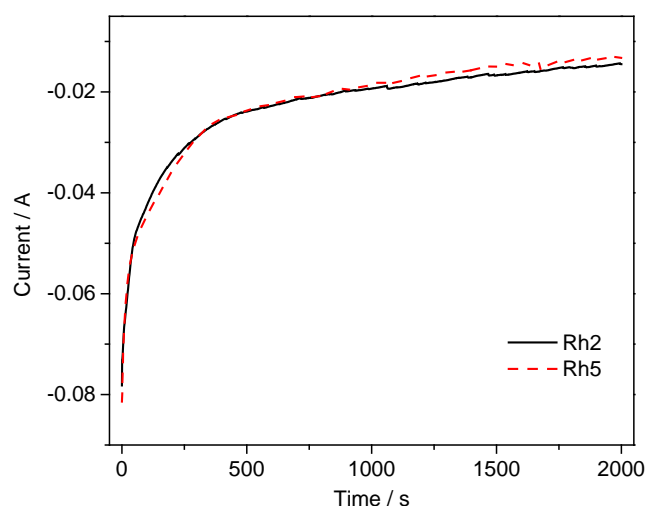
Figure 4.3. Current transient curves recorded during the electrodeposition of Rh/Mg/Al-HT like compounds on FeCrAl foam at -1.2 V *vs SCE* for 2000 s in electrolyte containing 0.06 M of $Rh(NO_3)_3$, $Mg(NO_3)_2$, and $Al(NO_3)_3$ (Rh/Mg/Al = 5/70/25 and 2/70/28 a.r. for Rh5 and Rh2, respectively).

4.3.2 Characterization of the catalysts

The better control in the deposition of the HT precursors influenced the properties of the coating both after calcination at 900 °C for 12 h (Fig. 4.1e-h) and catalytic tests (*vide infra*). The morphology and size of the catalyst particles were not largely altered by the thermal treatment and the film showed a small number of cracks and detachments. The stability against sintering of the particles may be related to the properties of HT-derived catalysts; it is well-known that the particle shape and size of HT compounds was maintained after calcination [35] and relatively high surface areas can be kept even after calcination at 900 °C [2]. To explain the enhanced adhesion of the film, the absence of the Rh- and Al- rich layer, which easily detached such as reported in our previous work [13], and the interaction between support and coating elements should be considered [29]. The latter involved the chemical reaction between Mg^{2+} from the coating and Al^{3+} from the foam giving rise to a $MgAl_2O_4$ phase. During calcination, the HT was decomposed and the foam was oxidized; at around 500 °C reactive MgO-type and gamma-Al_2O_3 phases developed in the coating and foam surface respectively, which could react at higher temperatures developing the spinel phase. SEM/EDS analysis of cross-sections confirmed an enrichment in Al of the coating near to the metal support, more remarkable in thin films (Fig. 4.1g).
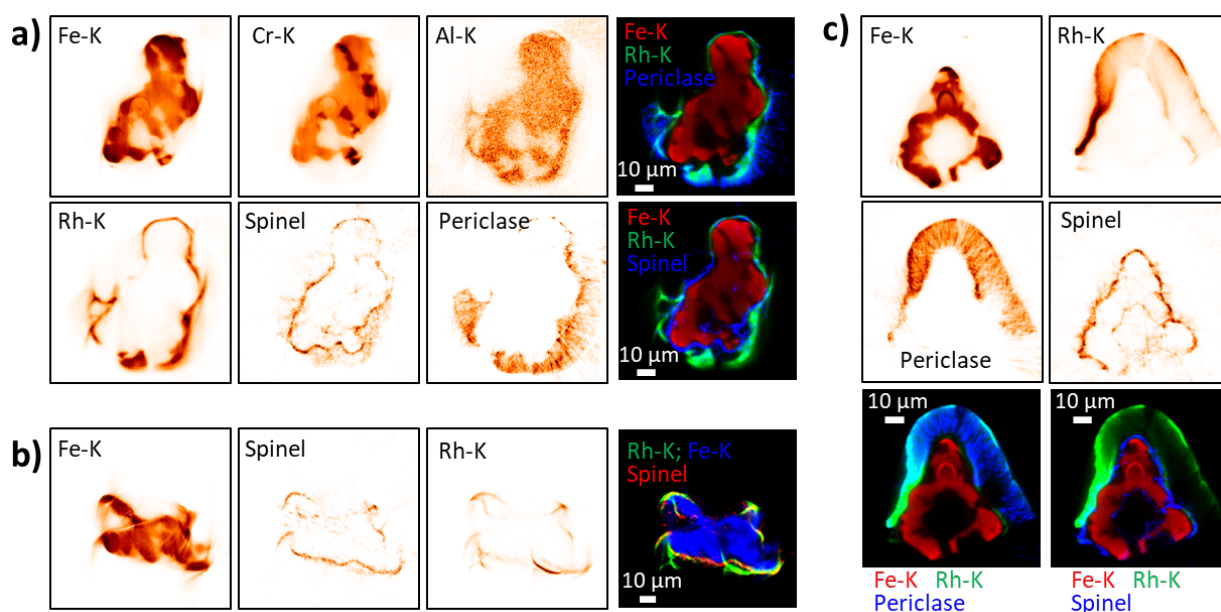
Figure 4.4. Nano-XRF/nano-XRD distributions on the catalysts. a) Rh2; b) Rh5 (thin coating); c) Rh5 (Mg-rich thick coating).

To better study the distribution of crystalline phases in the structured catalysts, combined nano-XRF/XRD tomography analyses using synchrotron radiation were performed on selected struts of Rh5 and Rh2 catalysts. Struts coated with thick Mg/Al and Mg-rich layers as well as thin layers were analyzed, Fig. 4.4. This technique gave the distribution of the elements and crystalline phases in virtual strut cross-sections of the as-prepared structured catalysts, making it possible to simultaneously study both support and coating [29]. The use of a nanosize beam increased the spatial resolution in the data obtained. The chemical composition of metal support and coating was obtained from tomographic reconstructions with a 200-nm nominal resolution, while the detection limits for low Z elements, like Mg and Al, were poor due to the low absorption cross-section and air absorption respectively.

Using averaged diffraction patterns, the support was shown to consist of Fe-Cr and chromium-iron carbide phases. Due to the large domain sizes with respect to the nanometric X-ray beam, the support can only be visualized by use the Fe and Cr fluorescence which showed a homogeneous Fe distribution while Cr was enriched in certain areas.

In the coating, the crystalline phases periclase, MgO, and spinel, $MgAl_2O_4$, were identified, characteristic of HT compounds calcined at 900 °C [2]. Their domain sizes were small enough to form Debye rings in the diffraction pattern and hence their spatial distribution could be visualized. The distribution of the phases depended on the coating composition. In Mg/Al thick layers, both MgO and $MgAl_2O_4$ phases distributed in the coating, Fig. 4.4a, but the concentration of the spinel phase increased close to the foam surface. In Mg-rich layers, Fig. 4.4c, the spinel phase formed a thin layer of 0.2 to 2 μm close to the foam surface while the periclase phase formed a thicker layer up to 10-15 μm on top. In thin films, such as those in the inner cavities of the struts (Fig. 4.4a, c) and in some struts inside the foam cylinders (Fig. 4.4b), only the spinel phase developed. These results confirmed the solid-state reaction between Mg^{2+} from the coating and Al^{3+} from the foam during calcination.

The Rh loading did not show to have a characteristic effect on coating thickness or crystalline composition. No Al_2O_3 phases, expected to develop due to the oxidation of the foam, could be detected, probably due to the coating support-interaction. The Rh distribution was visible due to its fluorescence but no direct indication of its inclusion in a crystalline structure could be derived from diffraction (e.g. change in spinel or periclase lattice parameters or identification of other Rh containing phases). This was most likely due to the low Rh loading [29]. Spatially Rh was colocalized with periclase (Fig. 4.4a-c) or with spinel in its absence (Fig. 4.4b). This was characteristic of coprecipitated HT-derived catalysts Rh-MgO or $Rh-MgAl_2O_4$.

4.3.3 Catalytic test

The performances of Rh5 and Rh2 structured catalysts in the CPO of CH_4 to syngas were evaluated with tests at different oven temperature (750 and 500 °C), concentration of the reaction mixture ($CH_4/O_2/N_2$ = 2/1/20 and 2/1/4 v/v) and GHSV value (126,000 – 23,000 h^{-1}). Average CH_4 conversion, H_2 and CO selectivities and H_2/CO ratio values obtained over four and three different Rh5 and Rh2 coated cylinders, respectively, were summarized in Fig. 4.5 and Table 4.1.
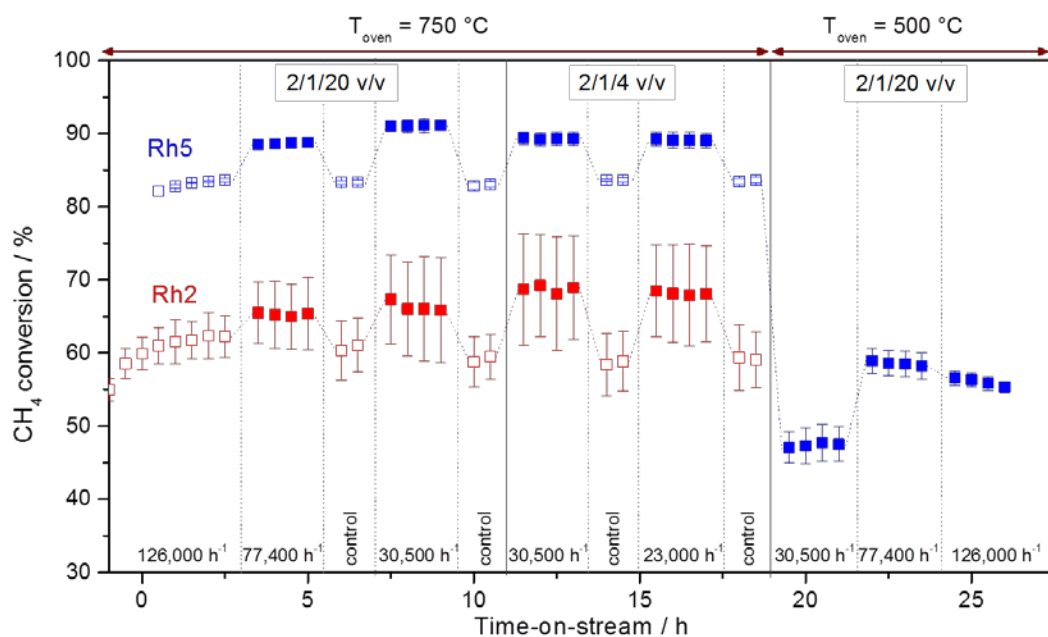
Figure 4.5. CH_4 conversion over Rh5 and Rh2 catalysts at several reaction conditions. The data correspond to the average of four and three catalytic tests over different samples for Rh5 and Rh2, respectively. A longer time was required to reach stable performances in the initial reaction condition for Rh2, the 0 in the x-scale only corresponded to Rh5 catalyst.

Table 4.1. Selectivity in H_2, CO, and H_2/CO ratio of Rh5 and Rh2 catalysts in CPO of CH_4 at different reaction conditions. Average values of four analyses in each reaction conditions were displayed. For Rh2 catalysts these values were collected on three different foams instead of four foams for Rh5

T_{oven} /^oC	$CH_4/O_2/N_2$ / v/v	GHSV / h^{-1}	Rh5			Rh2		
			Sel. H_2 / %	Sel. CO / %	H_2/CO	Sel. H_2 / %	Sel. CO / %	H_2/CO
750	2/1/20	126,000	89.0 ± 1.1	92.5 ± 0.6	1.91 ± 0.02	70.7 ± 6.4	81.1 ± 0.4	1.74 ± 0.01
		77,400	88.4 ± 0.9	91.6 ± 0.7	1.93 ± 0.02	70.4 ± 6.6	79.2 ± 2.5	1.78 ± 0.01
		30,500	90.6 ± 1.8	95.6 ± 0.8	1.90 ± 0.03	77.7 ± 7.9	80.6 ± 5.0	1.93 ± 0.00
	2/1/4	30,500	86.7 ± 1.1	92.0 ± 0.6	1.88 ± 0.03	73.0 ± 8.1	80.8 ± 4.5	1.81 ± 0.00
		23,000	86.4 ± 0.8	91.7 ± 0.5	1.88 ± 0.03	73.8 ± 8.5	79.3 ± 4.0	1.86 ± 0.00
500	2/1/20	30,500	60.2 ± 3.4	49.3 ± 5.4	2.47 ± 0.25	-	-	-
		77,400	67.1 ± 1.5	64.9 ± 3.5	2.08 ± 0.08	-	-	-
		126,000	67.6 ± 0.4	66.7 ± 1.4	2.00 ± 0.09	-	-	-

The catalysts obtained from Rh5 HT-tailored coatings outperformed some previous structured catalysts in terms of activity and stability [13] - also considering that these tests were performed at doubled GHSV values (same gas flow but using one instead of two foam cylinders) - and performances were close to those of coprecipitated powder catalysts [2]. At 750 °C, stable, high and reproducible conversion and selectivity values were reached after a short activation period in the initial reaction condition ($CH_4/O_2/N_2 = 2/1/20$ v/v, 126,000 h^{-1}), probably due to the reduction of hardly reducible Rh^{3+} species [13]. In diluted reaction conditions, conversion steadily increased up to 92% by decreasing GHSV due to a lower amount of CH_4 to be converted. The selectivity in H_2 was lower than the selectivity in CO (88 – 91% *vs* 92 – 96%), thus a syngas with H_2/CO molar ratio around 1.90 was produced, Table 4.1. Increasing the concentration of the feed ($CH_4/O_2/N_2 = 2/1/4$ v/v, 30,500 and 23,000 h^{-1}), stable CH_4 conversions close to 90% were still achieved, despite the higher partial pressure of the reactants and the higher temperatures that could deactivate the catalyst. The H_2/CO ratio slightly decreased since the reverse water gas shift reaction [36] may be favored at concentrated conditions due to higher temperatures. The stability of the catalysts was confirmed by control tests, in which an 83% constant conversion was obtained.

The enhanced activity of Rh5 structured catalysts was further demonstrated by feeding the 2/1/20 v/v gas mixture at 500 °C oven temperature; all the samples were active and CH_4 conversion values around 47, 58, and 56% were attained at 30,500, 77,400, and 126,000 h^{-1}, respectively. However, the standard deviation of conversion values was larger than that in tests at 750 °C and they slightly deactivate at 77,400, and 126,000 h^{-1} (0.7 and 1.3 %, respectively). The increase in the conversion moving from 30,500 to 77,400 h^{-1} may be related to the development of a higher heat amount inside the catalytic bed. At 126,000 h^{-1}, the effect of high GHSV, short contact time, became more important and lowered the performances, although it was not possible to measure the temperature profiles to support this statement. The contribution

of the water gas shift (WGS) reaction at low temperature was clearly observed in the test at 30,500 h^{-1}, the syngas contains a H_2/CO ratio around 2.4 (Selectivity in $H_2 = 60\%$; Selectivity in $CO = 50\%$). The differences between selectivity values were reduced as the GHSV increased (Selectivity in $H_2 = 67$ and 68%; Selectivity in $CO = 65$ and 67% at 77,400 and 126,000 h^{-1}, respectively), likely related to an increase in the temperature, producing a $H_2/CO = 2.0$ syngas.

The decrease in the metal loading in Rh2 catalysts largely decreased the performances and the reproducibility of the data; at 750 $^{\circ}$C oven temperature in all reaction conditions, CH_4 conversion values were about 20% less than Rh5 conversions with a larger standard deviation (change from 1.5 to 7.7% depending the reaction conditions) as seen in Fig. 4.5. Moreover, the catalyst activated more slowly in the initial tests at 126,000 h^{-1}. The largest differences between the different tested samples may be related to the heat generated inside the catalytic bed; at low catalytic performances, the contribution of the heat developed to sustain the reaction may be more remarkable and it may change from sample to sample. The selectivities in CO and H_2 were 12 – 18% lower than those of Rh5 sample, with H_2/CO ratios close to 2. However, it was worth to note that the performances were rather stable with time-on-stream. The differences in activity were more remarkable by setting the oven temperature at 500 ºC; indeed, decreasing the external heat the Rh2 catalyst was not active.

To investigate the stability of Rh5 catalysts, a 24 h time-on-stream test was performed after the above activity tests over two different samples. Three reaction cycles were run at 30,500 h^{-1}, including tests at 500 and 750 °C with diluted and concentrated gas mixtures, respectively. After every cycle, the reactor was shut-down by cooling to room temperature under N_2 atmosphere. The results are displayed in Fig. 4.6. The conversion was around 48% and 88% at 500 and 750 °C, respectively, during the first cycle. Only a slight deactivation of 2 and 1% at low and high oven temperatures, respectively, was observed at the end of the tests, suggesting a good stability with time-on-stream of the catalysts under the reaction conditions here studied.
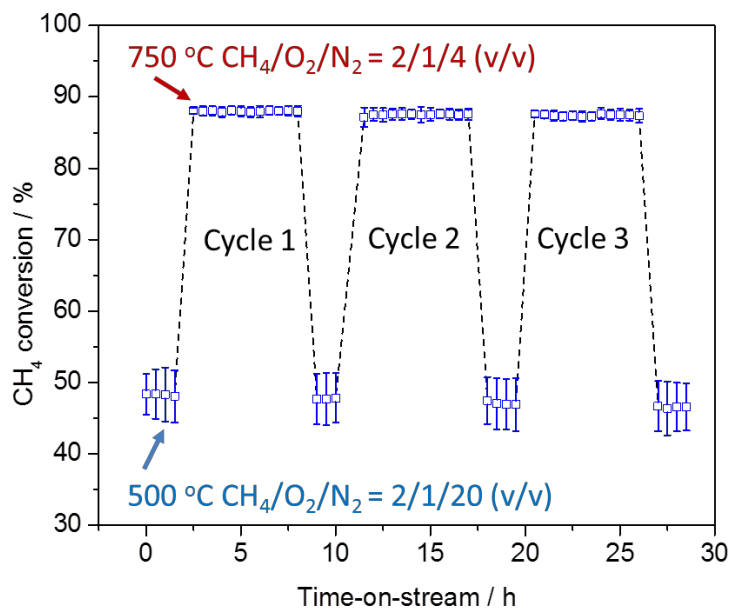
Figure 4.6. CH_4 conversion during stability tests on Rh5 samples at GHSV = 30,500 h^{-1}. The data correspond to the average of 2 catalytic tests over different samples.

4.3.4 Spent catalysts

The temperature and gas composition varied along the catalytic bed, therefore different deactivation processes, (sintering, detaching, and coking) could take place in catalysts depending on the position in the bed. To study these phenomena, Rh5 and Rh2 spent catalysts were characterized by FESEM, n-XRF/XRD tomography, HRTEM, and micro-Raman. The results commented for Rh5 samples correspond to catalysts after long-term tests, i.e. after ca. 50 h time-on-stream.

Although some partial detachment was found at the inlet of the catalytic bed, where the highest temperatures were reached, in general the morphology of the coating was rather preserved during catalytic tests, i.e. no particle sintering, and extended detachment occurred, as evidenced in Fig. 4.7a. Combined n-XRF/XRD tomography further confirmed the stability of the structured catalysts under the reaction conditions here reported. The distributions of periclase, spinel phases and Rh XRF signals were similar than those in fresh catalysts (Fig. 4.7f). Most importantly, the alloy was stable under CPO reaction conditions and no further

oxides segregated. From these results, it could be stated that despite the absence of the Al_2O_3 protective layer, catalyst coating preserved the foam from oxidation under partial oxidation tests.

Only in few regions of Rh5 sample, aggregates of Rh particles (15 – 30 nm) could be identified by FESEM, (Fig. 4.7b), although the presence of Rh all over the surface of Rh5 and Rh2 catalysts was confirmed by EDS. To get insight into the properties of Rh metal particles, some powder was scraped from the upper part of the spent foam cylinders, namely at the inlet of the catalytic bed, and investigated by HRTEM/STEM, Fig. 4.7c, d. Rh nanoparticles were found both on the external surface or embedded in ill- and well-defined nano-hexagonal shaped particles, due to the bulk characteristics of catalysts [37]. STEM-EDS analyses confirmed that they contained both Mg and Al. High magnification images confirmed that Rh was dispersed on both MgO and $MgAl_2O_4$ phases, Fig. 4.7e, in agreement with XRF/XRD results. A narrow Rh metal particle size distribution between 1 to 5 nm was obtained for both Rh2 and Rh5 catalysts (Fig. 4.7g, h), which slightly shifted toward smaller dimensions for the former; however, it was not possible to establish a relationship between particle size and crystalline phases as previously reported for HT-derived catalysts [2]. The small Rh^0 particle size, despite the high Rh loading, i.e. 5 a.r., was characteristic of HT-derived catalysts. These features may be responsible for the enhanced catalytic performances of Rh5 catalysts. The low activity of Rh2 catalyst suggested that a thicker loading was necessary to balance the lower number of active sites.
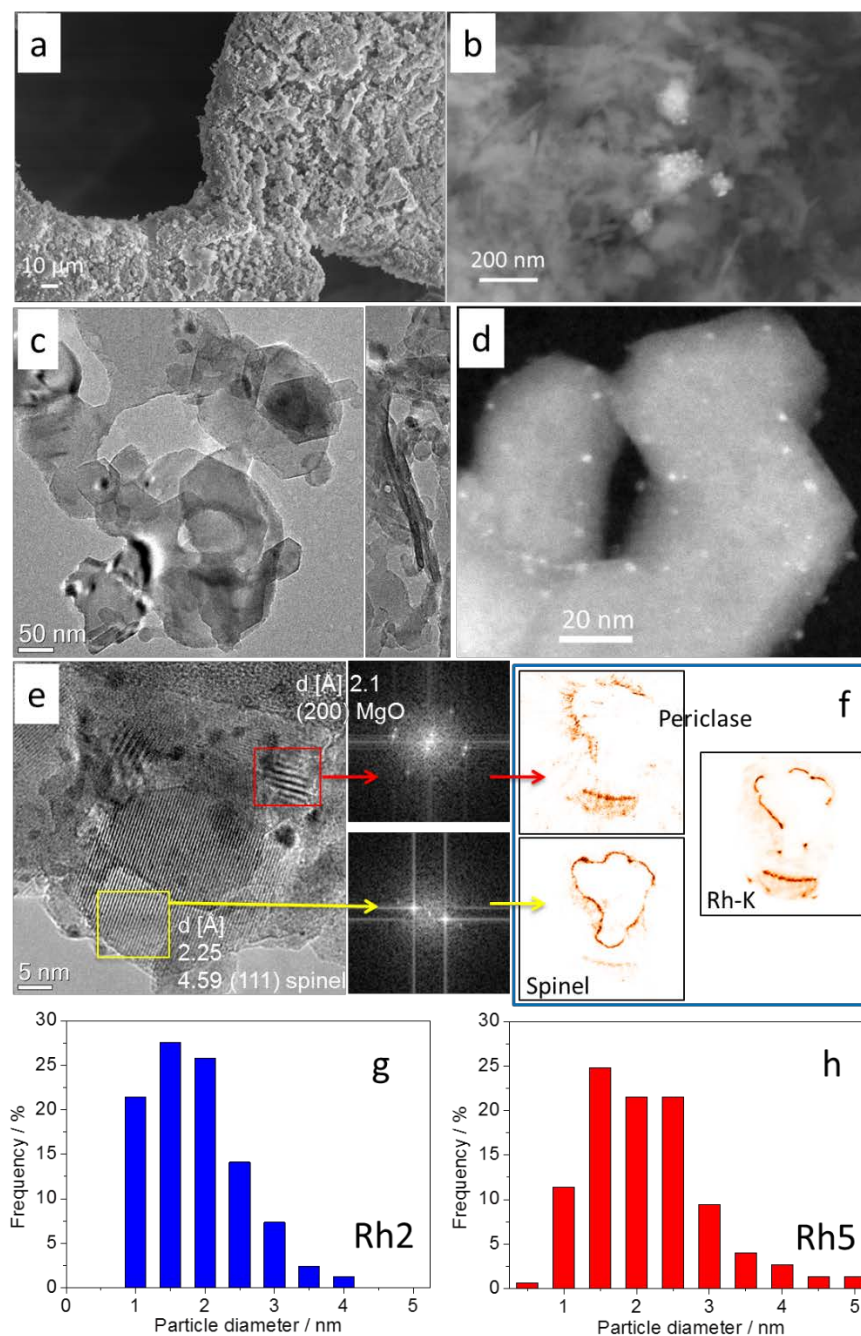
Figure 4.7. Characterization of spent catalysts: (a, b) FESEM images, (c, d, e) HRTEM and STEM-HAADF images; (e) FFT of the indicated regions of the TEM image; (f) nanoXRF/ XRD distributions; (g, h) Rh particle size distributions of Rh2 and Rh5, respectively.

The above commented techniques did not give any evidence about the formation of carbon deposits on the surface of the catalysts; therefore, to better investigate this feature micro-Raman analyses were performed along the length of the spent foam cylinders, Fig. 4.8. No carbon was present in the coating at the inlet of the catalytic bed, where oxidation reactions occurred, and

only in some few regions of the foam surface at the middle and outlet of the bed the characteristic D and G bands of carbon were registered at ca. 1340 and 1590 cm^{-1}, respectively. They were more intense at the middle of the bed, i.e. where CH_4 reforming took place; however, their detection in some regions and their low intensity suggested a small carbon formation over these catalysts after 50 h time-on-stream.
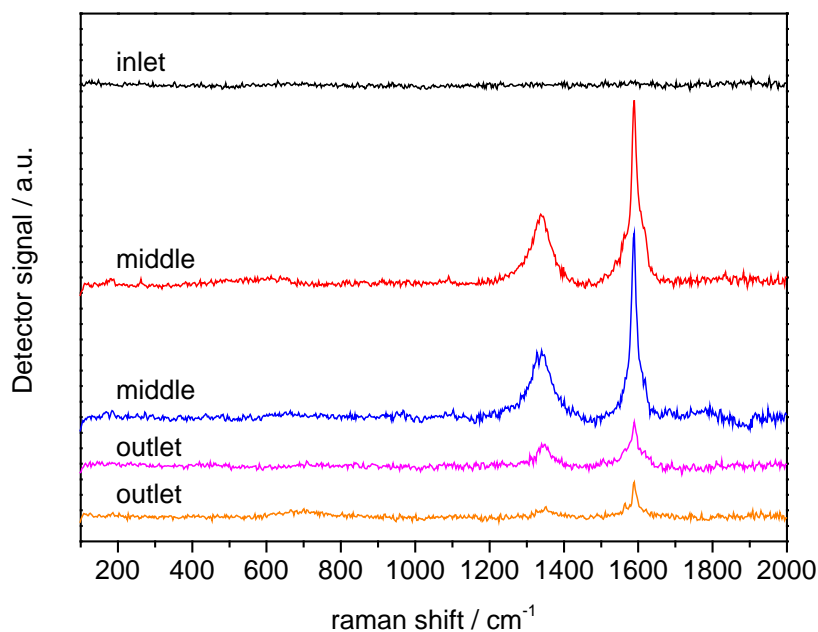
Figure 4.8. Raman spectra of spent Rh5 catalyst, regions of interest were placed at the inlet, middle and outlet of the catalytic bed.

4.4 Conclusions

The feasibility of the electrodeposition to *in situ* synthesize Rh/Mg/Al hydrotalcite-type compounds with controlled properties on the surface of FeCrAl foams of small pore size in an easy and fast way was demonstrated. The use of a two-compartment flow-cell probably due to separation of cathodic and anodic compartments and the replenishment of the electrolyte solution in the electrode-electrolyte interface, allowed to evenly deposit Rh/Mg/Al 5-20 μm coatings with a hydrotalcite structure and composition similar to the nominal one, avoiding the sequential precipitation of the solids previously reported. Although, some deviations were found in few regions.

Consequently, after calcination at 900 °C and reduction treatment, coatings were mainly made of catalysts with properties close to coprecipitated ones, i.e. MgO and $MgAl_2O_4$ with Rh nanoparticles well dispersed and good thermal stability, decreasing the detachment and crack formation. Moreover, the simultaneous thermal decomposition of the HT structure and the oxidation of the alloy led to the development of a $MgAl_2O_4$ film at the interface between the foam and the coating due to the chemical interaction between Mg^{2+} from the coating and Al^{3+} from the support, which increased the adherence to the support.

The enhanced properties of the coatings influenced the catalytic activities. Active and stable performances in the Catalytic Partial Oxidation to CH_4 were achieved whenever the Rh loading was 5% a.r. (i.e. Rh/Mg/Al = 5/70/25), a thicker coating should be necessary to achieve similar performances with the 2% a.r. catalyst to balance the number of active species.

The versatility of HT-type compounds as precursors of catalysts for H_2 and syngas production processes using both methane and biomass-derived feedstocks, and for many others, and the advantages of metallic foams *vs* honeycomb monoliths may open new applications of the electrodeposited materials once their properties are under control.

Chapter 4

4.5 References

1. F. Cavani, F. Trifirò, A. Vaccari, Catal. Today 11 (1991) 173–301.

2. F. Basile, P. Benito, G. Fornasari, A. Vaccari, Appl. Clay Sci. 48 (2010) 250–259.

3. G. Centi, S. Perathoner, Microporous Mesoporous Mater. 107 (2008) 3–15.

4. A. Montebelli, C.G. Visconti, G. Groppi, E. Tronconi, C. Cristiani, C. Ferreira, S. Kohlerd, Catal. Sci. Technol. 4 (2014) 2846–2870.

5. F. Basile, P. Benito, G. Fornasari, V. Rosetti, E. Scavetta, D. Tonelli, A. Vaccari, Appl. Catal. B: Environ. 91 (2009) 563–572.

6. R. Chai, Y. Li, Q. Zhang, S. Fan, Z. Zhang, P. Chen, G. Zhao, Y. Liu, Y. Lu, ChemCatChem 9 (2017) 268–272.

7. F. Basile, P. Benito, G. Fornasari, M. Monti, E. Scavetta, D. Tonelli, A. Vaccari, Catal. Today 157 (2010) 183–190.

8. A. Casanovas, N.J. Divins, A. Rejas, R. Bosch, J. Llorca, Int. J. Hydrog. Energy 42 (2017) 13681–13690.

9. F. Kovanda, K. Jirátová, Appl. Clay Sci. 53 (2011) 305–316.

10. I. Reyero, I. Velasco, O. Sanz, M. Montes, G. Arzamendi, L.M. Gandía, Catal. Today 216 (2013) 211–219.

11. Z. Lü, F. Zhang, X. Lei, L. Yang, S. Xu, X. Duan, Chem. Eng. Sci. 63 (2008) 4055–4062.

12. P. Benito, M. Monti, W. De Nolf, G. Nuyts, G. Janssen, G. Fornasari, E. Scavetta, F. Basile, K. Janssens, F. Ospitali, D. Tonelli, A. Vaccari, Catal. Today 246 (2015) 154–164.

13. P. Benito, G. Nuyts, M. Monti, W. De Nolf, G. Fornasari, K. Janssens, E. Scavetta, A. Vaccari, Appl. Catal. B Environ. 179 (2015) 321–332.

14. S. Yoon, J.-Y. Yun, J.-H. Lim, B. Yoo, J. Alloys Compd. 693 (2017) 964–969.

15. Y. Liu, N. Fu, G. Zhang, M. Xu, W. Lu, L. Zhou, H. Huang, Adv. Funct. Mater. 27 (2017) 1605307.

16. X. Zhu, C. Tang, H.F. Wang, B.Q. Li, Q. Zhang, C. Li, C. Yang, F. We, J. Mater. Chem. A 4 (2016) 7245–7250.

17. Z. Li, M. Shao, H. An, Z. Wang, S. Xu, M. Wei, D.G. Evans, X. Duan, Chem. Sci. 6 (2015) 6624–6631.

18. X. Lu, C. Zhao, Nature Commun. 6 (2015) 6616.

19. L. Jiang, Y. Sui, J. Qi, Y. Chang, Y. He, Q. Meng, F. Wei, Z. Sun, Y. Jin, Part. Part. Syst. Charact. 34 (2017) 1600239.

20. V. A. Ettel, Apparatus and foam electroplating process, WO 2007/121549.

21. A. Jung, M. Weinmann, H. Natter, Electroforming and electrodeposition on complex 3D geometries: Special Requirements and New Methods, in M. Aliofkhazraei, A.S.H. Makhlouf

(Eds.), Handbook of Nanoelectrochemistry: Electrochemical Synthesis Methods, Properties and Characterization Techniques, Springer, 2016, pp 941–970.

22. J. Zhang, E. J. Juárez-Pérez, I. Mora-Seró, B. Viana, T. Pauporté, J. Mater. Chem. A 3 (2015) 4909–4915.

23. C. Devivier, V. Tagliaferri, F. Trovalusci, N. Ucciardello, Mater. Des. 86 (2015) 272–278.

24. T. Loewenstein, A. Hastall, M. Mingebach, Y. Zimmermann, A. Neudeck, D. Schlettwein, Phys. Chem. Chem. Phys. 10 (2008) 1844–1847.

25. A.S. Batchellor, S.W. Boettcher, ACS Catal. 5 (2015) 6680−6689.

26. M. Nobial, O. Devos, B. Tribollet, J. Cryst. Growth 327 (2011) 173–181.

27. R. Abdallah, F. Geneste, T. Labasque, H. Djelal, F. Fourcade, A. Amrane, S. Taha, D. Floner, J. Electroanal. Chem. 727 (2014) 148–153.

28. F. Basile, P. Benito, S. Bugani, W. De Nolf, G. Fornasari, K. Janssens, L. Morselli, E. Scavetta, D. Tonelli, A. Vaccari, Adv. Funct. Mater. 20 (2010) 4117–4126.

29. P. Benito, W. De Nolf, G. Nuyts, M. Monti, G. Fornasari, F. Basile, K. Janssens, F. Ospitali, E. Scavetta, D. Tonelli, A. Vaccari, ACS Catal. 4 (2014) 3779–3790.

30. L.E. Basini, A. Guarinoni, Ind. Eng. Chem. Res. 52 (2013) 17023−17037.

31. B. Enger, R. Lødeng, A. Holmen, Appl. Catal. A 346 (2008) 1−27.

32. M. Cotte, E. Pouyet, M. Salomé, C. Rivard, W. De Nolf, H. Castillo-Michel, T. Fabris, L. Monico, K. Janssens, T. Wang, P. Sciau, L. Verger, L. Cormier, O. Dargaud, E. Brun, D. Bugnazet, B. Fayard, B. Hesse, A.E. Pradas del Real, G. Veronesi, J. Langlois, N. Balcar, Y. Vandenberghe, V. A. Solé, J. Kieffer, R. Barrett, C. Cohen, C. Cornu, R. Baker, E. Gagliardini, E. Papillon. J. Susini, J. Anal. At. Spectrom. 32 (2017) 477−493.

33. W. De Nolf, F. Vanmeert, K. Janssens, J. Appl. Crystallogr. 47 (2014) 1107–1117.

34. A. Ballarini, P. Benito, G. Fornasari, O. Scelza, A. Vaccari, Int. J. Hydrog. Energy 38 (2013) 15128–15139.

35. J.C.A.A. Roelofs, J.A. van Bokhoven, A.J. van Dillen, J. W. Geus, K.P. de Jong, Chem. Eur. J. 8 (2002) 5571-5579.

36. M. Maestri, D. Livio, A. Beretta, G. Groppi, Ind. Eng. Chem. Res. 53 (2014) 10914−10928.

37. P. Benito, V. Dal Santo, V. De Grandi, M. Marelli, G. Fornasari, R. Psaro, A. Vaccari, Appl. Catal. B Environ. 179 (2015) 150–159.

Chapter 5. Rh-based structured catalyst on NiCrAl foam and the reactivity in the catalytic partial oxidation of CH$_4$

Chapter 5

5.1 Introduction

In chapter 4, FeCrAl open-cell foams were proposed as supports in the development of structured catalyst for high-temperature processes, i.e. the catalytic partial oxidation of methane [1-5], in which the foams were exploited to decrease the pressure drop, avoid the formation of hot spots, and enhance the flexibility of the reactor design [6-9]. In such harsh reaction conditions, the substrates must show superior high-temperature properties and corrosive resistance. In addition, for the development of structured catalyst, the interaction between the support and the deposited materials plays a vital role on the adhesion of the coating and hence on the stability of the catalyst [1]. FeCrAl alloy shows a good oxidation resistance because it can enable the alloy to form an alumina scale and ensure a stable oxidation resistance at high temperatures [10]. Cr plays an important role since it can prevent the internal oxidation before the establishment of alumina layer [11]. However, at high temperatures, in some cases Cr could migrate into the catalytic materials influencing on the properties of the catalyst [12, 13].

NiCrAl is known as a super-alloy system due to the superior strength of coherent γ' Ni_3Al and solid solution of Cr in γ-Ni matrix. Under oxidation conditions, both Cr and Al improved corrosion and oxidation resistance by forming a native, and adherent oxide film while Ni slows down the diffusion speed of Al to the surface to create the oxide scale before Cr is oxidized, which could poison the catalytic layer of the structured catalyst [11]. Therefore, NiCrAl foam is suitable as support for high temperature processes operating under oxidizing atmosphere, e.g. steam reforming of biogas or auto thermal reforming of dodecane [14, 15]. In addition, NiCrAl foams are commercial products, making them available for possible uses in industrial catalysts [16, 17].

The electrodeposition route could be used to coat NiCrAl foams as previously reported for FeCrAl ones in Chapter 4. However, it should be considered that this coating method is strongly

dependent on the characteristics of the support such as electrical conductivity, geometrical surface, and chemical composition, which determine the properties of the coating. For instance, a surface layer of metal oxides may cause an increase of electrical resistance, and hence decrease in the current density. Moreover, Ni is known to catalyze the water reduction with the evolution of H_2, which could lead to the formation of cracks and detachment of the coating.

This chapter aims to investigate the coating of Rh/Mg/Al HTs on NiCrAl foams by electrodeposition, paying attention to the effect of the pretreatment on the properties of the coating and on the metal coating interaction. The catalysts were tested in the catalytic partial oxidation of CH_4 at high temperature to study the reactivity as well as oxidation resistance of the foam under such harsh reaction conditions.

5.2 Experimental

5.2.1 Catalyst preparation

The catalysts were prepared by the same set-up (double compartment electrochemical flow cell) and electrolytic solution Rh/Mg/Al = 5/70/25 a.r. as described in chapter 4, except the differences in the working electrode (NiCrAl foam instead of FeCrAl foam) and the treatment of the foam by electrochemical route before doing the synthesis.

From a commercial panel (3 mm thickness) of NiCrAl foam (60 ppi) supplied by Alantum, disks (10 mm of diameter) were cut, then washed in acetone and distilled water, and dried at 40 °C for 24 h before using. The alloy is composed of approximate 20 wt.% Cr, 8 wt.% Al, and the rest of Ni, according to the supplier Alantum [13, 17].

Prior to the coating, the foams were pre-treated by: i) an electrochemical process consisting on 10 scans of LSV (from 0 to -1.4 V, scan rate 50 mV s^{-1}) in KNO$_3$ 0.3 M using a single compartment three-electrode electrochemical cell [18]; ii) chemical etching with HCl 1 M for 5 min. After treatment, the foams were washed thoroughly with distilled water before being

transferred to the double compartment electrochemical flow cell where the coating process was carried out.

The electrolyte was a $Rh(NO_3)_3$, $Mg(NO_3)_2$, and $Al(NO_3)_3$ solution with total concentration 0.06 M and Rh/Mg/Al = 5/70/25 a.r. The electrodepositions were performed at -1.2 V for 2000 s and flow rate of electrolyte 2 mL min^{-1}. These parameters chosen from the best synthesis conditions for the deposition of Rh/Mg/Al HTs on FeCrAl foams described elsewhere [1-3] and in chapter 4. A two-branch electrical contact made of Pt wire (0.5 mm diameter) was inserted symmetrically into the foam (about 1.5 mm each side along its radius) to make the working electrode, detailed information can be found in chapter 4. After coating, the foams were rinsed in distilled water followed by drying in an oven at 40 ^oC for 24 h. Eventually, the coated foams were calcined at 900 ^oC in static air for 12 h and named as Rh5-NiCrAl and E-Rh5-NiCrAl catalyst for the samples without pretreatment or treatment by the electrochemical route, respectively.

5.2.2 Characterization of the coatings

The catalysts were characterized at different stages including after electrodeposition, calcination, and catalytic test by several techniques: XRD, SEM/EDS, HRTEM. All instruments and methods can be referred in chapter 4.

In addition, the surface area of the catalyst was determined by N_2 adsorption/desorption at -196 °C. The measurements were carried out using a Micromeritics ASAP 2020 instrument. Samples were degassed under vacuum, heated up to 150 °C and maintained for 30 min before performing the measurement. The specific surface area (S_{BET}) was calculated using the Brunauer-Emmett-Teller (BET) multiple-point method in the relative pressure range p/p^0 from 0.05 to 0.3.

Chapter 5

5.2.3 Catalytic test

CPO tests were conducted at atmospheric pressure using a quartz reactor (i.d. 10.0 mm) with one, two or four-foam cylinder to study effect of GHSV as well as to compare with the catalyst prepared on FeCrAl foam in chapter 4. The foam fitted well with the wall of the reactor to minimize any by-pass flow. To measure temperature profile inside the catalytic bed, an axial through channel of 2 mm diameter was created in the centerline of the catalytic bed. A tightly fitted thermowell made of quartz was inserted in the channel with a sliding thermocouple inside allowing to measure the temperature along the length of the foam bed during the tests. Before carrying out the tests, the catalyst was reduced in-situ with 7.0 L h^{-1} H_2/N_2 (1/1) gas mixture at 750 ^oC for 2 h.

The activity of the catalysts was evaluated by modifying the reaction conditions, i.e. setting up the oven at two temperature values (T_{oven} = 750 and 500 ^oC), modifying the Gas Hourly Space Velocity (GHSV) from 126,000 to 23,000 h^{-1} (corresponding to the test of four-foam catalyst, and double for the one used two foams) and feeding different concentrations of reagents ($CH_4/O_2/N_2$ = 2/1/20 and 2/1/4 v/v). Reaction conditions either feeding diluted gas mixtures ($CH_4/O_2/N_2$ = 2/1/20 v/v) or at a low oven temperature reduced the amount of heat developed by the exothermic reactions, making it possible to highlight the differences among catalysts. On the other hand, tests with a concentrated gas mixture ($CH_4/O_2/N_2$ = 2/1/4 v/v) and high oven temperature (750 °C) were used to study the stability of the catalysts against deactivation by sintering, coking and oxidation. Control tests were carried out after each reaction condition by feeding the initial one ($CH_4/O_2/N_2$ = 2/1/20 v/v, 126,000 h^{-1}) to check deactivation/activation processes. The instrument and method for analyses of gas composition were the same as described in chapter 4.

5.3 Results and discussion

5.3.1 Characterization of the HT precursors and the obtained catalysts

The composition of the bare NiCrAl foam identified by EDS analyses showed average values of approximate 70 wt.% Ni, 21 wt.% Cr, and 9 wt.% Al, which were close to the values declared by the supplier. The replacement of Fe by Ni in the NiCrAl foam improved its electrical conductivity as the electrical resistivity of Fe (96.1 nΩ m) was slightly higher than that of Ni (69.3 nΩ m) [19]. It was expected that the higher electrical conductivity would have been an advantage to perform the electrosynthesis of HT compounds. Unfortunately, when NiCrAl foams were electrodeposited following the same procedure than with FeCrAl foams, the foams were not well coated, and only a thin and inhomogeneous coating deposited, probably due to the presence of an oxide layer on its surface (Fig. 5.1), and it would appear that this layer caused a negative effect during the electrodeposition.
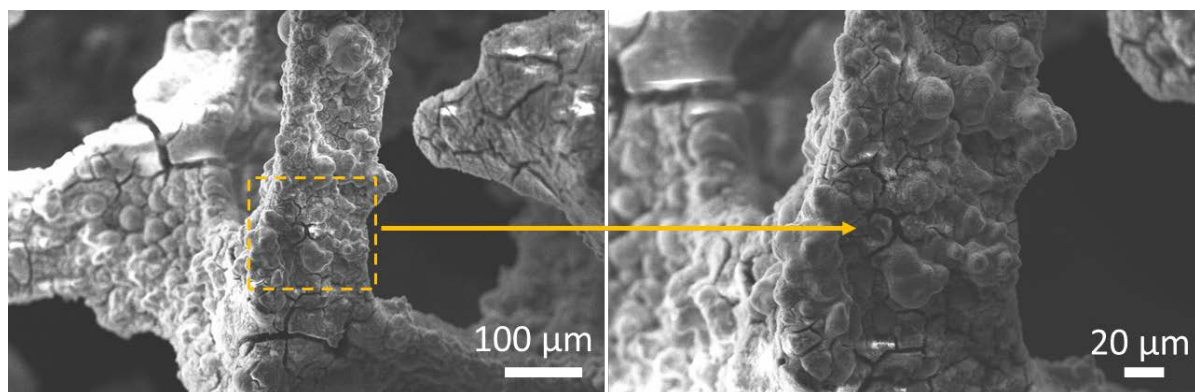
Figure 5.1. SEM images of Rh5-NiCrAl catalyst without pretreatment.

To overcome this issue, the foam was pretreated by an electrochemical procedure consisting on 10 LSV cathodic scans between 0 and -1.4 V in KNO_3 0.3 M solution, aimed to reduce the oxide layer. The currents recorded during this pretreatment (Fig. 5.2a) revealed that the onset of the LSV curve on NiCrAl was shifted to less cathodic potentials after the first scan, indicating that the surface of the foam might be activated, and 10 scans seemed to be sufficient to clean the surface, since only minor changes in the shape of the curve occurred after the 10th

scan. It was noted that probably nickel oxide on NiCrAl was easier to be reduced than surface iron oxide on FeCrAl since the onset of the LSV on NiCrAl was at less cathodic potential than that on FeCrAl foam (Fig. 5.2b). However, nickel oxide may cause a more significant increase of electrical resistance than that of iron oxides, resulting in a low current density exchanged during the electrosynthesis, and hence generating insufficient pH for the precipitation of HT compounds. In fact, Sun et al. found that FeO provided significantly larger electrical conductivity than NiO in ceramic slag containing higher 12 wt.% of each oxide [20]. In other words, nickel oxide layer in NiCrAl foam was more detrimental than the iron oxide layer in case of FeCrAl foam for the electrodeposition. After the electrochemical pretreatment, the whole foam surface was covered by the HT materials with a solid loading of ca. 4.2 wt.%.
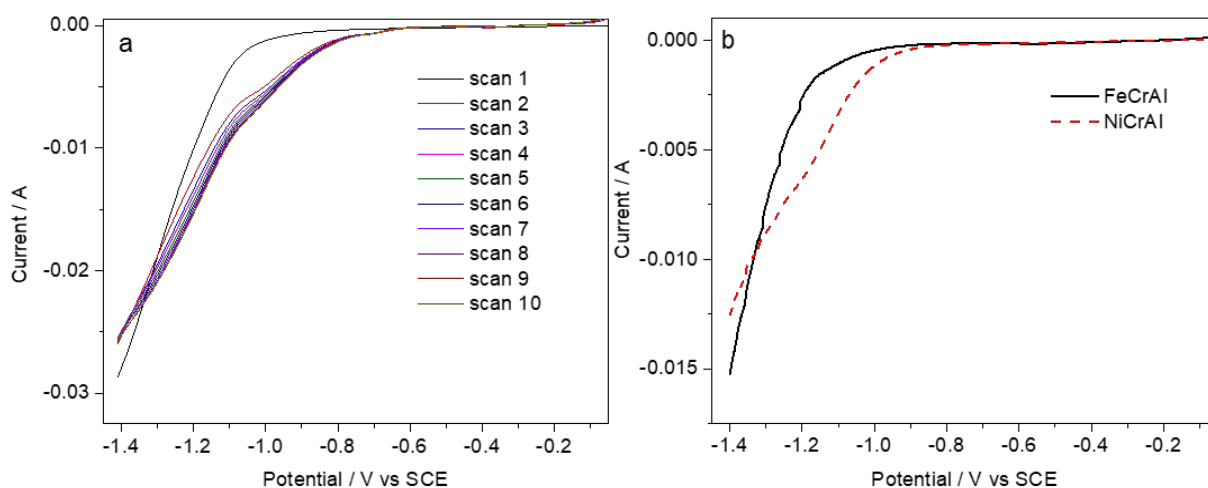
Figure 5.2. LSV curves recorded from 0 to -1.4 V in KNO_3 0.3 M: a) 10 scans on NiCrAl foam (scan rate 50 mV s^{-1}) and b) comparison of FeCrAl (80 ppi) and NiCrAl (60 ppi) foam (scan rate 0.5 mV s^{-1}).

A slightly thicker coating with similar properties was observed in the case of the HCl treatment. Despite this pretreatment provided a higher loading, the composition of the surface of the alloy was modified since a massive dissolution occurred in such strong acidic media (the HCl solution changed color from colorless to light green), making it an unrecommended choice.

From these results, it could be concluded that the pretreatment step was mandatory to coat NiCrAl foams unlike the case of FeCrAl foams under the same synthesis conditions, and that

the electrochemical one was more suitable to remove the oxide scale without modifying the foam composition.

The best sample obtained after the electrochemical pretreatment was further characterized by SEM/EDS and the results were displayed in Fig. 5.3. In some locations having cracks, the thickness of the layer was estimated to be ca. 15 µm. Two layers of coating with different morphologies were distinguished: platelet-like and spherical agglomerates of nanoparticles in the thin inner and thick outer layers, respectively, which were representative of electrodeposited materials like the ones on FeCrAlloy foams. The EDS spectra of the two mentioned layers were displayed on the top-right of Fig. 5.3. It was noted that even in very thin coatings, Rh was present (Fig. 5.3s3) and well-defined compositions were identified in spectrum of the thick layer (Fig 5.3s2). To obtain more precise EDS results, an average Rh/Mg/Al a.r. ratio was estimated from the data obtained in three foams, and the obtained result was quite close to the nominal one of the electrolyte (the inset table of Fig. 5.3).

Element	Rh	Mg	Al
Atomic ratio (%)	4.2 ± 1.7	64.2 ± 2.3	31.7 ± 2.6
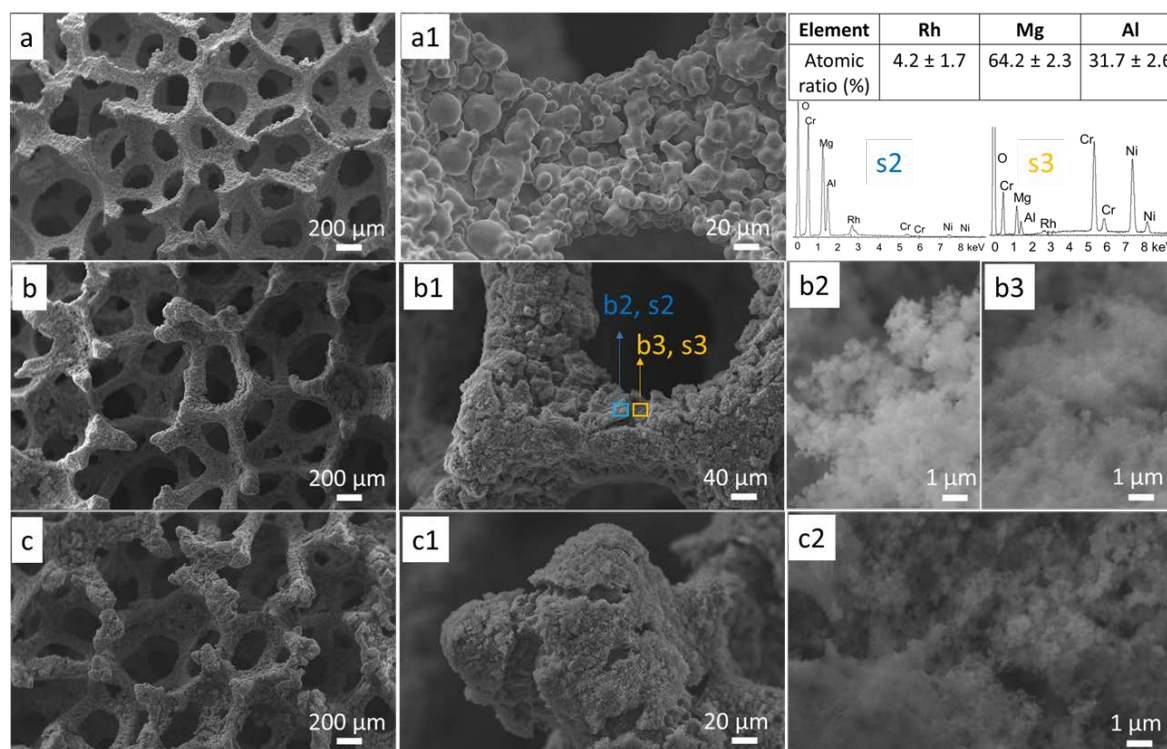
Figure 5.3. SEM/EDS characterization of Rh5 catalyst on NiCrAl foam: Bare foam (a and a1); electrodeposited (b, b1, b2, and b3); and calcined (c, c1, and c2); composition of electrodeposited sample (inset table); and EDS spectrum representing for thick and thin layers (s2 and s3).

It is, therefore, possible to conclude that the electrodeposition of Rh/Mg/Al HTs on NiCrAl foams was controlled like the previous deposition on FeCrAl foams (chapter 4), but with a mandatory pretreatment step. It was noted that despite a slightly lower solid loading on NiCrAl than on FeCrAl (4.2 vs 4.6 wt.%), the amount of the solid electrodeposited was similar for both cases. However, there may have been a slight difference in the quality of the coating in terms of thickness and cracks, since a slightly thinner layer with more cracks was observed in the case of the electrodeposition on NiCrAl foams. The former may be related to a bumpier surface of NiCrAl than FeCrAl foam due to the foam production method, considering that the distribution of similar amount of electrodeposited solid on a larger surface area may generate a thinner layer material. However, the smaller pore size of FeCrAl may balance the bumpy surface of NiCrAl. The presence of more cracks in the NiCrAl catalysts may be associated with the formation of hydrogen bubbles due to enhancement of water hydrolysis by Ni in NiCrAl as indicated by a fluctuation in the current transition curves during the electrosynthesis (Fig. 5.4).
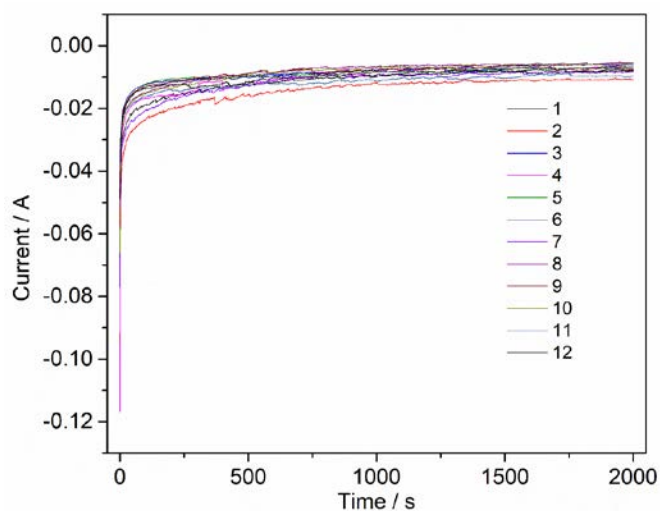
Figure 5.4. Current transient curves recorded at -1.2 V for 2000 s during the electrodeposition on 12 samples of NiCrAl foams in 0.06 M nitrate solution containing Rh/Mg/Al = 5/70/25 (a.r.).

XRD analyses of the electrodeposited and calcined samples were performed to identify the crystalline phases obtained through electrodeposition and after calcination (Fig. 5.5). The characteristic reflections of HT compounds intercalated with CO_3^{2-} were identified in the

patterns (Fig. 5.4a), like results obtained with Rh/Mg/Al HTs deposited on FeCrAl foam as reported in chapter 4. Some unidentified reflections could be related to the support.
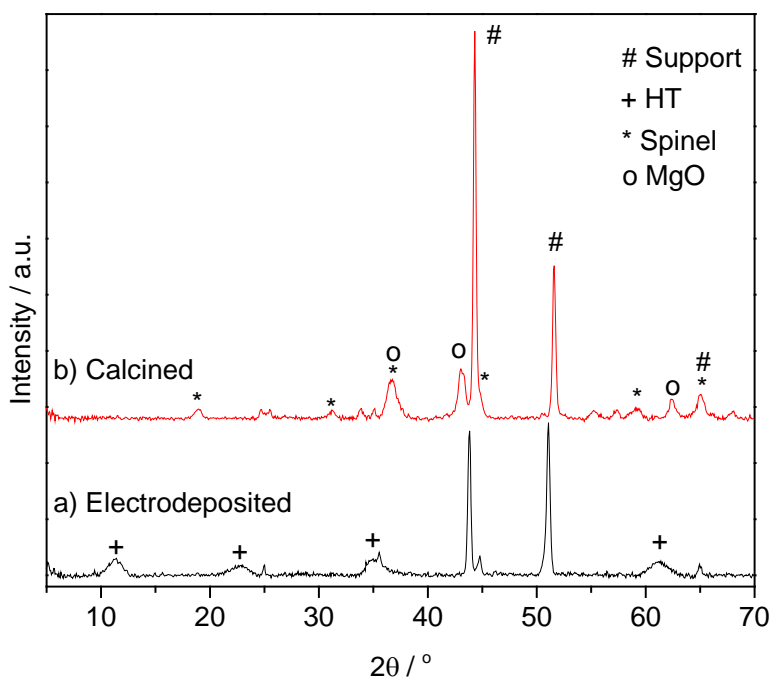
Figure 5.5. XRD patterns of E-Rh5-NiCrAl catalyst: a) electrodeposited and b) calcined sample.

The catalyst precursors were calcined at 900 °C for 12 h to obtain the final structure of the catalyst (Fig. 5.3c-c2). Thermal treatment did not significantly change the morphology and size of the catalyst particles despite of the development of a small number of cracks. Such high temperature treatment led to the formation of the spinel and MgO phases characteristics of HT-derived catalysts, as identified in XRD patterns (Fig. 5.4b), in which Rh^{3+} species were distributed and stabilized. In addition, some unidentified reflections may be related to not only the support but also some unknown oxides developed during the calcination.

The N_2 adsorption-desorption isotherm recorded on the structured catalyst was displayed in Fig. 5.6. It was a type IIb, characteristic of non-porous or macroporous materials with interparticle pores due to the aggregation of platelet particles [21]. The surface area calculated by the BET method was ca. 1.8 m^2 g^{-1} for whole foam catalyst or 41.7 m^2 g^{-1} referred for the mass of coated material.
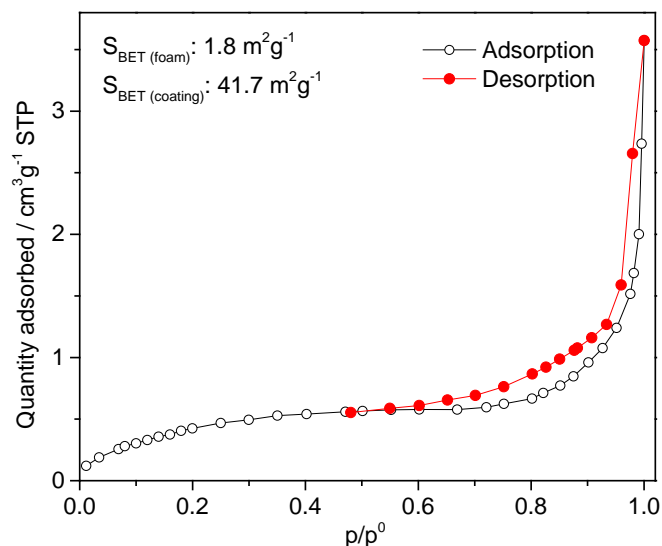
Figure 5.6. N_2 adsorption-desorption isotherm at -196 °C of E-Rh5-NiCrAl structured catalyst.

In previous study, it was found that during thermal treatment at 900 °C, not only the HT-like materials were transformed but also an interaction between them and Al from the alloy led to form a thin spinel layer on the foam surface and hence increase the adhesion of the coating [1]. A similar phenomenon may take place in this case due to a similar composition of the coating material and the presence of Al in the alloy. Moreover, Ni existing in the alloy may possibly react with Al from the coating which could form another type of spinel besides the one created by solid state reaction between Mg from the coating and Al from the alloy as reported in Chapter 4.

5.3.2 Catalytic tests

The catalytic performances of E-Rh5-NiCrAl structured catalysts in the CPO of CH_4 to syngas were tested with a four- or two-foam catalytic bed at 750 °C oven temperature, in both diluted and concentrated mixtures of the feedstock ($CH_4/O_2/N_2 = 2/1/20$ and $2/1/4$ v/v) and GHSV values ranging from 126,000 – 23,000 h^{-1} for four foams (and double for two foams). The results of CH_4 conversion, H_2 and CO selectivities as well as H_2/CO ratio were summarized in Fig. 5.7 and Table 5.1.

Table 5.1. Selectivities in H_2, CO, and H_2/CO ratio of E-Rh5-NiCrAl catalyst in CPO of CH_4 at different reaction conditions. Average values of four analyses in each reaction conditions were displayed

T_{oven} /^{o}C	$CH_4/O_2/N_2$ / v/v	GHSV / h^{-1}	E-Rh5-NiCrAl		
			Sel. H_2 / %	Sel. CO / %	H_2/CO
750	2/1/20	126,000	79.4 ± 1.9	89.3 ± 0.5	1.78 ± 0.04
		77,400	81.0 ± 2.1	91.1 ± 0.3	1.78 ± 0.04
		30,500	84.8 ± 1.8	96.7 ± 0.3	1.75 ± 0.03
	2/1/4	30,500	79.1 ± 2.7	91.1 ± 1.9	1.74 ± 0.02
		23,000	78.1 ± 2.8	89.1 ± 2.7	1.75 ± 0.01
500	2/1/20	30,500	47.6 ± 1.2	39.4 ± 0.9	2.42 ± 0.03
		77,400	51.7 ± 0.7	53.8 ± 0.1	1.92 ± 0.02
		126,000	48.3 ± 0.4	52.3 ± 0.3	1.85 ± 0.01

The behavior of the catalytic coatings on NiCrAl foams in a four-foam bed configuration was very similar to that on FeCrAl foams. At 750 ^{o}C, a short activation period occurred in the initial condition ($CH_4/O_2/N_2$ = 2/1/20 v/v, 126,000 h^{-1}), before reaching a CH_4 conversion ca. 78%. probably due to the reduction of hardly reducible Rh^{3+} species [1, 3]. In diluted concentration of the feedstock, the conversion increased steadily with a decrease of GHSV and achieved a maximum conversion of 90.5% at 30,500 h^{-1} due to a lower amount of CH_4 to be converted. Selectivity of H_2 was in the range of 79.4 to 84.8%, it was lower than that of CO about 10 – 12%, resulting in a H_2/CO ratio around 1.8 (Table 5.1). Feeding with more concentrated feedstocks ($CH_4/O_2/N_2$ = 2/1/4 v/v, GHSV 30,500 and 23,000 h^{-1}) led to a steady decrease in CH_4 conversion, probably due to a higher partial pressure of the reactants. In addition, slight decreases in the selectivity of both H_2 and CO, and hence a lower H_2/CO ratio, were observed (Table 5.1) since the reverse water gas shift reaction may be favored at concentrated condition due to larger amount of heat produced during the reaction [22]. High temperature may cause the formation of hot spots inside the catalytic bed and could deactivate the catalyst [2, 3]. Remarkably, the slight deactivation of the catalysts observed in both

concentrated and diluted feedstocks (mainly with the tests at low GHSV), was partially reversible as the activities were steadily recovered with TOS under the control tests. This behavior was similar to the same type of catalysts reported in our previous study [3]. In the CPO the deactivation may be influenced by the sintering and oxidation of Rh particles, the partial detachment of the coating as well as other factors like low amount of active phase or appearance of poison agents from the foam during TOS, however the re-activation suggested either reduction of some oxidized Rh species or the gasification of some deposited carbon.

The E-Rh5-NiCrAl structured catalysts were active when feeding the 2/1/20 v/v gas mixture at 500 °C oven temperature; CH_4 conversion values around 42, 49, and 45% were attained at 30,500, 77,400, and 126,000 h^{-1}, respectively, and the selectivities in H_2, CO and syngas ratio were shown in Table 5.1. The behavior of the catalysts was similar to the one reported in chapter 4, although the CH_4 conversions were lower than those from 5-10%. However, in some cases, the catalysts only worked at the first reaction conditions, and then deactivated.
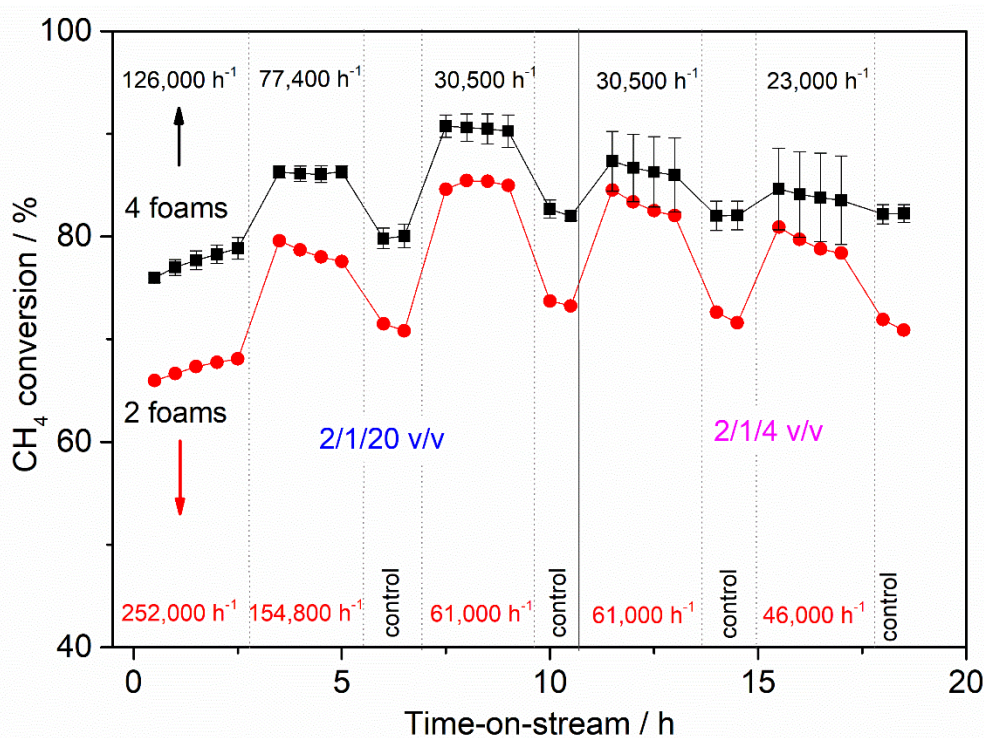
Figure 5.7. CH_4 conversion of E-Rh5-NiCrAl structured catalysts for CPO of CH_4 at $T_{oven} = 750$ °C. Noted that in the first reaction conditions, the results of the last five in total eight measurements were shown.

To further study the effect of the GHSV on catalytic performances, the tests were performed with a two-foam-bed configuration (i.e. doubling the GHSV). In overall, the trend of the performances with reaction conditions was like the tests with the four-foam bed but the activity decreased. After slightly increasing in CH_4 conversion from 66 to 68% during the first reaction condition, the catalysts were then gradually deactivated with a decrease of CH_4 conversion about 0.5-2.7% depending on the reaction condition, especially, at high concentration of feedstock. The selectivity of H_2 and CO as well as H_2/CO decreased slightly. The deactivation of the catalyst at concentrated feedstock may be due to oxidation of Rh species or carbon formation as the activity was recovered or even increased after each control tests. Observation of lower activities in comparison with four-foam catalyst may be related to shorter part of the two-foam bed where the "steam reforming" reaction taking place as explained in our previous work [2, 3]. It was noteworthy that the differences in activity were more remarkable by setting the oven temperature at 500 ℃; indeed, decreasing the external heat the two-foam catalyst was not active, probably due to a low amount of Rh active sites, which was similar to the case of comparison between Rh5 and Rh2 catalyst in chapter 4.

To verify this assumption, gas phase temperature profiles along the length of the catalytic bed were measured and displayed in Fig. 5.8. The catalytic performances - including activation with increasing time-on-stream (TOS), activity and stability of the catalysts - could be explained by both the coating properties and the reactions taking place in the catalytic bed. According to the mechanism reported in the literature [23, 24], CH_4 is firstly converted by exothermic total or partial oxidation reactions and then by the endothermic steam reforming. Considering that the former reactions are fast and controlled by O_2 mass-transfer, the whole differences in CH_4 conversion and selectivity may be mainly related to the ability of the catalyst to perform the consecutive steam reforming reaction [3]. In general, the temperature profile of the structured reactor during the CPO of CH_4 could be divided into two zones: i) upstream of

the foam where the thermal couple collected the heat by radiation from the hot walls of the reactor and front face of the foam, ii) inside the foam with an appearance of a hot spot, followed by a decrease to adiabatic outlet temperature [25, 26]. The hot spot resulted from the balance between the exothermic oxidation and endothermic steam reforming [26], and their formation may be influenced by reaction conditions as well as the properties of the structured supports (thermal conductivity, and pore density) [27].

In Fig. 5.8a, in diluted feedstock and high GHSV ($CH_4/O_2/N_2$ = 2/1/20 v/v, GHSV 126,000 h^{-1}), after 30 min of TOS (1st analysis), a hot spot with maximum temperature of 840 ^{o}C was reached at the distance 4 – 5 mm from the top of the bed, followed by a steep drop in temperature until the end of the catalytic bed. Such high temperature, in comparison to the 750 ^{o}C set in the oven, indicated that the exothermic reactions took place in zone I of the bed, where some hardly reducible Rh^{3+} species in the catalyst were not completely reduced to Rh^0 after the reduction step. With increasing TOS, the reaction conditions may help to reduce a part of these species and the endothermic steam reforming was favored, and hence the maximum temperature went down and from 6th analysis it was kept at about 820 ^{o}C and almost unchanged even at 15th analysis (a control test) after playing with different reaction conditions. This evidenced that the activity was steadilty recovered with TOS even if there was a slight deactivation during the tests at concentrated feedstock.

The effect of the GHSV on the temperature by feeding diluted and concentrated gas mixtures were shown in Fig. 5.8b and c, respectively. In a diluted feedstock, as expected, the higher the GHSV, the longer the oxidation zone; moreover, a higher maximum temperature was reached in the temperature profile, in agreement with the results obtained on Rh/α-Al_2O_3 80 ppi foam [28]. For instance, in Fig. 5.8b, the lengths of the catalytic bed required to reach the maximum temperature for GHSV 126,000, 77,400, and 30,500 h^{-1} were 4 mm (T_{max} = 823 ^{o}C), 3 mm (T_{max} = 807 ^{o}C), and 2 mm (T_{max} = 764 ^{o}C), respectively. A lower flow rate provided

a lesser amount of methane to be converted and a shortening of the exothermic zone. Hence, a larger amount of the active sites would be utilized to convert CH_4 by steam reforming in the second zone [1-3]. This agreed with an increase in CH_4 conversion as mentioned before in Fig. 5.7.
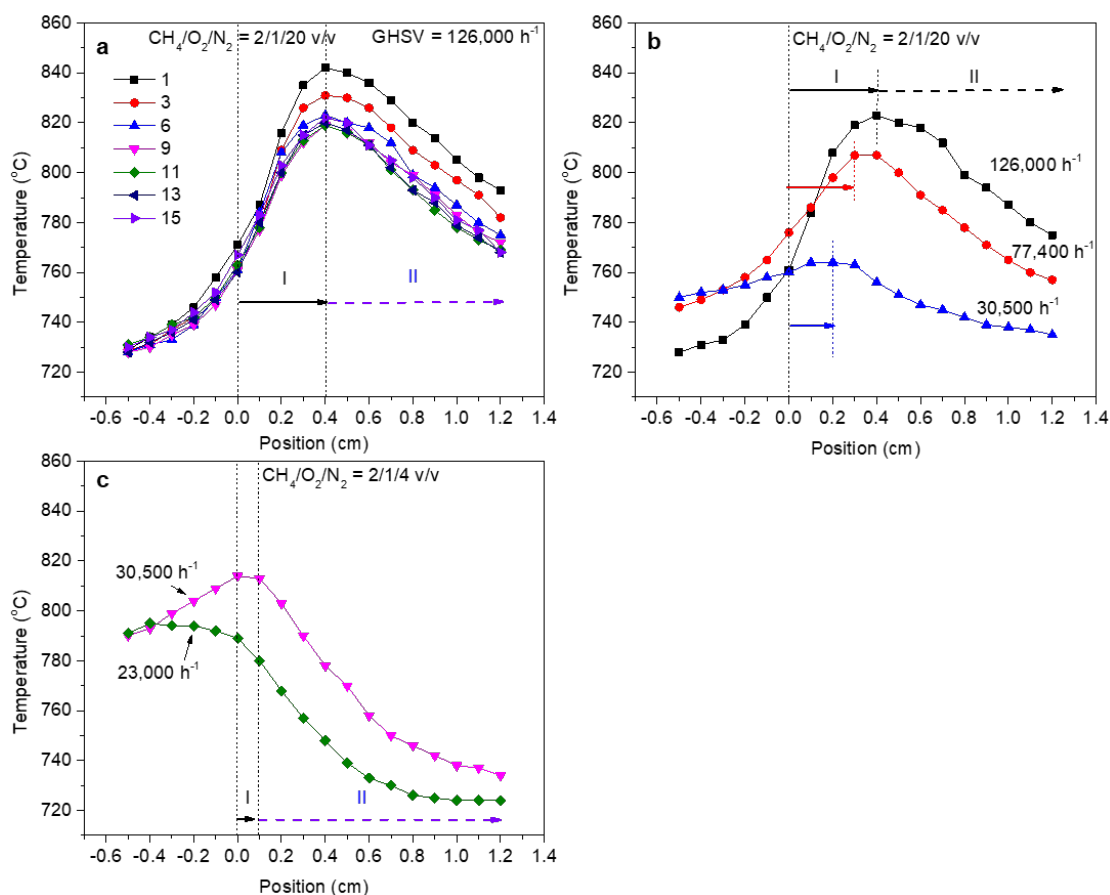
Figure 5.8. Temperature profiles measured during reactivity tests of four-foam bed of E-Rh5-NiCrAl structured catalyst for CPO of CH_4: a) measured during the first reaction conditions (1, 3, 6th), and control tests after each reaction conditions (9, 11, 13, 15th) to check if the catalyst was deactivated, b) recorded at 3rd analysis of each reaction condition in diluted gas, c) the same as b but in concentrated gas.

By feeding a more concentrated gas mixture, the trend of temperature profile changed significantly. While the temperature profiles for diluted conditions showed a rather flat, linear drop after the T_{max}, the temperature profiles in concentrated conditions went down steeply toward the end of the second zone and then exhibited a flat decrease. As shown in Fig 5.8c, while the initial oxidation zone required only 1 mm to reach the maximum temperature for

concentrated feedstock (pink curve Fig. 5.8c) instead of 2 mm in case of diluted reactants at the same GHSV =30,500 h^{-1} (Fig. 5.8b blue curve). At lower GHSV = 23,000 h^{-1}, the initial zone seemed to be at the entrance of the catalytic bed. T_{max} was measured at around 814 ^{o}C and 795 ^{o}C at 30,000 and 23,000 h^{-1}, respectively. A higher T_{max} temperature in the former might cause a sintering or reversible oxidation of Rh particles and these explained why the conversions decreased while lowered GHSV values.
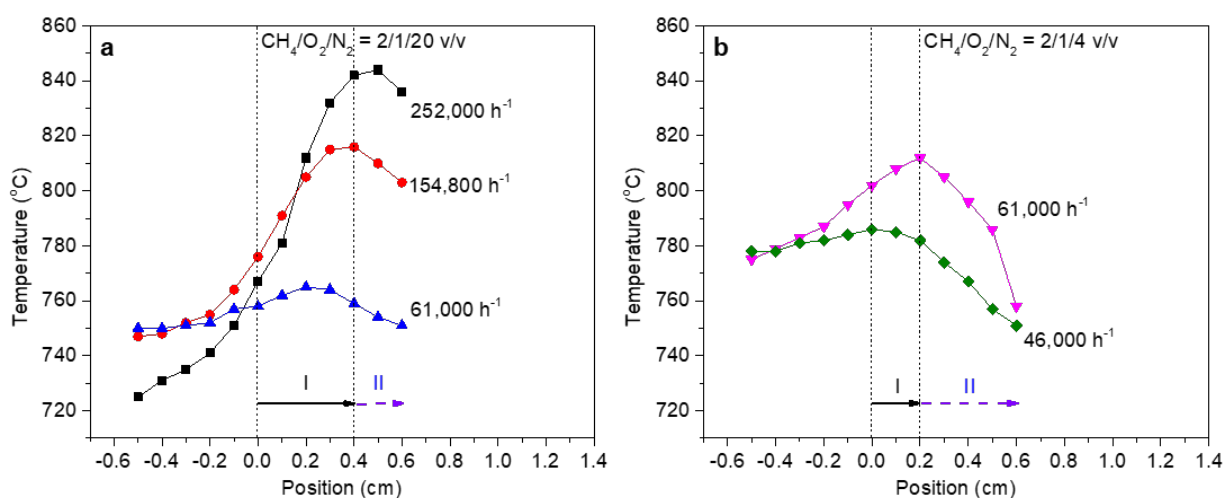
Figure 5.9. Temperature profiles measured during reactivity test of two-foam bed of E-Rh5-NiCrAl structured catalyst for CPO of CH$_4$. a) recorded at 3rd analysis of each reaction condition in diluted gas, b) in concentrated gas.

Doubling GHSV by decreasing of half the length of the catalytic bed (testing with only two foams instead of four foams), the shapes of the temperature profiles were close those of four-foam tests as long as the catalyst was present (Figure 5.9a, b). In diluted feedstocks, the lengths of oxidation zone were similar for both 2 and 4 foams, despite some differences were found in the T_{max} at high GHSV, e.g. 844 ^{o}C (black curve Fig. 5.9a) *vs* 823 ^{o}C (black curve, Fig. 5.8b). Meanwhile, in the reforming zone, the outlet temperatures were always higher than in tests with a 4-foam bed, and the temperature gaps were wider at a higher GHSV. In the case of the 2-foam bed, the same length for oxidation zone but shorter length for reforming explained the lower CH$_4$ conversions (Fig. 5.8). In contrast, during the tests in concentrated gas, the lengths of the oxidation zones were gradually longer than respect tests in the cases of 4-foam bed, and

T_{max} were slightly lower, e.g. 786 °C (green curve Fig. 5.9a) *vs* 795 °C (green curve, Fig. 5.8b). But similar to the tests in diluted gas, the outlet temperatures in these cases were about 25 °C higher than those under the same reaction condition of the four-foam tests. Slightly longer lengths of the oxidation zones in the tests of 2-foam bed compared to those of 4-foam bed meant the heat consumed by steam reforming in the former was lesser than those in the latter. This may represent for both a lower conversion and slight deactivation of the catalyst in the concentrated gas (Fig. 5.8).

5.3.3 Spent catalysts

The properties of the catalysts after testing at different reaction conditions were characterized by SEM/EDS, HRTEM and micro-Raman. The first foam in the catalytic bed, where the oxidation processes took place and high temperatures were reached, was selected to have information about the stability of the coating as well as the sintering of Rh particles (SEM/EDS, HRTEM, and micro-Raman), while the last foam of the bed was used to investigate the coke formation (SEM/EDS and micro-Raman).

The coating on the first foam of the four-foam bed was preserved during the catalytic tests without neither particle sintering nor change of morphology (spherical and platelet-like), or large detachment taking place, in comparison with the calcined sample, as observed by SEM analysis in Figure 5.10a, b. Making a general comparison with the structured catalysts on FeCrAl foams, the coating of the spent catalyst in this case seemed to be more stable. As discussed in chapter 4, the coating could be stabilized by the formation of $MgAl_2O_4$ spinel layer on the interface coating/alloy. In the case of NiCrAl foam, it was expected to also form a second type of spinel like $NiAl_2O_4$. Unfortunately, the analysis of the nanoXRD/nanoXRF data (like the one in Chapter 4) is still processing to confirm this hypothesis.
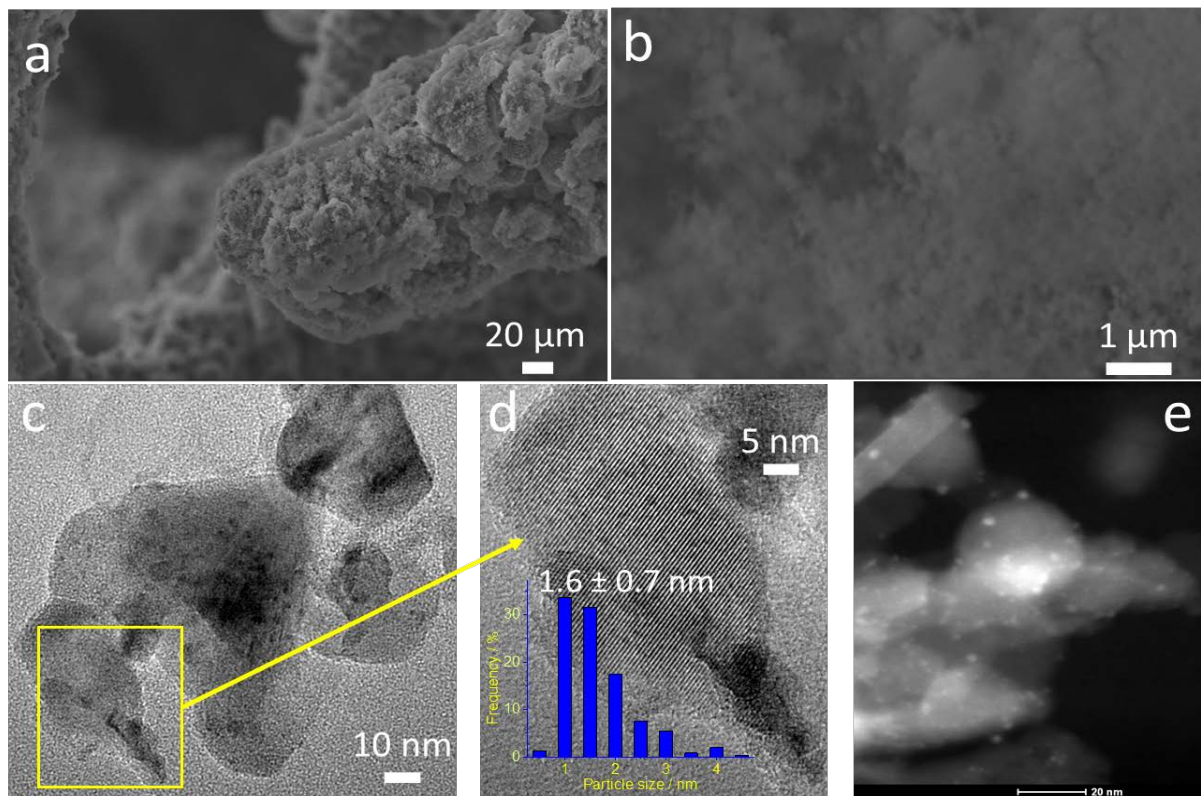
Figure 5.10. SEM images (a, b) and HRTEM images (c, d, e) of the spent catalysts (the first foam of the four-foam catalytic bed, near the entrance of the inlet gas).

Since the catalyst on NiCrAl showed a slight deactivation during the tests in concentrated feedstock rather than similar catalyst on FeCrAl foam reported in chapter 4, it was possible that the catalyst may be suffered to some issues of the deactivation like oxidation, sintering or carbon formation. To verify both the sintering of Rh particles and coke formation, the coating layer was scrapped from the first foam of four-foam bed and characterized by HRTEM/STEM, as shown Figure 5.10c-e. Rh nanoparticles were observed in either external surface or embedded in ill- and well-defined nano-hexagonal shaped species, which was very similar to the one obtained on FeCrAl foam reported in Chapter 4. Estimation of particle size over 250 particles from different TEM images resulted in a narrow distribution of 1-4 nm of Rh^0 particles, despite the quite high Rh loading (5 a.r.), a characteristic of HT-derived catalysts [29, 30]. Remarkably, the formation of carbonaceous structure like multiwall carbon nanotubes was not observed in high resolution TEM images [29].

As in HRTEM images, it was not observed any evidence of carbon deposition, the first and last foam in the catalytic bed were submitted to Raman characterization. No carbon bands were detected in Raman spectra, thus confirming the absence of carbon deposits. This may be due to a high resistance to carbon formation of the catalyst as observed on FeCrAl foam.

5.4 Conclusions

Following the work in chapter 4, the electrosynthesis demonstrated to be feasible to coat different types of metallic foams, e.g. NiCrAl foams with Rh/Mg/Al HT, similar to FeCrAl. Although a pretreatment step was necessary for the former as the oxide layer on its surface could decrease significantly the electrical conductivity of the substrate, resulting in a poor electrodeposited layer. Despite of similar solid loadings and presence of small and well-stabilized Rh nanoparticles in both catalytic coatings prepared on NiCrAl and FeCrAl foams, the former catalyst exhibited a satisfactory catalytic performance for the CPO of CH_4 but a slightly lower stability than that of the latter. This could be related to some issues requiring further studies to make an accurate comparison between the two types of supports, e.g. effect of foam pore size, increase of solid loading, interaction between NiCrAl support and Rh/Mg/Al coating with special attention on the presence of surface Cr.

5.5 References

1. P. Benito, W. de Nolf, G. Nuyts, M. Monti, G. Fornasari, F. Basile, K. Janssens, F. Ospitali, E. Scavetta, D. Tonelli, A. Vaccari, ACS Catal. 4 (2014) 3779-3790.

2. P. Benito, M. Monti, W. De Nolf, G. Nuyts, G. Janssen, G. Fornasari, E. Scavetta, F. Basile, K. Janssens, F. Ospitali, D. Tonelli, A. Vaccari, Catal. Today 246 (2015) 154-164.

3. P. Benito, G. Nuyts, M. Monti, W. De Nolf, G. Fornasari, K. Janssens, E. Scavetta, A. Vaccari, Applied Catal. B Environ. 179 (2015) 321-332.

4. P. Benito, M. Monti, I. Bersani, F. Basile, G. Fornasari, E. Scavetta, D. Tonelli, A. Vaccari, Catal. Today 197 (2012) 162-169.

5. F. Basile, P. Benito, G. Fornasari, M. Monti, E. Scavetta, D. Tonelli, A. Vaccari, Catal. Today 157 (2010) 183-190.

6. A. Montebelli, C.G. Visconti, G. Groppi, E. Tronconi, C. Cristiani, C. Ferreira, S. Kohler, Catal. Sci. Technol. 4 (2014) 2846-2870.

7. E. Tronconi, G. Groppi, C.G. Visconti, Curr. Opin. Chem. Eng. 5 (2014) 55-67.

8. P. Aghaei, C.G. Visconti, G. Groppi, E. Tronconi, Chem. Eng. J. 321 (2017) 432-446.

9. M. Bracconi, M. Ambrosetti, M. Maestri, G. Groppi, E. Tronconi, Chem. Eng. J. 315 (2017) 608-620.

10. J. Huang, H. Fang, X. Fu, F. Huang, H. Wan, Q. Zhang, S. Deng, J. Zu, Oxid. Metals 53 (2000) 273-287.

11. G. Walther, B. Klöden, B. Kieback, R. Poss, Y. Bienvenu, J. D. Bartout, A New PM Process for Manufacturing of Alloyed Foams for High Temperature Applications., PM2010 Proceedings - PM Lightweight & Porous Materials, (2010).

12. H. Choe, Acta Mater. 52 (2004) 1283-1295.

13. H.G. Kim, S.H. Lim, Surf. Interf. Anal. 49 (2017) 880-884.

14. P.S. Roy, C.S. Park, A.S.K. Raju, K. Kim, J. CO_2 Utiliz. 12 (2015) 12-20.

15. W.Y. Choi, J.W. Lee, M.J. Kim, C.J. Park, Y.H. Jeong, H.-Y. Choi, N.-K. Park, T.J. Lee, Int. J. Precis. Eng. Manufact. Green Technol. 4 (2017) 183-189.

16. S. Kim, C.-W. Lee, Procedia Mater. Sci. 4 (2014) 305-309.

17. J.W. Kim, B.K. Choi, M.J. Jang, Patent US 20170210090 A1, 2017.

18. M. Monti, P. Benito, F. Basile, G. Fornasari, M. Gazzano, E. Scavetta, D. Tonelli, A. Vaccari, Electrochim. Acta 108 (2013) 596-604.

19. D.R. Lide (ed), CRC Hand book of Chemistry and Physics, 84th ed., Section 12, Properties of Solids, Electrical Resistivity of Pure Metals, CRC Press, Boca Raton, Florida, 2003.

20. C. Sun, X. Guo, Trans. Nonferrous Met. Soc. China 21 (2011) 1648-1654.

21. K.S.W. Sing, Pure Appl. Chem. 57 (1985) 603-619.

22. M. Maestri, D. Livio, A. Beretta, G. Groppi, Ind. Eng. Chem. Res. 53 (2014) 10914-10928.

23. B. Christian Enger, R. Lødeng, A. Holmen, Appl. Catal. A Gen. 346 (2008) 1-27.

24. T. Liu, C. Snyder, G. Veser, Ind. Eng. Chem. Res. 46 (2007) 9045-9052.

25. A. Donazzi, M. Maestri, B.C. Michael, A. Beretta, P. Forzatti, G. Groppi, E. Tronconi, L.D. Schmidt, D.G. Vlachos, J. Catal. 275 (2010) 270-279.

26. A. Donazzi, D. Livio, A. Beretta, G. Groppi, P. Forzatti, Appl. Catal. A Gen. 402 (2011) 41-49.

27. G. Landi, P.S. Barbato, S. Cimino, L. Lisi, G. Russo, Catal. Today 155 (2010) 27-34.

28. D.D. Nogare, N.J. Degenstein, R. Horn, P. Canu, L.D. Schmidt, J. Catal. 277 (2011) 134-148.

29. P. Benito, V. Dal Santo, V. De Grandi, M. Marelli, G. Fornasari, R. Psaro, A. Vaccari, Appl. Catal. B Environ. 179 (2015) 150-159.

30. F. Basile, P. Benito, G. Fornasari, A. Vaccari, Appl. Clay Sci. 48 (2010) 250-259.

Chapter 6. Pd-CeO₂ structured catalysts for CO oxidation process

In this work, the catalysts were prepared at Laboratory of Process Development group (Professor G. Fornasari and P. Benito), University of Bologna, and then tested for CO oxidation at Laboratory of Catalysis and Chemical Processes LCCP, group of professor E. Tronconi and G. Groppi, Politecnico di Milano.

Chapter 6

6.1 Introduction

Pd-CeO$_2$ catalysts on honeycomb monoliths are the base of three-way catalysts (TWC) [1]. These so-called structured catalysts, merge the activity of Pd and the oxygen storage of CeO$_2$ in the coating with low pressure drop and enhanced mass and heat transfer of the support. Open-cell metallic foams are getting increasing interest as an alternative to conventional honeycomb monoliths as 3D supports; they are light-weight, have a specific mechanical strength, and large geometric surface area, its open cellular structure provides a disruptive ad tortuous flow path and hence an exceptional mixing as well as supply or release of the heat to/from the surface [2]. Integration of Pd-CeO$_2$ on metallic foams is, therefore, a promising option for TWC converters [3]. Moreover, these structured catalysts could find application in processes where the activity of Pd-CeO$_2$ has been demonstrated, such as methane combustion [4-7] and water gas shift [8-10] since metallic foams have reported to provide unique combination of high low-temperature activity/selectivity, good stability, oscillation suppression, low pressure drop at high-throughput operation, enhanced heat transfer and low Pd usage in methane combustion (deoxygenate) [11] and the redistribution of the heat over the bed allows to increase the CO conversion and the reaction rate in the latter [12].

The properties of the structured catalysts based on metallic foams are related to geometric parameters, i.e. pore and strut diameter and void fraction, which can be tailored by foam producers. They not only determine the geometrical surface area for coating but also the pressure drop, mass and heat transfer coefficients [13-15]. The smaller the pores, the larger the surface area available to be coated with the catalytic layer and the better the mass and heat transfer; however, a balance between pore size and pressure drop should be considered.

Conventional washcoating is usually carried out to deposit catalytic layers on medium and large pore open-cell foam supports, i.e. 20, 40, 60 ppi [16-18]. Few works deal with the coating of small pore size foams [19], probably for problems due to pore blockage and inhomogeneous

coating distribution. Other techniques, such as galvanic displacement [20] and hydrothermal synthesis followed by incipient wetness impregnation of the active phase [21] have been proposed to coat foams up to 100 ppi. The former allows to deposit Pd directly onto the foam, but without co-deposition of oxide layer. In the latter, it is possible to integrate simultaneously an oxide or its precursor on the foam, but the precipitation may also occur in the bulk of the solution, with the consequent loss in efficiency.

The electro-base generation method is suitable to coat 60-80 ppi metallic foams with hydroxides such as hydrotalcite-type compounds to obtain structured catalysts after thermal treatment [22, 23]. CeO_2 can be also easily synthesized by this method, although most of the published works report the coating of simple shaped supports such as foil (Ni), sheet (stainless steel), disc (Pt, Au, Platized silicon wafer, stainless steel) [24-26]. Coatings with tailored morphology (flaky [26, 27], compact particles [26], nanocubes and nanowires [28]) and thickness (from nanostructured films [24, 27] to 30 μm [25]), whose main applications is the suppression of corrosion processes and in fuel cells, can be obtained on steel. The deposition involves the electrogeneration of a base in the electrode/electrolyte interface; when the pH suitable for the Ce^{3+} precipitation is attained $Ce(OH)_3$ is firstly obtained, then Ce^{3+} is oxidized and the hydroxide dehydrated subsequently transform into CeO_2 [29]. This is rather easily achieved in short times after application of a constant cathodic potential or current to the working electrode immersed in either a $Ce(NO_3)_3$ or a $CeCl_3$ solution saturated with O_2 or air [24, 27].

The electrodeposition is more challenging when performed on complex shaped supports and in presence of a highly reducible cation in the electrolytic solution, such as the case of the electrodeposition of Pd-CeO_2 catalysts on metallic foams. To achieve a highly active structured catalyst, for instance in the mass transfer limited CO oxidation, the coating thickness, distribution and adhesion to the metallic support are of paramount importance [30], but also the Pd oxidation state [31], particle size [31-33] and interaction with the CeO_2 (forming a Ce_{1-}

$_x$Pd$_x$O$_{2-\delta}$ solid solution) [34, 35]. Catalysts with such properties are prepared by coprecipitation with a base [33, 36-39], namely by the same process that should occur during the electrobase generation method. However, the electrodeposition conditions may provoke the uncontrolled deposition of large metallic particles and thin coatings, such as recently reported during the electrodeposition of Pt/CeO$_2$ on FeCrAl foams [40].

In this chapter, it is reported for the first time the one-step electrodeposition of Pd-CeO$_2$ catalysts on high or medium density cell FeCrAl foams (580 and 1200 μm cell size, corresponding to 100 and 60 ppi). The type of Pd and CeO$_2$ species obtained by electrodeposition and after thermal treatment, the quality of the coating and the catalytic activity in the CO oxidation were investigated. For comparison purposes, the foams were also coated with sole CeO$_2$.

6.2 Experimental

6.2.1 Catalyst preparation

FeCrAl open-cell foam in shape of 9 mm disks (100 and 60 ppi, thickness 1.9 and 3.1 mm, respectively) cut from commercial panels were used as structured supports. Prior to use, the foams were subsequently washed in acetone, water and then dried at 40 °C for 24 h. Electrolyte was an aqueous solution 0.15 M containing PdCl$_2$ (> 99%, Sigma-Aldrich) and Ce(NO$_3$)$_3$ (> 98%, Sigma-Aldrich) with atomic ratio (a.r.) Pd/Ce = 3/97 to give a Pd nominal loading of 2 wt.% in the final catalyst. It was noted that a given amount of PdCl$_2$ calculated for 250 mL electrolyte was firstly dissolved in 10 mL distilled water with the addition of 0.1 g concentrated HCl (37%) and kept under stirring and heating at 50 °C. When the solution became transparently orange color, the rest of water and Ce(NO$_3$)$_3$ were then added to obtain desirable solution. The final pH of the electrolyte before doing the synthesis was approximate 2.5–2.7. For comparison purpose, samples containing only CeO$_2$ were also synthesized from a 0.15 M Ce(NO$_3$)$_3$ electrolyte.

Electrodepositions were performed in the same instrument used in chapter 4. The working electrode (W.E.) was the FeCrAl alloy foam disc and it was assembled by a two-pronged Pt electrical contact. The working and counter electrode compartments were separated by a glass frit tube to avoid the mixture of the electrochemical reaction products. The R.E. was in electrolytic contact with the main compartment *via* a Luggin capillary placed close 1 mm to the surface of the foam cylinder. All potentials were reported with respect to SCE. Selection of $PdCl_2$ and its respective synthesis conditions were chosen from several preliminery tests using different Pd precursors ($PdCl_2$, $Pd(NO_3)_2$, $Pd(NH_3)_4(NO_3)_2$) and electrochemical parameters including applied potential (-1.1 – -1.35 V), concentration (0.03 – 0.15 M), and synthesis time (500 – 2000 s). Taking advantages from that, the electrodepositions were performed at -1.2 V vs SCE for 500 s with circulation of the electrolyte at a flow rate of 2 mL min^{-1} as described in chapter 4. It should be noted that in these electrolytes, the set-up reached a low uncompensated resistance (R_u) ca. 1-2 Ω in all of experiments. After electrodeposition, the coated foams were thoroughly washed with distilled water and dried at 120 ^{o}C for 24 h. The samples were then calcined at 550 ^{o}C for 10 h with a ramp rate of 10 ^{o}C min^{-1}.

6.2.2 Characterization of the coatings

The catalysts were characterized at different stages including after electrodeposition, calcination, and catalytic test by several techniques including XRD, SEM/EDS, FESEM, HRTEM, H_2-TPR, micro-Raman, nitrogen adsorption-desorption, and XPS.

All instruments are the same as mentioned in Chapter 3 and 4. It was noted that HRTEM was performed for both calcined and used catalysts (both top and bottom side of the used catalyst were analysed since the temperature were much different between them during the catalytic tests as mentioned later).

H_2-TPR was carried out in an AutoChem II (Chemisorption analyzer, Micromeritics) with

one coated foam. The catalyst was firstly outgassed at 150 °C under 30 mL min^{-1} of He for 30 min. After cooling to -10 °C by vapor of liquid N_2, the carrier gas was switched to 5% H_2/Ar (v/v) at 30 mL min^{-1}. When the baseline was stable, the temperature was increased to 900 °C with a ramp of 10 °C/min, while the amount of H_2 consumed was measured by means of a thermal conductivity detector (TCD).

Micro-Raman spectra were *in situ* recorded by a Renishaw Raman Invia spectrometer configured with a Leica DMLM microscope using Ar$^+$ laser source (λ = 514.5 nm, P_{out} = 30 mW considering the decrease in power due to the plasma filter) during SEM/EDS analysis. By this way, it is possible to analyse in different locations of the foams (either thick or thin layer (in cracks)) where the compositions were identified by EDS. In each measurement, the laser power was set by 10% of the source and the signal was accumulated by four individual spectra with an acquisition time of 10 s. The electrodeposited and calcined samples were analysed in situ with SEM/EDS while the used catalysts were analysed without coupling of SEM/EDS.

X-ray photoelectron spectra (XPS) were collected using a Physical Electronics PHI 5700 spectrometer with non-monochromatic Mg K$_\alpha$ radiation (300 W, 15 kV, and 1256.6 eV) with a multi-channel detector. Spectra of foams were recorded in the constant pass energy mode at 29.35 eV, using a 720 μm diameter analysis area in two different points. Charge referencing was measured against adventitious carbon (C 1*s* at 284.8 eV). A PHI ACCESS ESCA-V6.0 F software package was used for acquisition and data analysis. A Shirley-type background was subtracted from the signals. Recorded spectra were always fitted using Gaussian–Lorentzian curves to determine the binding energies of the different element core levels more accurately.

6.2.3 Catalytic test

The CO oxidation reaction was carried out in a 9-mm inner diameter tubular microreactor with one coated foam which was placed between two pairs of bare foams on the top and at the

bottom to ensure a homogeneous distribution of the flow through the catalytic bed. Two thermocouples were put in contact with the top and the bottom foam to measure the temperatures of the inlet and outlet gas stream, respectively.

Air and carbon monoxide were fed through independent lines and mass flow controllers, then were mixed and preheated to a set temperature before entering the reactor. The effluent concentrations of reactants and products were measured online by using a gas chromatograph (HP 6890) equipped with two thermal conductivity detectors and two packed columns: the first column was filled with Molecular Sieve 5A 80/100 mesh being suitable to separate O_2, N_2, and CO while the second one was packed with Porapak Q 80/100 to analyze CO_2.

The inlet stream containing CO (1-3% v/v) in air (STP) was fed into the reactor at different flow rate from 1 to 9 SLM (standard liter per min). The inlet temperature was increased stepwise, and at each temperature point, CO conversion was measured after the steady-state conditions were reached.

A complete conversion of CO (~100%) was obtained when the reaction was also conducted at a low flow rate (1 SLM), indicating that the system has no problem with channeling effect along the reactor tube. In addition, the blank tests were also carried out with the presence of five bare foams or without any foam. In these tests, at a temperature lower than 350 $^{\circ}$C the conversion of CO was negligible while at 400 $^{\circ}$C the CO conversion was approximate 5%.

6.3 Results and discussion

6.3.1 Characterization of as-deposited and calcined foams

The foams of both pore size (60 and 100 ppi) were easily and quickly coated by a sole cerium-containing 5 μm film of graded morphology, i.e. platelet-like particles with their planes oriented perpendicular to the foam surface, giving rise to a highly porous coating characteristic of electrodeposited CeO_2 [27], and a very compact layer laying on it (Fig. 6.1a-a3 and Fig. 6.2a-a2).
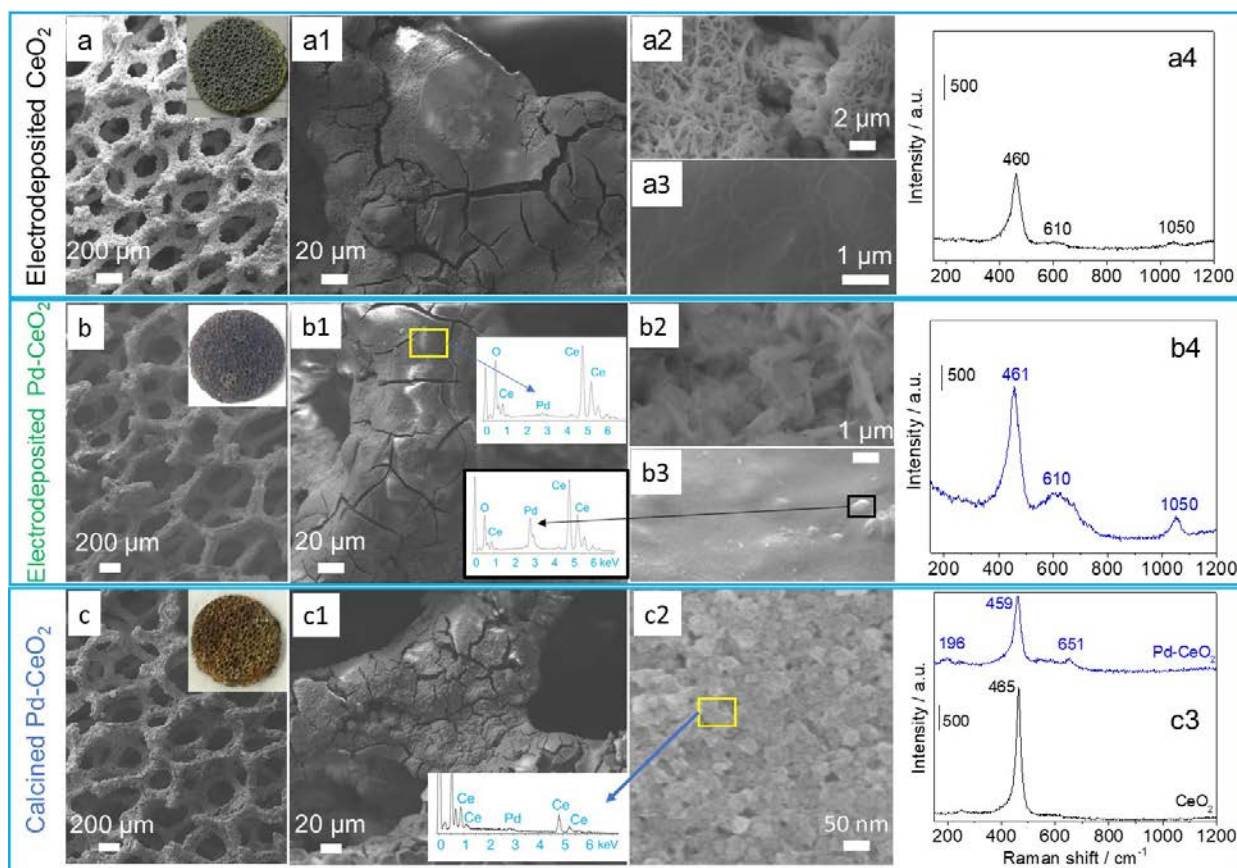
Figure 6.1. SEM images of CeO_2 and $Pd-CeO_2$ coated on 100 ppi foams: electrodeposited CeO_2 (a, a1, a2, a3); electrodeposited $Pd-CeO_2$ (b, b1, b2, b3); calcined $Pd-CeO_2$ (c, c1, c2 (FESEM)); *in situ* Raman spectra coupled with SEM (a4, b4, c3).

A graded morphology has been previously reported [41], however, in that case the outer layers showed a needle-like morphology and the inner layers were more compact. Solid loadings of ca. 11-12 wt.% were deposited on both types of foams. The solids provided specific surface area values around 8.8 and 13.6 m^2 g^{-1} for 60 and 100 ppi foams respectively, which normalized to the solid loading corresponded to 75.9 and 121.4 m^2 $g^{-1}_{coating}$. The N_2 adsorption/desorption isotherms obtained were due to macroporous or non-porous materials with interparticle pores (Fig. 6.3) [42].
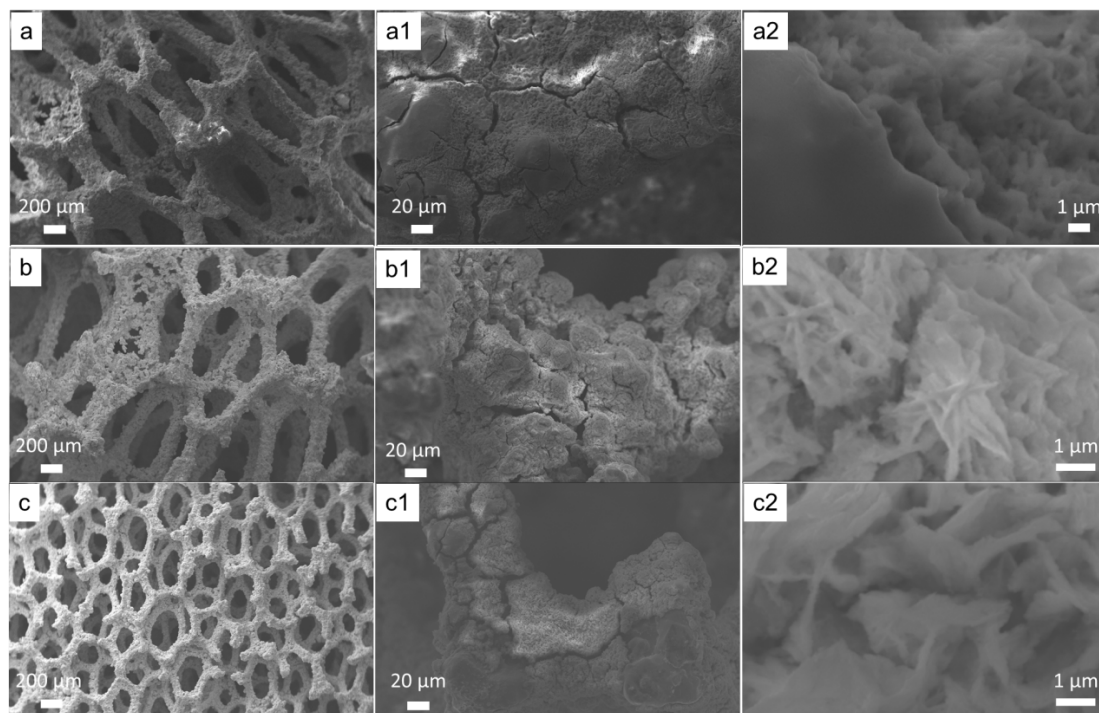
Figure 6.2. SEM images of CeO$_2$ on 60 ppi foam: electrodeposited (a, a1, a2, a3); calcined sample (b, b1, b2); and on 100 ppi foam calcined sample (c, c1, c2).

The structural characterization of the films by XRD confirmed the formation of the cubic fluorite CeO$_2$ phase (Fig. 6.4a). The coexistence of the F$_{2g}$ mode of CeO$_2$ at ca. 460 cm^{-1} and a shoulder at ca. 610 cm^{-1} in the Raman spectra indicated the presence of structural defects such as oxygen vacancies (Fig. 6.1a4). The small band registered at 250 cm^{-1} was due to the normal Raman inactive (IR active) second-order transverse acoustic (2TA) mode, which was also related to the presence of defects [43, 44]. This band was previously reported in electrodeposited CeO$_2$ [28].

Table 6.1. Solid loadings electrodeposited on 60 and 100 ppi foams and the specific surface area (S$_{BET}$) values and normalized to the solid loading of the coated materials (fresh and calcined)

Sample	Load (wt.%)		S$_{BET}$ (m^2 g^{-1})			
	Fresh	Calcined	Fresh	Fresh coating	Calcined	Calcined Coating
CeO$_2$ – 60 ppi	11.6	10.3	8.8	75.9	7.1	68.9
CeO$_2$ – 100 ppi	11.2	10.2	13.6	121.4	9.4	92.1
Pd-CeO$_2$ – 60 ppi	22.7	18.1	11.3	49.8	11.1	61.3
Pd-CeO$_2$ –100 ppi	22.6	17.2	11.9	52.7	10.8	62.8
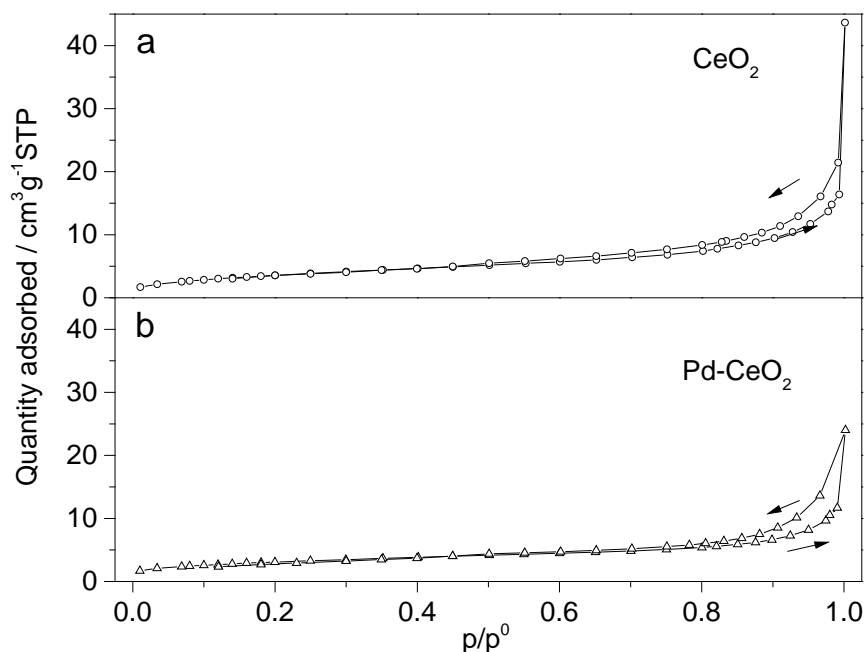
Figure 6.3. N$_2$ adsorption-desorption isotherms at -196 °C of electrodeposited samples on 100 ppi foams: a) CeO$_2$ and b) Pd-CeO$_2$.

A good and reproducible coverage of the foams was also achieved with Pd-CeO$_2$ coatings (Fig. 6.1b-b3, Fig. 6.5a-a3), nonetheless a larger amount of material deposited. Solid loadings were around 22 ± 3 wt.% regardless of the pore size. The coatings were made by porous and compact layers like for CeO$_2$, and except in some regions, where Pd clusters were clearly identified (Fig. 6.1b3 and EDS spectrum in Fig. 6.1b1), Pd species seemed to be well dispersed. Namely EDS analysis detected Pd but their particles were not found (EDS spectrum in the inset of Fig. 6.1b1); in those areas, average Pd/Ce a.r. around 3/97 was estimated, similar to the nominal value in the electrolytic solution. However, ICP analysis of the detached coatings gave a 5/95 atomic ratio for both types of foams, since it measured both well dispersed and clusters. Thus, the actual Pd loading in the catalysts was 3 wt.% Pd instead of 2 wt.%. The higher coating loading provided larger total surface area values, around 11 – 12 m^2 g^{-1} for both 60 and 100 ppi foams (Table 6.1). However, making a comparison among the values referred to the mass of coating, it could be observed that Pd decreased the surface area of the solids to around 50 m^2 g^{-1}.
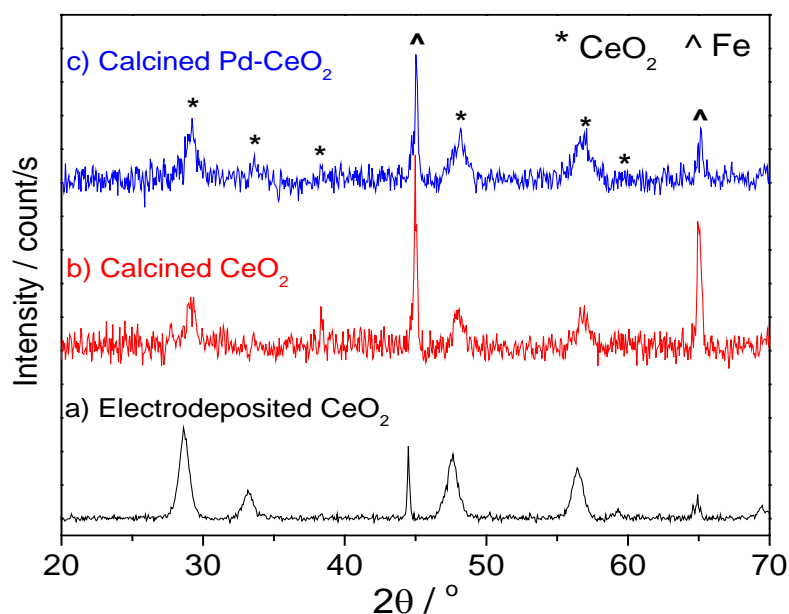
Figure 6.4. XRD patterns of CeO$_2$ and Pd-CeO$_2$ catalysts: a) electrodeposited CeO$_2$; b) calcined CeO$_2$; c) calcined Pd-CeO$_2$.

XRD patterns agreed with SEM/EDS data, only the reflections of cubic CeO$_2$ were registered like for electrodeposited CeO$_2$, without identifications of either Pd^0 or PdO phases. Both broadening and shifting of the F$_{2g}$ mode towards lower Raman shifts and the increase in intensity of the defect band, suggested the incorporation of Pd in the CeO$_2$ matrix [38, 45] (Fig. 6.1b4). The band at ca. 1050 cm^{-1} was related to nitrate species entrapped into the CeO$_2$ structure during the electrodeposition [29, 46].
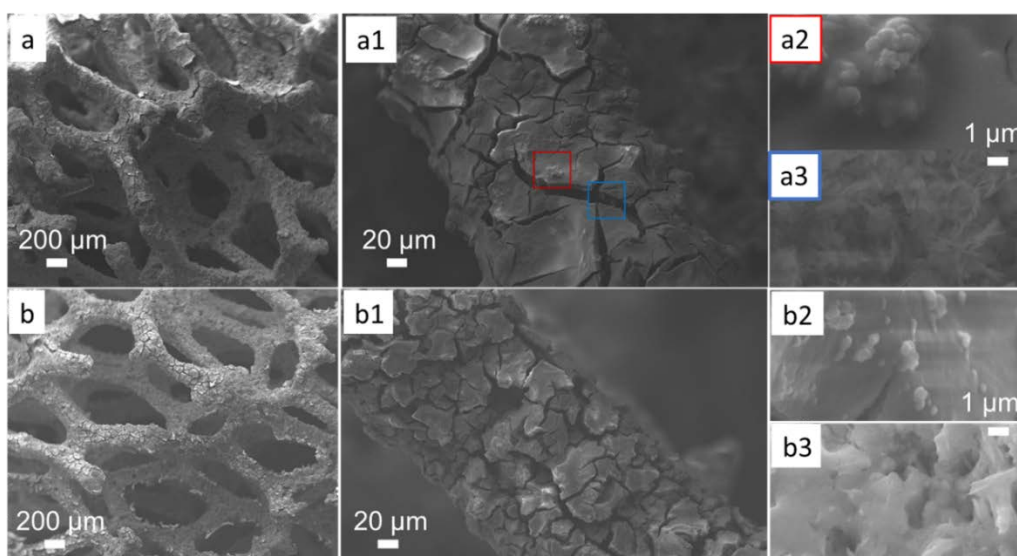
Figure 6.5. SEM images of Pd-CeO$_2$ coated on 60 ppi foam: electrodeposited (a, a1, a2, a3); calcined (b, b1, b2, b3).

The Pd $3d$ core level spectra showed two doublets at binding energy (BE) 335.5-340.7 and 337.9-343.2 eV confirming the presence of two types of Pd species on the coating surface (Fig. 6.6). The band at 335.5 eV was related to the presence Pd^0, while the one at 337.9 eV was attributed to the formation of the $Pd_xCe_{1-x}O_{1-\delta}$ solid solution [31, 34, 47, 48]. It was noted that no peaks associated to PdO (at BE ca. 337 eV) were observed despite they were identified by Raman; it could be due to the inhomogeneous distribution of PdO or its presence in the bulk of the solid. Concerning to Ce $3d$ core level spectra (Fig. 6.6b), in all cases four spin-orbit doublets denoted as v and u could be observed. Three doublets were ascribed to the presence of Ce^{4+}: v (~882.3 eV) and u (~ 901.0 eV); v'' (~888.7 eV) and u'' (~ 907.3 eV); v''' (~898.5 eV), u''' (~917.0 eV). Meanwhile a doublet v' (~885.3) and u' (~ 903.7 eV) was assigned to Ce^{3+} [49, 50]. Both Ce^{4+} and Ce^{3+} were therefore present in the electrodeposited solids, but with a major presence of Ce^{4+}.
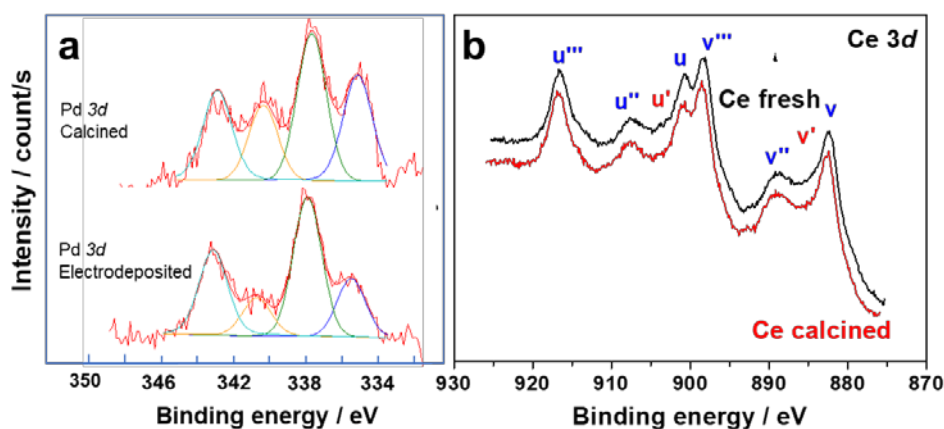
Figure 6.6. XPS spectra of Pd-CeO$_2$ coated on 100 ppi foams: a) Pd $3d$ and b) Ce $3d$.

The characterization results revealed that nitrate reduction provoked the easy and homogeneous precipitation of CeO_2 on the foam surface. In the presence of Pd^{2+} species in the electrolytic solution, an increase of local pH by the electro-base generation method allowed the incorporation of Pd^{2+} into the CeO_2 structure forming the solid solution, as previous reported for conventionally coprecipitated samples [37]. The massive deposition of large Pd metallic particles was decreased, but not completely avoided, probably because of the use of $PdCl_2$

precursors [51]. The electrochemical reduction of Pd^{2+}, but also to the interfacial reduction reaction between Pd^{2+} and Ce^{3+}, which occurs after mixing Ce^{3+} precursor with Pd^{2+} and ammonia [52] could contribute to the formation of Pd^0 particles.

To obtain the final catalysts, coated foams were calcined at 550 °C for 10 h. Both the compact and porous layers were observed in SEM images (Fig. 6.1c-c1, Fig. 6.5b2-b3). Cracks developed due to shrinking of the solid during weight loss (ca. 22 wt.% coating) and shearing stresses, these had a larger effect on the stability of compact than porous layers, indeed a partial detachment of the former was observed in some regions. Moreover, in the thinnest CeO_2 coatings crack formation decreased. The presence of Pd was confirmed by EDS but, like in the as prepared samples, no Pd particles were observed even at high magnification FESEM images (Fig. 6.1c2). Thus, it could be stated that the well dispersed Pd particles in the electrodeposited solids were not largely altered during calcination treatment and that they coexisted with the locally aggregated Pd particles.

To further investigate the morphology of the coatings at a higher resolution, HRTEM images of powders scratched away from the foam surfaces were collected (Fig. 6.7). These images evidenced that the compact and porous layers were built by CeO_2 nanoparticles with an average size of 5-15 nm (sole CeO_2, Fig 6.7a) and 3-10 nm (Pd-CeO_2, Fig. 6.7b). The platelet-like particles identified by SEM were made by agglomerates of these nanoparticles. The combined analysis of HAADF images and EDS spectra showed the presence of well dispersed palladium species after thermal treatment (Fig. 6.7b3-b5). They could be related to Pd^{2+} in the CeO_2 matrix forming the solid solution, since the peak at BE 337.7 eV was still recorded in the XPS spectra (Fig. 6.6). The Ce $3d$ core level spectra of the fresh and calcined samples were very similar, with a major presence of Ce^{4+}, but a slight lower proportion of Ce^{3+} was observed for the calcined sample. The Pd^{2+} species in the CeO_2 matrix may explain the decrease in the sintering of CeO_2 structure during calcination of Pd-CeO_2 in comparison to

CeO_2 samples indicated by HRTEM (Fig. 6.7a2, b1), Raman (Fig. 6.1c3) and specific surface area values (Table 6.1); namely, less crystalline nanoparticles (corresponding to more diffuse SAED diffraction rings) and a broader F_{2g} mode. Moreover, a larger surface area decreases occurred during calcination for CeO_2 than for $Pd-CeO_2$ coatings. However, it should be taken into account that measured specific surface area values may deviate from actual coating S_{BET} values since the weight gain due to the oxidation of the foam was not considered. Raman spectra of the bare calcined foam (Fig. 6.8) showed bands due to Fe_2O_3 (hematite) [53] or Fe^{3+} partially substituted in the Al_2O_3 lattice [54]. Indeed, in a previous article, the characterization μ-XRF/XRD of FeCrAl foams calcined at 500 °C showed the formation of γ-Al_2O_3 and chromium oxides [22]. However, it should be remarked that coating with CeO_2 is reported as a method to protect metallic support corrosion, thus a good and adhesive coating could play two roles: providing a highly catalytic activity and preventing the damage of the support.
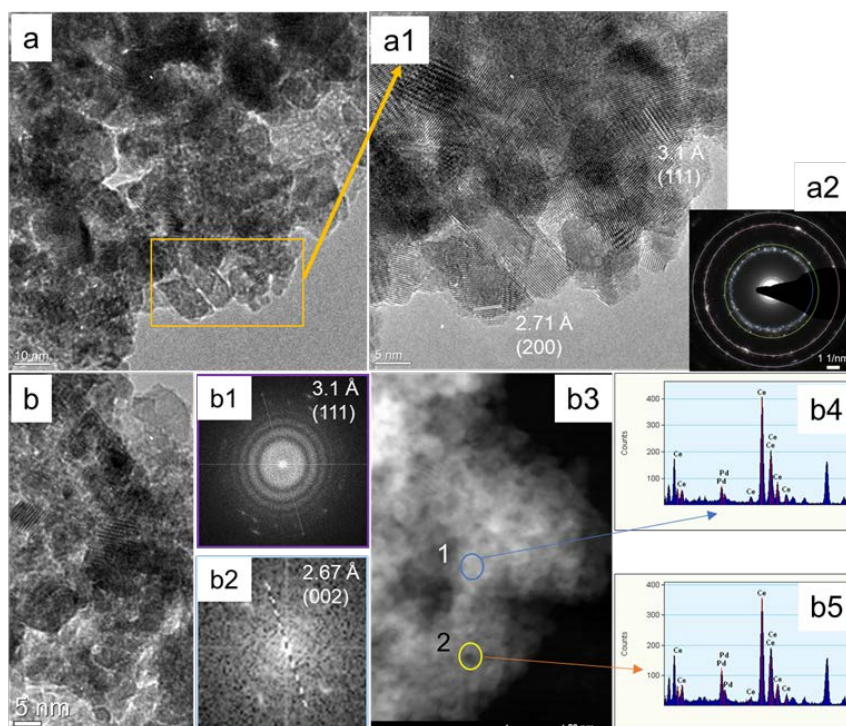
Figure 6.7. Characterization of powders scratched from CeO_2 and $Pd-CeO_2$ coated foams (100 ppi). CeO_2: a) and a1) HRTEM images, a2) SAED. $Pd-CeO_2$: b) HRTEM images, b1 and b2) SAED, b3) STEM-HAADF image, b4 and b5) EDS spectra from figure b1 (b4 taken in bright zone while b5 recorded in black dot zone).

Besides well-dispersed palladium ionic species, XPS confirmed the presence of Pd^0 with a BE around 335.5 eV (Fig. 6.6). Moreover, the Raman spectra of calcined $Pd-CeO_2$ samples developed two bands at 196 and 651 cm^{-1} (Fig. 6.1c3). The latter was attributed to the B_{1g} vibrational mode of square planar $[PdO_4]$ subunits in the PdO structure [38, 55], which could be formed in some regions of the coating with a high Pd/Ce ratio since it suppressed the formation of the solid solution [56]. Thus, the small peak at 196 cm^{-1} could also be related to the E_{u1} forbidden mode of PdO_4 [57], however, it was shifted from the 165 cm^{-1} expected value in PdO, and its intensity did not follow the same trend than the B_{1g} mode. Hence, it was attributed it to PdO_4 in the ceria lattice as previously reported by Gualyev et al. [38]. It should be remarked that XRD patterns of the coated foams did not show any Pd^0 and PdO crystalline phase, suggesting either a low amount or poor crystallinity (Fig. 6.4c).
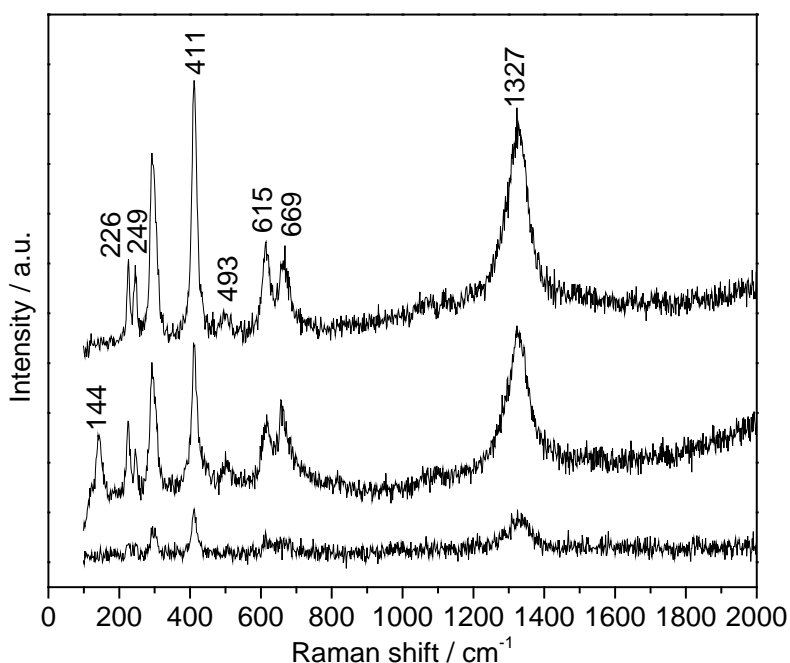
Figure 6.8. Raman spectra of bare foam (100 ppi) calcined at 550 °C for 10 h taken at 3 different places.

The H_2 reducibility of the catalysts was dependent on the above textural and structural characterizations (Fig. 6.9). The H_2 consumption profile of the sole-CeO_2 showed the reduction steps of surface (520 °C) and bulk ceria (755 °C) [58], the intensity of the former agreed with the surface areas reported in Table 6.1. In $Pd-CeO_2$ samples, two peaks were recorded at ca 65

and 150 °C, which may be related to the reduction of PdO and well dispersed palladium species interacting with the support, respectively [45, 59-61]. The reduction of CeO_2 could be overlapped in the second peak since palladium promoted its reduction, this promotion was also observed by the shift of the CeO_2 surface reduction towards lower temperatures and the decrease of the surface to bulk areas ratio. Despite Pd^0 particles were in the catalyst, the typical decomposition of palladium hydrides was not observed [62, 63].
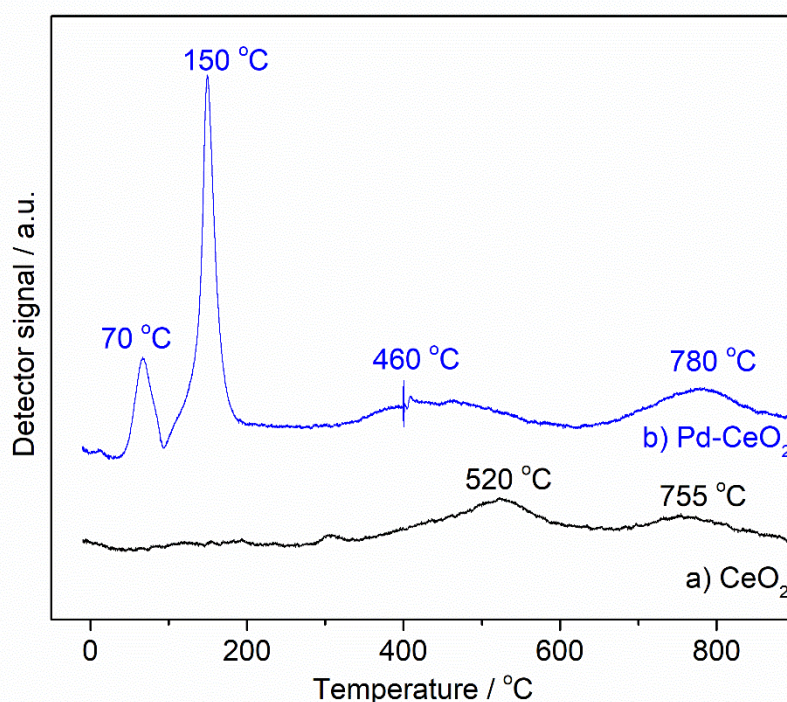
Figure 6.9. H_2-TPR of a) CeO_2 and b) Pd-CeO_2 coated on 100 ppi foams.

6.3.2 Catalytic activity

The catalytic tests were aimed to evaluate both the activity and stability of the coating under harsh reaction conditions with GHSV up to $4.5*10^6$ or $2.7*10^6$ h^{-1} for 100 and 60 ppi foam, respectively. It was noted that one test was carried out at flow rate of 1 standard liter per min (SLM) 3% CO, and a complete conversion of CO was obtained at around 250 °C, confirming that there was no channeling effect in the reactor.

The activity of the coating was proven by tests at 3 SLM (GHSV = $1.5*10^6$ and $9.1*10^5$ h^{-1} for 100 and 60 ppi foam, respectively) with different CO concentrations (0.8, 2 and 3% v/v),

in which the catalysts reached the regime of mass transfer limitation (Fig. 6.10). CO conversion were negligible at low temperatures up to 150 ℃, and the reactions ignited at around 170 - 210 ℃ with an increase of temperature. The lower the CO concentration in the inlet stream, the lower the ignition temperature, e.g. ca. 170, 200, and 210 ℃ for 0.8, 2, and 3% CO v/v, respectively (Fig. 6.9a). A similar trend was also observed for 60 ppi foams (Fig. 6.9b). This behavior was characteristic of the CO oxidation having a negative reaction order with respect to CO [64]. Upon the ignition point, the reaction instantly reached CO conversion values of 90 and 93% for 60 and 100 ppi foam, respectively, and then the conversions were almost constant with an increase of temperature. In addition, the catalyst achieved almost similar CO conversion at the steady state upon the ignition point, regardless the CO concentration. These characteristics of CO conversion provided an evidence that the catalysts were working under the state of diffusion-controlled regime [13].

It was noted that the performances of the Pd electrosynthesized catalysts were comparable with those of a Pd structured catalyst prepared by washcoating. For instance, Giani et al. [30] reported 96% CO conversion under the same reaction conditions (3 SLM, 3% CO v/v) on Pd/γ-Al$_2$O$_3$ washcoated on FeCrAl foam (40 ppi). It was remarked that both catalysts contained similar Pd loading (3 wt.%) but the length of the catalytic bed in that work was 6 mm, instead of 1.9 and 3.1 mm for 100 and 60 ppi foam, in this case. Although present data did not allow to compare directly due to unidentical conditions, some general reasons might be considered for the differences between two catalysts, related to not only morphology, adhesion, thickness of the coating, but also the chemical nature of the catalysts (Pd/CeO$_2$ vs Pd/γ-Al$_2$O$_3$), for instance, it was reported that Pd/CeO$_2$ was better than Pd/γ-Al$_2$O$_3$ for CO oxidation [65].
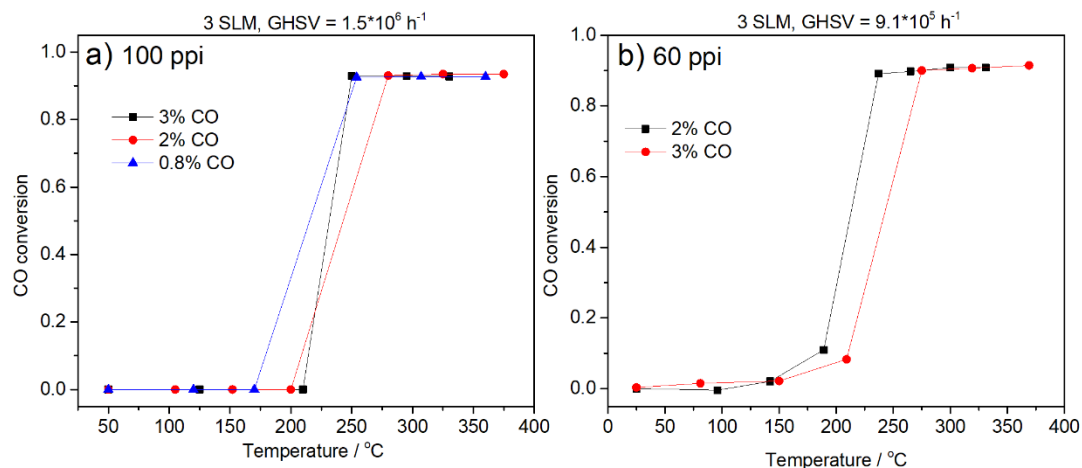
Figure 6.10. CO conversion (vs inlet temperature) of Pd-CeO$_2$ on a) 100 ppi; b) 60 ppi foam catalysts.

To evaluate the stability of the catalysts regarding the mechanical stability of the coating and the chemical stability of the active phase, a series of tests was carried out in mass transfer limited-regime at different flow velocities from 1 to 9 SLM on both types of foams, 100 ppi (GHSV = $5*10^5$ and $4.5*10^6$ h^{-1}) and 60 ppi (GHSV = $3.1*10^5$ and $2.7*10^6$ h^{-1}). After the ignition point, the reaction was carried out for about 2 h at different temperatures (at least 3 points), then the CO stream was shut down and the catalyst was cooled down in air flow before another test was done. The selected results of CO conversion at different flow rates on both catalysts were shown in Fig 6.11. For 100 ppi foam, when increasing the flow rate from 3 to 9 SLM, the CO conversion decreased from 93% to 84%. The effect of flow rate on CO conversion was more pronounced for the larger pore foam since the CO conversion went down 16% (from 90% at 3 SLM to 76% at 9 SLM). A control test at 3 SLM 3% CO was repeated after the tests at 6 and 9 SLM to confirm the stability of the coating as well as the activity of the catalysts. The results showed that there was no decrease in the CO conversion values, thus confirming that the electrodeposition was able to coat both medium and small pore foam with a stable layer against thermal cycles.
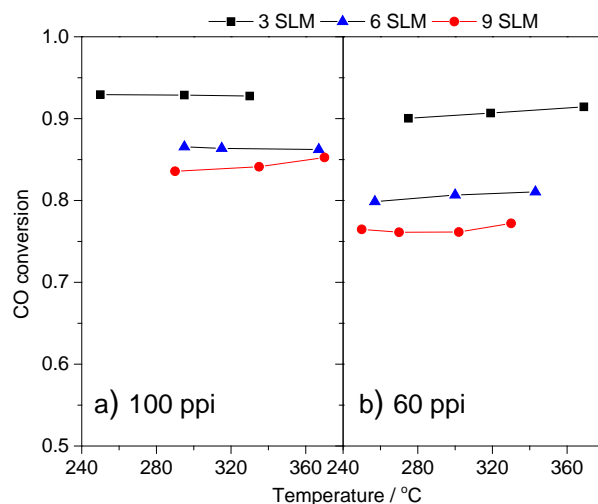
Figure 6.11. Effect of gas flow rate (3 % CO) on CO conversion (vs inlet temperature) on Pd-CeO$_2$: a) 100ppi; b) 60 ppi foam catalysts.

It was noted that once the reaction was ignited, heat produced from the reaction led the outlet temperature to increase quickly to steady state temperature, meanwhile the inlet temperature also rose but at a slower rate due to heat gradients. When the system reached the steady state, the temperature gap measured at the inlet and the outlet depended on the flow rate and CO concentration in the feed stream. For example, at 1 SLM and 3% CO, the gap was about 50 °C, and when increasing the flow rate from 3 to 9 SLM, the gap was extended to 100 – 120 °C. Moreover, at 2% CO, 3 SLM, the difference in temperature was around 75 – 80 °C. Higher flow velocity should mean more heat generated due to larger amount of CO in the feed, however the conversion decreased at high GHSV and the heat was also dissipated faster: hence, a balance between heat generation and dissipation could be considered to explain the effect of flow rate on the gap between the inlet and the outlet temperature.

6.3.3 Spent catalysts

Catalysts were characterized after long term catalytic tests to investigate whether the high flow rates, reaction atmosphere and temperatures, as well as transient conditions (start-up and shut-down) modified the coating adhesion and palladium species. Special attention was paid to

analyse different regions of the spent foam disks, since axial temperature gradients generated during reaction conditions, i.e. 100-120 °C difference between the inlet and outlet of the bed.
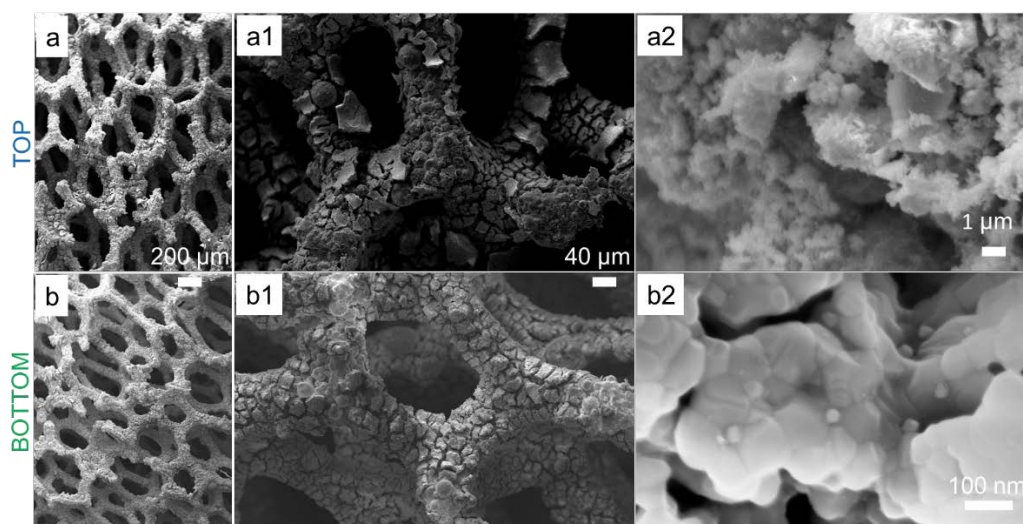
Figure 6.12. SEM images taken from different sides of spent Pd-CeO$_2$ 100 ppi catalyst: top view (a, a1, a2) and bottom view (b, b1, b2 (FESEM)).

The coating on the top of the foam disk, i.e. at the inlet of the catalytic bed was less stable than the one at the bottom, being partially detached (Fig. 6.12, Fig. 6.13). Conversely, the morphology of the CeO$_2$ support particles was not modified at the entrance of inlet and well dispersed Pd species were found, while the sintering of both the support and Pd occurred at the outlet of the bed, where spherical Pd particles, of around 25 nm were identified by FESEM (Fig. 6.9b2).
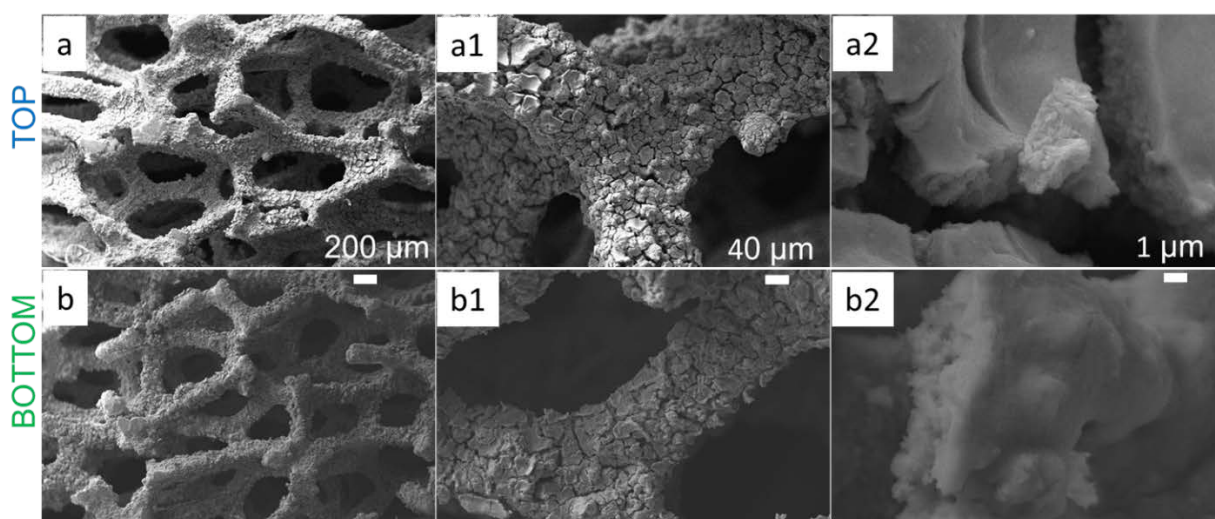
Figure 6.13. SEM images taken from different sides of spent Pd-CeO$_2$ 60 ppi catalyst: top view (a, a1, a2) and bottom view (b, b1, b2).

HRTEM images (Fig. 6.14) confirmed that the coating placed at the inlet of the bed was made by CeO_2 nanoparticles with dispersed Pd species and Pd particles in the 2-7 nm range (average size 4.1 ± 1.3 nm). On the other hand, both large CeO_2 (up to 100 nm) and Pd (average size 14.9 ± 8.6 nm) particles were identified at the outlet of the bed, the latter being distributed both on the surface and in the bulk of ceria particles.
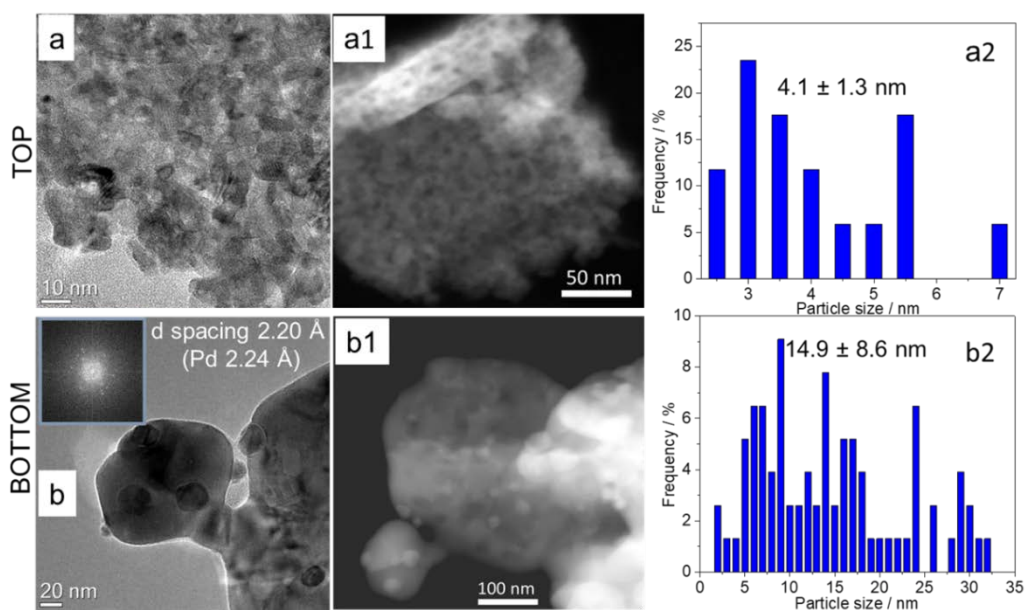
Figure 6.14. HRTEM images of spent Pd-CeO_2 100 ppi catalysts collected from different sides of foam: top (a, a1, a2) and bottom (b, b1, b2). STEM-HAADF (a1 and b1) and particle size distribution (a2 and b2).

XRD patterns showed a more intense and narrower (111) reflection of Pd^0 in the bottom than in the top of the foam disk in agreement with FESEM and HRTEM data (Fig. 6.15a). However, from the diffraction patterns the sintering of CeO_2 seemed to take place regardless of the position in the bed. The narrowing of the F_{2g} mode in the Raman spectra supported the sintering of the CeO_2 during reaction conditions (Fig. 6.15b), however this effect was more remarkable at the outlet of the bed. Observation of the band at 640 cm^{-1} in the bottom but not in the top of foam may be related to sintered Pd species in the former, which agreed with XRD, FESEM, and HRTEM data.
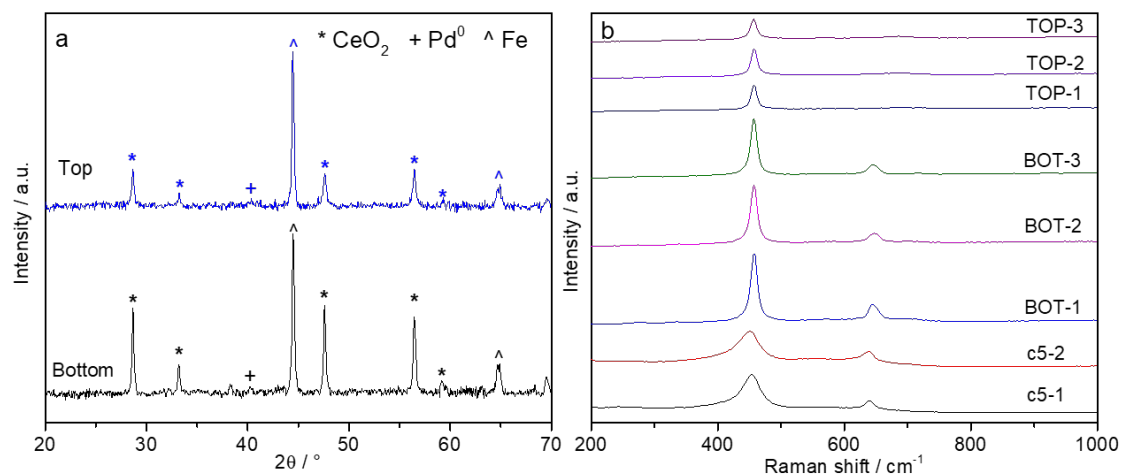
Figure 6.15. XRD patterns (a) and Raman spectra (b) of spent 100 ppi Pd-CeO$_2$ catalysts. In figure b, c5-1 and c5-2 were two spectra of calcined samples, while TOP- and BOT- were spectra for top and bottom side, respectively.

6.4 Conclusions

The electrodepositions of both CeO$_2$ and Pd-CeO$_2$ coating on high pore density FeCrAl foams (60 and 100 ppi) were demonstrated. The method was highly efficient to coat the foam with sole CeO$_2$, a good coating was easily and quickly obtained regardless of the pore size. In the coexistence of Pd, despite the presence of a highly reducible cation, the composition of the deposited layer was quite close to the nominal value of the electrolytic solution in almost all coated area, except in some locations, where the presence of Pd clusters were observed. The characteristics of the coating in terms of structural and redox properties were close to those of Pd-CeO$_2$ catalyst prepared by co-precipitation, in which Pd strongly interacted and was well dispersed into the CeO$_2$ support.

Under harsh reaction conditions (GHSV up to $4.5*10^6$ and $2.7*10^6$ h^{-1} for 100 and 60 ppi foam, respectively) of CO oxidation, Pd-CeO$_2$ structured catalysts coated on both 60 and 100 ppi foams exhibited satisfactory performances in terms of activity and stability, even after several thermal cycles of shut-down and start-up. These results may be related to a good coating homogeneity and stability with time-on-stream. Indeed, the high GHSV values led to a partial

detachment of the coating on the top of the bed but they did not largely modify the morphology of the coating, which still contained well dispersed Pd particles (4 – 6 nm) in the nanoceria support. While the catalyst was partially sintered (15 – 25 nm) at the outlet of the bed because of the higher temperatures but the coating was rather stable.

Chapter 6

6.5 References

1. T. Montini, M. Melchionna, M. Monai, P. Fornasiero, Chem. Rev. 116 (2016) 5987-6041.

2. E. Tronconi, G. Groppi, C.G. Visconti, Curr. Opin. Chem. Eng. 5 (2014) 55-67.

3. J.K. Kim, B.K. Choi, M.J. Jang, Metal foam stack and manufacturing method therefor, US patent 20170210090 A1, Alantum, 2017.

4. S. Colussi, A. Gayen, M. Farnesi Camellone, M. Boaro, J. Llorca, S. Fabris, A. Trovarelli, Angew. Chem. 48 (2009) 8481-8484.

5. S. Colussi, A. Trovarelli, E. Vesselli, A. Baraldi, G. Comelli, G. Groppi, J. Llorca, Appl. Catal. A Gen. 390 (2010) 1-10.

6. A.D. Mayernick, M.J. Janik, J. Catal. 278 (2011) 16-25.

7. M. Cargnello, J.J.D. Jaén, J.C.H. Garrido, K. Bakhmutsky, T. Montini, J.J.C. Gámez, R.J. Gorte, P. Fornasiero, Science 337 (2012) 713-717.

8. R.J. Gorte, AIChE J., 2010. DOI 10.1002/aic.12234.

9. S. Hilaire, X. Wang, T. Luo, R.J. Gorte, J. Wagner, Appl. Catal. A Gen. 215 (2001) 271-278.

10. M. Cargnello, T. Montini, S. Polizzi, N.L. Wieder, R.J. Gorte, M. Graziani, P. Fornasiero, Dalton Transactions 39 (2010) 2122-2127.

11. Q. Zhang, X.-P. Wu, Y. Li, R. Chai, G. Zhao, C. Wang, X.-Q. Gong, Y. Liu, Y. Lu, ACS Catal., 6 (2016) 6236-6245.

12. V. Palma, D. Pisano, M. Martino, Int. J. Hydrog. Energy 42 (2017) 23517-23525.

13. L. Giani, G. Groppi, E. Tronconi, Ind. Eng. Chem. Res. 44 (2005) 4993-5002.

14. G. Incera Garrido, F.C. Patcas, S. Lang, B. Kraushaar-Czarnetzki, Chem. Eng. Sci. 63 (2008) 5202-5217.

15. P. Aghaei, C.G. Visconti, G. Groppi, E. Tronconi, Chem. Eng. J. 321 (2017) 432-446.

16. A. Montebelli, C.G. Visconti, G. Groppi, E. Tronconi, S. Kohler, H.J. Venvik, R. Myrstad, Appl. Catal. A Gen. 481 (2014) 96-103.

17. M. Frey, T. Romero, A.-C. Roger, D. Edouard, Catal. Today 273 (2016) 83-90.

18. F.J. Méndez, O. Sanz, M. Montes, J. Guerra, C. Olivera-Fuentes, S. Curbelo, J.L. Brito, Catal. Today 289 (2017) 151-161.

19. P.S. Roy, C.S. Park, A.S.K. Raju, K. Kim, J. CO_2 Utiliz. 12 (2015) 12-20.

20. Q. Zhang, Y. Li, R. Chai, G. Zhao, Y. Liu, Y. Lu, Appl. Catal. B Environ. 187 (2016) 238-248.

21. R. Chai, Z. Zhang, P. Chen, G. Zhao, Y. Liu, Y. Lu, Micropor. Mesopor. Mater. 253 (2017) 123-128.

22. P. Benito, W. de Nolf, G. Nuyts, M. Monti, G. Fornasari, F. Basile, K. Janssens, F. Ospitali, E. Scavetta, D. Tonelli, A. Vaccari, ACS Catal. 4 (2014) 3779-3790.

23. P. Benito, G. Nuyts, M. Monti, W. De Nolf, G. Fornasari, K. Janssens, E. Scavetta, A. Vaccari, Appl. Catal. B Environ. 179 (2015) 321-332.

24. I. Zhitomirsky, A. Petric, Mater. Lett. 40 (1999) 263-268.

25. L. Arurault, P. Monsang, J. Salley, R.S. Bes, Thin Solid Films 466 (2004) 75-80.

26. Y. Hamlaoui, F. Pedraza, C. Remazeilles, S. Cohendoz, C. Rébéré, L. Tifouti, J. Creus, Mater. Chem. Phys. 113 (2009) 650-657.

27. L. Yang, X. Pang, G. Fox-Rabinovich, S. Veldhuis, I. Zhitomirsky, Surf. Coat. Technol. 206 (2011) 1-7.

28. P. Bocchetta, M. Santamaria, F. Di Quarto, J. Appl. Electrochem. 39 (2009) 2073-2081.

29. L. Arurault, B. Daffos, F.X. Sauvage, Mater. Res. Bull. 43 (2008) 796-805.

30. L. Giani, C. Cristiani, G. Groppi, E. Tronconi, Appl. Catal. B Environ. 62 (2006) 121-131.

31. A.I. Boronin, E.M. Slavinskaya, I.G. Danilova, R.V. Gulyaev, Y.I. Amosov, P.A. Kuznetsov, I.A. Polukhina, S.V. Koscheev, V.I. Zaikovskii, A.S. Noskov, Catal. Today 144 (2009) 201-211.

32. G. Glaspell, L. Fuoco, M.S. El-Shall, J. Phys. Chem. B 109 (2005) 17350-17355.

33. G. Li, L. Li, D. Jiang, Y. Li, J. Shi, Nanoscale 7 (2015) 5691-5698.

34. K.R. Priolkar, P. Bera, P.R. Sarode, M.S. Hegde, S. Emura, R. Kumashiro, N.P. Lalla, Chem. Mater. 14 (2002) 2120-2128.

35. M. Cargnello, V.V.T. Doan-Nguyen, T.R. Gordon, R.E. Diaz, E.A. Stach, R.J. Gorte, P. Fornasiero, C.B. Murray, Science 341 (2013) 771-773.

36. H. Liang, J.M. Raitano, G. He, A.J. Akey, I.P. Herman, L. Zhang, S.-W. Chan, J. Mater. Sci. 47 (2012) 299-307.

37. E.M. Slavinskaya, R.V. Gulyaev, A.V. Zadesenets, O.A. Stonkus, V.I. Zaikovskii, Y.V. Shubin, S.V. Korenev, A.I. Boronin, Appl. Catal. B Environ. 166-167 (2015) 91-103.

38. R.V. Gulyaev, T.Y. Kardash, S.E. Malykhin, O.A. Stonkus, A.S. Ivanova, A.I. Boronin, Phys. Chem. Chem. Phys. PCCP 16 (2014) 13523-13539.

39. G. Li, L. Li, D. Jiang, J. Phys. Chem. C 119 (2015) 12502-12507.

40. E. Verlato, S. Barison, S. Cimino, L. Lisi, G. Mancino, M. Musiani, F. Paolucci, Chem. Eng. J. 317 (2017) 551-560.

41. B. Bouchaud, J. Balmain, G. Bonnet, F. Pedraza, Appl. Surf. Sci. 268 (2013) 218-224.

42. K.S.W. Sing, Pure Appl. Chem. 1985, 603-619.

43. Z. Hu, X. Liu, D. Meng, Y. Guo, Y. Guo, G. Lu, ACS Catal. 6 (2016) 2265-2279.

44. B.M. Reddy, A. Khan, Y. Yamada, T. Kobayashi, S. Loridant, J.-C. Volta, J. Phys. Chem. B 107 (2003) 5162-5167.

45. M. Kurnatowska, L. Kepinski, W. Mista, Appl. Catal. B Environ. 117-118 (2012) 135-147.

46. Y. Hamlaoui, C. Rémazeilles, M. Bordes, L. Tifouti, F. Pedraza, Corros. Sci. 52 (2010) 1020-1025.

47. S. Hinokuma, H. Fujii, M. Okamoto, K. Ikeue, M. Machida, Chem. Mater. 22 (2010) 6183-6190.

48. R.V. Gulyaev, E.M. Slavinskaya, S.A. Novopashin, D.V. Smovzh, A.V. Zaikovskii, D.Y. Osadchii, O.A. Bulavchenko, S.V. Korenev, A.I. Boronin, Appl. Catal. B Environ. 147 (2014) 132-143.

49. J.M. Gatica, R.T. Baker, P. Fornasiero, S. Bernal, G. Blanco, J. Kašpar, J. Phys. Chem. B 104 (2000) 4667-4672.

50. Y. Zhao, K. Tao, H.L. Wan, Catal. Commun. 5 (2004) 249-252.

51. J.A. Abys, Palladium Electroplating, Modern Electroplating, John Wiley & Sons, Inc.2010, pp. 327-368.

52. X. Wang, D. Liu, J. Li, J. Zhen, F. Wang, H. Zhang, Chem. Sci. 6 (2015) 2877-2884.

53. D.L.A. de Faria, S. Venâncio Silva, M.T. de Oliveira, J. Raman Spectrosc. 28 (1997) - 878.

54. A. Zoppi, C. Lofrumento, E.M. Castellucci, P. Sciau, J. Raman Spectrosc. 39 (2008) 40-46.

55. P. Bera, K.C. Patil, V. Jayaram, G.N. Subbanna, M.S. Hegde, J. Catal. 196 (2000) 293-301.

56. C.I. Hiley, J.M. Fisher, D. Thompsett, R.J. Kashtiban, J. Sloan, R.I. Walton, J. Mater. Chem. A 3 (2015) 13072-13079.

57. J.R. McBride, K.C. Hass, W.H. Weber, Phys. Rev. B 44 (1991) 5016-5028.

58. F. Giordano, A. Trovarelli, C. de Leitenburg, M. Giona, J. Catal. 193 (2000) 273-282.

59. L. Meng, J.-J. Lin, Z.-Y. Pu, L.-F. Luo, A.-P. Jia, W.-X. Huang, M.-F. Luo, J.-Q. Lu, Appl. Catal. B: Environ. 119-120 (2012) 117-122.

60. H. Zhu, Z. Qin, W. Shan, W. Shen, J. Wang, J. Catal. 225 (2004) 267-277.

61. Y. Luo, Y. Xiao, G. Cai, Y. Zheng, K. Wei, Appl. Catal. B Environ. 136-137 (2013) 317-324.

62. V.A.d.l.P. O'Shea, M.C. Álvarez-Galván, J.L.G. Fierro, P.L. Arias, Appl. Catal. B Environ. 57 (2005) 191-199.

63. S. Gil, J. Garcia-Vargas, L. Liotta, G. Pantaleo, M. Ousmane, L. Retailleau, A. Giroir-Fendler, Catalysts 5 (2015) 671-689.

64. E. Tronconi, G. Groppi, Chem. Eng. Sci. 55 (2000) 6021-6036.

65. M.-F. Luo, Z.-Y. Hou, X.-X. Yuan, X.-M. Zheng, Catal. Lett. 50 (1998) 205-209.

Chapter 7. Open-cell metallic foams coated by electrodeposition for catalytic decomposition of N₂O

In this work, the catalysts were prepared at Laboratory of Process Development group (professor G. Fornasari and P. Benito), University of Bologna, and then tested for N_2O decomposition at Group of professor R. Palkovits, RWTH Aachen University.

7.1 Introduction

A significant increase of nitrous oxide (N_2O) concentration in the atmosphere has been recognized as an important environmental issue because it is possibly responsible for not only global warming but also the depletion of stratospheric ozone layer [1-3]. Although main sources of N_2O are generated by natural processes in lands and oceans, the contributions from anthropogenic originators, namely, use of fertilizers, burning of biomass, combustion of fossil fuels, wastewater treatment, and industrial activities are also considerable [4]. Depending on the sources of N_2O, its abatement could be achieved by either limiting its formation or using end-of-pipe remediation technologies. Regarding industrial activities, especially adipic acid and nitric acid production, in which this gas is an inevitable byproduct, the use of an after-treatment method such as the catalytic decomposition is preferable. Several kinds of catalysts have been reported active for the catalytic decomposition of N_2O; they are classified into three main groups: noble-metal-supported catalysts, metal oxides, and zeolite-based catalysts [4].

The first group decomposes N_2O into N_2 and O_2 at relatively low temperatures with a satisfactory activity, and Rh-based catalysts are the most active. It was reported that Rh supported on ceria [5-10] or hydrotalcite-derived materials [11-13] showed good reactivity for N_2O conversion. Both two supports possess high surface area, promote the prevention of sintering of noble metals, and thus stabilizes their well-dispersed state. Ceria support is of interest due to its oxygen storage capacity in which oxygen could be provided or withdrawn from its structure, enhancing the rate determining step of N_2O decomposition [8]. An evidence of electronic interaction between RhO_x and CeO_2, which enhances the stability of Rh species on ceria surface of RhO_x/CeO_2 catalyst, was found by Martinez-Arias et al. [14]. Hydrotalcite-like compounds (HTs) are well-known as catalyst precursors because they are able not only to host a very large number of bivalent and trivalent cations with a high dispersion in their

structure but also to form thermal-stable materials with high surface area after calcination [15]. This could explain for the high performance of Rh-containing HTs catalysts in N_2O decomposition.

Among the second group, based on metal oxides, Co_3O_4 has been reported as the most promising material [4, 16-20] because it can provide a sustainable redox Co^{3+}/Co^{4+} couple playing a vital role in the formation of surface-oxygen intermediates that recombine next into dioxygen and the preservation of the spinel structure under oxidizing conditions unlike other transition-metal spinels [21]. It is also noted that for Co-based catalysts a residue of alkali from the precipitating agent used during the preparation could strongly influence on the catalytic activity due to a change in the catalyst electronic properties [20, 22, 23].

As mentioned above, although Rh-based materials are highly potential for N_2O decomposition, their applications are still limited due to a high cost. Another issue that needs to be considered is the pressure drop generated during the operation at high gas hourly space velocity (GHSV). Pieterse and Van Den Brink mentioned in the description of their invention in an US patent [24] that this reaction could be operated in a wide range of GHSV changing from 200 – 200,000 h^{-1} under gas pressures around 1-50 bara (bar atmosphere). Such high GHSV conditions may stress conventional pelletized catalyst in terms of pressure drop and mechanical resistance. One proposed solution is the use of structured catalysts. In fact, the idea of using structured supports such as ceramic foams and honeycombs for this reaction was already registered by Jantsch et al. in the US patent [25]. However, they only demonstrated the performance of Rh-based catalysts coated on Raschig rings. It was also noted that Riley and Richmond possessed patents in both US and EU in which they described in detail the idea of using structured supports to decrease the pressure drop and the visible overview of structured catalysts with the coating layer containing noble metal oxide (Pd, Pt, Ir, Os, Ru, Au, In, Rh) dispersed on rare earth metal oxides [26]. However, in practice, few studies investigated the

use of structured catalysts for N_2O decomposition, namely structured supports (monolith or wire-mesh) coated with both noble [27-31] or non-noble metal [32-34]. Ceramic monoliths (e.g. cordierite) were decorated with a thin layer of washcoat (e.g. γ-Al_2O_3, zeolite) followed by impregnation of active elements (e.g. Rh, Pt, Co, Fe). So far, the use of metal foams as catalyst for N_2O decomposition has not been reported. However, it could be a possible option to develop mechanically stable catalysts for the decomposition of N_2O to reduce the pressure-drop under operation at high GHSV of the reaction. Moreover, metal foams could prevent the formation of hot spots inside the catalyst bed due to the exothermic N_2O decomposition, especially when treating highly concentrated streams such as those out of the adipic acid plant, up to 30 % v/v [35].

Taking advantage of the electro-base generation method developed by us to coat FeCrAl foam for the catalytic partial oxidation of CH_4 as reported in some previous works [36, 37] as well as in chapter 4-6, this chapter mainly focused on the coating of the FeCrAl foams with different types of materials, representing for unary (Co), binary (Rh/Ce), and ternary (Rh/Mg/Al) element system, and reported the first time their catalytic application for abatement of N_2O at low concentration. In addition, we made a comparison of the activity of the best catalyst selected from this work with pelletized ones prepared by conventional co-precipitation method.

7.2 Experimental

7.2.1 Catalyst preparation

Open-cell FeCrAl foams (80 ppi, panel, 7 mm thickness) was cut in cylindrical shape (diameter x height = 8.0 x 7.0 mm) and used as supports in the preparation of structured catalysts. It was noted that the volume and mass of the foams used in this work were smaller about 2.7 and 4.8-fold, respectively, than those of the ones reported in chapter 4, although both

were the same pore size (80 ppi). This may cause some differences in properties of the structured catalysts as shown in next sections.

Electrosyntheses were carried out in the same electrochemical cell used in chapter 4. Working electrode (W.E.) was an FeCrAl cylinder foam required to be coated. The electrolytes were aqueous solutions containing metal nitrate salts corresponding to a desired composition of as-prepared catalysts: i) $Co(NO_3)_2$ 0.15 M; ii) a mixture of $Rh(NO_3)_3$ and $Ce(NO_3)_3$ 0.15 M and atomic ratio Rh/Ce = 3/97; iii) a mixture of $Rh(NO_3)_3$, $Mg(NO_3)_2$ and $Al(NO_3)_3$ 0.06 M and atomic ratio Rh/Mg/Al = 2/70/28. The potential applied for all the cases was -1.2 V *vs* SCE, but the time was modified, 500 s for the first two types of electrolytes with higher concentration while 1500s for the third. It was noted that these electrochemical parameters were chosen from preliminary studies in which the concentration (0.06 – 0.15 M), potential applied (-1.1 – -1.2 V vs SCE), and synthesis time (500 – 2000 s) were modified. However, to sum up the work, this thesis only presented the best results obtained. The compositions of the electrolytes were similar to pelletized catalysts reported in the literature for this reaction [7, 35] but modified with an increase in Rh loading due to less material deposited on the foam. The obtained catalysts were denoted as Co, $Rh-CeO_2$, and Rh-HT. After electrosynthesis, the coated foams were washed with distilled water and then dried at 40 °C for 24 h. Eventually the calcination step was conducted at 600 °C for 6 h.

For comparison purposes, Co and Rh-HT catalysts were also prepared by co-precipitation. A 1.0 M nitrate solution of Co or Rh/Mg/Al = 2/70/28 a.r. was dropped wise into a batch reactor containing 100 mL of a Na_2CO_3 solution to prepare Co or Rh-HT powder catalysts, respectively. The pH was controlled at 10 ± 0.2 by adding dropwise a NaOH 1.0 M solution. The amount of Na_2CO_3 was calculated by charge balance of the system when a trivalent cation substituted a divalent one in the brucite structure with an excess amount of 50 %. The resulting slurry was aged for 0.5 h at 60 °C, filtered and washed thoroughly with warm distilled water

(60 °C). For Rh-CeO$_2$ powder catalyst, a nitrate solution 1.0 M of Rh/Ce = 0.15/99.85 a.r. was co-precipitated using NH$_4$OH at pH 10 and room temperature, and the slurry was aged for 30 min. The final products were dried at room temperature for 24 h and subsequently calcined at 600 °C for 6 h. For catalytic tests, the powder catalysts were pelletized and a fraction of materials with particle size in range of 0.25-0.50 mm was collected and used.

7.2.2 Characterization

The catalysts were characterized by SEM/EDS, XRD, micro-Raman, N$_2$ adsorption-desorption, temperature programmed reduction by hydrogen (H$_2$-TPR), and HRTEM. Information of the methods and instruments can be found in chapter 3, 4 and 6.

H$_2$-TPR was performed in an AutoChem II (Chemisorption analyzer, Micromeritics) with two coated foams. The catalyst was firstly outgassed at 150 °C under 30 mL min^{-1} of He for 30 min. After cooling to 30 °C under He gas, the carrier gas was switched to 5% H$_2$/Ar (v/v) at 30 mL min^{-1}. When the baseline was stable, the temperature was increased to 900 °C with a ramp of 10 °C min^{-1}, while the amount of H$_2$ consumed was measured by means of a thermal conductivity detector (TCD).

7.2.3 Catalytic test

The catalytic decomposition of N$_2$O was performed in a quartz reactor (ID 8 mm) containing two foams of catalyst (diameter 8 mm and height 7 mm). Prior to each experiment, the catalyst was outgassed at 500 °C for 0.5 h under mL min^{-1} of N$_2$ then cooling down to 50 °C. After that 80 mL min^{-1} of a gas mixture containing 1000 ppm N$_2$O in N$_2$ balance was switched on to pass through the catalyst bed. The reaction was carried out at atmospheric pressure and in a range of temperatures from 50 °C to 600 °C with an interval of 50 °C. At each temperature, the reaction was stabilized for half an hour before sending to quantify N$_2$O concentration. The gas composition in the outlet stream was analyzed by Infrared Spectroscopy

using an Agilent Cary 660 equipped with a Pike 2 m heated gas cell. N_2O conversions were calculated by:

$$\text{Conv. } N_2O = \frac{F_{N_2Oin} - F_{N_2Oout}}{F_{N_2Oin}} * 100$$

The best catalyst was tested under harsh reaction conditions with 1000 ppm N_2O + 200 ppm NO + 2% O_2 in N_2 balance. In addition, the stability test was also carried out in this feedstock for 24 h but the oven temperature was set constant at 450 ^{o}C.

Turn over reaction rate (TOR) of the reaction (mol N_2O m^{-2} s^{-1}) was calculated by equation:

$$r = \frac{n.X}{W.S_{BET}} \qquad\qquad \text{(Equation 7.1)}$$

where n is molar flow rate of N_2O (mol s^{-1}), X is N_2O conversion under reaction conditions, W is weight of the catalyst (g), and S_{BET} is specific surface area of the catalyst (m^2 g^{-1}). It is noted that TOR represents a true reaction rate only under differential reactor conditions (conversion lower than 15%), otherwise being an average reaction rate. In this chapter, it is reported the TOR at low conversion (<20% conversion) in the graphs and average TOR at T_{50} (temperature that 50% N_2O is converted) in the tables for comparison purposes with data in the literature.

7.3 Results and Discussion

7.3.1 Characterization of the coated foams

7.3.1.1 Cobalt catalyst

SEM images at different magnifications of the foam after being electrodeposited in the cobalt nitrate bath are displayed in Fig.7.1b-b3, for comparison purposes images of a bare foam were included in Fig 7.1a-a2. The foam surface was covered by a compact blue layer with solid loading of approximate 27.1 ± 2.7 wt.% (Table 7.1). This loading was almost double of the

loading obtained with Rh-HT materials commented in this chapter (section 7.3.1.3) and much higher than Rh/Mg/Al HT compound reported in chapter 4. Some main factors may be considered to explain this behavior, namely the properties of the support, synthesis conditions, and nature of the cation being precipitated, and difference of molecular weight between Rh/Mg/Al HTs and Cobalt hydroxides. Since the foam used in this work had a lower density (about 1.8-fold) than the one reported in chapter 4, the same amount of electrodeposited solid obtained would have led to a higher loading on the former than that on the latter.
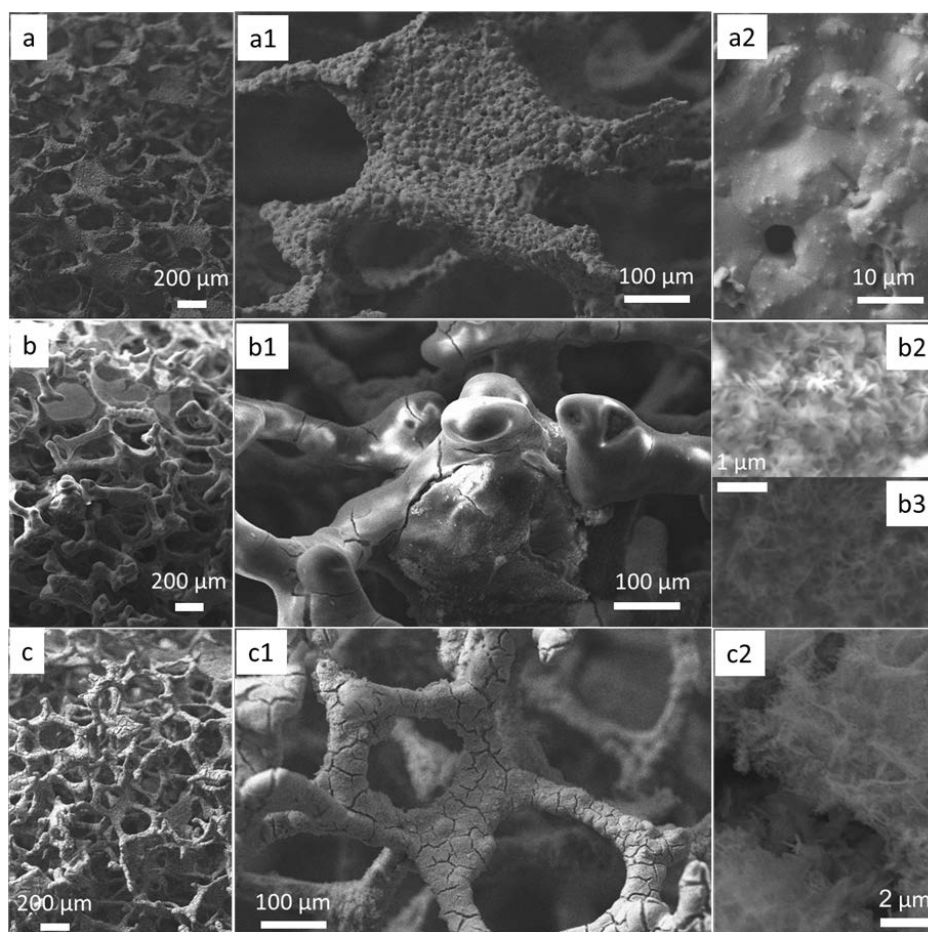
Figure 7.1. SEM images of open-cell foams coated with Cobalt materials: bare foam (a, a1, a2); electrodeposited (b, b1, b2, b3); and calcined samples (c, c1, c2).

When it was made a comparison between the Co and Rh-HT samples prepared in this chapter with the same type of foams, the synthesis parameters could have been of paramount of importance. Since the applied potential was kept at the same -1.2 V vs SCE value in both

cases, concentration and synthesis time (0.15 M and 500 s *vs* 0.06 M and 1500 s) may have a contribution in the coating properties. However, preliminary electrodepositions were performed at those two synthesis conditions with cobalt showing similar loadings, indicating that the effect of synthesis conditions in this comparison was minor. The last but most important factor was the nature of cations being precipitated. Cobalt (II) hydroxide is formed at a lower pH than the pH required for precipitating Mg-Al HT based materials. In fact, at 0.15 M, pH at around 7.3 (calculated from equilibrium solubility constant $K_s = 6.93*10^{-15}$ [38]) is sufficient for the precipitation of Cobalt hydroxide, instead of around 8.5 for Mg-Al HTs as shown in chapter 2 and 3. It should be remembered that the electrodeposition involved a heterogeneous precipitation in which the pH value was slightly modified and hence required a lower value [39].

Table 7.1. Properties of structured catalysts and powder catalysts

Sample	Composition [a] (a.r.)	Fresh loading (wt.%)	Calcined loading (wt.%)	S_{BET} ($m^2 g^{-1}$)		
				Foam [b]	Coating [c]	Pellet [d]
Co	Co = 100	27.1 ± 2.7	18.3 ± 2.3	3.3	18.0	24.7
Rh-CeO$_2$	Rh/Ce = 2.8/97.2	54.1 ± 4.8	42.6 ± 2.7	11.4	26.8	61.0
Rh-HT	Rh/Mg/Al = 1.8/72.6/25.6	14.5 ± 2.7	8.4 ± 1.7	7.8	93.0	289.0

[a] Determined by EDS, [b] for whole two coated foams, [c] only the coating, [d] powder catalysts prepared by co-precipitation.

The coating of Cobalt hydroxide had few cracks and did not block the foam pores. In some locations, having cracks the layer thickness was estimated to be about 15-18 µm containing a 6-8 µm top layer from SEM images, which was much thicker than those previously reported around 4-5 µm for electrodeposited Co(OH)$_2$ [40, 41]. This coating was composed of nanoparticles (100–300 nm) with a needle-like morphology (Fig. 7.1b2 and b3) typical of α-

Co(OH)$_2$ electrodeposited on Ni foam [40] or stainless steel plate [41]. A graded particle size was obtained, larger particles grew near the support (Fig. 7.1b2), and the size decreased as the layer thickness increased (Figure 7.1b3).

The formation of a single cobalt hydroxide phase was expected [41], however, despite some trials we were not able to record diffraction patterns where the reflections of the coating were observed. It could be related to the poor crystallinity of the deposited phase rather to a low amount of material, since we were able to record the patterns for other coated foams containing lower solid loadings. To obtain information about the crystalline nature of the solid deposited, the sample was analyzed by micro-Raman, Fig. 7.2a. The two representative peaks of Co(OH)$_2$ were recorded at 518 and 451 cm^{-1}, which were associated to CoO (A$_g$) symmetric stretching and OCoO bending modes, respectively [42]. It was noted that the presence of the band at 518 cm^{-1} raman shift and the absence of the band at around 601 cm^{-1} may allow to confirm the α-Co(OH)$_2$ structure in electrosynthesized sample [43]. In addition, the broad band centered at around 3600 cm^{-1} was attributed to the ν_{OH} of water and hydroxyl in the layer of Co(OH)$_2$; as well as the sharp peak at 1051 cm^{-1} was assigned to the ν_1 symmetric stretching mode of NO$_3^-$ species which could be both adsorbed or intercalated in the Co(OH)$_2$.
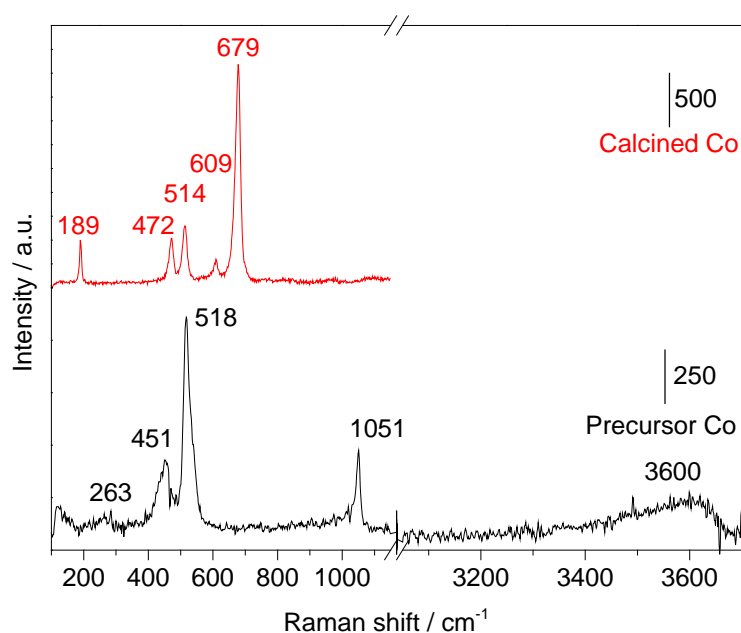
Figure 7.2. Raman spectra of open-cell foams coated with Cobalt materials.

After calcination at 600 ℃ for 6 h, the coating phase was probably transformed into the spinel Co_3O_4 structure. The loading decreased to 18.3 ± 2.3 wt.% due to water and NO_x removal. During the thermal treatment some narrow cracks developed, the coating was still stable Fig. 7.1c-c1. The needle-like morphology was maintained, and larger particle sizes (about 200 – 400 nm) were observed in both two layers (Fig. 7.1c2).

Raman spectra of the calcined catalysts, displayed in Fig. 7.2, showed five peaks assigned to the Co_3O_4 spinel structure. The most intensive band at 679 cm^{-1} was assigned to the A_{1g} mode. Three peaks at 189, 514, and 609 cm^{-1} were associated to the F_{2g} mode, while the last one at 472 cm^{-1} was related to E_g mode [44]. An absence of bands at 3600 and 1051 cm^{-1} confirmed that all hydroxides and nitrate were removed.
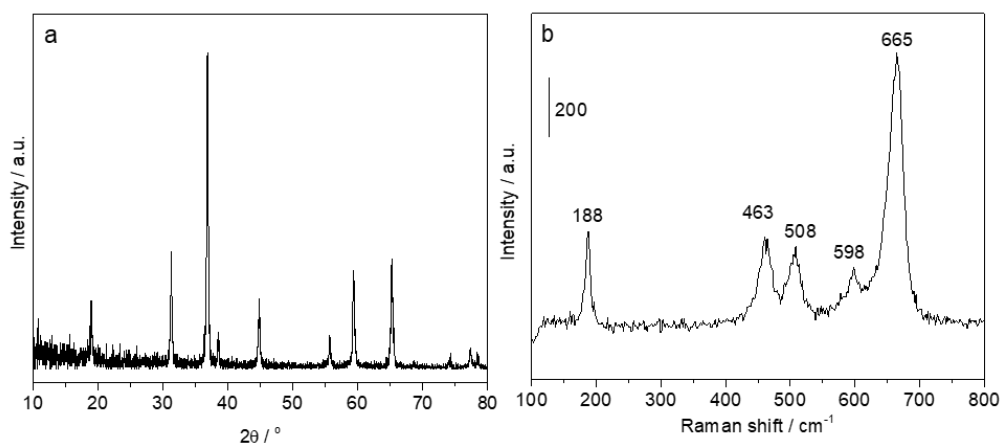
Figure 7.3. Co powder calcined catalyst prepared by co-precipitation: a) XRD pattern and b) Raman spectrum.

The powder catalyst prepared by co-precipitation was characterized by XRD and Raman to verify if it had similar properties than those of Co structured catalyst (Fig.7.3). All peaks of XRD pattern (Fig. 7.3a) were well matched with Co_3O_4 spinel structure [45]. Co-precipitation catalyst also presented five peaks in Raman spectrum, but only one peak at 188 cm^{-1} was the same Raman shift of Co structured catalyst, the other four peaks were shifted to lower values (Fig. 7.3b). This indicated that there may be differences in the structure of Co spinel obtained from two methods.

The reducibility of Co structured and powder catalyst were analysed by H_2-TPR and

presented in Fig. 7.3. H_2 was consumed mainly in range from 300 to 500 °C, in which a shoulder at 350 °C could be associated to reduction of Co_3O_4 to CoO, while a major peak at ca. 415 °C may be attributed to the reduction of bulk CoO to Co. Compared to the co-precipitated catalyst, the electrosynthesized structured catalyst was easier to be reduced since the peaks were shifted to lower temperatures. The shape of the curves was similar to H_2-TPR profiles of Co_3O_4 prepared by combustion method [17] or of a commercial product [18] although the maximum temperature (T_{max}) again depended on preparation method. Indeed, T_{max} of the electrodeposited Co catalyst was lower (around 60 °C) than that of the combustion catalyst but higher than the commercial one. This may be probably related to particle size and surface area of the spinel. It was noted that the reducibility of the catalyst may influence on the reactivity, in fact the order of T_{max} was the same of the reactivity order, as will be explained in section 7.3.2. Surface area of the Co catalyst was around 3.3 m^2 g^{-1}, corresponding to 18 m^2 $g^{-1}_{coating}$, which was slightly lower than Co powder catalyst prepared by co-precipitation (Table 7.1).

Figure 7.4. H_2-TPR of Co structured (a) and powder (b) catalysts.

7.3.1.2 Rh-CeO$_2$ catalyst

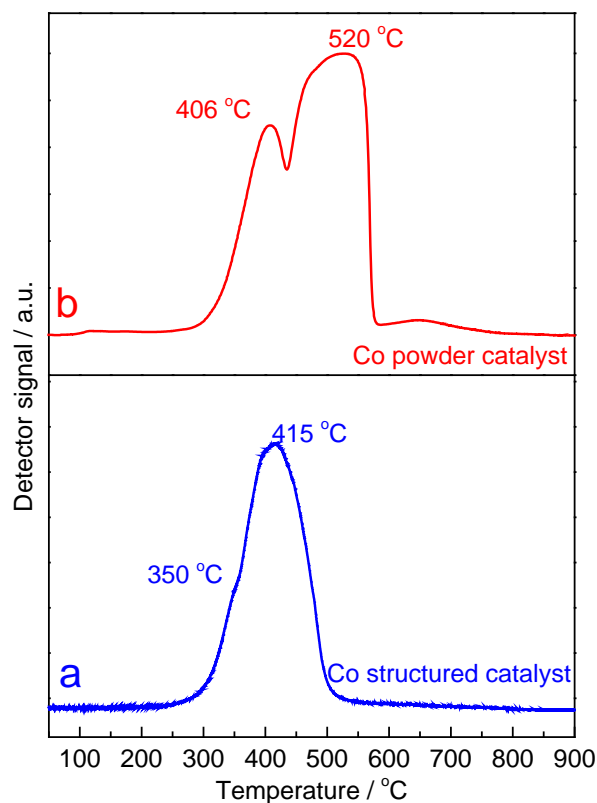In case of the binary deposit of Rh and Ce, in overview, the coating was thicker than that of Co catalyst, resulting a decrease in the diameter of the pores of the foam after electrodeposition as shown in Fig.7.5a, a1. Probably, the precipitation of cerium hydroxide was easier than that of cobalt hydroxide due to a lower pH requirement. However, more cracks appeared on the coating surface than in the case of Co catalyst; these cracks may be related to either formation of hydrogen gas bubbles during electrodeposition or shearing stress between the coating and the foam surface during drying process because of the thick layer. The deposit loading was 54.1 ± 4.8 wt.% (Table 7.1), and it consisted of two layers, the first one near the foam surface was more porous, while the outer one was more compact, but both were made of nanoparticles with a needle-like shape. Similar to Co catalyst, these nano-sheets grew in different layers: the inner one with bigger particle size (200 - 400 nm) than the outer (80 - 200 nm) estimated from Fig. 7.5a2 and a3, respectively. It was also noted that the coating could reach thicknesses of 20 – 30 µm, as observed by SEM in some location having cracks. Since the synthesis conditions were the same as Pd-CeO$_2$ structured catalyst in chapter 6, a much higher amount of solid deposited in Rh-CeO$_2$ catalyst may be related to two main factors: higher density of the foam used in the former than in the latter (although difference in shape may be also influence) and the nature of cations Pd *vs* Rh. Remarkably, in the former the pH of the electrolyte Pd/Ce was quite low 2.5 – 2.7 and impossible to increase more without formation of complex or precipitation due to sensitivity of Pd cations, whereas in the latter, Rh/Ce solution was adjusted pH to 3.8 before performing the syntheses. This may favor partial reduction of Pd cations during the electrodepositon as evidenced by SEM/EDS and XPS in chapter 6. In contrast, here it was not observed the presence of Rh metallic particles in the coating. Such contribution of the reduction would consume partially total charge transfer during electrosynthesis and may lead to lower amount of OH$^-$ generation, resulting a lower

amount of solid deposited in the cases of Pd-CeO$_2$ catalyst.

The composition of the coating was estimated by EDS analyses at 6-10 regions of interest for 3 samples, the average Rh/Ce value obtained was 2.8/97.2 as shown in Table 7.1. This ratio was very close to the nominal value in the electrolytic solution (Rh/Ce = 3/97) indicating that the electrodeposition allowed to control quite well the composition of the deposit in the case of binary component deposition with Rh. It was noted that the electrosynthesis was able to control better the composition of Rh-CeO$_2$ than the composition of Pd-CeO$_2$ under the same synthesis conditions. Indeed, in the latter, the Pd/Ce was around 3/97 in most of the surface of the coating, except in some locations where the presence of Pd metallic particles were identified by EDS, resulting in a final ratio Pd/Ce = 5/95 as identified by ICP analyses (chapter 6).
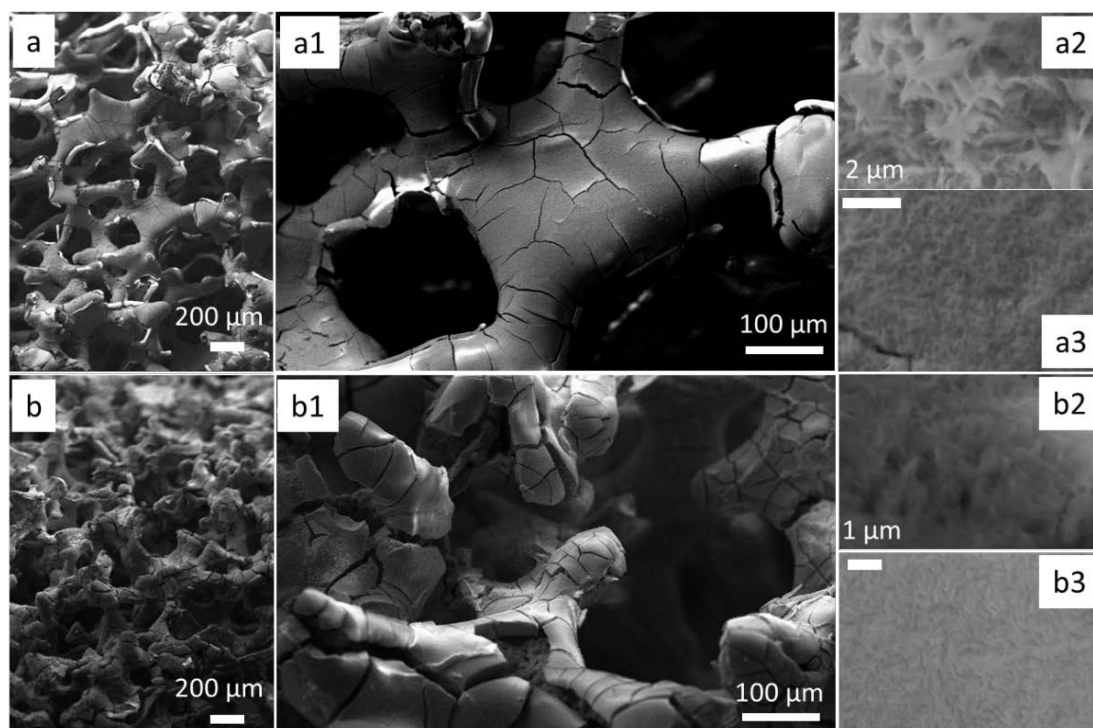
Figure 7.5. SEM images of open-cell foams coated with Rh-CeO$_2$ materials: electrodeposited (a, a1, a2, a3); calcined sample (b, b1, b2, b3).

The crystalline phase of the precursor in the coating was examined by XRD and shown in Fig. 7.6. XRD patterns confirmed that the electrodeposited coating was mainly composed of fluorite CeO$_2$ phase, without reflections related to Rh, in agreement with SEM/EDS data,

indicating that Rh^{3+} species may be simultaneously precipitated in ceria structure or precipitated as well-dispersed hydroxide. In addition, one unidentified sharp reflection at around $2\theta = 27.7°$, may be related to the support.
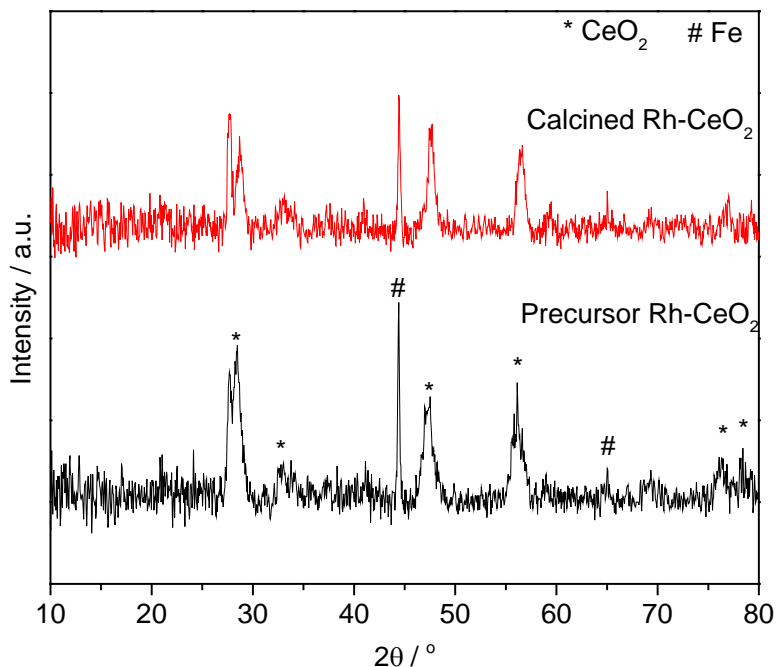
Figure 7.6. XRD patterns of Rh-CeO₂ structured catalyst.

To understand whether Rh incorporated into the ceria structure, the samples were analyzed by micro-Raman. As can be seen in Fig. 7.7, Raman spectra of as-deposited Rh-CeO₂ precursor showed the peak at 460 cm⁻¹ ascribed for the symmetric vibration of F_{2g} mode of Ce–O in CeO₂. The asymmetry of this peak allowed to predict the presence of oxygen vacancies or foreign ions such as nitrate [46]. The band around 605 cm⁻¹ supported the formation of oxygen defects in CeO₂ structure, which could be also related to a partial substitution of Ce^{4+} by Rh^{3+} in the fluorite framework. The peak at 1048 cm⁻¹ could be assigned for free nitrate ion originated from the electrolyte and remained in the deposit after electrodeposition.

During calcination, the removal of water and nitrates occurred, resulting in a decrease of the solid loading to 42.6 ± 2.7 wt.% (Table 7.1). The coating kept the needle-like morphology, but the nano-sheet was slightly aggregated, and the cracks were extended (Fig. 7.5b-b3). The extension of the cracks may be due to the thick layer of the materials. XRD pattern of the

calcined sample was similar to the pattern of the fresh sample, suggesting the absence of segregated Rh_2O_3 during thermal treatment (Fig. 7.6). Raman spectrum of Rh-CeO$_2$ catalyst confirmed that after calcination the CeO$_2$ phase was more crystalline since the characteristic F_{2g} mode became more intense and sharper (Fig. 7.7). Also, the dehydration and decomposition of nitrate was confirmed by the disappearance of the bands at 3532 and 1048 cm^{-1} compared to the spectrum of the precursor. The coated foam had a surface area of around 11 m^2 g^{-1}, which corresponded to ca. 27 m^2 g$^{-1}_{coating}$. This value was slightly less than a half of surface area of the powder catalyst (Table 7.1).
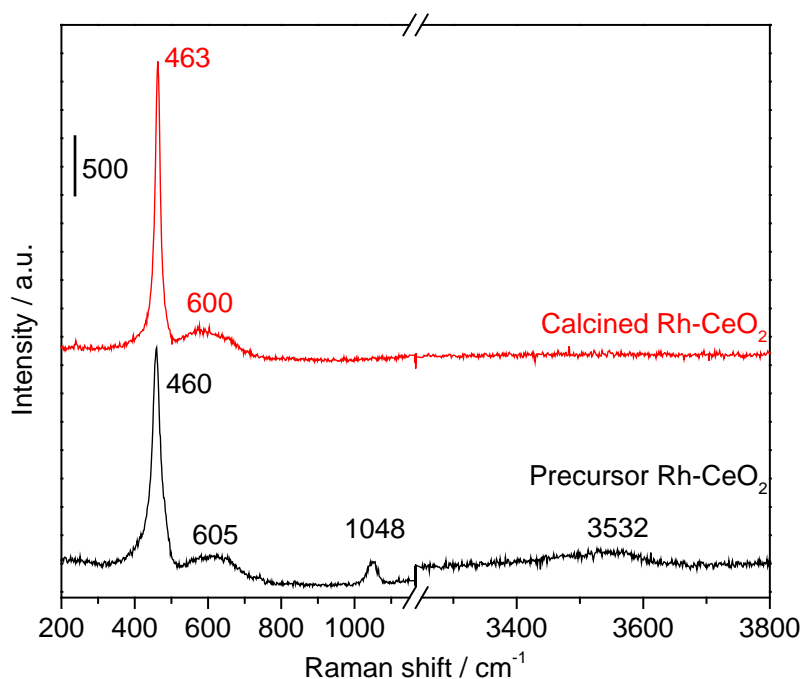
Figure 7.7. Raman spectra of Rh-CeO$_2$ structured catalyst.

H$_2$-TPR profile of Rh-CeO$_2$ structured and powder catalysts were displayed in Fig. 7.8. For Rh-CeO$_2$ structured catalysts, three distinct peaks of H$_2$ consumption were observed. The first one at ca. 180 °C was probably attributed to the reduction of Rh^{3+} species [7, 8], although the contribution of surface CeO$_2$ could not be discarded [47]. It was noted that this peak was shifted towards higher temperatures compared to the lowest temperature peak of a Rh-CeO$_2$ powder catalyst prepared by impregnation method [7, 8], but was slightly lower than that of the co-precipitated Rh-CeO$_2$ catalyst. It was, therefore, assumed that in the Rh-CeO$_2$ prepared by

electrodeposition or coprecipitation, Rh^{3+} species were well dispersed and strongly interacting with CeO_2 support compared to the one prepared by impregnation reported in the literature. The other two peaks of H_2 consumption centered at ca. 415 and 800 °C were assigned to the reduction of the surface and bulk Ce^{4+} species to Ce^{3+}, respectively [48]. These two peaks were different from those of $Rh-CeO_2$ powder catalysts, since in the structured catalyst, both two peaks were shifted to lower temperature. It was noted that in powder catalyst, the peaks at 268 and 375 °C could be contributed also from the reduction of surface CeO_2 [47]. It would appear that preparation method significantly influenced the redox properties of $Rh-CeO_2$ catalysts.
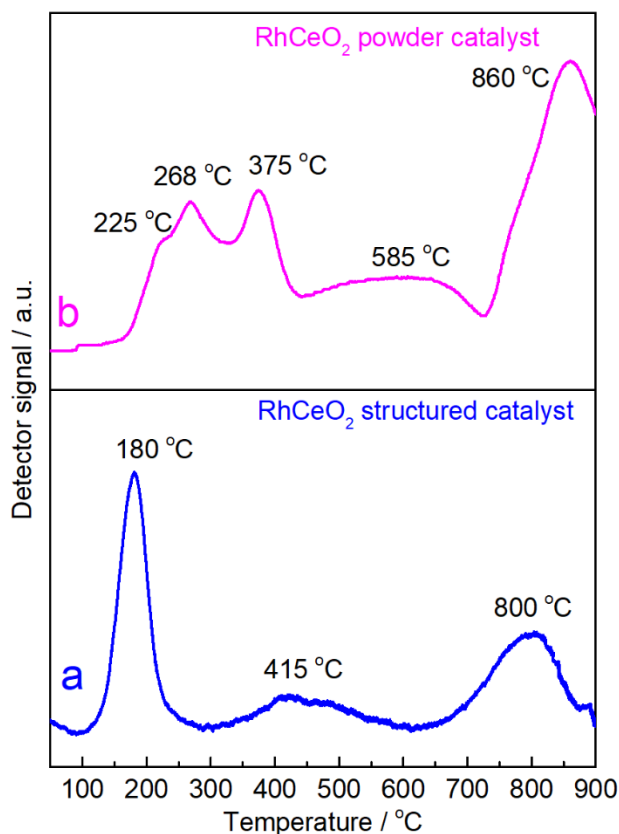
Figure 7.8. H_2-TPR of $Rh-CeO_2$ a) structured and b) powder catalyst.

7.3.1.3 Rh-HT catalyst

In the last case when ternary composition Rh/Mg/Al was deposited, the coating was thinner than those previously commented with a loading of 14.5 ± 2.7 wt.% (Table 7.1). Layer

thickness, estimated from SEM images where the cracks existed, ranged between 5–20 µm. The layer was composed of spherical and platelet-like nanoparticles (Fig. 7.9a-a2) as previously reported in chapter 4. The composition of the coating was also calculated from EDS spectra of three different samples and Rh/Mg/Al molar ratio was 1.8/72.6/25.6. In short summary, the morphology and composition of the coating were similar to the same type of catalyst reported in chapter 4, the solid loading, however, was higher even using a shorter coating time. The reason could be related to the lower density of the foam used in this work (about 1.8-fold) as previously explained for comparison of $Rh-CeO_2$ and $Pd-CeO_2$ catalyst in section 7.3.1.2. Secondly, it may be because of the foam size, since the volume of the foam was about 2.65-fold smaller than that of the one used in chapter 4. In the screening tests, under the same conditions, prolonging the synthesis time at 2000 s led to pore blockage in some locations.
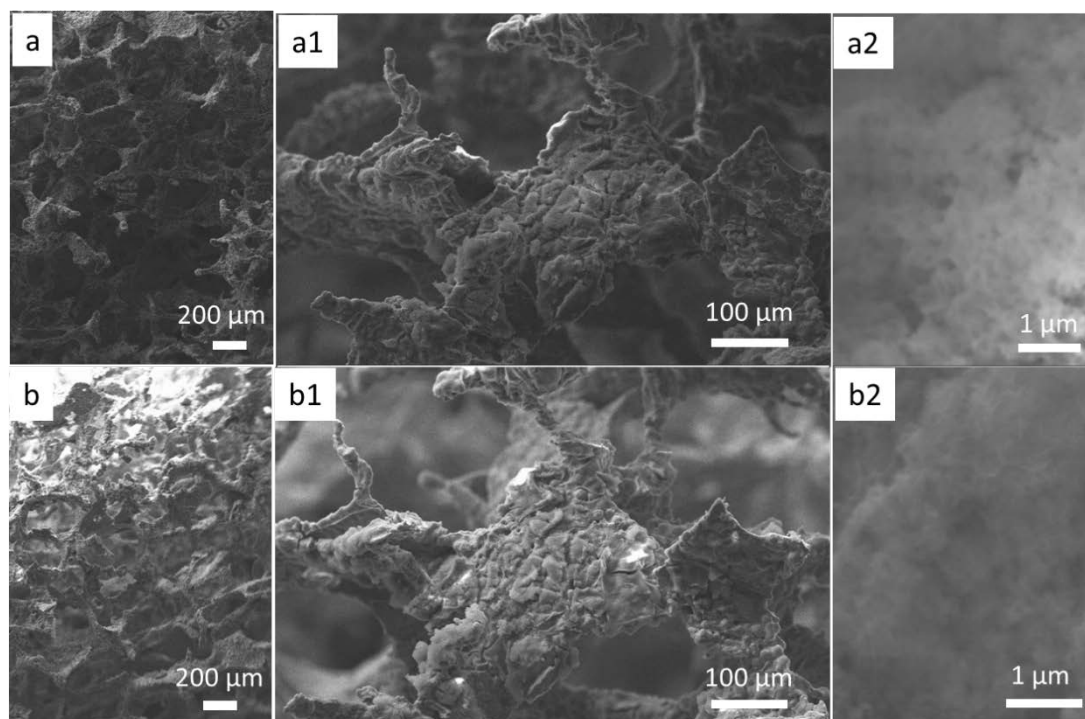
Figure 7.9. SEM images of open-cell foams coated with Rh-HT materials: electrodeposited (a, a1, a2) and calcined sample (b, b1, b2).

Calcination at 600 °C led to the formation of a mixed oxide with high surface area in which

Rh was incorporated, but did not largely alter the morphology and the size of the catalyst particles (Fig. 7.9b-b2). To further investigate the properties of the coating, the powder scratched from the foam surface was characterized by HRTEM and the results were displayed in Fig. 7.10. HRTEM image showed support particles with not well-defined shape (Fig 7.10a), small and homogeneous Rh species was observed in STEM/HAADF image (Fig. 7.10b). Average Rh-containing species particle size was ca. 2.0 ± 1.1 nm, which was in ideal range for N_2O decomposition as proposed by Beyer et al. [6]. SAED evidenced the presence of MgO (d-spacing 1.18 and 1.45 Å) and $MgAlO_x$ mixed oxide (d-spacing 2.05 and 2.41 Å) (Fig. 7.10a), characteristic of coprecipitated HT-derived compounds calcined at around 600 ^oC [49].
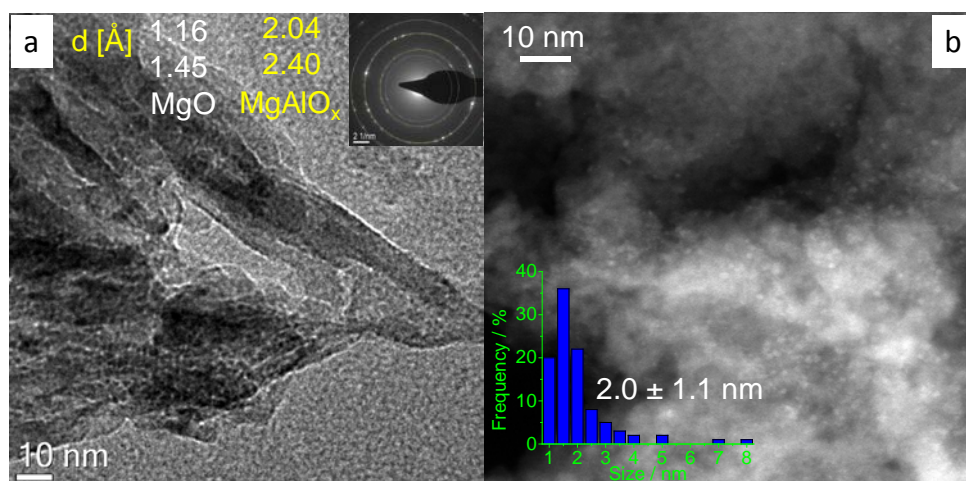
Figure 7.10. TEM images of Rh-HT catalyst: a) HRTEM (inset figure: SAED); b) STEM/HAADF (inset figure: particle size distribution).

The temperature profiles during H_2-reduction of Rh-HT powder and structured catalyst were displayed in Fig. 7.11. Only one maximum of hydrogen consumption peak at ca. 372 ^oC, attributed to the reduction of Rh^{3+} species in mixed oxide structure, was shown [49]. This peak was at higher temperature than that of the powder catalyst prepared by co-precipitation, indicating that Rh was more difficult to be reduced in the structured catalyst, which was possible due to effect of preparation methods, electrosynthesis and co-precipitation.
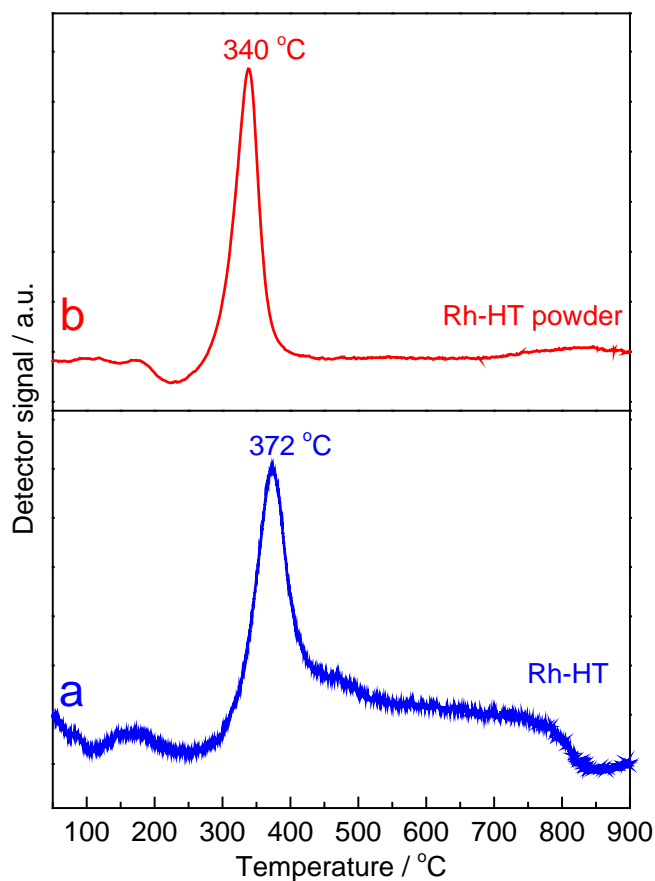
Figure 7.11. H_2-TPR of Rh-HT a) structured and b) powder catalysts.

Powder Rh-HT catalyst was further examined by XRD analyses and the results were displayed in Fig. 7.12. XRD patterns of Rh-HT powder catalyst confirmed typical characteristic of HT precursor and the mixed oxides obtained by calcination at 600 °C (Fig. 7.12) [50]. These phases agreed with those identified by SAED in HRTEM images of the structured catalyst. However, the calculated surface areas were significant different, about 289 $m^2 g^{-1}$ for the co-precipitation powder catalyst but only around 93 $m^2 g^{-1}$ for the coating of the structured catalyst (Table 7.1). This may be because of preparation methods.
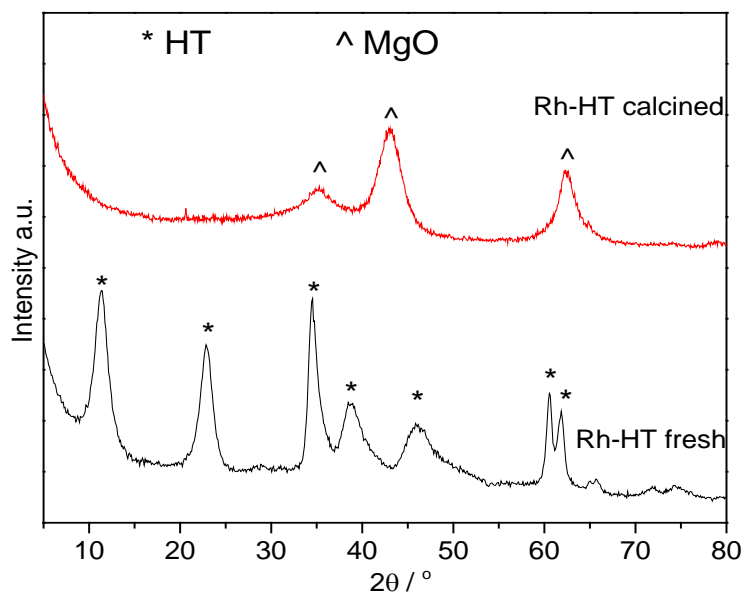
Figure 7.12. XRD patterns of Rh-HT powder prepared by coprecipitation.

In summary, the electrodeposition method allowed to coat FeCrAl open-cell foams with different kinds of catalytic materials (Co, Rh-CeO$_2$ and Rh-HT) which possessed quite similar characteristic of corresponding powder catalysts in terms of structure and redox properties. Thus, it was expected that these structured catalyst systems could exhibit good catalytic performances although they carry only a small amount of the solid materials. All three catalysts were therefore subjected to N$_2$O decomposition process and the results are discussed next section.

7.3.2 Catalytic tests

7.3.2.1 General comparison of three kinds of structured catalysts

For the N$_2$O decomposition tests, a pair of coated foams was loaded inside the quartz reactor. The total amount of actual catalysts, corresponding to the catalytic layers were approximately 25, 58, and 10 mg for Co, Rh-CeO$_2$, and Rh-HT, respectively. Decomposition of 0.1 vol.% N$_2$O/N$_2$ over the three types of catalysts at temperature 50 – 600 ^{o}C concerning both N$_2$O conversion and reaction rate were presented in Fig. 7.13. A pair of bare foams calcined at 600 ^{o}C was also tested under the same reaction conditions for comparison purposes.
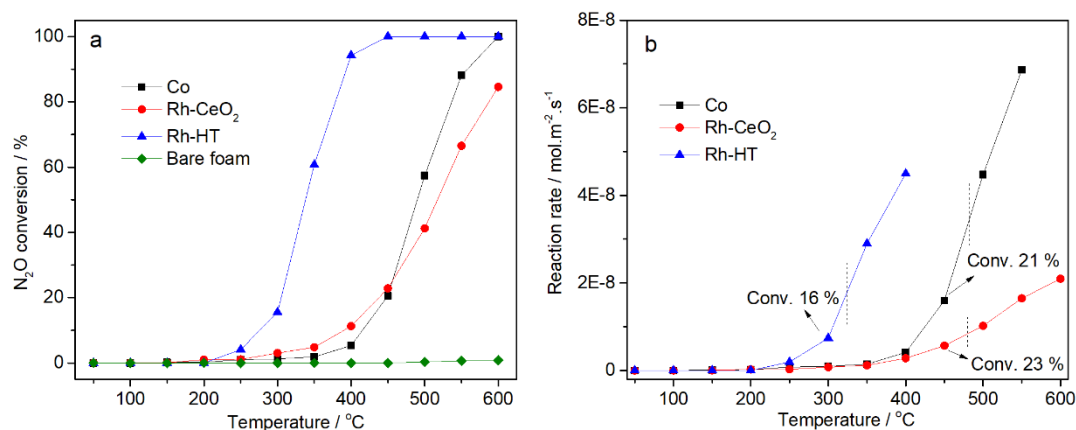
Figure 7.13. Catalytic decomposition of N_2O on open-cell foams coated with different materials: a) Light-off curves, b) Reaction rates. Reaction conditions: 80 mL min^{-1} of 1000 ppm N_2O/N_2, two coated foams. Dot lines in Figure b marked the left zones that the reaction rates were calculated at respectively low conversion.

The bare foam was inactive for N_2O decomposition showing a negligible conversion of N_2O at 600 $^{\circ}$C ($< 1\%$) (Fig. 7.13a). It was therefore stated that the bare foam was inert for this reaction. All the three catalysts were active for N_2O decomposition, but their performances were significantly different. Rh-HT was the most active, ignited at 250 $^{\circ}$C and reached full conversion of N_2O at 450 $^{\circ}$C. N_2O started to decompose on Co catalyst at 350 $^{\circ}$C and converted completely at 600 $^{\circ}$C. While Rh-CeO$_2$ exhibited the same ignition temperature as Co but obtained only 85 % of N_2O conversion at 600 $^{\circ}$C. T_{50}, temperature at which 50 % of N_2O was converted for three catalysts, followed the order: Rh-HT (335 $^{\circ}$C) < Co (490 $^{\circ}$C) < Rh-CeO$_2$ (515 $^{\circ}$C).

It was quite difficult to compare the N_2O decomposition performances of these types of catalysts and the ones reported in the literature due to dissimilarity in the reaction conditions. N_2O decomposition rate (r, also called turn over reaction rate TOR, nmol N_2O m^{-2} s^{-1}) may be an accurate assessment to do that [4]; the results of TOR for the structured catalysts used in this work are displayed in Fig. 7.13b and the TOR values at T_{50} were summarized in Table 7.1. In the following sections, the values obtained will be commented separately.

7.3.2.2 Cobalt catalyst

TOR of Co catalyst was 39 (nmol N_2O m^{-2} s^{-1}, at 490 ^oC), which was higher than the one of Co_3O_4 powder catalyst (less than 30 nmol N_2O m^{-2} s^{-1}, at 500 ^oC) reported by Kaczmarczyk et al. [21]. However, this value was lower than value of Co_3O_4 commercial powder catalyst (about 135 nmol N_2O m^{-2} s^{-1}, at 400 ^oC) reported by Maniak's group [18]. It was worthy to note that these results were performed in different reaction conditions. In a work with more similar reaction conditions (0.3 g catalyst, 90 mL min^{-1} of 1000 ppm N_2O/N_2) performed on Co_3O_4 powder catalyst prepared by combustion method, Franken et al. [17] presented a TOR of 24.3 nmol N_2O m^{-2} s^{-1} (calculated at T_{50} around 550 ^oC). To make a better comparison with pelletized catalysts, the Co_3O_4 catalyst prepared by coprecipitation was tested under the same reaction conditions but with 300 mg of catalyst and its TOR was around 7.3 nmol N_2O m^{-2} s^{-1}. It can be therefore highlighted that Co structured catalyst exhibited better TOR in comparison to Co_3O_4 powder catalyst prepared by combustion or precipitation method. This could be related to its high specific surface area, particle size, or the reducibility as reported regarding the effect of preparation method of Cobalt spinels on their activity of N_2O decomposition [16, 51]. The comparison of TOR of Co structured catalyst and other Co catalysts in literature was summarized in Table 7.2.

Table 7.2. Comparison of turn over reaction rate between Co structured catalyst and Co catalysts in literature

Preparation method	S_{BET} (m^2 g^{-1})	T_{max} H_2-TPR (^oC)	TOR (nmol N_2O m^{-2} s^{-1})	Ref
Combustion	4.2	ca. 410, 480	24.3 (550 ^oC)	[17]
Electrodeposition	17.8	ca. 350, 415	16.0 (450 ^oC) 39.0 (490 ^oC)	This thesis
Coprecipitation	24.7	406, 520	7.3 (450 ^oC)	This thesis
Commercial product	16.0*	ca. 415	135.0 (400 ^oC)	[18]
Co-precipitation	10.0	-	ca. 30.0 (500 ^oC)	[21]

* from supplier

7.3.2.3 Rh-CeO₂ catalyst

Rh-CeO$_2$ catalyst exhibited a TOR of 12.0 nmol N$_2$O m^{-2} s^{-1}, at 515 $^{\circ}$C (T$_{50}$) while Konsolakis calculated in his review [4] that 0.5 wt.% Rh-CeO$_2$ powder catalyst reached to TOR of 5.0 nmol N$_2$O m^{-2} s^{-1}, at light-off temperature 250 $^{\circ}$C (T$_{50}$ = 280 $^{\circ}$C). For comparison purposes, the results obtained with the Rh$_{0.15}$Ce$_{99.85}$O$_x$ powder catalyst prepared by precipitation method were reported. It was noted that 1.2 g of this catalyst (small pellet form 0.25-0.5 mm) not only occupied similar volume of the two coated foams, but also contained approximately the same Rh amount in the coating of the two foam catalysts (1.2 g Rh$_{0.15}$Ce$_{99.85}$O$_x$ vs 58 mg Rh$_3$Ce$_{97}$O$_x$). By this way, it was more comparable for comparison purposes, under similar GHSV and Rh loading. Comparison of both N$_2$O conversion and TOR between Rh-CeO$_2$ pelletized and structured catalyst were displayed in Fig. 7.14.
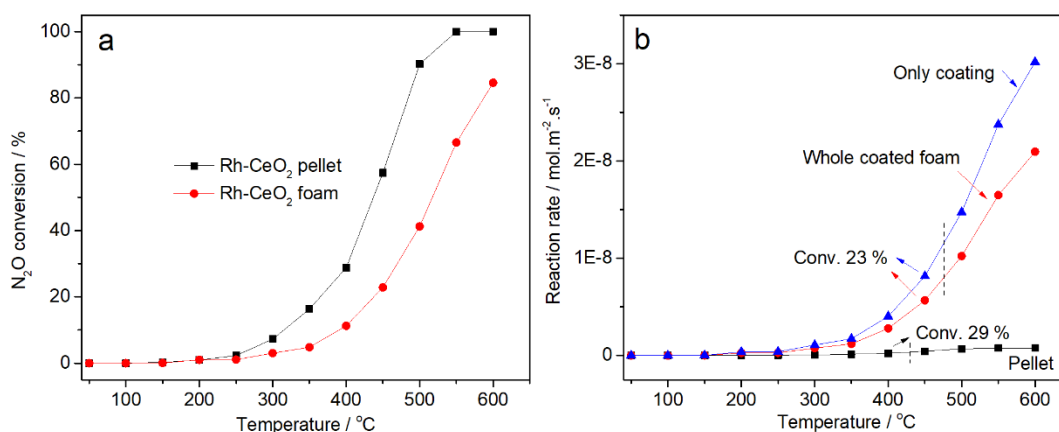
Figure 7.14. N$_2$O decomposition on Rh-CeO$_2$ structured and pellet catalysts: a) Light-off curves and b) Reaction rates calculated based on consideration either whole coated foam or only the coating, in comparison with pelletized catalyst. Dot lines in Figure b marked the left zones that the reaction rates were calculated at respectively low conversion.

The pelletized catalyst exhibited higher conversion than the foam catalyst at the same reaction temperature, but much lower TOR than those obtained for the foam calculated by either considering the whole coated foam or only the coating, the differences being more remarkable at temperatures above 400 $^{\circ}$C. For example, at 500 $^{\circ}$C, TOR of the coating was ca.

14.7 nmol N_2O m^{-2} s^{-1}, which was higher than the TOR of the whole foam (10.2 nmol N_2O m^{-2} s^{-1}) and much greater than that of the pelletized catalyst (only 0.7 nmol N_2O m^{-2} s^{-1}). The differences in catalytic performance of the two types of Rh-CeO$_2$ catalysts may be related to properties of the coating such as surface area, size of Rh particles, and reducibility. The present data just allowed to show about the possible enhancement of TOR on the foam catalyst.

7.3.2.4 Rh-HT catalyst

TOR of Rh-HT catalyst at T_{50} was 24.0 nmol N_2O m^{-2} s^{-1}, medium value among three catalysts, but it was not feasible to have similar data for comparison purpose from literature since the works reported the conversion versus temperature in unidentical reaction conditions than those used in this thesis. However, the light-off curve of this sample was quite close to the one reported by Centi et al. on the same type of material (1% N_2O/He, light off at 300 °C and full conversion at 490 °C) [12]. A comparison with coprecipitated catalyst in pellet form was also performed.

To keep the same GHSV in tests with foam and pelletized catalysts, 10 mg of Rh-HT pellet (0.25 – 0.5 mm particle size) was diluted with a HT-derived $Mg_{70}Al_{30}$ to obtain a catalyst bed of 1.4 cm in length, corresponding to the height of two coated foams of Rh-HT structured catalyst, and a comparison of the catalytic performances was displayed in Fig. 7.15. HT ($Mg_{70}Al_{30}$) played as an inert because its contribution for N_2O decomposition up to 500 °C was negligible. Pelletized catalyst only exhibited a slightly higher activity than the structured catalyst ($\Delta T_{50} = 20$ °C), but the ignition and the full N_2O conversion temperatures were almost the same (Fig.7.15a). As the reaction conditions were identical between the two cases, the differences in catalytic performances could be related to properties of the catalyst system such as amount of active phase and the role of the structured support. It was worthy to note that the amount of Rh in Rh-HT was slightly lower than nominal value as indicated in Table 7.1, this

could be the possible reason to explain why it was slightly less active than the pelletized one with nominal composition. Moreover, electrosynthesized Rh-HT structured catalyst guaranteed free alkali, while Rh-HT pellet prepared by coprecipitation may have some traces of residual Na, which could influence on the activity of the catalyst.

TOR based on either whole coated foam or only the coating was calculated and compared with the pelletized catalyst as shown in Fig. 7.15b. Whenever the reaction was ignited, the foam always provided higher TOR than that of the pelletized catalyst regardless of the two ways, TOR of the foam catalyst was calculated. The differences in TOR between foam and pellet catalysts were more significant when temperature increased up to 350 ^{o}C. At this temperature, when both catalysts did not reach a full conversion, the coating exhibited slightly higher TOR than that of the whole coated foam and almost double of TOR of the pellet catalysts (TOR_{pellet} = 18 < $TOR_{whole foam}$ = 29 < $TOR_{coating}$ = 34 nmol N_2O m^{-2} s^{-1}). It could probably be related to the enhancement of the foam support or the properties of electrosynthesized coating materials. Since there was a large difference in surface area between the pellet catalyst and the coating of the structured catalyst, further study is necessary to verify this point.

As Rh-HT was the most active catalyst based on T_{50}, it was selected for perform further tests in the presence of both O_2 and NO, and for carrying out a stability test under the presence of inhibitors NO and O_2 for 24 h, the results are displayed in Fig. 7.16. The catalyst was sensitive in the presence of O_2 and NO in the gas mixture. As a result, T_{50} was shifted to higher temperatures (455 ^{o}C) in comparison with the one (335 ^{o}C) in pure N_2O/N_2 stream as shown in Fig. 7.16a. The decreasing in the performance of N_2O decomposition in the co-existence of such species is one general issue of catalysts for N_2O decomposition due to their competitive adsorption on the active sites [29, 52].
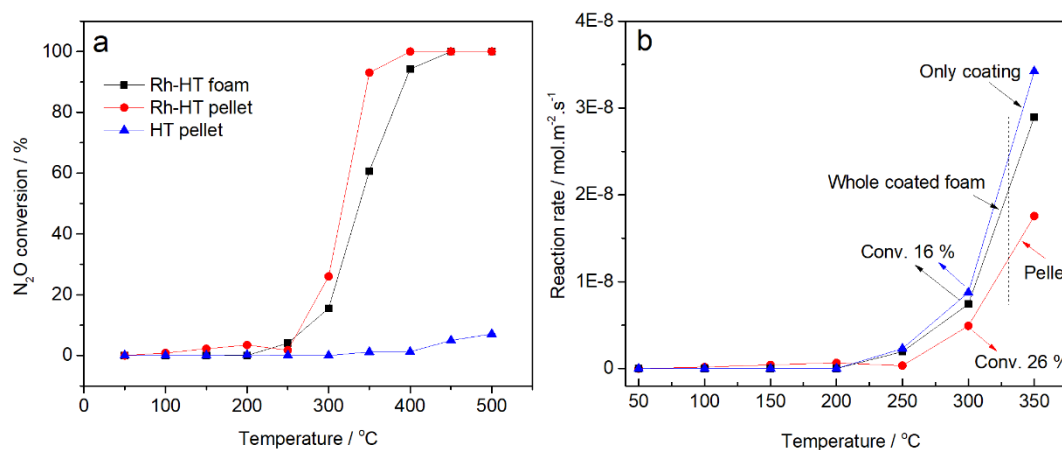
Figure 7.15. Comparison of structured and pellet catalyst ($Rh_2Mg_{70}Al_{28}$): a) Light-off curves and b) Reaction rates calculated based on consideration either whole coated foam or only the coating, in comparison with pelletized catalyst. Dot lines in Figure b marked the left zones that the reaction rates were calculated at respectively low conversion.

The catalyst was then submitted to a long-term test under the same feedstock but setting the oven temperature constant at 450 °C. The catalyst was slightly deactivated, and the catalytic activity went down from 60 to around 50% after 24 h (not shown). It was noted that the decrease in the activity may be due to a small amount of the catalyst on the foam. In fact this behavior may be common for the structured catalyst in general since the foam reactor operated close to intrinsic properties of the catalyst. The catalytic performance was highly sensitive to the catalyst deactivation, unlike the pelletized catalysts which may offer the advantage of a long-term buffer due to the larger amount of active materials [53]. The particle size of Rh species strongly influenced on the activity for N_2O decomposition, and the promising one was in range of 2.1 – 2.4 nm, while 1.2 – 1.4 nm range exhibited a lower performance as investigated by Beyer et al. [6].
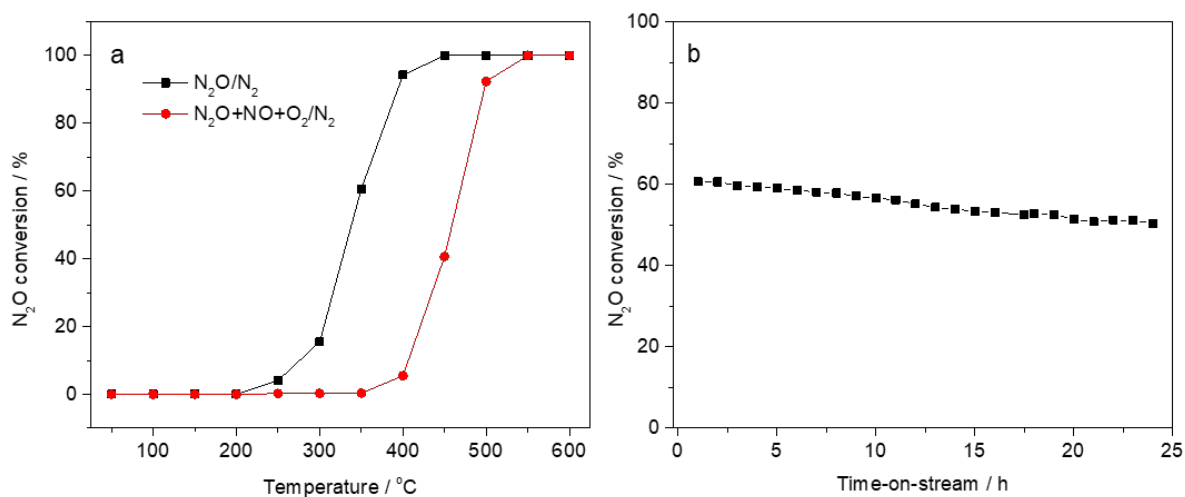
Figure 7.16. Catalytic decomposition of N_2O on Rh-HT catalyst: a) light off curves in presence of inhibitors and b) stability test.

7.3.3 Characterization of spent catalysts

7.3.3.1 Cobalt catalyst

After catalytic tests, SEM images revealed that both the adherence and morphology of the layers were almost the same as in the calcined catalyst without extension of the cracks (Fig. 7.17).
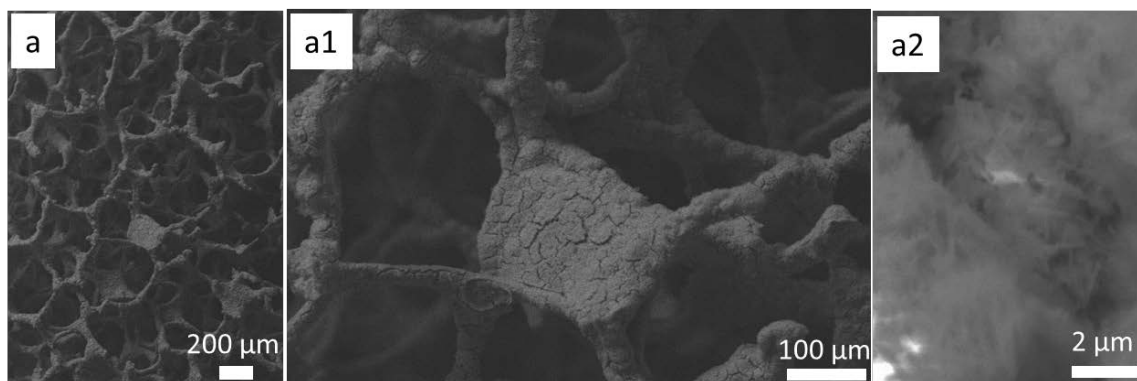
Figure 7.17. SEM images of spent Co structured catalyst.

To verify that there was no change in the phase after reaction, the catalyst was additionally examined by Raman analysis. Only the five peaks at 188 (F_{2g}), 468 (F_g), 510 (F_{2g}), 604 (F_{2g}), and 670 (A_{1g}) cm^{-1} associated with cubic Co_3O_4 structure were observed as in the Raman spectrum of calcined sample.

7.3.3.2 Rh-CeO₂ catalyst

Similar to Co catalyst, neither the adherence nor the morphology of the coating layer was modified after catalytic tests (Fig. 7.18). Although some detachments appeared, they may be related to the use of compressed air for removing the foams out of the reactor.

Figure 7.18. SEM images of spent Rh-CeO₂ structured catalyst.

In the Raman spectra, no remarkable changes either in the main CeO_2 F_{2g} mode (461 cm^{-1}) or in the shoulder at 600 cm^{-1} due to the presence of defects. The spectra of the spent catalyst also exhibited a less intense band at around 240 cm^{-1} (Fig. 7.19). This band could be due to the normal Raman inactive second order transverse acoustic (2TA) mode related to the presence of defects as observed in calcined CeO_2 sample (250 cm^{-1}) in chapter 6, or it was probably associated to RhO_x species as reported by Parres-Esclapez's group [10]. In addition, a small band at around 845 cm^{-1} may be assigned to the O-O stretching vibration of dioxygen species bound to two-electron defects on the CeO_2 surface [54]. This indicated that the catalytic process may modify the surface defects of the catalyst.
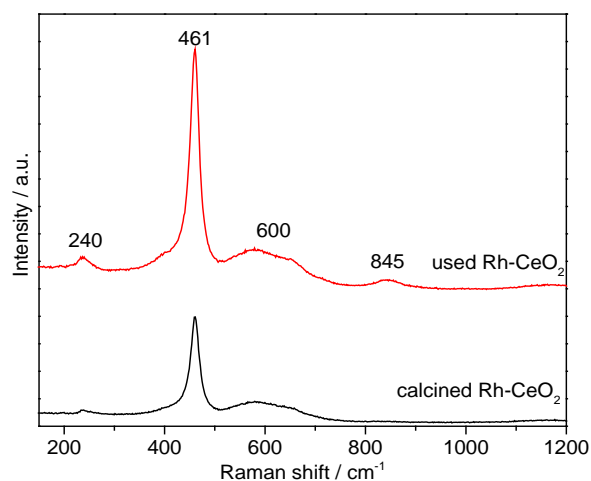

Figure 7.19. Raman spectra of calcined and used Rh-CeO₂ catalysts.

HRTEM was used to analyze Rh particle size of Rh-CeO$_2$ after catalytic test. However, Rh particles were hardly distinguished from Ceria support due to a low contrast between them [9]. STEM/HAADF images (Fig. 7.20) allowed to approximately estimate a small particle distribution in the range of ca. 3.1 ± 1.1 nm, these species may be probably related to Rh^{3+} species incorporated into matrice of oxide structures of Rh-based catalysts after calcination or under oxidation conditions during the catalytic tests [12]. Selected area electron diffraction (SAED) in a high magnification TEM image confirmed the presence of the fluorite structure of CeO$_2$ (d-spacing 1.88 and 3.13 Å) (Fig. 7.20a) in agreement with Raman and XRD characterization. Beyer and co-workers [6] investigated Rh-based catalysts on different supports and they proposed that 2.1 – 2.4 nm of Rh particle sizes would perform better catalytic activity for N$_2$O decomposition than a smaller one (1.0 – 1.4 nm). In fact, their Rh-CeO$_2$ (0.19 wt.% Rh, average particle size 1.2 nm) exhibited T$_{50}$ at 289 $^{\circ}$C for 1000 ppm N$_2$O + 5% O$_2$, but the catalyst was calcined at lower temperature (450 $^{\circ}$C) reduced in hydrogen flow before conducting the reaction. Unfortunately they did not report the activity in terms of reaction rate as this could provide a better way to compare the catalysts prepared by different methods and tested under different reaction conditions [4]. However, this may give a hint to improve the preparation method in terms of particle size control.
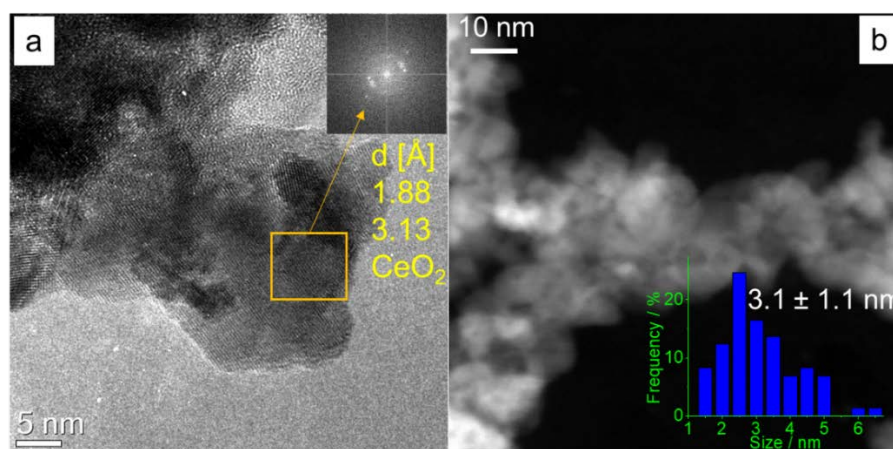

Figure 7.20. TEM images of Rh-CeO$_2$ spent catalyst: a) HRTEM image and FFT of the indicated region, b) STEM-HAADF image and particle size distribution.

7.3.3.3 Rh-HT

Like the first two catalysts – Co and $Rh-CeO_2$, the coating of Rh-HT spent sample was still stable without changing morphology or sintering (Fig. 7.21). In addition, the catalytic test conditions did not modify the textural properties of the spent catalyst since the surface area of the spent structured catalyst was around 8 m^2 g^{-1}, almost similar to surface area value of the calcined structured catalyst.
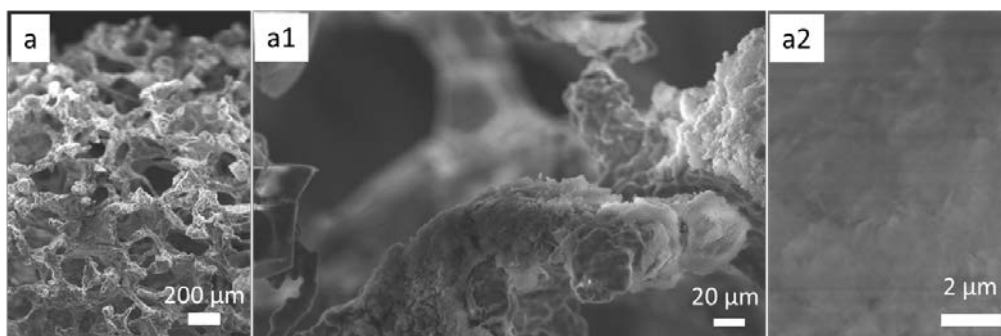
Figure 7.21. SEM images of Rh-HT spent catalyst.

In short summary for characterization part of the spent catalysts, the coatings of all three structured catalysts were still stable after the catalytic tests, and probably without changing in morphology and surface area. However, it was possible to have some changes in surface defects of $Rh-CeO_2$ catalyst. For Co and Rh-HT catalysts, present data was not sufficient to comment about this.

7.4 Conclusions

This chapter has demonstrated that the electrodeposition technique is able to coat small pore FeCrAl foams with variety of catalyst precursors containing either noble or non-noble metal materials like Co_3O_4, $Rh-CeO_2$, and Rh-HT. In all three cases, the coatings had a well-controlled composition, without pore blockage, and were stable during the calcination. The three catalysts were active for N_2O direct decomposition and the catalytic performances depended on the types of coating catalyst.

Under the tested reaction conditions, among the three, Rh-HT was the most active one and reached full conversion at 400 ºC, whereas Co reached complete conversion of N_2O at 600 ºC and Rh-CeO$_2$ even required a higher temperature. These values were not comparable with the ones in the literature, due to differences in both catalyst loading and reaction conditions. However, the catalytic performances of the structured catalysts were satisfactory in terms of turnover reaction rate, a more reliable parameter to compare catalysts tested under different reaction conditions. Remarkably, in comparison with small pelletized catalysts prepared by co-precipitation under appropriate reaction conditions (catalyst volume, active phase loading, feedstock), the structured catalysts exhibited much higher reaction rates.

Since it was the first time that open-cell foams coated by electrosynthesis were used as structured catalysts for N_2O abatement, the catalysts still need to be improved. Nevertheless, the feasibility of preparing structured catalyst integrating open-cell foam and catalyst precursors containing Co, Ce, Rh open a wide-range of applications of structured catalysts in environmental catalytic processes.

Chapter 7

7.5 References

1.   M. Strokal, C. Kroeze, Curr. Opin. Environ. Sus. 9-10 (2014) 108-121.

2.   B. A. Hungate, J. S. Dukes, M. R. Shaw, Y. Luo, C. B. Field, Science 302 (2003) 1512-1513.

3.   A. R. Ravishankara, J. S. Daniel, R. W. Portmann, Science 326 (2009) 123-125.

4.   M. Konsolakis, ACS Catal. 5 (2015) 6397-6421.

5.   K. Yuzaki, T. Yarimizu, K. Aoyagi, S. I. Ito, K. Kunimori, Catal. Today 45 (1998) 129-134.

6.   H. Beyer, J. Emmerich, K. Chatziapostolou, K. Köhler, Appl. Catal. A Gen. 391 (2011) 411-416.

7.   S. Imamura, J. I. Tadani, Y. Saito, Y. Okamoto, H. Jindai, C. Kaito, Appl. Catal. A Gen. 201 (2000) 121-127.

8.   A. Buenolopez, I. Suchbasanez, C. Salinasmartinezdelecea, J. Catal. 244 (2006) 102-112.

9.   S. Parres-Esclapez, M.J. Illán-Gómez, C.S.-M. de Lecea, A. Bueno-López, Appl. Catal. B Environ. 96 (2010) 370-378.

10.   S. Parres-Esclapez, I. Such-Basañez, M.J. Illán-Gómez, C. Salinas-Martínez de Lecea, A. Bueno-López, J. Catal. 276 (2010) 390-401.

11.   S. Alini, F. Basile, A. Bologna, T. Montanari, A. Vaccari, Stud. Surf. Sci. Catal. 143 (2000) 131-139.

12.   G. Centi, A. Galli, B. Montanari, S. Perathoner, A. Vaccaria, Catal. Today 35 (1997) 113-120.

13.   J. Pérez-Ramírez, J. Overeijnder, F. Kapteijn, J.A. Moulijn, Appl. Catal. B Environ. 23 (1999) 59-72.

14.   A. Martínez-Arias, J. Soria, J. C. Conesa, J. Catal. 168 (1997) 364-373.

15.   F. Cavani, F. Trifirò, A. Vaccari, Catal. Today 11 (1991) 173-301.

16.   G. Grzybek, S. Wójcik, K. Ciura, J. Gryboś, P. Indyka, M. Oszajca, P. Stelmachowski, S. Witkowski, M. Inger, M. Wilk, A. Kotarba, Z. Sojka, Appl. Catal. B Environ. 210 (2017) 34-44.

17.   T. Franken, R. Palkovits, Appl. Catal. B Environ. 176-177 (2015) 298-305.

18.   G. Maniak, P. Stelmachowski, A. Kotarba, Z. Sojka, V. Rico-Pérez, A. Bueno-López, Appl. Catal. B Environ. 136-137 (2013) 302-307.

19.   D. Pietrogiacomi, M. C. Campa, L. R. Carbone, S. Tuti, M. Occhiuzzi, Appl. Catal. B Environ. 187 (2016) 218-227.

20.   P. Stelmachowski, F. Zasada, G. Maniak, P. Granger, M. Inger, M. Wilk, A. Kotarba, Z. Sojka, Catal. Lett. 130 (2009) 637-641.

21.   J. Kaczmarczyk, F. Zasada, J. Janas, P. Indyka, W. Piskorz, A. Kotarba, Z. Sojka, ACS Catal. 6 (2016) 1235-1246.

22.   L. Xue, C. Zhang, H. He, Y. Teraoka, Catal. Today 126 (2007) 449-455.

23.   L. Xue, H. He, C. Liu, C. Zhang, B. Zhang, Environ. Sci. Technol. 43 (2009) 890-895.

24.   J. A. Z. Pieterse, R. W. Van Den Brink, Patent US 7901648 B2, 2011.

25.   U. Jantsch, J. Lund, M. Gorywoda, M. Kraus, Patent US 20090130010 A1, 2009.

26. B.W. Riley, J.R. Richmond, Patent US 5200162 A, 1993.

27. V. Boissel, S. Tahir, C. A. Koh, Appl. Catal. B Environ. 64 (2006) 234-242.

28. M. Konsolakis, F. Aligizou, G. Goula, I. V. Yentekakis, Chem. Eng. J. 230 (2013) 286-295.

29. V. Rico-Pérez, S. Parres-Esclapez, M. J. Illán-Gómez, C. Salinas-Martínez de Lecea, A. Bueno-López, Appl. Catal. B Environ. 107 (2011) 18-25.

30. S. Suárez, C. Saiz, M. Yates, J. A. Martin, P. Avila, J. Blanco, Appl. Catal. B Environ. 55 (2005) 57-64.

31. S. Suárez, M. Yates, A. L. Petre, J. A. Martín, P. Avila, J. Blanco, Appl. Catal. B Environ., 64 (2006) 302-311.

32. L. del Río, G. Marbán, Appl. Catal. B Environ., 126 (2012) 39-46.

33. R. Zhang, K. Hedjazi, B. Chen, Y. Li, Z. Lei, N. Liu, Catal. Today, 273 (2016) 273-285.

34. T. Zhou, L. Li, C. Jie, Q. Shen, Q. Xie, Z. Hao, Ceram. Int. 35 (2009) 3097-3101.

35. G. Centi, S. Perathoner, F. Vazzana, M. Marella, M. Tomaselli, M. Mantegazza, Adv. Environ. Res. 4 (2000) 325-338.

36. P. Benito, G. Nuyts, M. Monti, W. De Nolf, G. Fornasari, K. Janssens, E. Scavetta, A. Vaccari, Appl. Catal. B Environ. 179 (2015) 321-332.

37. P. Benito, W. de Nolf, G. Nuyts, M. Monti, G. Fornasari, F. Basile, K. Janssens, F. Ospitali, E. Scavetta, D. Tonelli, A. Vaccari, ACS Catal. 4 (2014) 3779-3790.

38. D.R. Lide (ed), CRC Hand book of Chemistry and Physics, 84th ed., CRC Press, Boca Raton, Florida, 2003.

39. C. Sist, G.P. Demopoulos, JOM 55 (2003) 42-46.

40. W. J. Zhou, M. W. Xu, D. D. Zhao, C. L. Xu, H. L. Li, Micropor. Mesopor. Mater. 117 (2009) 55-60.

41. V. Gupta, T. Kusahara, H. Toyama, S. Gupta, N. Miura, Electrochem. Commun. 9 (2007) 2315-2319.

42. V.V. Pushkarev, V.I. Kovalchuk, J.L. d'Itri, J. Phys. Chem. B 108 (2004) 5341-5348.

43. J. Yang, H. Liu, W. N. Martens, R. L. Frost, J. Phys. Chem. C 114 (2010) 111-119.

44. V.G. Hadjiev, M.N. Iliev, I.V. Vergilov, J. Phys. C Solid State Phys. 21 (1988) L199-L201.

45. J. Rahbani, N.M. Khashab, D. Patra, M. Al-Ghoul, J. Mater. Chem. 22 (2012) 16361-16369.

46. P. Stelmachowski, G. Maniak, J. Kaczmarczyk, F. Zasada, W. Piskorz, A. Kotarba, Z. Sojka, Appl. Catal. B Environ. 146 (2014) 105-111.

47. B. Bouchaud, J. Balmain, G. Bonnet, F. Pedraza, Electrochim. Acta 88 (2013) 798-806.

48. F. Giordano, A. Trovarelli, C. de Leitenburg, M. Giona, J. Catal. 193 (2000) 273-282.

49. F. Basile, G. Fornasari, M. Gazzano, A. Kiennemann, A. Vaccari, J. Catal. 217 (2003) 245-252.

50. M. Jabłońska, K. Nothdurft, M. Nocuń, V. Girman, R. Palkovits, Appl. Catal. B Environ. 207 (2017) 385-396.

51. M.A. Zamudio, S. Bensaid, D. Fino, N. Russo, Ind. Eng. Chem. Res. 50 (2011) 2622-2627.

52. S.S. Kim, S.J. Lee, S.C. Hong, Chem. Eng. J. 169 (2011) 173-179.

53. C. Perbandt, V. Bacher, M. Groves, M. Schwefer, R. Siefert, T. Turek, Chemie Ingenieur Technik 85 (2013) 705-709.

54. V.V. Pushkarev, V.I. Kovalchuk, J.L. d'Itri, J. Phys. Chem. B 108 (2004) 5341-5348.

CONCLUSION REMARKS AND OUTLOOK

Achieving an active and stable coating with controllable composition and solid loading is mandatory for the preparation of structured catalysts. The electrodeposition method was proposed by our research group to coat open-cell metallic foams (FeCrAl) with hydrotalcite-like (HT) compounds for catalytic purposes a decade ago, and the obtained catalysts showed promising activities for steam reforming and catalytic partial oxidation of CH$_4$ at the early state of the research. However, there were still some gaps regarding the control of the deposit amount and composition, limiting therefore its applicability. This thesis aimed to fulfill the gaps to improve the deposition of HT compounds and to widen its applicability in the preparation of several hydroxides and oxides active in environmental applications. The main remarks obtained from this thesis are summarized as below:

- During the electrodeposition of HTs using a nitrate electrolyte, water, oxygen and nitrate reduction took place simultaneously. All of them contributed to the increase of local pH near the foam surface, but nitrate reduction was the only one providing pH values suitable for the precipitation of HTs. This was a crucial factor to achieve the target coating layers in terms of composition and thickness for catalytic applications. However, it was not systematically reported in the literature since the method usually involved the preparation of a few-micron coatings.

- During the electrodeposition, the rates of OH$^-$ generation and consumption were improtant to maintain target pH. In this respect, metal nitrate concentration played a key role in the control of the coating properties, which determined the activity/stability of the structured catalysts, since it governed not only the amount and distribution of electrodeposited materials on foam surfaces, but also the initial steps of the precipitation process. It was also noted that the pore blockage might appear when

using a more concentrated electrolyte, but it could be controlled by adjusting both synthesis time and applied potential. In addition, the formation of insulating materials and/or the inadequate replenishment of the solution at the electrode-electrolyte interface should be considered during the electrodeposition as they might favor the uncontrolled deposition of layers of different composition. While the former was a "passive" factor and difficult to be controlled, the latter was an "active" parameter that could be enhanced by flowing the electrolyte.

- By using a modified electrochemical setup where the electrolyte was flown during the electrodeposition, 5-20 µm Rh/Mg/Al HT coatings were deposited on small pore foams (80 ppi FeCrAl) without pore blockage. The coating composition was similar to the nominal value of the electrolyte and coprecipitated-like catalytic coatings were obtained after calcination. Moreover, a $MgAl_2O_4$ thin film developed at the interface between the support and the coating by chemical interaction, enhancing the stability of the coating. Active and stable performances of the catalysts in the CPO of CH_4 were achieved, overcoming those obtained by the same types of catalysts in previous studies.

- Replacing the foam support from FeCrAl to NiCrAl, a pretreatment step was mandatory to deposit a similar coating in terms of loading and chemical-physical properties. The catalysts exhibited a satisfactory performance in the CPO of CH_4; however, it was slightly deactivated with increasing TOS, especially in concentrated gas, requiring a further study to verify if it was due to the coating activity and stability or it was influenced by Cr or Ni in the alloy.

- The modified method for the electrodeposition was utilized for the preparation of other catalytic systems for the use in energy and environmental processes. Its feasibility to coat small pore FeCrAl foams with $Pd-CeO_2$ materials was

demonstrated. The thickness and composition of the deposited layer was quite well controlled, and except in some locations where the Pd clusters were observed, the obtained Pd-CeO$_2$ coating showed some coprecipitated catalyst-like properties. The catalysts showed good performances for CO oxidation in terms of activity and stability, even after thermal cycles of shut-down and start-up at high GHSV (up to $4.5*10^6$ h^{-1}). It was noted that in sole CeO$_2$ deposition, a more compact and stable coating was easily obtained. Additionally, the coating thickness could be unchallenging controlled by adjusting the concentration of the electrolytic solution and synthesis time, opening many options for the preparation of catalysts based on ceria materials.

- Electrodeposited structured catalysts were also demonstrated active in the N$_2$O decomposition. Co$_3$O$_4$, Rh-CeO$_2$ and Rh-HT, coatings with well-controlled composition, high surface area and 15 – 30 µm thicknesses, showed much higher reaction rates than pelletized catalysts prepared by coprecipitation.

In this Ph.D. thesis, the electrodeposition technique was successfully improved and applied to coat different active phases on open-cell metallic foams of several materials and pore sizes. However, to have a better control on the layer growth, thereby avoiding the crack formation and propagation, and to apply the electrodeposition for large scale commercial applications further studies are necessary.